“Weet je wat zo leuk is aan deze dienst, dat is dat jullie, doctoraatsstudenten, zo vriendelijk, behulpzaam en attent zijn.”

– Ans

Examination committee

Prof. dr. ir. Mia Eeckhout (Chairperson)
Department of Food Technology, Safety and Health, Ghent University

Prof. dr. Gianvito Vilé
Department of Chemistry, Materials and Chemical Engineering “Giulio Natta”,
Politecnico di Milano, Italy

Prof. dr. Shoubhik Das
Department of Chemistry, University of Antwerp

Prof. dr. Kristof Van Hecke
Department of Chemistry, Ghent University

Prof. dr. Johan Winne
Department of Organic and Macromolecular Chemistry, Ghent University

Prof. dr. ir. Sven Mangelinckx (Secretary)
Department of Green Chemistry and Technology, Ghent University

Promotors Prof. dr. ir. Christian Stevens
Department of Green Chemistry and Technology
Faculty of Bioscience Engineering, Ghent University

Prof. dr. ir. Veronique Van Speybroeck
Department of Applied physics
Faculty of Engineering and Architecture, Ghent University
Department of Physics and astronomy
Faculty of Sciences, Ghent University

Dean Prof. dr. Els Van Damme

Rector Prof. dr. ir. Rik Van de Walle

GHENT UNIVERSITY

FACULTY OF BIOSCIENCE ENGINEERING

Synthesis and application of covalent triazine frameworks in heterogeneous catalysis

ir. Jonas Everaert

Thesis submitted in fulfillment of the requirements for the degree of doctor (PhD) of Bioscience Engineering: Chemistry and Bioprocess Technology

Dutch translation of the title

Synthese en toepassing van covalente triazine roosters in heterogene katalyse

To be cited as

Everaert, J. (2023). Synthesis and application of covalent triazine frameworks in heterogeneous catalysis. PhD thesis, Ghent University, Belgium.

Cover illustration

Created with Fotor

ISBN 978-94-6357-624-6

This research was funded by

2017–2018 Special Research Fund (BOF-GOA, Ghent University)
2018–2022 Research Foundation - Flanders (FWO)

Copyright © 2023 Jonas Everaert

The author and the promotors give the authorization to consult and to copy parts of this work for personal use only. Every other use is subject to the copyright laws. Permission to reproduce any material contained in this work should be obtained from the author.

Dankwoord

Table of contents

List of abbreviations

a.u.	arbitrary units
AC	activated carbon
acac	acetylacetone
anhyd	anhydrous
aq	aqueous
arom	aromatic
ATR	attenuated total reflectance
BET	Brunauer–Emmett–Teller
BPR	back pressure regulator
bpy	2,2'-bipyridine
br	broad
calcd	calculated
CMP	conjugated microporous polymer
cod	cycloocta-1,5-diene
COF	covalent organic framework
conv.	conversion
COSY	correlated spectroscopy
Cp*	pentamethylcyclopentadienyl anion
CTF	covalent triazine framework
d	doublet
DCE	di(4-cyanophenyl)ethyne
DCM	dichloromethane
DFT	density-functional theory
DME	1,2-dimethoxyethane
DMF	*N,N*-dimethylformamide
DMSO	dimethyl sulfoxide
DRIFT	diffuse reflectance infrared Fourier transform

EDX	energy-dispersive X-ray
EOF	element organic framework
eq	equivalent(s)
ESI	electrospray ionization
FR	flow rate
FT-IR	Fourier transform infrared
GC	gas chromatography
HAADF	high-angle annular dark-field
HCP	hypercrosslinked polymer
HMF	5-(hydroxymethyl)furfural
ICP	inductively coupled plasma
IUPAC	International Union of Pure and Applied Chemistry
J	coupling constant
LC	liquid chromatography
m	multiplet
m/z	mass-to-charge ratio
*m*CPBA	*meta*-chloroperbenzoic acid
MFC	mass flow controller
MLCT	metal-to-ligand charge transfer
mL_N	milliliter normal (at 273.15 K, 1 atm)
MOF	metal–organic framework
mp	melting point
MS	mass spectrometry
NHC	N-heterocyclic carbene
NIR	near infrared
NMR	nuclear magnetic resonance
OES	optical emission spectroscopy
PAF	porous aromatic framework
PE	petroleum ether
PIM	polymer of intrinsic microporosity
pK_a	logarithmic acid dissociation constant
PMO	periodic mesoporous organosilica
POP	porous organic polymer
ppm	parts per million
PTFE	polytetrafluoroethylene

PXRD	powder X-ray diffraction
Py	pyridine
q	quadruplet
QSDFT	quenched solid density-functional theory
quant.	quantitative
Quat	quaternary
R_f	retention factor
rpm	rotations per minute
rt	room temperature
s	singlet
STEM	scanning transmission electron microscopy
t	triplet
TfOH	trifluoromethanesulfonic acid (triflic acid)
TLC	thin layer chromatography
TMS	tetramethylsilane
TOS	time-on-stream
XPS	X-ray photoelectron spectroscopy
δ	chemical shift
Δ	reflux temperature
θ	diffraction angle
ν_{max}	IR absorbance wavenumber

Goals & outline

Catalysts are an essential tool in the transition to sustainable industries. In the chemical industry, they are indispensable because they enable, control and accelerate the production of products we use every day. Hence, scientists continuously seek to improve catalyst performance. The quest to improve the design, robustness and recyclability of catalysts has brought research to the heterogenization of metal complexes on nanoporous support materials. At the end of previous century, the field of nanoporous materials was truly revolutionized by the introduction of *reticular chemistry*. This concept, in which molecular building blocks are assembled into well-ordered frameworks held together by strong bonds, has led to a wealth of possible and tailor-made nanoporous materials. The *covalent triazine frameworks*, or CTFs, are a prime example which are at the forefront of materials science. These porous materials are made exclusively from organic building blocks and are receiving great attention due to their chemical and thermal robustness.

In order to make progress in the field of reticular materials at Ghent University, an alliance was formed between three research groups:

- the Synthesis, Bioresources and Bioorganic Chemistry Research Group (SynBioC, Department of Green Chemistry and Technology, Ghent University),
- the Centre for Ordered Materials, Organometallics and Catalysis (COMOC, Department of Chemistry, Ghent University),
- the Center for Molecular Modeling (CMM, Ghent University).

As part of the collaboration, the PhD thesis in hand focuses on the exploration of covalent triazine frameworks as next-generation materials in heterogeneous catalysis. Their high specific surface area, modular design and outstanding thermal and chemical stability make them ideal candidates as support materials to enhance the performance of metal catalysts. By carefully selecting the CTF building blocks, the pore size, shape and functionality of the CTFs can be tailored to a specific application. To ensure that the active metal complexes do not leach, they should be anchored to the support material with strong and stable bonds. Particularly attractive for this purpose are CTFs where polydentate ligands have been used as molecular building blocks to provide robust binding sites within the framework. The surface then acts as one of the ligands in the coordination sphere

of the metal center. The immobilization of metal complexes on solid supports is intended to preserve the reactivity of the homogeneous metal complexes, while improving the separability of the catalysts and enabling their reuse.

The primary goal of this work is to investigate the potential of CTFs in heterogeneous catalysis through the synthesis of CTF-based catalysts followed by their characterization and application in chemical reactions. In particular, the focus is on CTFs containing nitrogen ligands as ubiquitous ligands in coordination chemistry. A comprehensive evaluation of the catalysts in batch reactions is complemented by a study on the practical application of the catalysts in continuous flow reactions.

This PhD thesis consists of five chapters. An introduction to the research topic is given in **Chapter 1**, then the research results are presented in **Chapters 2–4**, followed by the Conclusions and Outlook in **Chapter 5**.

Chapter 1 provides a general introduction to CTFs and discusses the main synthetic strategies for obtaining these materials. A brief historical overview of porous materials shows how CTFs stands out from other materials. In addition, a literature review sheds light on their application in heterogeneous catalysis, with an emphasis on thermocatalytic reactions.

Chapter 2 describes the synthesis of a series of new N-heterocyclic ligands functionalized with cyano groups. The cyano functionalities allow these compounds to be used as valuable building blocks in the synthesis of CTFs, while the nitrogen functionalities enrich the materials with numerous chelating sites to firmly anchor active metal complexes. By expanding the set of experimentally available building blocks, CTFs with distinct properties can be developed, which may lead to improved materials for catalysis.

Chapter 3 reports on the immobilization of a Rh complex on a bipyridine-based CTF and the application of the heterogeneous catalyst for the transfer hydrogenation of N-heteroarenes to prominent scaffolds in drug design. Hydrogenation in water with sodium formate as a hydrogen source is an attractive alternative to traditional hydrogenation with high-pressure hydrogen gas due to the mild reaction conditions and operational simplicity. Complexes based on Rh are among the most active catalysts for this reaction but are very expensive. The development of a heterogeneous analog that can be reused is therefore considered highly desirable. In addition, the transfer hydrogenation with the CTF catalyst in continuous flow is described.

Since heterogeneous catalysts are particularly well suited for use in continuous flow chemistry, **Chapter 4** presents an exploratory study of CTFs in flow oxidation reactions. The ability of these nitrogen-rich frameworks to activate molecular oxygen is exploited for the liquid-phase oxidative coupling of benzylamine as a model reaction. Transferring the batch oxidation reaction to flow

offers advantages such as improved mass transfer of oxygen gas and safety. Besides, catalyst separation steps are avoided as the CTF remains located in the packed-bed reactor.

Chapter 5 concludes on the main findings in this dissertation and provides an outlook on this area of research.

Chapter 1

Introduction to covalent triazine frameworks in catalysis

Abstract | This chapter introduces covalent triazine frameworks, or CTFs, and presents a literature review concerning their application in heterogeneous catalysis. The emphasis here is placed on their use as support materials in thermocatalytic reactions. A brief chronicle of the evolution of porous materials outlines the emergence of CTFs and is followed by a discussion of the main synthetic strategies. Firstly, attention is given to the general concept of catalysis.

1 Catalysis

Our modern-day society relies heavily on the chemical industry. It provides us with medicines, fertilizers, food additives, fuels, synthetic materials, etc., products that have become indispensable in our daily lives. At the same time, however, the industry threatens human health and the environment through its emissions, waste disposal and consumption of resources. To address these threats, the concept of green chemistry and its twelve principles have been established. The goal of green chemistry is to find safer chemicals and novel processes that reduce the overall footprint of the production industry and eliminate the use of hazardous substances.[1] The importance of catalysis in this concept is highlighted by the ninth principle, which recognizes the superiority of catalysts over stoichiometric reagents.[2] Catalysts are essential to the chemical industry and are used today in more than 85% of all chemical processes.[3-4] Their importance will only increase as the need for sustainability is recognized, along with the need for processes that are less energy intensive and produce less waste. Hence, scientists continuously seek to improve catalyst performance in terms of activity, selectivity, and durability.

But what makes catalysts so special? The classic definition of a catalyst is: a substance that accelerates a chemical reaction without itself being consumed. It does this by providing an alternative reaction pathway that is much more energetically favorable, as illustrated in Figure 1.1.[5-6] As the reactants interact with the catalyst, the alternative pathway passes through various transition states that require significantly less activation energy (E_a). The activation energy to overcome is usually provided by thermal energy. Therefore, catalysts allow chemical transformations to occur at lower temperatures, thereby reducing the energy required for heating.

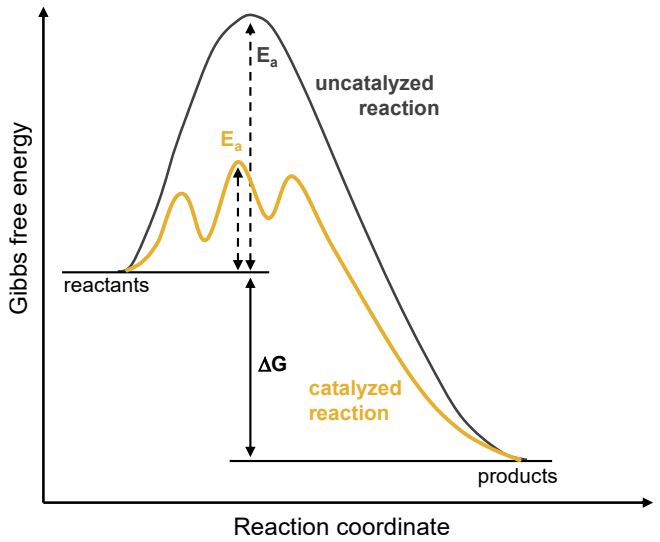

Figure 1.1. Schematic energy diagram for an uncatalyzed and catalyzed reaction. The overall activation energy required for the catalyzed reaction is much lower than that for the uncatalyzed reaction.

In addition to accelerating reactions, catalysts also control the selectivity of reactions that might otherwise give mixtures of products. The preferential promotion of one of the possible pathways maximizes yield and produces fewer unwanted side products.

Historically, the field of catalysis has been divided into three sub-disciplines: homogeneous catalysis, heterogeneous catalysis and biocatalysis. The latter involves the use of nature's catalysts, enzymes, to catalyze transformations. Enzymes exhibit excellent activities near room temperature and can catalyze reactions with exquisite selectivity, which arises from the specific three-dimensional structure of their active site.[7-8]

In homogeneous catalysis, the catalyst and reactants are in the same phase during the reaction. Coordination complexes are a prominent example. These catalysts generally consist of a discrete metal center surrounded by stabilizing organic ligands (Figure 1.2). The ligands provide the ability to fine-tune the catalytic performance with respect to activity, selectivity and stability, and range from a simple to highly sophisticated design.[9-10] Homogeneous metal complexes are typically well-defined compounds because their structure is easy to determine. Based on an understanding of their structure–activity relationship, a rational design of such catalysts can be achieved. However, being in the same phase as the reactants and products, separation and reuse of these expensive catalysts are often troublesome.[11]

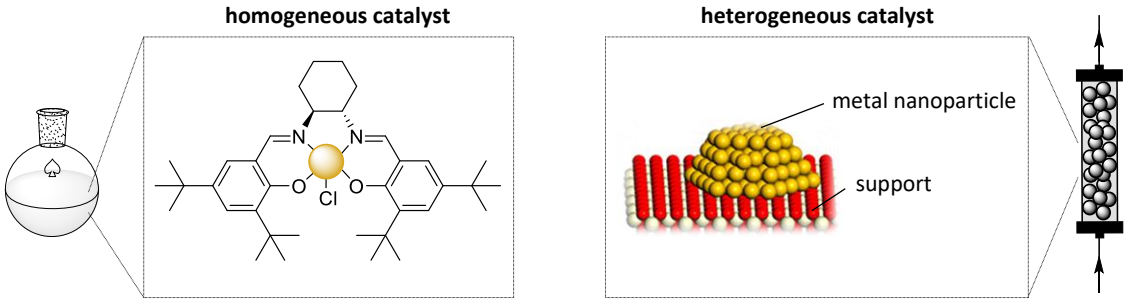

Figure 1.2. Two main types of catalysts: a metal complex as a homogeneous catalyst and a supported nanoparticle as a heterogeneous catalyst.

Heterogeneous catalysts are solids that catalyze reactions between molecules in the gas or liquid phase. The reaction then takes place at the interface. These catalysts have the advantage of being robust and easy to recover and reuse. In addition, they are more suitable for continuous processes because they can be fixed, for example, in a packed-bed reactor. In classical heterogeneous metal catalysis, the reaction takes place at the active sites of a solid metal surface. Since heterogeneous catalysis is a surface phenomenon, the activity of catalysts depends on the exposed surface area. To increase the surface area, particles are downsized to the nanoscale (1–10 nm). However, such nanoparticles tend to agglomerate and are therefore dispersed on high-surface-area solid supports (Figure 1.2).[12] Until recently, studies of heterogeneous catalysts have been largely

empirical, and a lack of understanding of the actual active sites has hampered the rational design of selective heterogeneous systems.[13-14] One strategy that bridges homogeneous and heterogeneous catalysis and combines the advantages of both is to anchor well-defined metal complexes on solid supports.[15-18] Typically, highly porous materials are used to host the metal complexes, as they provide a large surface area that allows for a high density of catalytic sites.

2 Nanoporous materials

Functional porous materials are of great interest because of their ability to interact with atoms, ions and molecules over a large internal surface area. Such materials have been widely exploited in a multitude of applications, covering gas adsorption, separation, catalysis, and sensing.[19] The pores in the materials are classified by the International Union of Pure and Applied Chemistry (IUPAC) according to their size: micropores have a diameter of less than 2 nm, mesopores between 2 and 50 nm, and pore sizes above 50 nm are classified as macropores.[20] Another way to group porous materials is by composition, with a distinction being made between inorganic, inorganic–organic composite, and organic materials. Here, a short historical overview of some breakthroughs in porous materials is given and how their evolution has contributed to the development of CTFs (Figure 1.3).

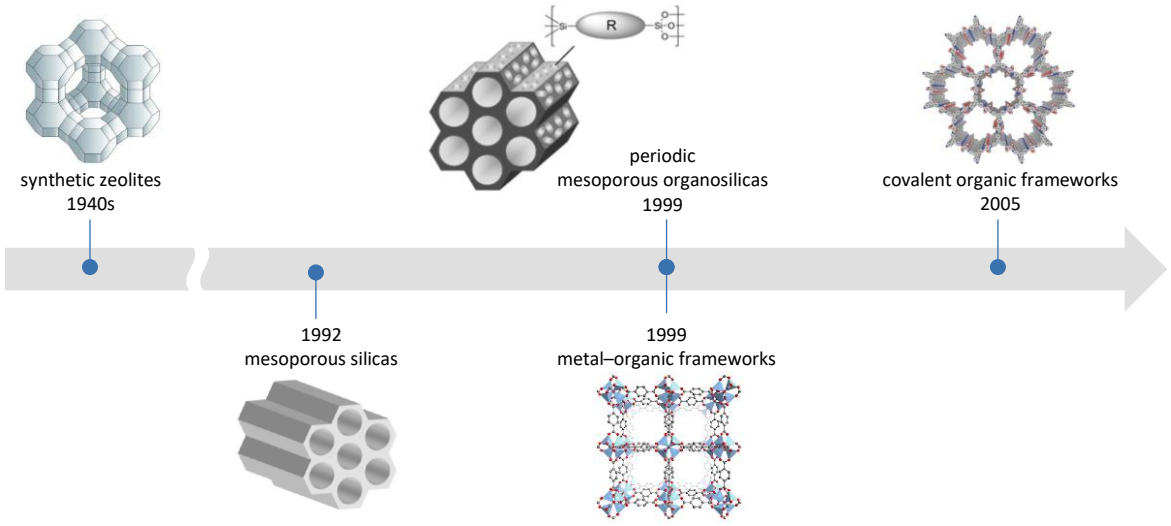

Figure 1.3. Milestones in the history of functional nanoporous materials.

Perhaps, the most representative material from the inorganic class of porous materials is zeolites. Zeolites are three-dimensional crystalline aluminosilicates with uniform pores of molecular dimensions (0.5–1.2 nm).[21-22] They occur naturally, but have been primarily produced synthetically since the 1940s and are widely used in catalytic cracking, adsorption and ion exchange applications.[23] Zeolites are the workhorses of today's chemical industry. However, their use is restricted by the limited ability to tailor the functionality of the material. In addition, their limited pore size makes zeolites inadequate for catalytic transformations involving bulky or branched molecules larger than their pore size. These shortcomings have led to an active search for materials which exceeded this pore-size limitation and are more amenable to rational synthesis. A real milestone was reached in 1992 when researchers at Mobil were able to prepare ordered mesoporous silicas by using micelles as template.[24-26] Materials could now be synthesized with unprecedented control over the pore size. The large pores of mesoporous silicas (2–50 nm) are able to accommodate much larger (bio)molecules, such as enzymes, and facilitate mass transfer.[27-29] Two well-established members of this family are MCM-41 and SBA-15.[25,30-31] These purely inorganic materials were soon followed by two prominent classes of hybrid organic–inorganic materials. The integration of organic moieties greatly expanded the diversity of porous materials and opened new avenues for tailoring the functionality toward high-end applications. One class consists of the periodic mesoporous organosilicas (PMOs), which were independently pioneered by Inagaki,[32] Stein,[33] and Ozin[34] in 1999. Their synthesis is very similar to that of MCM-type or SBA-type materials but employs organic bis-silane building blocks instead. Accordingly, the organic moieties are homogeneously distributed in the pore wall as an integral part of the framework.[35-36] A second class of hybrids includes the metal–organic frameworks or MOFs. By the work of Yaghi, a MOF whose pores did not collapse upon evacuation of their content made its debut in 1999.[37] Inspired by coordination chemistry, MOFs are composed of metal ions or metal clusters and rigid organic ligands that link the metallic centers to form crystalline, three-dimensional networks. Typical organic building blocks are carboxylic acids, N-heterocycles (especially imidazoles), phosphonic acids and sulfonic acids. By choice of the building blocks, different functionalities can be introduced and pores sizes can be tuned from microporous to mesoporous of almost 10 nm.[38-39] The materials are known for their record-breaking surface areas (> 6000 $m^2 g^{-1}$) and are therefore very promising in gas storage applications.[40-41] However, the use of MOFs in catalysis is limited to mild reactions because, with few exceptions, these materials generally have poor hydrothermal stability and are less chemically stable than zeolites.[42-43] In 2005, Yaghi *et al.* reported the successful synthesis of two crystalline, porous organic frameworks obtained by the condensation of phenylboronic acids.[44] Unlike MOFs, these materials did not contain any metal ions in their framework, but were composed entirely of rigid organic building blocks held together by strong covalent bonds. This pioneering research sparked the development of a new class of porous materials called covalent organic frameworks, or COFs, which will be discussed further in the following section.

In contrast to PMOs, where porosity is induced by a templated synthesis, porosity in MOFs and COFs is created by the self-templating of rigid building blocks into extended networks through strong covalent bonds. This so-called *reticular synthesis* approach allows a precise control of the pore size, topology, and functionalities of the materials, which are directed by the size, connectivity and geometry of the building blocks used in the assembling.[45-46] This concept allows materials to be designed with the best properties for their applications in mind. The modular construction and flexibility with which geometry, size and functionality of the building blocks can be varied, has led to an explosive growth of new porous materials having a diversity previously unknown.

3 Covalent organic frameworks

As mentioned above, COFs are entirely constructed from organic building blocks that are covalently linked together to form infinite network structures. Their constitution of only light elements, such as carbon, nitrogen, oxygen, boron and sulfur, makes them low-density materials, while the robust covalent bonds contribute to their high thermal and chemical stability. Depending on the geometry of the building blocks and their connectivity, COFs adopt either a two-dimensional (2D) or three-dimensional (3D) framework.[47-50] 2D COFs appear as layered structures as a consequence of the π–π stacking interactions between the large conjugated 2D sheets.[51] Due to their low weight, high specific surface area and modularity, COFs have been widely investigated in a multitude of potential application areas, including gas adsorption and separation,[52-53] energy storage,[54-55] heterogeneous catalysis,[56-57] photocatalysis,[58-59] sensing.[60-61]

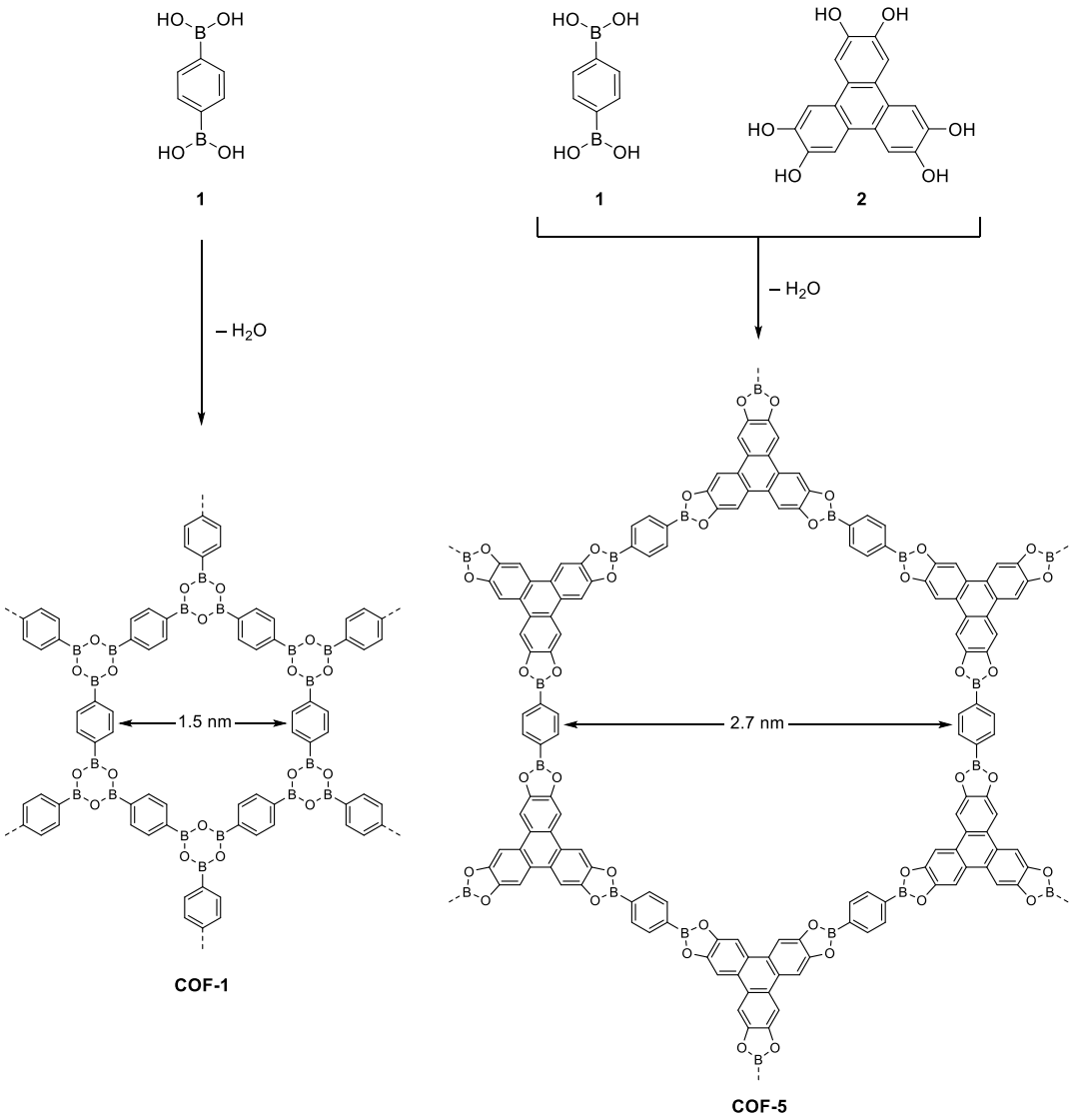

Scheme 1.1. Synthesis of the first COFs by condensation reaction with boronic acids.

For photocatalytic applications in particular, it is important that materials have a high degree of crystallinity. Amorphous materials generally perform worse as photocatalysts because the defects in the material disrupt the conjugation and prevent efficient charge separation and charge carrier mobility. In early studies, COF synthesis relied on the highly reversible condensation reaction with boronic acids to obtain crystalline frameworks (Scheme 1.1). During the synthesis, the reversibility of the bonds between the building blocks, or linkages, allowed self-correction of defects, resulting in highly crystalline structures. Unfortunately, the high reversibility was also reflected in the poor chemical stability of the material.[44,49] Hence, a trade-off had to be made between the degree of crystallinity and the chemical stability, which limited the applications. Since then, a myriad of linkage chemistries have been explored to result in COFs with improved chemical stability without (much) sacrifice of crystallinity.[62-63] A selection of these linkages is shown in Figure 1.4. To achieve crystallinity, reaction conditions need to be identified under which the building blocks can be linked with sufficient reversibility, which is in most cases a process of trial and error.

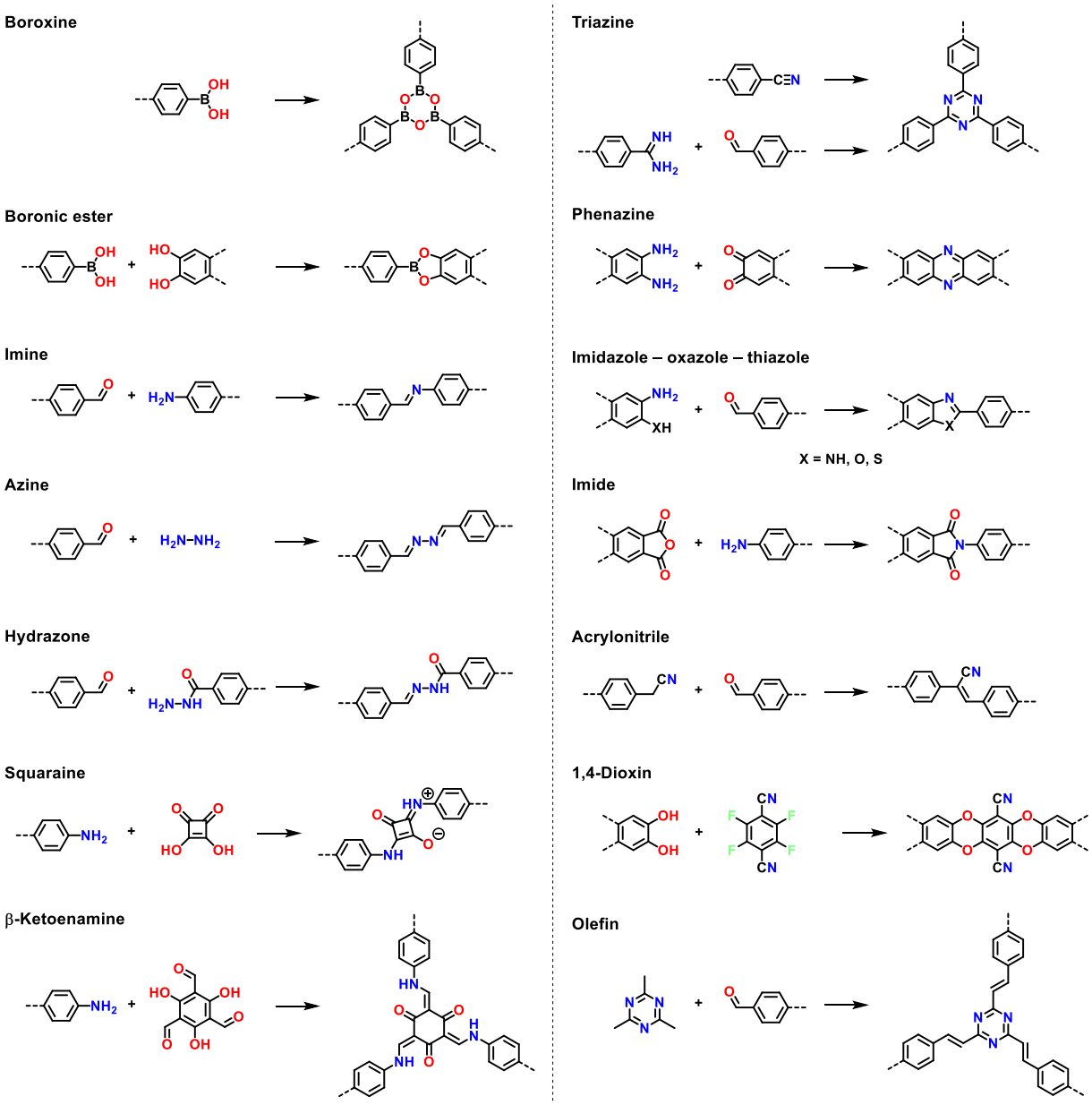

Figure 1.4. Selection of linkages explored for the synthesis of COFs.

In addition to well-ordered organic frameworks, amorphous analogs have been actively developed as well, and are all grouped under the umbrella of porous organic polymers (POPs). As crystallinity is no longer pursued in these polymers, additional linkage chemistries become available for their preparation, such as irreversible metal-catalyzed coupling reactions. POPs all share the characteristics of being highly porous, composed of lightweight elements, and bound by strong covalent bonds to hold their 2D or 3D structure.[64] The polymers are classified according to the type of linkage (Figure 1.5). One of the earliest POPs are the hypercrosslinked polymers (HCPs), which date back to the 1970s and are formed when solvent-swollen linear polystyrene chains are crosslinked by rigid bridges. A high degree of crosslinking prevents the collapse of the microporous structure. The crosslinking is typically achieved by a Friedel–Crafts reaction.[65] Polymers of intrinsic

microporosity (PIMs) were introduced in 2002 and are one-dimensional polymers composed of rigid twisted monomers that prevent an efficient packing of the chains and thereby induce microporosity.[66-67] Unlike typical POPs, PIMs can be soluble in solvents, which facilitates their solution processability, for example into thin films for batteries.[68] Conjugated microporous polymers (CMPs) are, as the name implies, fully conjugated in their backbone.[69] These polymers can be considered as the amorphous equivalent of COFs and their synthetic chemistries comprises the same condensation reactions as COFs, with the addition of metal-catalyzed coupling reactions.[64] A first example was developed in 2007 by the synthesis of poly(aryleneethynylene) network CMP-1 via a Sonogashira cross-coupling reaction. Closely related to CMPs are porous aromatic frameworks (PAFs), which are mainly synthesized via a Ni-catalyzed Yamamoto coupling reaction. However, PAFs do not possess extended π-conjugation due to the inclusion of sp^3-hybridized tetraphenylmethane nodes.[64,70] The Yamamoto coupling of tetrakis(4-bromophenyl)methane led in 2009 to PAF-1 as a first example. The polymer had an impressively high surface area of 5600 $m^2 g^{-1}$.[71] The silane, phosphorus, tin, antimony and bismuth analogs of PAFs are called element organic frameworks (EOFs).[72-74]

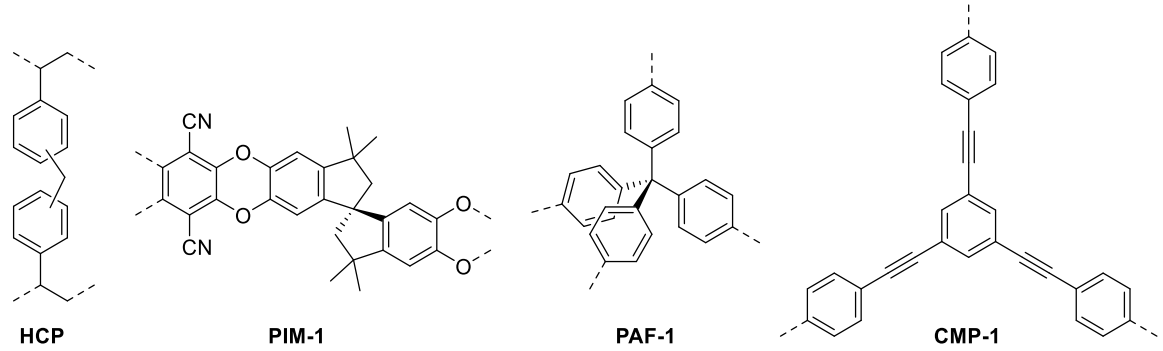

Figure 1.5. Examples of the different classes of POPs.

4 Covalent triazine frameworks

Of all the linkages explored, the triazine ring is one of the most stable ones, which prompted the development of an entire subclass of COFs, the covalent triazine frameworks (CTFs). These frameworks were first described in 2008 by Thomas and co-workers, who synthesized them from the trimerization of aromatic nitriles under ionothermal conditions (Scheme 1.2).[75] However, the formation of triazine oligomers by heating aromatic dinitriles was reported as early as 1962 by Toland, who used a series of metal halides as catalysts.[76] The method was further utilized by Vogel (Minnesota Mining and Manufacturing Co.)[77] in 1972 and by Miller (Texaco Inc.)[78] in 1973 to fabricate curable polymers. Thirty-five years later, Thomas *et al.* took up the polymerization concept and were the first to exploit the porosity of the triazine frameworks.

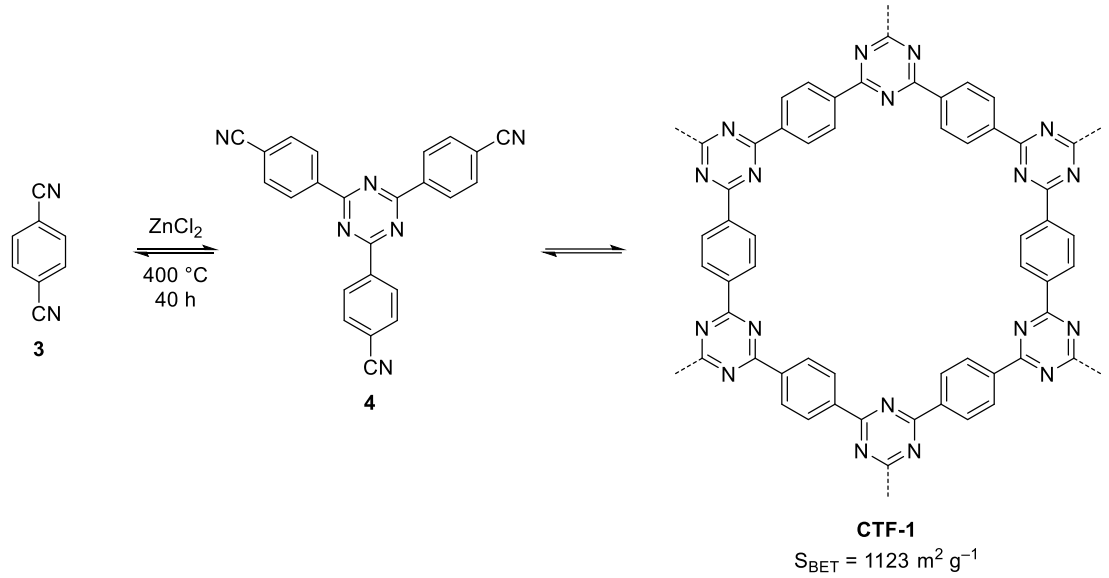

Scheme 1.2. Ionothermal trimerization reaction to synthesize CTF-1.

Due to the high strength of the triazine linkage, CTFs outperform many other COFs in terms of thermal and chemical stability. Thermal decomposition occurs only at temperatures above 400 °C and neither in strong acidic nor in basic environments do the materials show signs of degradation, as was demonstrated by Schüth *et al.*[79-80]

5 Synthetic strategies for CTFs

5.1 Ionothermal synthesis

While solvothermal methods are commonly used to prepare crystalline MOFs and COFs, an ionothermal approach was used to synthesize the first CTFs by Thomas *et al.* in 2008.[75,81-82] In this approach, the 1,3,5-triazine ring is formed by cyclotrimerization of aromatic nitrile monomers in the presence of excess zinc chloride ($ZnCl_2$). A temperature of or above 400 °C is used to ensure sufficient reversibility of the polymerization reaction. At these temperatures, $ZnCl_2$ melts and acts as both a solvent and as a Lewis acid that promotes the formation of triazine linkages.[75] To prevent escape of the aromatic building blocks by sublimation, the reaction is typically carried out in flame-sealed quartz ampoules, making the preparation of multiple reactions very time-consuming. Typical reaction times exceed 40 h to complete the polymerization process. Unfortunately, above 400 °C, decomposition reactions rapidly gain importance and provoke undesired carbonization of the polymeric scaffold, resulting in structural defects.[81-82] Consequently, the obtained CTFs present low degrees of crystallinity and appear as black powders. CTFs prepared by this method are generally amorphous with the exception of three examples so far, *i.e.*, CTF-0,[83] CTF-1,[75] and CTF-2.[84] These three CTFs are known to exhibit some degree of long-range order and are

respectively prepared from benzene-1,3,5-tricarbonitrile **5**, benzene-1,4-dicarbonitrile **3** and naphthalene-2,6-dicarbonitrile **6** (Figure 1.6).

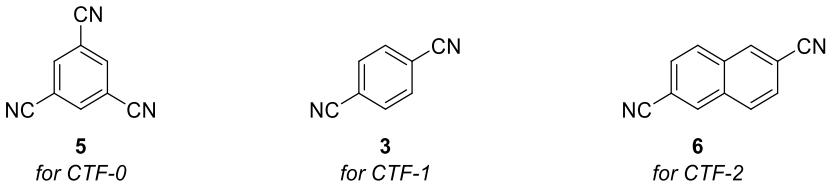

Figure 1.6. Building blocks which give crystalline CTFs in the ionothermal synthesis.

Lowering the reaction temperature to 300 °C reduces the degree of carbonization and yields yellowish CTFs, but requires extremely long reaction times. Even a period of seven days was not sufficient to complete the polymerization.[85] Instead, further increasing the synthesis temperature (> 600 °C) increases the surface area and mesoporosity of the CTFs. At higher temperatures, reopening of the triazine linkages can lead to local expansion of the network. Irreversible C–C bond formation then traps the locally expanded network with the formation of larger pores.[82,86] However, this comes at the expense of nitrogen content and structural integrity, which hinders the application as photocatalysts since the structural defects in the frameworks serve as charge carrier recombination sites.[85]

Although CTFs prepared by ionothermal polymerization generally lack a high degree of crystallinity, the CTFs possess high porosity and large specific surface areas. Accordingly, they show excellent performance in gas storage,[87-88] liquid-phase adsorption,[89-90] and as catalyst supports.[91] Various building blocks have been introduced into CTF materials, resulting in CTFs with different pore sizes and geometries, surface areas and functionalities. Figure 1.7 shows an overview of the most common building blocks.

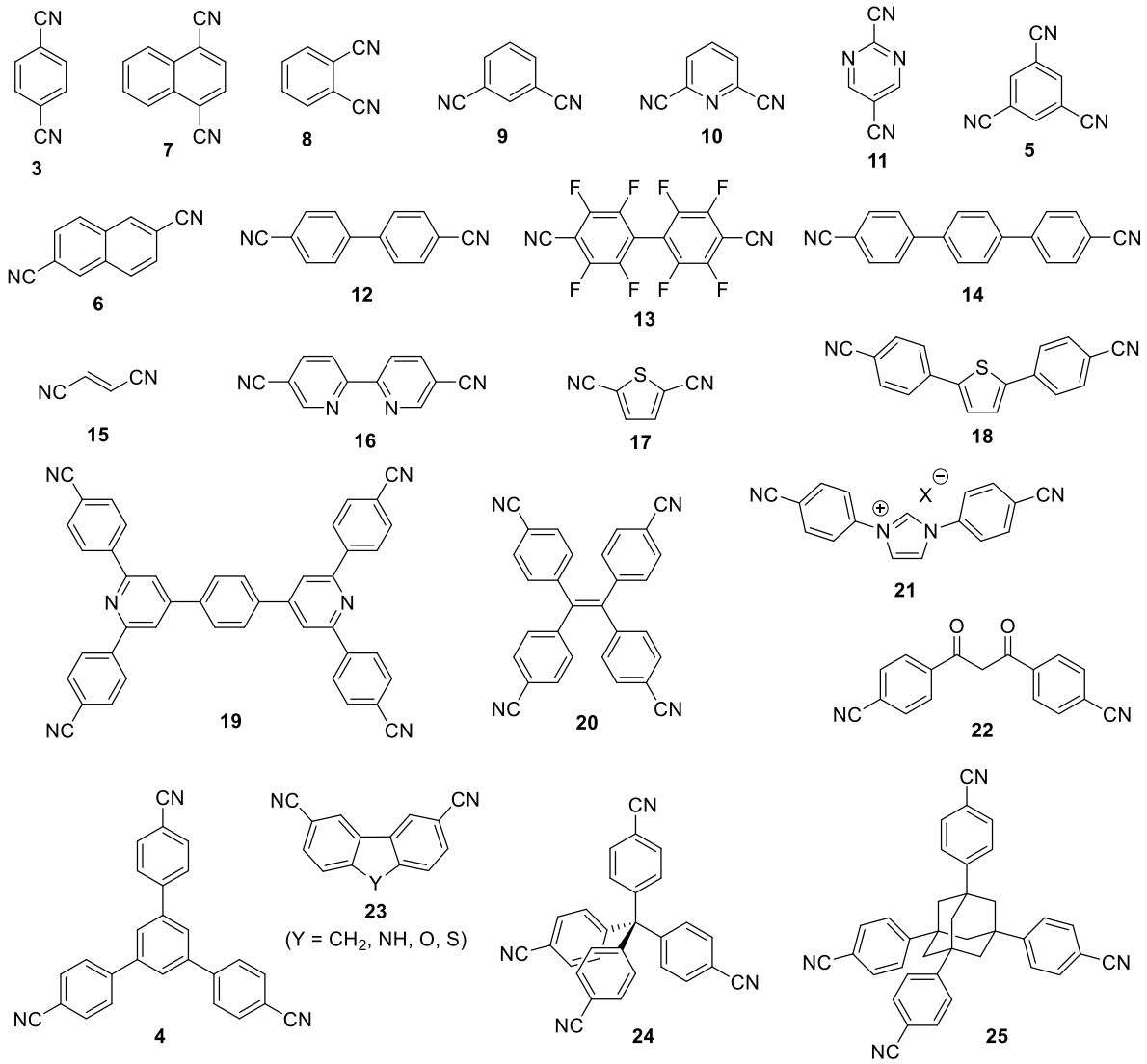

Figure 1.7. Common building blocks employed in the construction of CTFs.

Until recently, ionothermal synthesis was the conventional method for making CTFs. Unfortunately, the harsh conditions disrupt the long-range order of the materials and impose restrictions on the building blocks that can be used. In addition, the complete removal of metal residues ($ZnCl_2$) from the framework remains a challenge. Furthermore, due to carbonization, ionothermal CTFs are obtained as black powders with many structural defects and are hence excluded from applications involving interactions with visible light. It was therefore imperative to find new synthetic methods that require milder conditions. Over the past decade, other synthetic strategies have been developed, such as a phosphorus pentoxide-catalyzed method, a superacid-catalyzed method, amidine-based polycondensations, and a Friedel–Crafts method.

5.2 Condensation of amides

Instead of using nitriles to synthesize CTFs, Baek *et al.* (2018) employed aromatic primary amides as precursors and phosphorus pentoxide (P_4O_{10}) as the catalyst.[92] This approach produced highly ordered CTF-1 with a very high specific surface area of 2034 $m^2\ g^{-1}$. However, it requires temperatures as high as in the ionothermal synthesis (400 °C), which inevitably leads to some degree of carbonization. P_4O_{10} is known to convert amides into nitriles by dehydration and has also been reported to promote the trimerization of nitriles into triazines.[93-94] Hence, this method can also be applied with nitriles as monomers.[95] However, the crystallinity and porosity were higher for CTFs synthesized from amides than for CTFs synthesized from nitriles. Therefore, it was questioned whether the conversion of amides into CTFs involved the nitriles as intermediate or not. Subsequent research by Baek *et al.* (2021) indicated that direct condensation of the amides into triazine rings is the main pathway, rather than an indirect pathway in which the amides are first dehydrated to nitriles followed by the trimerization into triazine rings (Figure 1.8).[95] The condensation of amide monomers produces water, which reacts with P_4O_{10} to form phosphoric acid (H_3PO_4). The presence of these acidic protons has been shown to be beneficial for the crystallinity of the framework and may explain the discrepancy in crystallinity between amide- and nitrile-derived CTFs. This was recently also confirmed by Xu and co-workers (2022), who identified polyphosphoric acid ($H_6P_4O_{13}$) as a cheap yet highly efficient catalyst for CTF synthesis.[96] A series of highly ordered, albeit black-colored, CTFs with high specific surface area could be prepared by heating the nitrile monomers with a slight excess of polyphosphoric acid at 400 °C.

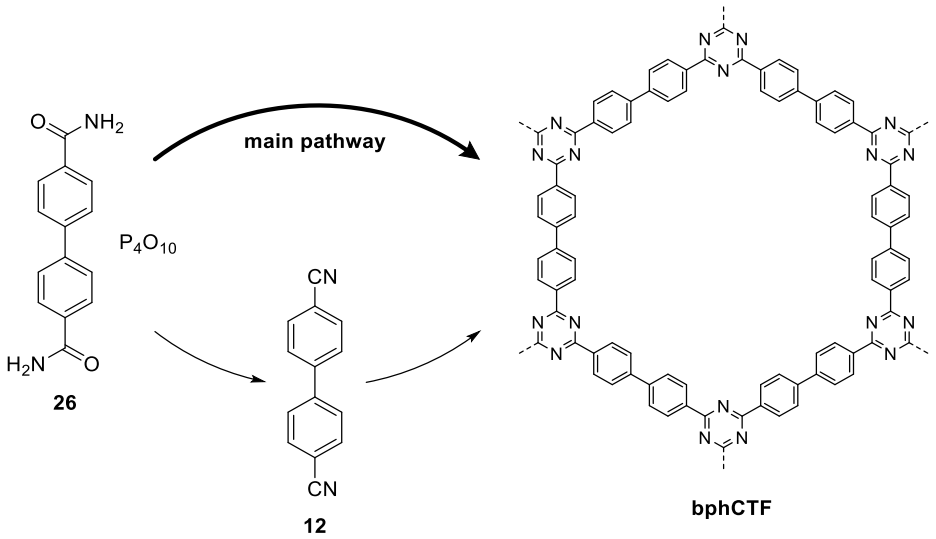

Figure 1.8. Amide trimerization occurs via direct condensation rather than via an indirect pathway to yield crystalline CTFs.

5.3 Superacid-catalyzed approach

In 2012, Cooper's group and Dai's group independently reported an alternative method for the synthesis of CTFs.[97-98] They employed the Brønsted superacid trifluoromethanesulfonic acid (TfOH) to activate the nitrile groups for trimerization. The synthesis can be done at room temperature, or with microwave irradiation (110 °C) for shorter reaction times. The building blocks can be used as such or dissolved in a solvent such as chloroform. This method offers several advantages over the ionothermal method, such as a reduction of reaction time from > 40 h to 10 min–16 h, circumvention of carbonization, and the removal of metal residues (Zn) is no longer an issue. CTFs produced by this approach appear as colored solids and have fluorescent properties, giving them potential in optoelectronic devices, photocatalysis and sensing applications.[99] However, most of the resulting CTFs suffer from a poor crystallinity. Moreover, specific surface areas and pore volumes are generally lower than those of CTFs obtained by ionothermal synthesis.

To overcome these shortcoming, a number of modified acid-catalyzed methods have been reported, including the use of silica templates in combination with TfOH vapors at 100 °C to form highly porous hollow or mesoporous CTFs.[100-101] Another method yielded highly ordered CTFs with high surface areas after a two-step transformation. In this method, neat monomers were first exposed to TfOH vapors at 250 °C for 12 h, followed by a brief thermal treatment of the material at 350 °C for 2 h.[102] In a recent advance, Xu's group was able to shorten the process by using microwave irradiation. Mixtures of monomer and TfOH were heated under constant microwave irradiation to obtain crystalline CTFs within 20 minutes.[103] High temperatures of 225 °C were reached for only a few minutes, thereby preserving the structural order. Reproducibility and scalability up to the hundred-gram level highlight the industrial viability of this method.

5.4 Amidine-based polycondensation approach

In 2017, Tan *et al.* developed a synthesis in solution based on the polycondensation between amidine hydrochlorides and aldehydes.[104-105] The reaction is typically carried out with cesium carbonate (Cs_2CO_3) as the base and dimethyl sulfoxide (DMSO) as the optimal solvent, and proceeds under gradual gentle heating (from 60 to 120 °C) for more than four days, without the need for an inert atmosphere. The formation of triazine linkages involves the reversible formation of a Schiff base and Michael adduct, followed by an irreversible cyclization and dehydrogenation (Scheme 1.3). This method proceeds without carbonization and yields colored CTFs, but the materials generally lack long-range order and are amorphous in nature.

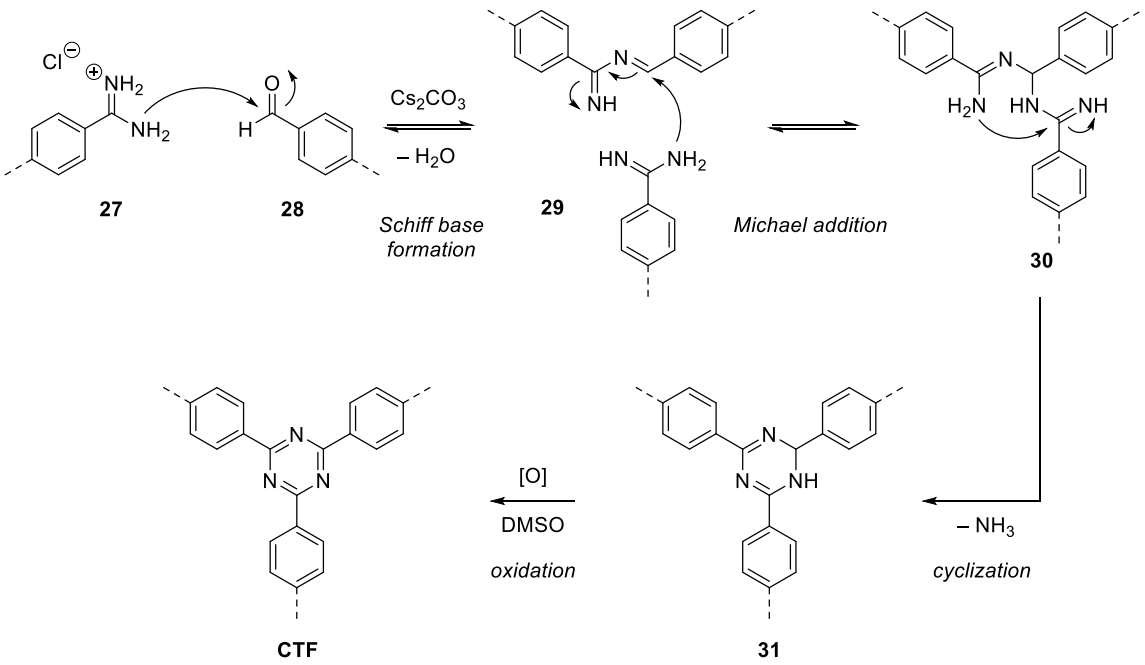

Scheme 1.3. Cascade reactions in the formation of CTFs from amidine hydrochloride and aldehyde precursors.

Later, the same group developed strategies to slow down the nucleation process and crystal growth in order to produce crystalline CTFs. Accordingly, amidine hydrochloride monomers are used in combination with benzylic alcohols. The corresponding aldehyde is then slowly generated *in situ* by oxidation of the alcohol in DMSO.[106] Another key factor affecting the reaction rate is temperature. It is critical to keep the polymerization reaction at a low temperature (100 °C) in the initial step to ensure slow oxidation of the alcohol. Subsequently, an elevated temperature (180 °C) promotes crystal growth and improves the crystallinity of the material. This strategy yields highly crystalline CTFs with improved photocatalytic performance compared to amorphous CTFs. A second strategy to reduce the number of nuclei in the reaction system involves the controlled addition of one of the monomers. For example, the slow feeding of aldehyde into the system produces materials with excellent crystallinity.[107-108]

Besides benzylic alcohols, benzylic amines can also be employed in the polycondensation reaction, thereby extending the range of suitable monomers available.[109] In this method, the crystallinity of the CTFs is also significantly influenced by the selected base, as the base adjusts the reversibility of the Schiff base formation and Michael addition reaction steps. A trend toward higher crystallinity for stronger bases was observed by Zhang *et al.*, reaching the highest crystallinity with KO*t*Bu as the strongest base in the screening.[109]

Due to the relatively low temperatures and practical setup, the amidine-based polycondensation method represents a highly promising methodology for the synthesis of CTFs in future research. The CTFs synthesized by this method are well-ordered and retain their photoactive properties which unlocks their use in photocatalysis. However, a drawback of this method is the limited

availability of commercial amidines. Thus, the amidine monomer has yet to be synthesized, which can be quite challenging.[110]

5.5 Friedel–Crafts reaction

Porous CTFs have also been synthesized by a simple Friedel–Crafts reaction of cyanuric chloride **32** and electron-rich aromatic building blocks.[111-113] The polymerization proceeds via electrophilic aromatic substitution and is typically carried out in dichloromethane under reflux conditions with an excess of anhydrous $AlCl_3$ or methanesulfonic acid as the catalyst (Scheme 1.4).[114] Unlike the aforementioned approaches, in this method the triazine moiety is introduced from the beginning and not generated during the synthesis of the CTF. Since the building blocks do not have the requisite of bearing functional groups, they are often readily available and inexpensive. The resulting materials have high surface areas (> 1000 $m^2\ g^{-1}$) but are completely amorphous.

A mechanochemical Friedel–Crafts method was applied by Troschke *et al.* (2017) for the synthesis of a series of CTFs. By performing the reaction in a ball mill, frameworks with specific surface areas up to 590 $m^2\ g^{-1}$ and a narrow pore size distribution were obtained in quantitative yields in less than 3 h. The method has the advantage of being solvent-free and is therefore promising for scale-up production.[115]

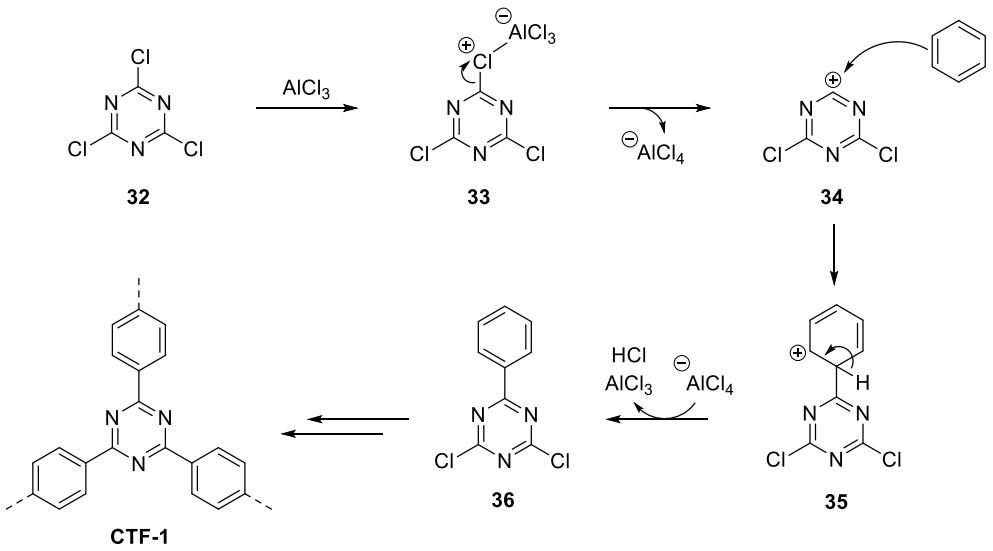

Scheme 1.4. Synthesis of CTF-1 via Friedel–Crafts reaction of cyanuric chloride **32** and benzene.

6 CTFs as support materials in catalysis

The high nitrogen content and excellent robustness of CTFs make them particularly attractive for catalytic applications.[80,91] In catalytic reactions, a CTF can act either as a catalyst itself or as a support material for active metal species.[116-117] A typical reaction in which CTFs have been used as

catalysts themselves, is the cycloaddition of CO_2 with epoxides to form cyclic carbonates.[83,118-121] The oxidation of benzylic alcohols and imines and the reduction of nitroarenes have also been reported.[122-124] In addition, CTFs have also been developed for photocatalysis, for example in the photocatalytic water splitting.[125-126] As a support, the numerous nitrogen functionalities improve the metal–support interaction and thus the resistance of metal particles to agglomeration and associated deactivation.[127] The modular nature of CTFs allows the embedding of ligand motifs in the backbone, to which metal complexes can firmly coordinate and mimic their homogeneous analog. This allows the reactivity and selectivity of the metal complex to be maintained while improving the separability and durability of the catalyst.

The following part concerns a review of the literature wherein CTFs have been applied as metal supports in thermocatalytic reactions. The CTFs for these applications are usually synthesized by the ionothermal synthesis method, unless otherwise stated.

A first example demonstrating the potential of CTFs as metal support was reported by Schüth and co-workers.[79,128] The authors prepared a CTF from 2,6-dicyanopyridine **10** and took advantage of the numerous 2,2'-bipyridine motifs in the framework to coordinate $PtCl_2$ using K_2PtCl_4 as a precursor (Scheme 1.5). In this way, the resulting heterogeneous Pt catalyst resembled the known molecular Periana's catalyst **37**.[129] Pt-CTF exhibited similar high activity (turnover numbers (TONs) ~300) and selectivity as the homogeneous catalyst for the direct, low-temperature oxidation of methane by SO_3 in fuming sulfuric acid at 215 °C. The catalytic reaction yields methanol as methyl bisulfate. The electron-withdrawing effect of the sulfate group provides product protection by inhibiting further oxidation. Hydrolysis of methyl bisulfate liberates the desired methanol. Remarkably, despite the drastic reaction conditions, the activity of the catalyst was well maintained over at least six catalytic runs. This illustrates the remarkable strength of the CTF material and its strong coordination ability towards metal cations.

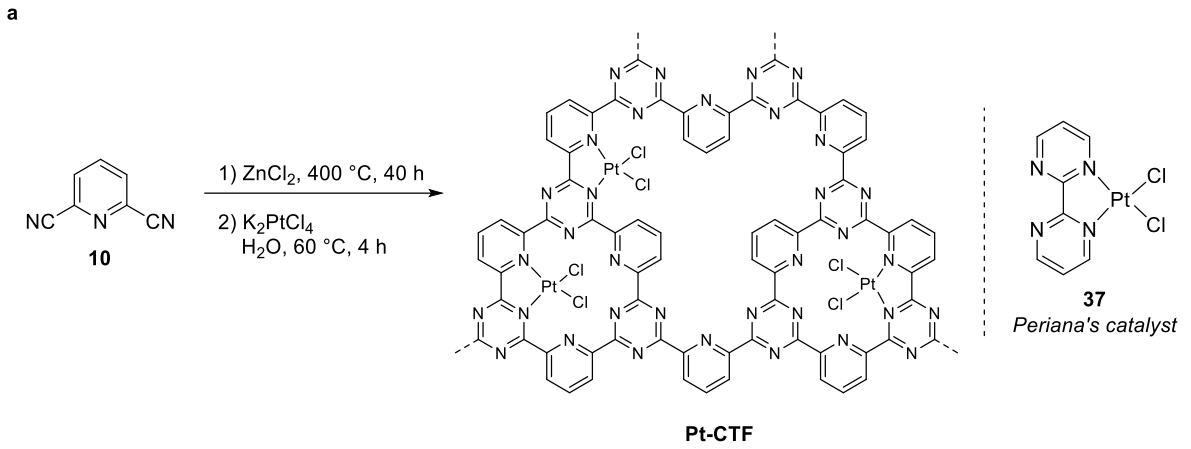

Scheme 1.5. (a) Synthesis of Pt-CTF as heterogeneous analog of Periana's catalyst **37**. (b) Selective oxidation of methane to methanol via the methyl bisulfate intermediate.

Thomas and co-workers immobilized Pd nanoparticles on CTF-1 (Pd/CTF) and compared its catalytic performance in the oxidation of glycerol **38** with that of Pd nanoparticles on activated carbon (Pd/AC) (Scheme 1.6).[130] Both catalysts showed similar activity in the first run. However, upon reuse, a strong deactivation was already observed for Pd/AC, while Pd/CTF showed a decreasing activity only after the fourth run. The activity loss of both materials was attributed to the agglomeration of Pd particles as observed by transmission electron microscopy (TEM). For Pd/CTF, however, the agglomeration was slowed down due to the numerous nitrogen functionalities that improve the interaction of the nanoparticle with the support.

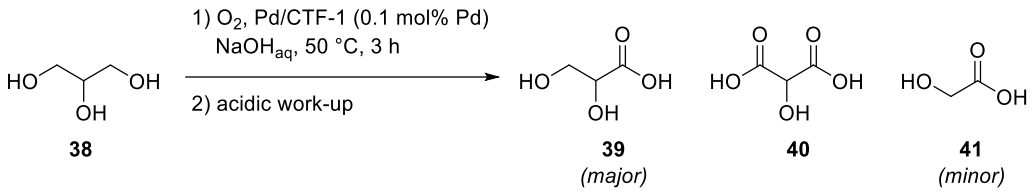

Scheme 1.6. Oxidation of glycerol catalyzed by Pd/CTF-1.

The synthesis of CTFs makes support materials with a high nitrogen content readily accessible. The beneficial effect of the nitrogen functionalities was further demonstrated by Chan-Thaw *et al*.[131] Pd nanoparticles stabilized on CTF-1 and nitrogen-doped carbon nanotubes were smaller and more uniform in size than those on activated carbon and carbon nanotubes. This in turn enhanced their catalytic activity as illustrated for the aerobic oxidation of benzyl alcohol to benzaldehyde.

Due to the higher nitrogen content, the durability of Pd/CTF was superior to that of Pd on nitrogen-doped carbon nanotubes.

The superior catalytic activity of CTF-supported Pd nanoparticles over activated-carbon-supported Pd nanoparticles was also highlighted by He *et al.* in the hydrogenation of N-heteroarenes with H_2.[132] For each N-heteroarene, the reaction with Pd/CTF-1 proceeded faster than with conventional Pd/AC, up to 3.6 times faster in the case of *N*-methylpyrrole hydrogenation. The superior reactivity of Pd/CTF-1 was also reflected in the hydrogenation of 1,10-phenanthroline **42** (Scheme 1.7). In contrast to Pd/AC, the hydrogenation with Pd/CTF-1 afforded the further hydrogenated octahydro-product **44**. TEM images of Pd/CTF-1 showed well-dispersed Pd nanoparticles that were significantly smaller than those on activated carbon. The high activity of Pd/CTF-1 was further attributed to the increase in electron density on the Pd nanoparticles governed by the electron-rich nitrogen functionalities in the CTF.

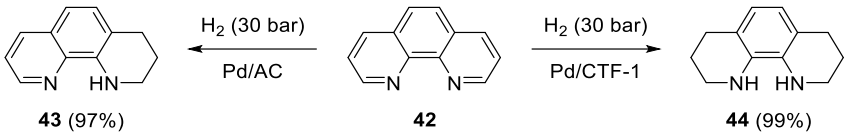

43 (97%) **42** **44** (99%)

Scheme 1.7. Hydrogenation of 1,10-phenanthroline with Pd/AC and Pd/CTF-1.

Motivated by the high efficiencies of half-sandwich Ru, Rh, Ir–bipyridine complexes for the homogeneous reduction of CO_2 to formic acid and for the reverse reaction, considerable efforts have been devoted to immobilize these metal complexes on CTFs as efficient and reusable heterogeneous catalysts.[133]

Gascon *et al.* anchored a molecular Cp*Ir(III) complex (Cp* = η^5-pentamethylcyclopentadienyl anion) onto a mixed-linker CTF for the production of hydrogen gas from aqueous formic acid (Scheme 1.8).[134] The CTF was constructed from 2,6-pyridinedicarbonitrile **10** and 4,4'-biphenyldicarbonitrile **12** in a 1/2 ratio. While the biphenyl monomer induced mesoporosity to enhance reactant diffusion, the pyridine moieties introduced bipyridinic coordination sites with inherent basicity. The air-stable Cp*Ir@CTF proved to be highly active and durable, achieving record-high turnover frequencies (TOFs) up to 27 000 h^{-1} and attaining TONs up to 1.06 x 10^6 under continuous feeding. Interestingly, no auxiliary base was required for the catalyst to operate efficiently, as the deprotonation of formic acid was mediated by the pyridinic moieties in the framework.

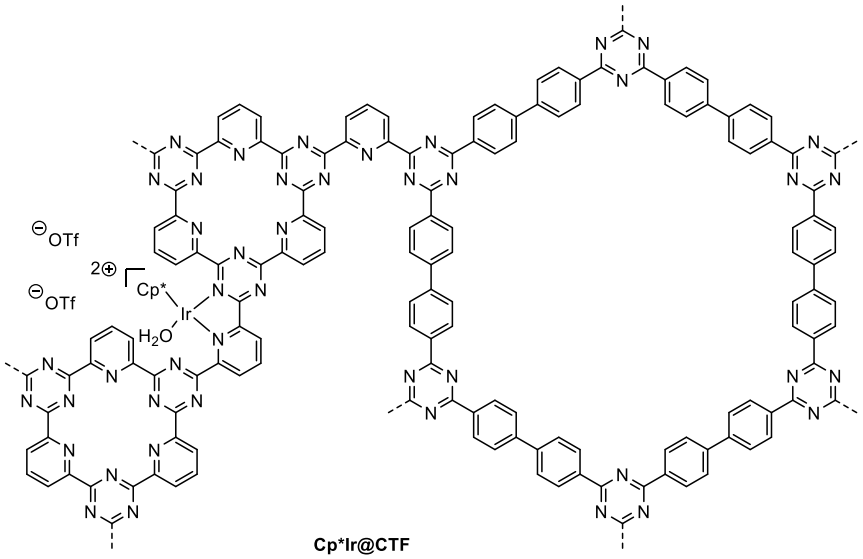

Scheme 1.8. Schematic representation of Cp*Ir@CTF.

Later, in an attempt to bring the CTF-based catalyst one step closer to real-life applications, the CTF powder was shaped into spherical particles using the polyimide Matrimid® as a binder.[135] This resulted in a more mechanically robust and tractable material. Even though polymer penetration into the CTF led to substantial pore blockage, the CTF spheres were still porous and could be loaded with a Cp*Ir(III) complex. Both CTF powder and shaped spheres were applied for the hydrogenation of CO_2 to formate. Unfortunately, the CTF spheres showed much lower activity than the CTF powder, but could be recovered without any loss of material.

The next stage of technical refinement addressed the issue of diffusion limitations in porous particles. To this end, CTFs were coated on highly open monolith supports (Figure 1.9).[136] To achieve a thin film of coating, the monoliths were immersed in a solution of monomers and $ZnCl_2$ in acetone and subjected to ionothermal polymerization conditions (500 °C for 10 h). Characterization of the materials showed that the CTF coatings were of the same in nature as the powdered CTFs. The CTF-coated monolith functionalized with a Cp*Ir(III) complex showed enhanced catalytic activity in the dehydrogenation of formic acid compared to the CTF powder, achieving an unprecedented TOF of 207 200 h^{-1} at 80 °C. The authors attributed the enhanced catalytic performance to the shorter diffusion path length in the monolith coating and to the improved mass transfer from the bulk liquid to the coated channel wall. In addition, the recyclability of the catalyst also benefited from the coating on monoliths, as the high TOF value was consistently achieved in five reaction runs. Much better performance was also obtained for a CTF-coated monolith functionalized with $PtCl_2$ in the oxidation of methane to methanol. Both examples illustrate the importance of catalyst formulation.

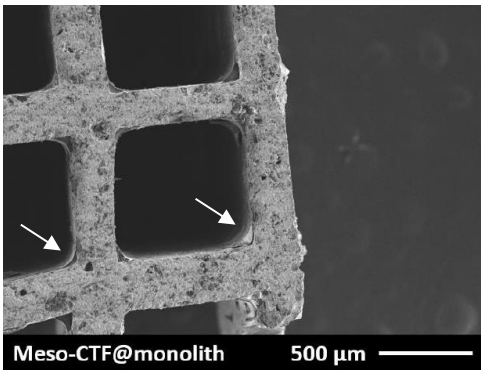

Figure 1.9. Scanning electron microscopy (SEM) image of a CTF-coated monolith. The coating layer is indicated by the arrows. (Adapted from ref. 136)

In the same period, Yoon's group immobilized a Cp*Ir complex and a Cp*Rh complex on a similar CTF to catalyze the aqueous-phase hydrogenation of CO_2 to formate.[137-138] To obtain a CTF with embedded bipyridinic sites, the authors synthesized 2,2'-bipyridine-5,5'-dicarbonitrile **16** as a building block directly containing the bipyridine motif (Scheme 1.9). Bipyridine CTF (bpy-CTF) had high porosity and abundant bipyridine sites for coordination with $[Cp^*IrCl_2]_2$ and $[Cp^*RhCl_2]_2$. In the hydrogenation of CO_2, higher activity was observed for Cp*Ir@bpy-CTF than for Cp*Rh@bpy-CTF. At 120 °C and 80 bar equimolar CO_2/H_2 in aqueous triethylamine solution, Cp*Ir@bpy-CTF reached an initial TOF of 5300 h^{-1} and a maximum TON of 5000 after 2 h. These values were the highest values reported for a heterogeneous system at that time. Nevertheless, a progressive loss of activity of about 10% in each cycle was observed for Cp*Ir@bpy-CTF during recycling, probably due to the leaching of Ir species, as demonstrated by ICP-OES analysis.

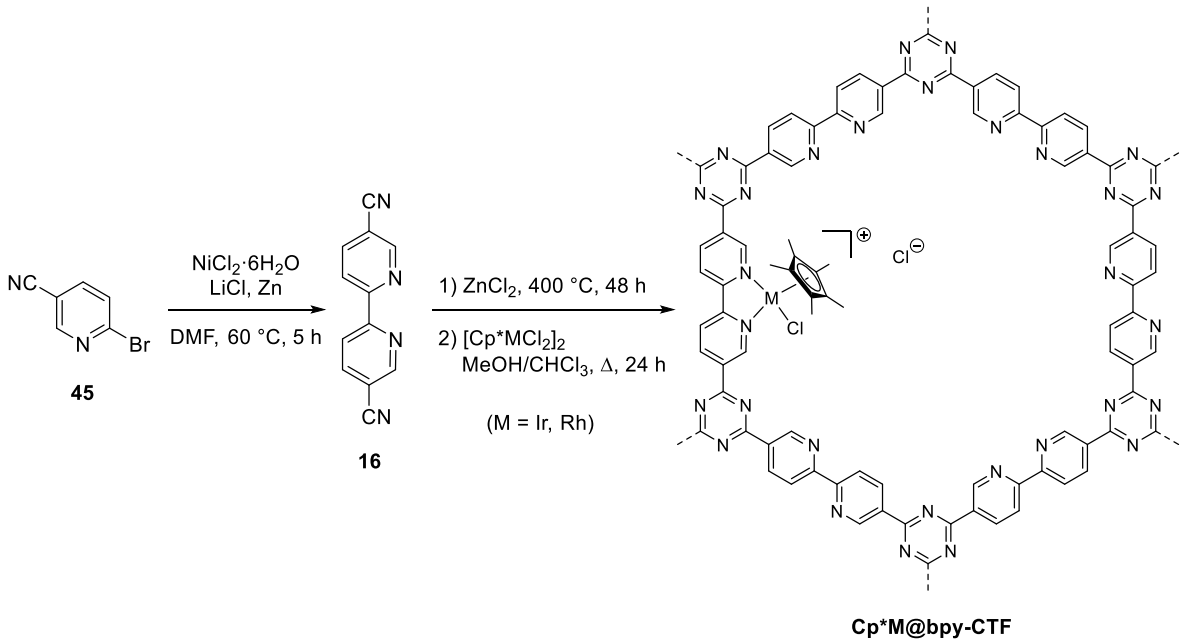

Scheme 1.9. Synthesis of Cp*M@bpy-CTF.

$[Ru(C_6Me_6)Cl_2]_2$ (C_6Me_6 = hexamethylbenzene) immobilized on bpy-CTF gave a lower TOF of 2640 h^{-1} than Cp*Ir@bpy-CTF under identical reaction conditions.[139] During recycling tests, a similar gradual decrease in activity was also observed for (C_6Me_6)Ru@bpy-CTF. Consequently, the group conducted a computational study for the Cp*Ir@CTF, to gain insight into the leaching mechanism of Ir species.[138] Density-functional theory (DFT) calculations suggested that the dissociation of the Ir–bpy bond was likely induced by proton transfer to bipyridine upon H_2 hydrogenolysis at Ir sites (Scheme 1.10a). Based on these findings and assuming a similar decomposition pathway for the Ru analog, the authors suggested the replacement of the Cp* and C_6Me_6 ligands by oxyanionic ligands such as acetylacetonate ($acac^-$), capable of intercepting the proton transfer to bipyridine (Scheme 1.10b). Therefore, a Ru(III)–acac complex immobilized on bpy-CTF was synthesized. [bpy-CTF-Ru$(acac)_2$]Cl attained a high TOF of 22 700 h^{-1} at 120 °C under 80 bar CO_2/H_2 in aqueous triethylamine. Moreover, the catalyst indeed showed excellent recyclability without loss of activity over four consecutive runs.

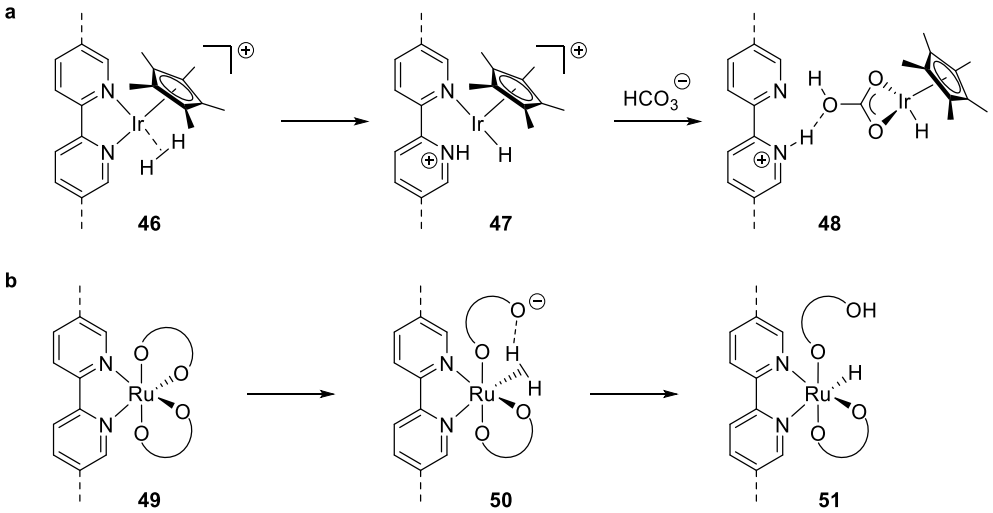

Scheme 1.10. (a) Proposed mechanism for the cleavage of Ir–bpyCTF induced by the protonation of the bipyridine ligand. (b) Design strategy with oxyanionic ligand(s) to intercept the proton transfer and prevent dissociation of bipyridine. (Adapted from ref. 139)

In a previous effort to enhance the activity of the immobilized Cp*Ir complex for CO_2 hydrogenation, the group introduced cationic imidazolium moieties into the CTF.[140] Based on X-ray photoelectron spectroscopy (XPS) studies, the imidazolium moiety was assumed to act as an N-heterocyclic carbene (NHC) ligand for the Cp*Ir complex upon treatment of the CTF with triethylamine (Scheme 1.11). Ir-NHC-CTF showed impressive catalytic activity for the hydrogenation of CO_2 to formate. At 120 °C and 80 bar CO_2/H_2, the catalyst achieved an initial TOF of 16 000 h^{-1}, which is three times higher than that of Cp*Ir@bpy-CTF under identical conditions. The authors attributed the excellent catalytic activity to the increased electron density on the Ir sites conferred by the strong σ-donating and weak π-accepting abilities of the NHC ligand. Despite

the ability of NHC ligands to form strong bonds with metals, approximately 7% of the initial Ir loading leached from the CTF over three reaction cycles.

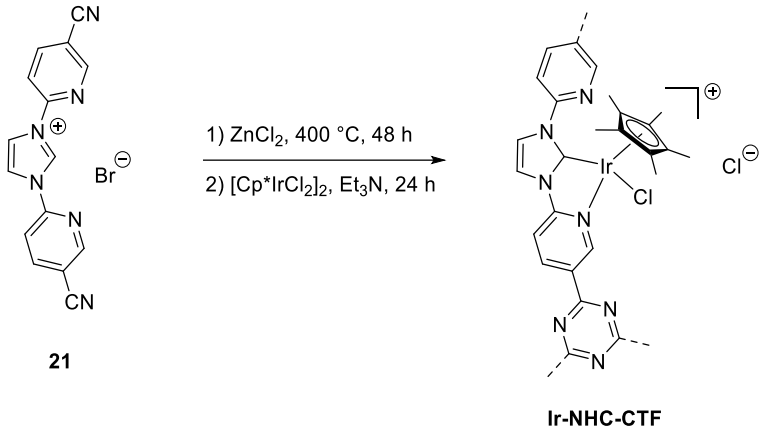

Scheme 1.11. Synthesis of Ir-NHC-CTF.

In parallel work, the bpy-CTF-supported Rh and Ir catalysts were applied for the transfer hydrogenation of carbonyl compounds **52** to alcohols **53** (Scheme 1.12, method A).[141] The reactions were carried out in water using inexpensive and environmentally benign formic acid/sodium formate as the hydrogen source. This attractive reduction method avoids the use of stoichiometric toxic metal hydrides ($NaBH_4$, $LiAlH_4$) and the need for special equipment when using flammable hydrogen gas as the reducing agent. The catalysts showed pH-dependent activity, reaching their highest activity at pH 3.5. A small series of acetophenone derivatives were converted at a slightly elevated temperature. As expected, electron-withdrawing substituents on the phenyl ring accelerated the reaction while the opposite was true for electron-donating groups. Here, the Rh catalyst showed superior activity to the Ir analog. However, the Ir catalyst largely maintained its activity during four consecutive runs, unlike the Rh catalyst.

The search for an industrially viable heterogeneous catalyst led the researchers to the immobilization of the simple, less expensive $RuCl_3 \cdot xH_2O$ complex. Its immobilization on bpy-CTF resulted in a simple, yet very effective heterogeneous catalyst for the transfer hydrogenation of carbonyl compounds (Scheme 1.12, method B).[142] Whereas hardly any activity was observed for [bpy-CTF-$RuCl_3$] at pH 3.5, maximum activity was achieved at pH 7.0. The supported Ru catalyst showed higher activity than the supported Ir and Rh catalysts, however the latter two catalysts were operated at 40 °C while the former catalyst was operated at a higher temperature of 80 °C, which may enhance its catalytic activity. The high activity of the Ru catalyst was well maintained during the recycling experiments, with only an 8% loss in conversion after five reaction cycles.

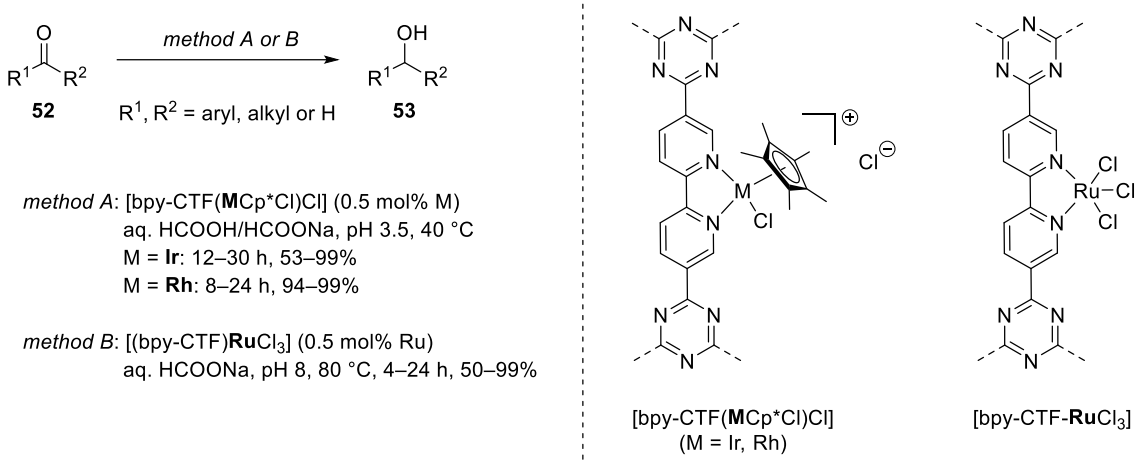

Scheme 1.12. Transfer hydrogenation of carbonyl compounds with Ir, Rh or Ru catalysts supported on bpy-CTF.

[bpy-CTF-$RuCl_3$] was also found to have high activity for the hydrogenation of CO_2 to formate.[143] The catalyst selectively converted CO_2 to formate with an unprecedented initial TOF of 38 800 h^{-1} and a TON of 20 000 in 2.5 h. Remarkably, the heterogenized Ru complex exhibited higher catalytic activity in the reaction than the homogenous $RuCl_3$ complex. XPS measurements after immobilization showed a shift of the Ru 3d signal toward lower binding energies, indicating the formation of electron-rich Ru centers upon coordination with the bipyridine ligand.

Because of the outstanding catalytic activity, simplicity and good recyclability of the Ru-based system, Yoon and co-workers developed a continuous CO_2 hydrogenation process in a trickle-bed reactor.[144] A cost-effective CTF support was obtained by mixing the expensive 2,2'-bipyridine-5,5'-dicarbonitrile monomer with a large amount of inexpensive benzene-1,4-dicarbonitrile **3** (or terephthalonitrile, TN). In addition, the TN monomer improved the porosity of the framework and brought about a doubling of the specific surface area (1251 $m^2\ g^{-1}$ *vs.* 684 $m^2\ g^{-1}$).[143-144] Ru/bpyTN-30-CTF manifested outstanding stability, reaching a total TON of 524 x 10^3 without significant deactivation after 30 days of continuous operation at 120 °C and 120 bar CO_2/H_2 pressure. Such a robust and efficient immobilized Rh catalyst demonstrated a high feasibility for the practical manufacture of formate from CO_2/H_2.

Isolated metal species are prone to agglomeration to nanoparticles under reducing conditions, which result in a deactivation. Very recently, Iemhoff *et al.* demonstrated the stability of Ir species on CTF under strongly reducing conditions.[145] When immobilized Ir(acac)(cod) complex was exposed to a H_2 atmosphere at 400 °C, the Ir complexes did not form nanoparticles, but transformed upon loss of the acac ligand into a single-atom Ir catalyst stabilized by the CTF (Scheme 1.13). Interestingly, this catalyst showed greatly increased activity and selectivity for the dehydrogenation of formic acid compared to Ir(acac)/CTF. The reductive treatment also significantly improved the stability of the Ir catalyst during recycling. However, reducing conditions

above 400 °C induced the formation of small metal clusters accompanied by a decrease in the catalytic activity.

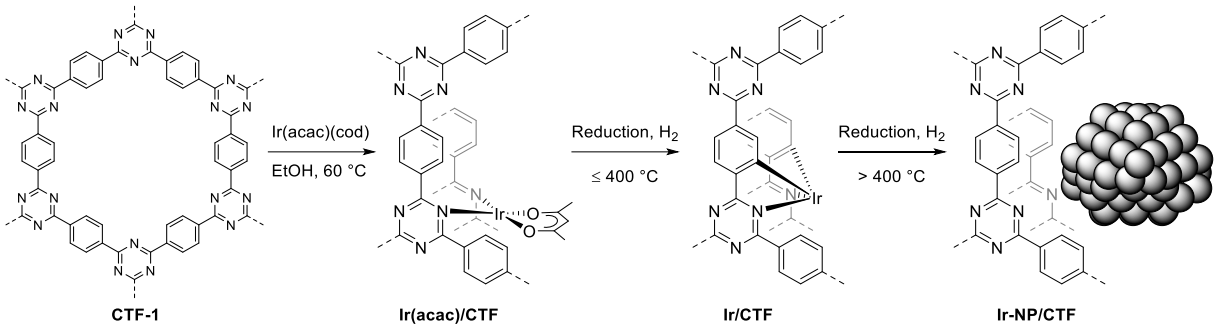

Scheme 1.13. Functionalization of CTF-1 with Ir(acac)(cod) and subsequent reduction under hydrogen atmosphere. (Adapted from ref. 145)

The superior CO_2 uptake capacities of CTFs, due to the high affinity of the greenhouse gas to triazine units, make them attractive materials for carbon capture and utilization (CCU). This was demonstrated by Zhang *et al.* who prepared a new CTF derived from di(4-cyanophenyl)ethyne (CTF-DCE) in which Ag nanoparticles were embedded.[146] The CTF itself exhibited an excellent capacity for CO_2 capture of 4.3 mmol g^{-1} at 273 K and 1 bar. Subsequently, CTF-DCE-Ag was applied for the direct carboxylation of phenylacetylenes **54** with CO_2 under atmospheric pressure, achieving excellent yields (81–91%) (Scheme 1.14).

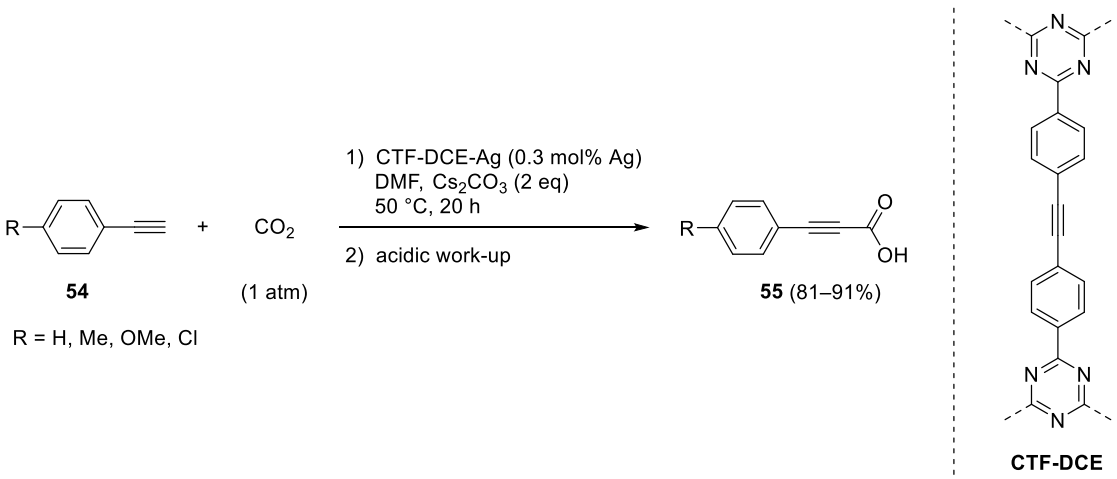

Scheme 1.14. Carboxylation of terminal alkynes with CO_2.

The catalytic activity of a biphenyl CTF functionalized with Pd nanoparticles was investigated in the double carbonylation of aryl iodides with amines by Wang *et al.*[147] The CTF was prepared by the Brønsted superacid method with TfOH, which gave the CTF as a yellow solid. Various aryl iodides **56** could be applied in the double carbonylation with different amines **57** to afford α-ketoamides **58** (Scheme 1.15). Aryl iodides with electron-withdrawing groups gave much lower

yields and poor selectivity. At a reaction temperature of 70 °C, amide **59** was obtained in small amounts as a side product, but became the main product when the temperature was raised to 100 °C. The conversion was efficient under CO at atmospheric pressure, whereas much higher pressures are generally required. Initially, Pd/CTF showed no change in its activity during the cycling experiment, but then the activity slightly decreased during the subsequent use due to the aggregation of the nanoparticles as evidenced by a TEM investigation.

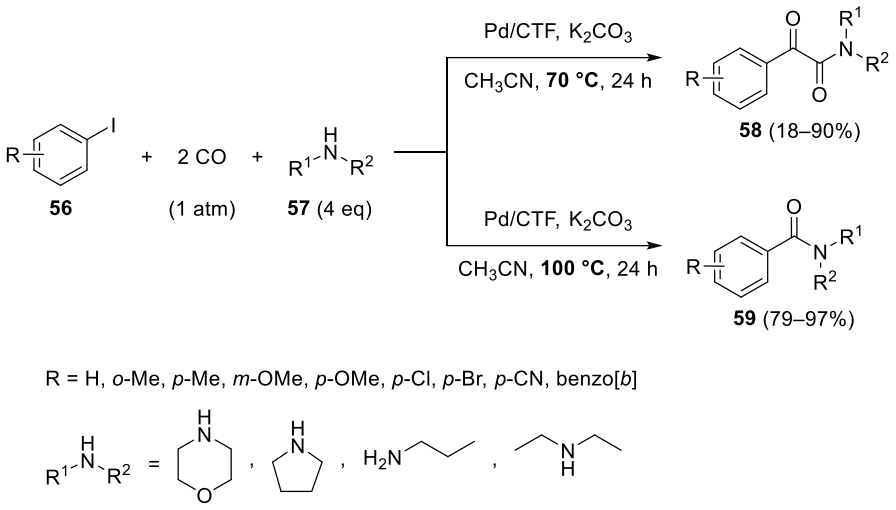

Scheme 1.15. Pd/CTF-catalyzed double carbonylation with amines at 70 °C and aminocarbonylation at 100 °C.

Yoon's group prepared the bimetallic [bpy-CTF-Al(OTf)$_2$][Co(CO)$_4$] system for the ring-expansion carbonylation of propylene oxide to β-butyrolactone (Scheme 1.16a).[148] To immobilize the metals, bpy-CTF was treated with an excess of Al(OTf)$_3$ in methanol under hydrothermal conditions at 100 °C. OTf$^-$ anions could be exchanged for [Co(CO)$_4$]$^-$ by using a K[Co(CO)$_4$] solution at room temperature. Though, ICP-OES analysis revealed a much lower Co concentration than expected, indicating that not all OTf$^-$ counterions could be exchanged. The Al^{3+} ions in the framework act as a Lewis acid, activating propylene oxide, while the Co(CO)$_4$ anions effectuate the ring opening at the least hindered carbon, followed by the migratory insertion of CO. The catalyst allowed the complete conversion of the epoxide in 24 h and 60 bar of CO pressure with 90% selectivity and with acetone as the only side product. Upon reuse, the catalyst slightly lost activity and selectivity, which may arise from partial discharge of [Co(CO)$_4$]$^-$ anions.

The group utilized the same CTF to immobilize [Co(CO)$_4$]$^-$ anions within the pores,[149] thereby obtaining a mimic of the [imidazolium][Co(CO)$_4$] ionic liquids which have been studied for epoxide carbonylation.[150] The [Co(CO)$_4$]$^-$ anions were easily introduced into the materials by anion exchange with K[Co(CO)$_4$]. The ionic liquid-based cobaltate CTF was active for the direct ring-opening carbonylation of propylene oxide **60** in methanol to methyl 3-hydroxybutyrate **62** with 86% selectivity (Scheme 1.16b). Full conversion was achieved after 24 h of reaction with the CTF,

while it was achieved after 11 h with the homogeneous counterpart at a lower temperature and lower CO pressure. The recycling test demonstrated that the catalyst could be reused, but with a 15% decrease in conversion over five runs. Therefore, in a subsequent study, Yoon and co-workers designed a bis-imidazolium-based CTF to improve to the stability of the $[Co(CO)_4]^-$ anions during the catalytic process (Scheme 1.16c). [Bis-imidazolium-CTF][$Co(CO)_4$] showed increased activity and selectivity, and its activity was maintained longer during recycling.

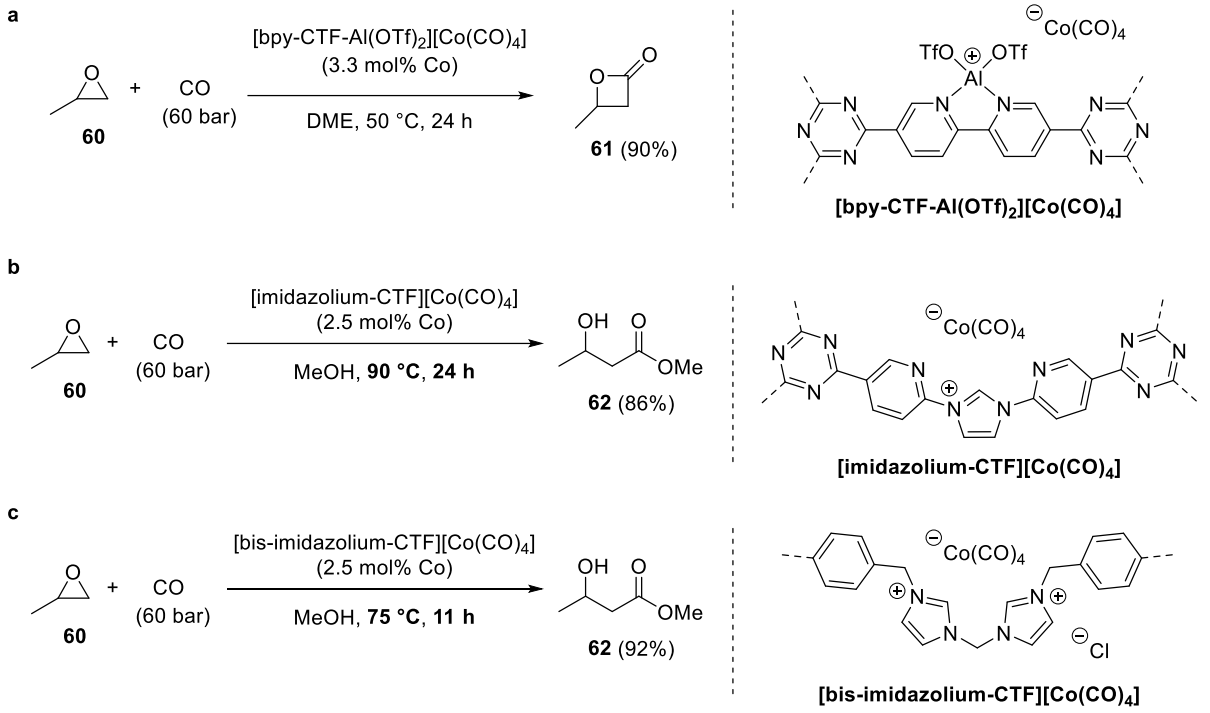

Scheme 1.16. Co-catalyzed ring-expansion (a) and ring-opening (b, c) carbonylation of propylene oxide **60**.

Palkovits and co-workers prepared several CTFs based on four different aromatic building blocks. Coordination of molecular $RuCl_3 \cdot xH_2O$ followed by a reduction resulted in a high metal dispersion of Ru(0) species on the frameworks. The catalysts were applied for the oxidation of 5-(hydroxymethyl)furfural **63** (HMF) with air and in absence of a base (Scheme 1.17).[151] HMF, a biomass-derived platform chemical, could be selectively oxidized to furan-2,5-dicarbaldehyde **64** using methyl *tert*-butyl ether as the solvent at 80 °C and 20 bar of air pressure. In contrast, in water and at 140 °C, HMF was selectively converted to furan-2,5-dicarboxylic acid **66**.[152] Microporous CTFs showed lower activities than mesoporous CTFs and the fine dispersion of the Ru(0) species on the CTFs had a positive effect on the activity compared to the commercial Ru/AC and Ru/Al_2O_3. In addition, the high nitrogen content of the CTFs imparted higher hydrophilicity to the materials, which had a further positive effect on the catalytic performance in water. However, the deposition of HMF and (polymeric) products on the catalysts posed an obstacle in both reactions. Furthermore, in the recycling experiment, the catalysts had to be reactivated under harsh conditions (350 °C, H_2 flow) due to the oxidation of the Ru nanoparticles.

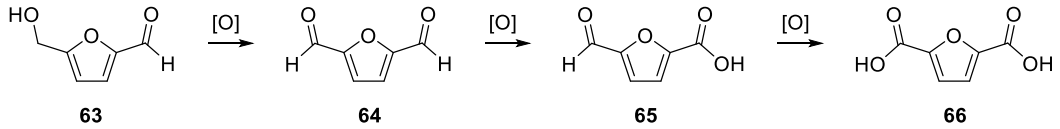

Scheme 1.17. Oxidation of 5-(hydroxymethyl)furfural **63**.

Abednatanzi *et al.* applied a bipyridine CTF, bipy-CTF, as a support for a Cp*Ir(III) complex to catalyze the aerobic oxidation of alcohols.[153] The oxidation reaction was performed in toluene at 100 °C in the presence of Cs_2CO_3 and molecular oxygen as a green oxidant. Interestingly, the activity of the heterogeneous catalyst far exceeded that of its homogeneous counterpart due to the abundant nitrogen sites in the CTF activating molecular oxygen and the alcohol substrates. High conversions were generally achieved for a wide range of benzylic alcohols (38–99%), while aliphatic alcohols gave much lower conversions (14–22%). High conversions (> 89%) were also obtained in ethyl acetate and in water, adding to the environmental friendliness of the reaction. However, in the case of ethyl acetate, the possible occurrence of the transesterification reaction was not mentioned.[154] The catalyst maintained its high activity for at least seven catalytic runs.

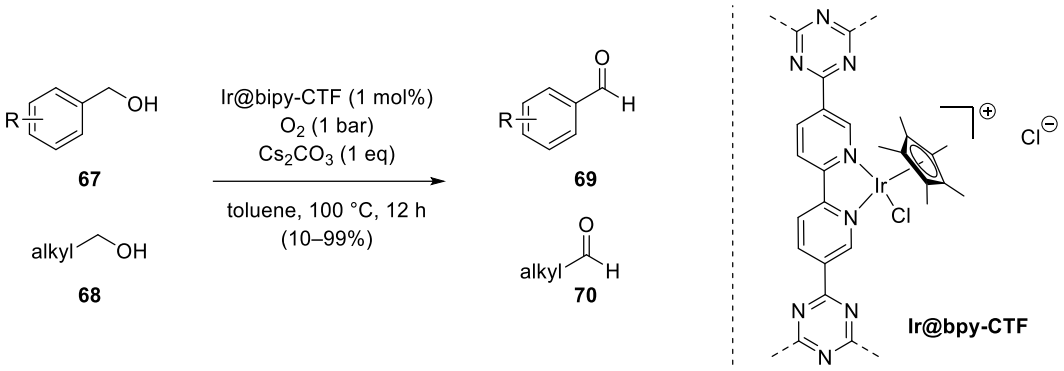

Scheme 1.18. Aerobic oxidation of benzyl alcohols **67** and aliphatic alcohols **68** with Ir@bpy-CTF as the catalyst.

The same Cp*Ir(III) complex was immobilized on a CTF prepared from 2,6-pyridinedicarbonitrile by Liu *et al.* and the catalyst was applied for the N-methylation of amines with methanol in a hydrogen autotransfer process (Scheme 1.19a).[155] Herein, methanol was first dehydrogenated to formaldehyde with the formation of an Ir-hydride species. Condensation between amine **71** and formaldehyde resulted in the formation of the imine intermediate, which was subsequently hydrogenated by the Ir–hydride species to afford N-methylated amine **72**/**73**. The reaction was carried out in methanol at 125 °C in the presence of Cs_2CO_3 to obtain very high yields (80–94%). Both aromatic and aliphatic amines readily underwent transformation, with the difference that aliphatic amines underwent N,N-dimethylation due to their higher nucleophilicity. The catalyst could be recycled at least six times with retention of the high activity. The scope could be further expanded to the N-methylation of sulfonamides **74**, again yielding the methylated product **75** in high yields (Scheme 1.19b).

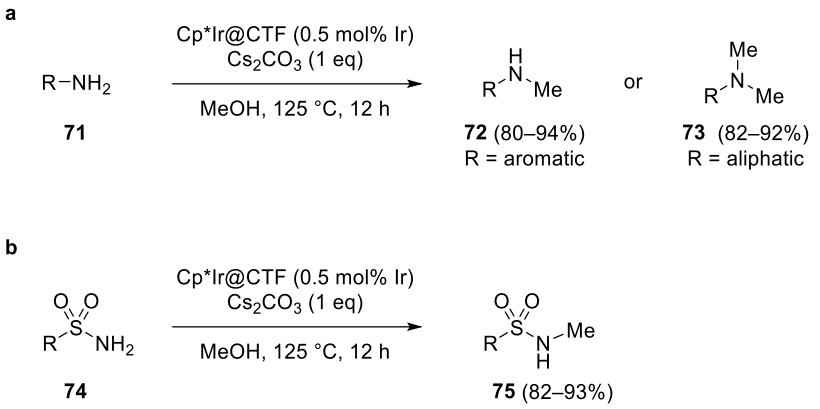

Scheme 1.19. N-methylation of (a) amines **71** and (b) sulfonamides **74** with methanol catalyzed by Cp*Ir@CTF.

In a follow-up study, the catalysis of Cp*Ir@CTF was generalized to the alkylation of aminobenzenesulfonamides **76** with various aliphatic and benzylic alcohols **77** (Scheme 1.20).[156] The reaction with secondary alcohols gave lower yields (56–60%) than with primary alcohols (80–91%) and the alkylation occurred selectively on the sulfonamide. The CTF for anchoring the Ir complex was slightly modified. By using pyrazine-2,5-dicarbonitrile as the monomer, a CTF with more uniform coordination sites was obtained. The heterogeneous catalyst could be reused in the reaction for at least six cycles without obvious loss of activity.

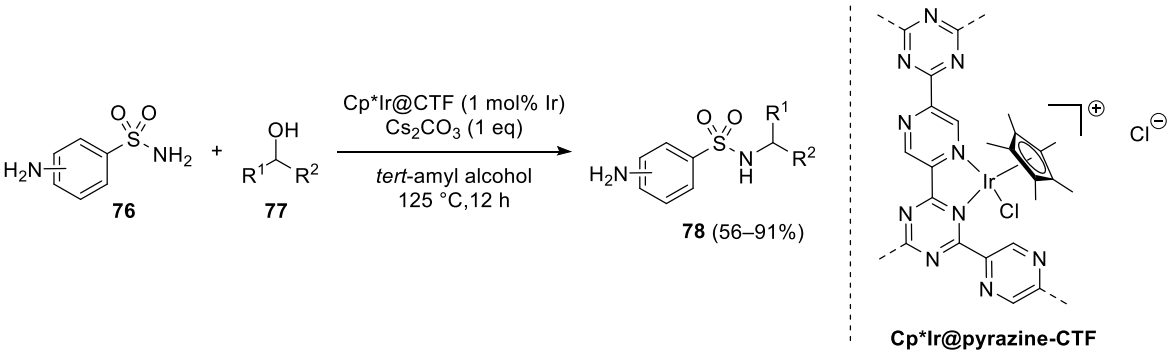

Scheme 1.20. N-alkylation of aminobenzenesulfonamides with alcohols catalyzed by Cp*Ir@pyrazine-CTF.

Van Der Voort *et al.* functionalized bipyridine-CTF with $[Ir(OMe)(cod)]_2$ (cod = cycloocta-1,5-diene) toward a stable and efficient catalyst for the C–H borylation of arenes **79** and heteroarenes **80** with bis(pinacolato)diboron (B_2pin_2) **81** (Scheme 1.21). The direct conversion of aryl C–H bonds to aryl C–B bonds yielded valuable intermediates for organic synthesis, most notably used in the Suzuki–Miyaura cross-coupling reaction. Ir(I)@bpyCTF showed excellent regioselectivity in the borylation of aryl C–H bonds, which was governed by the steric accessibility of the C–H bonds. In contrast, the regioselectivity for heteroarenes depended more on electronic effects. The catalyst exhibited high stability in the recycling test of five consecutive runs, although a gradual decrease in catalytic activity was observed.

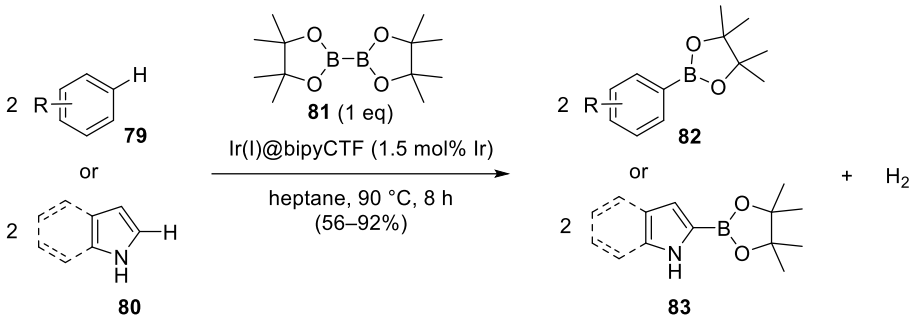

Scheme 1.21. C–H borylation of arenes **79** and heteroarenes **80** catalyzed by Ir(I)@bipyCTF.

Away from the platinum-group metals, Van Der Voort and co-workers anchored $Cu(OAc)_2$ to CTF containing 5,6,11,12,17,12-hexaazatrinaphthylene (HATN) moieties. The rigid and planar tris-bidentate building block was synthesized via the condensation between hexaketocyclohexane **84** and 3,4-diaminobenzonitrile **85** (Scheme 1.22a). The Cu@HATN-CTF showed good catalytic activity for the Henry reaction between aromatic aldehydes **87** and nitromethane to produce β-nitroalcohols **88** (Scheme 1.22b). Higher yields were obtained for benzaldehydes with electron-withdrawing substituents on the phenyl ring. The acetate ligands on Cu(II) facilitate the deprotonation of nitromethane and proved to be very important in the catalysis, as no reaction was observed for HATN-CTF coordinated to $CuCl_2$. Cu@HATN-CTF was highly reusable as no loss of activity was observed during eight consecutive reactions.

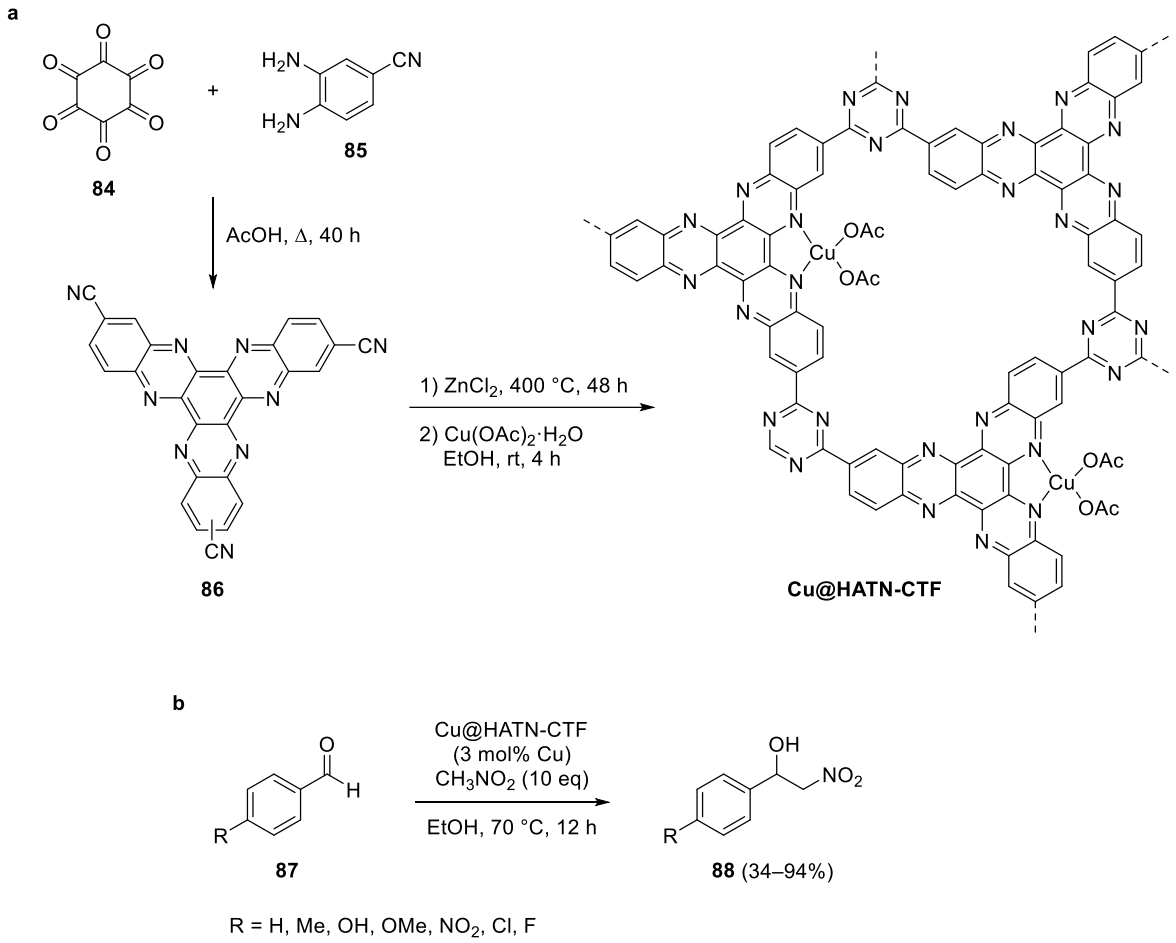

Scheme 1.22. (a) Synthesis of Cu@HATN-CTF and (b) Henry reaction of benzaldehydes **87** with nitromethane catalyzed by Cu@HATN-CTF.

Oxygen-containing ligands have also been incorporated into CTFs. For example, Van der Voort *et al*. introduced the acetylacetone (acac) motif into a CTF by the trimerization of 4,4'-malonyldibenzonitrile **91** (Scheme 1.23a). A strong carbonyl stretching band in the infrared spectrum confirmed the presence of the acac group after the ionothermal synthesis and infrared spectroscopy, solid-state NMR spectroscopy and XPS analysis confirmed the successful coordination of $VO(acac)_2$ with the acac groups in the CTF. V@acac-CTF showed outstanding activity in the modified Mannich-type reaction between equimolar amounts of various 2-naphthols or phenols **92** and *N*-methylmorpholine *N*-oxide **93** (Scheme 1.23b).[157]

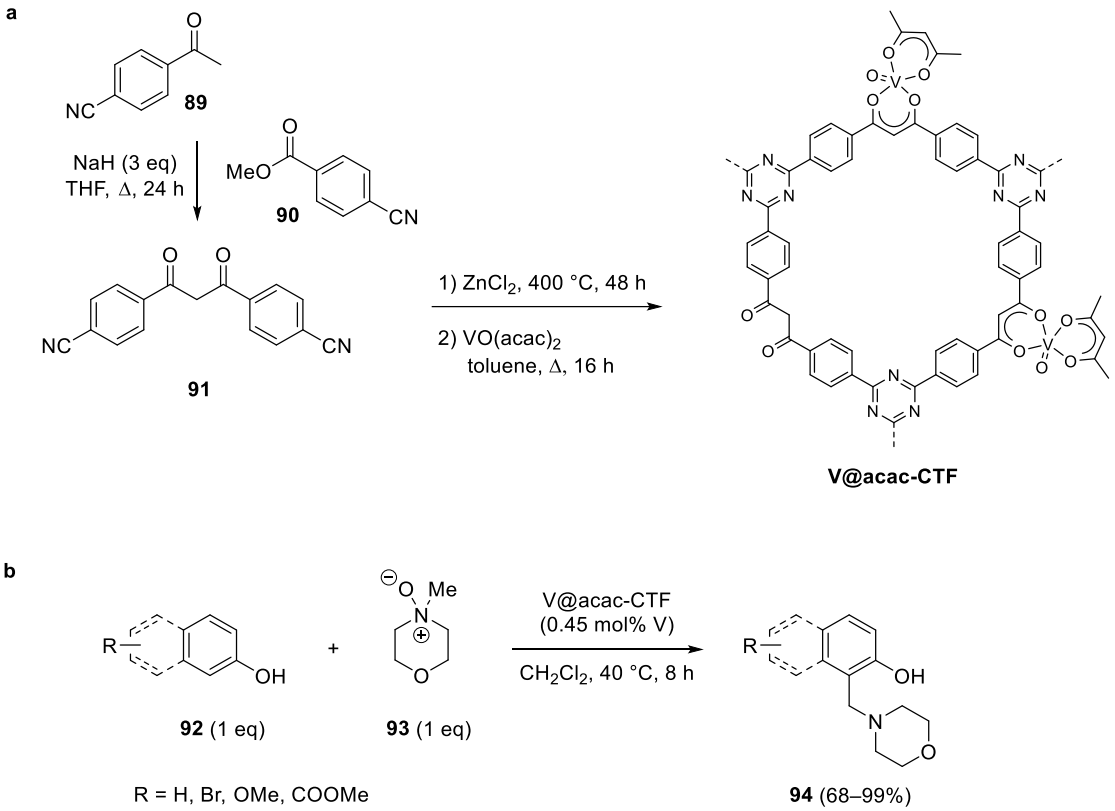

Scheme 1.23. (a) Synthesis of V@acac-CTF and (b) V@acac-CTF-catalyzed Mannich-type reaction.

7 Conclusion

Covalent triazine frameworks (CTFs) have attracted much attention as an emerging class of highly nanoporous materials. Their functional versatility and high stability make them attractive to serve as heterogeneous catalysts or catalyst supports, providing benefits in recovery and reuse.

While the ionothermal synthesis at ≥ 400 °C dominates early research, mild synthetic methods are beginning to take over. The substantial efforts of recent years to develop CTF syntheses that avoid carbonization have led to the amidine-based polycondensation method as most promising for further development of CTFs. This method has made well-ordered CTFs accessible at low temperatures, which unlocked more advanced applications of CTFs, such as photocatalysis. Nevertheless, ionothermally synthesized CTFs have shown great promise as versatile hosts for both molecular and nanoparticulate catalytic species, as discussed in this chapter. Their success as catalyst supports results from their intrinsic nitrogen-rich scaffold, which provides strong coordination of metal complexes and efficient stabilization of nanoparticles.

In addition to the nitrogen-rich triazine moieties, well-known ligands such as (bi)pyridine, N-heterocyclic carbene and acetylacetone have been incorporated into CTFs by polymerization of the corresponding nitriles. However, the incorporation of various other nitrogen ligands remains

untouched due to the challenging synthesis of the building blocks, but is addressed in this PhD thesis by the development of synthetic routes.

Significant progress has been made in the mild synthesis of CTFs, but there is still room for further improvement to bring CTF synthesis to large-scale production in a cost-effective and sustainable manner. In addition, while most of the reported catalytic reactions with CTFs have been performed in batch mode, the use of CTF catalysts in continuous flow setups is from an industrial point of view much more relevant than in batch reactors. Flow reactions offer the advantages of improved mass and heat transfer, shorter reaction times, consistent product quality and process safety. Therefore, this PhD thesis aims to investigate the applicability of CTFs in continuous flow reactions.

Chapter 2

Synthesis of CTF building blocks

Abstract | Covalent triazine frameworks (CTFs) based on polydentate ligands are highly promising supports for anchoring catalytic metal complexes. The modular nature of CTFs allows tailoring of the composition, the pore size and shape, and functionality of the material to the chosen application. Access to a wide range of chelating building blocks is therefore essential. In this regard, we have expanded the available set of CTF building blocks with new cyano-functionalized N-heterocyclic ligands. This work presents the synthesis of the six ligands which vary in their denticity and the extent of their aromatic system. By expanding the set of experimentally available building blocks, CTFs with distinct properties can be developed, which may aid in the rational design of improved materials for catalysis.

Based on | J. Everaert, M. Debruyne, F. Vanden Bussche, K. Van Hecke, T. S. A. Heugebaert, P. Van Der Voort, V. Van Speybroeck, C. V. Stevens. Synthesis of nitrile-functionalized polydentate N-heterocycles as building blocks for covalent triazine frameworks. *Synthesis* **2023**, *55*, 333–340. (Published online in 2021)

Contributions | Methodology, synthesis, and characterization: JE, MD, FVB – Crystallography: KVH – Conceptualization and supervision: TH, PVDV, VVS, CS.

1 Introduction

1,4-Diazadiene ligands, such as 2,2'-bipyridine, 2,2'-biquinoline and 2,6-bis(benzimidazolyl)pyridine, are among the most widely used ligands in the construction of metal complexes.[158-159] This family of ligands strongly chelates many transition metal ions, resulting in highly stable complexes that often exhibit interesting photophysical and photoredox properties as a result of the metal-to-ligand charge transfer (MLCT).[160] Thus, these scaffolds have found applications in many areas of chemistry, including fine chemical synthesis,[161] CO_2 reduction,[162] water splitting,[163-164] solar cell development,[165] electroluminescent devices,[166] and cancer therapy.[167] The introduction of functional groups on the ligands not only allows fine-tuning of the activity of the complex, but also allows the ligands to be incorporated into macromolecular structures. Indeed, functionalized 1,4-diazadienes have attracted widespread attention in supramolecular chemistry and materials science.[36,168-173] An example of materials that are gaining traction are the covalent triazine frameworks (CTFs). These extended porous organic frameworks are derived from the cyclotrimerization of aromatic nitriles to triazines, which gives them superior chemical and thermal stability.[75,107] Trimerization is typically accomplished either by the ionothermal synthesis in molten $ZnCl_2$ or by catalysis of triflic acid.[75,97,102] A more recently developed method involves the polycondensation of an amidine, often prepared from the nitrile, and an in situ generated aldehyde.[104,106] Using cyano-functionalized 1,4-diazadiene ligands as building blocks in the CTF synthesis provides frameworks with strong coordination sites to anchor catalytic metal complexes.[174-176] This, together with their remarkable robustness, makes CTFs attractive as metal supports in the design of heterogeneous catalysts.[91]

The modular nature of CTFs allows the framework to be tailored to the application in mind by varying the building blocks. Access to a wide range of building blocks is thus essential and brings further advances in the tailored design of CTFs. Nonetheless, very few polydentate N-ligands with cyano substituents are commercially available, and some are exceedingly expensive. In addition, efficient synthetic protocols for the synthesis of these ligands, especially with cyano functionalities, have seldomly been described in the literature. Therefore, synthetic routes to new chelating CTF precursors are highly relevant.

In our research on the development of CTFs as metal supports, the lack of diversity in the available building blocks prompted us to expand the range of accessible chelating building blocks. To this end, we synthesized a set of six cyano-functionalized N-heterocycles suitable as building blocks in CTF synthesis (Figure 2.1). In this chapter, we report the synthetic methods toward the N-heterocycles, which were developed with a view to their practical use in multigram synthesis. Once the N-heterocycles are assembled into CTFs, a variety of frameworks are obtained that differ in pore sizes and denticity of the coordination sites. Eventually, the expanded spectrum of building blocks will enhance the diversity of engineered CTF materials and foster their further application.

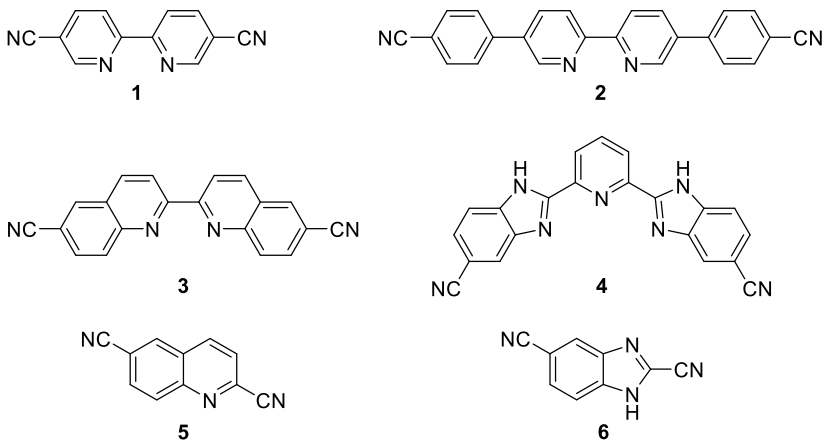

Figure 2.1. Set of synthesized cyano-functionalized N-heterocyclic ligands.

2 Results and discussion

2,2'-Bipyridine is the most simple member of the polypyridine ligand family, and therefore perhaps the most widely used one.[159] 2,2'-Bipyridine-5,5'-dicarbonitrile **1** is a commonly used building block in CTF synthesis[153,174-175] and is commercially available, but at very high prices (*e.g.*, € 500/g at Sigma-Aldrich[177]). We therefore sought an efficient way of synthesizing bipyridine **1**. Early synthetic methods relied on the dehydration of 2,2'-bipyridine-5,5'-dicarboxamide as described by Baxter and Connor and by Janiak *et al.*[178-179] However, it was found that a twofold sublimation was necessary to obtain the product in satisfactory purity, resulting in a diminished yield of 43%. Besides, three additional reaction steps are required starting from commercially available and affordable 5,5'-dimethyl-2,2'-bipyridine to obtain 2,2'-bipyridine-5,5'-dicarboxamide.[180] An elegant and more direct approach has been reported by Duan and co-workers, which proceeded via the reductive homocoupling of 2-bromo-5-cyanopyridine under nickel catalysis.[181] In contrast to conventional coupling methods, which require high loadings of ligand,[182-183] the authors took advantage of the *in situ* formed Ni–bpy complex, which could efficiently catalyze the coupling in the absence of external ligand. The latter is of interest because it could avoid a tedious purification step.

Following Duan's procedure, we synthesized bipyridine **1** using 2-bromo-5-cyanopyridine **8** in a reductive coupling with 5 mol% $NiCl_2 \cdot 6H_2O$ in the presence of activated zinc dust at 60 °C. Full conversion was already achieved within 30 minutes as determined by LC-MS analysis. After workup by extraction with chloroform and precipitation, bipyridine **1** was isolated in 93% yield as a pure product according to ^{1}H NMR analysis. Unfortunately, difficulties were encountered in reproducing this result on a regular basis when using the described conditions. In some of our attempts, the formation of a side product occurred to a large extent. Based on ^{1}H and ^{13}C NMR spectroscopy and the detected mass-to-charge ratio (m/z) of 182 $[M + H]^+$ in LC-MS analysis, the

side product was identified as 2,2'-bipyridine-5-carbonitrile **8** (Figure 2.2). The mechanism of the decyanation, however, was not elucidated.

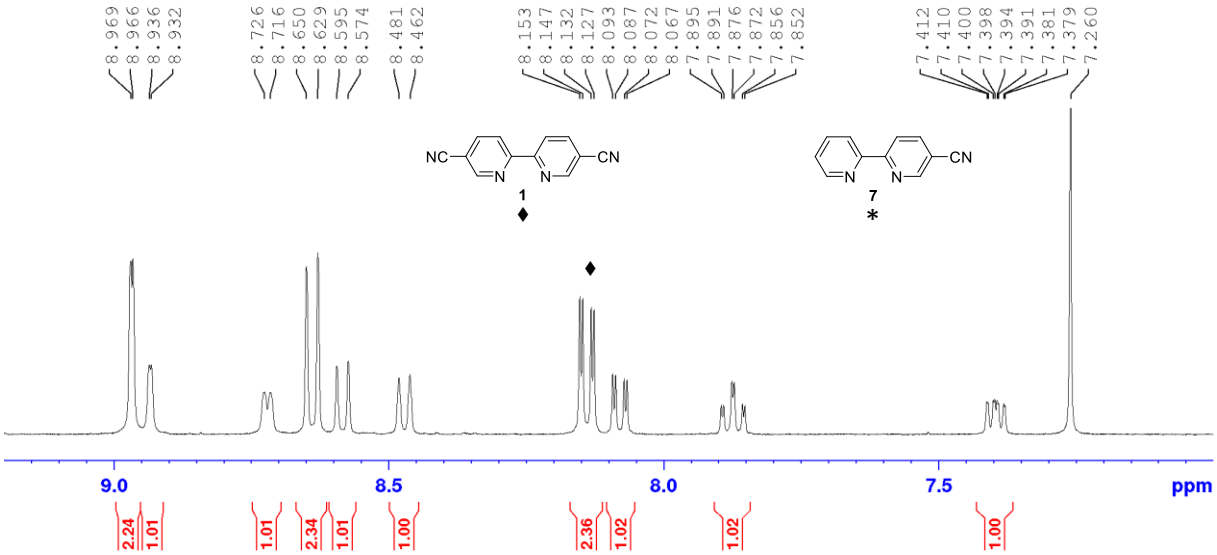

Figure 2.2. ^{1}H NMR spectrum ($CDCl_3$) of the crude reaction mixture containing monocyanobipyridine **7** (*) and dicyanobipyridine **1** (♦) in a 46/54 ratio. Ni-catalyzed reductive homocoupling of 2-bromopyridine-5-dicarbonitrile **8** under the reaction conditions described by Duan *et al.*[181] yielded inconsistent formation of undesired monocyanobipyridine **7**.

Attempts to suppress this capricious side reaction by varying the amounts of nickel precursor, zinc or LiCl were unsuccessful. Instead, the temperature of the exothermic reaction was found to play a key role in the reaction outcome. By keeping the temperature at 50 °C instead of the prescribed 60 °C and using a temperature controller to prevent temperature overshoot, the formation of side product was avoided and full conversion to bipyridine **1** was achieved in a consistent manner (Scheme 2.1). The use of 2-chloro-5-cyanopyridine in the optimized homocoupling was also possible, but resulted in a sluggish reaction, reaching 83% conversion after 18 h, due to the lower reactivity of the 2-chloropyridine.

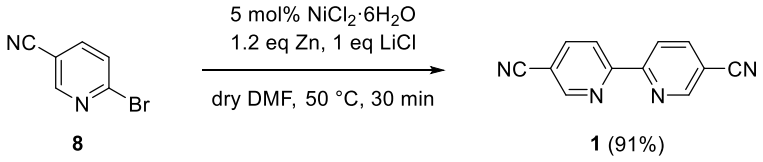

Scheme 2.1. Optimized synthesis of 2,2'-bipyridine-5,5'-dicarbonitrile **1**.

In addition to the optimized synthesis of bipyridine **1**, five new N-heterocyclic ligands were synthesized. The first new ligand we targeted first was the extended bipyridine congener, bis(4-cyanophenyl)-2,2'-bipyridine **2**. The use of extended bipyridine building blocks in the CTF synthesis could create mesopores that facilitate mass transfer in the catalytic process. For the synthesis of bipyridine **2**, an approach in which the 2,2'-bipyridine core is brominated and subsequently elongated through a cross-coupling reaction was considered as the most straightforward route.

To selectively brominate the bipyridine scaffold at the C5 and C5' positions, 2,2'-bipyridine **9** was first converted to its dihydrobromide salt **10** using aqueous HBr as shown in previous reports (Scheme 2.2).[184-185] Subsequent heating of bipyridine salt **10** in neat bromine at 170 °C for 72 h in a sealed pressure tube, afforded a crude product containing mono- and dibromobipyridine **11**/**12** in an average ratio of 43/57. Crystallization from a DMF/ethanol mixture gave the pure dibromo derivative **12** in a yield of 46%, based on the initial amount of bipyridine **9**. The residue with partially reacted bipyridine could be recycled in the next run of the reaction. Prolonging the reaction time to seven days did not result in appreciably higher yields (48%) of dibromobipyridine **12**, whereas raising the temperature or the number of bromine equivalents led to polybrominated derivatives which could not be separated from dibromobipyridine **12** by crystallization. Finally, Suzuki-Miyaura cross-coupling with 4-cyanophenylboronic acid **13** under $Pd(PPh_3)_4$ catalysis, successfully effected the extension of bipyridine **12** and afforded bis(4-cyanophenyl)-2,2'-bipyridine **2** in 92% yield.

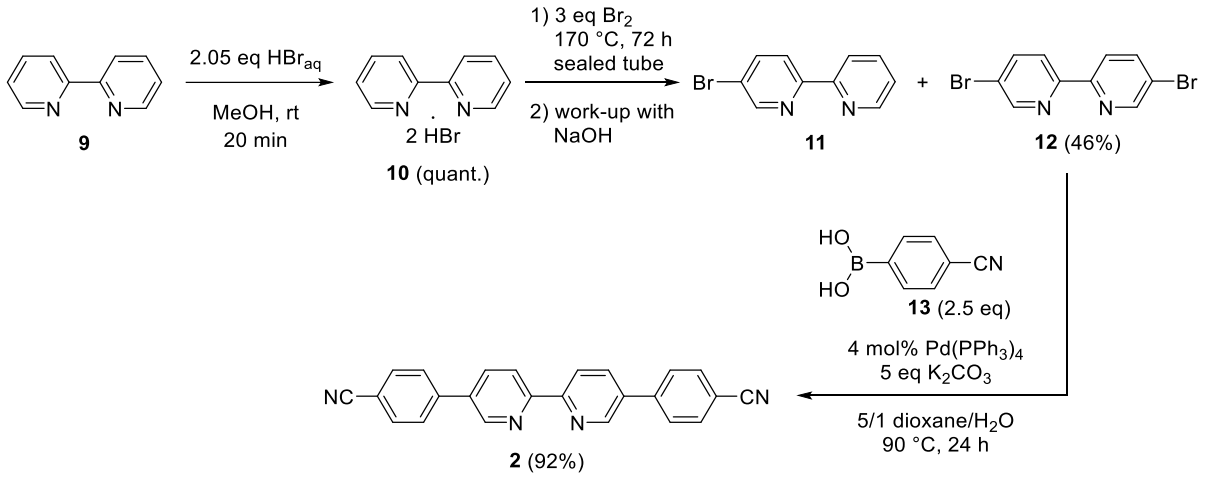

Scheme 2.2. Synthesis of 5,5'-bis(4-cyanophenyl)-2,2'-bipyridine **2**.

Bipyridine **2** gave only a low ionization signal in LC-MS analysis and the low solubility of the compound in common NMR solvents made it difficult to confirm the structure of the reaction product. Therefore, the structure of bipyridine **2** was unambiguously established by single-crystal X-ray analysis (Figure 2.3).

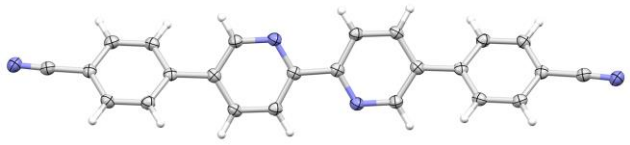

Figure 2.3. Molecular structure of bipyridine 2, showing thermal displacement ellipsoids* at the 50% probability level.

As a third bidentate N-ligand, we aimed to synthesize 2,2'-biquinoline-6,6'-dicarbonitrile **3**, a dibenzo analog of bipyridine **1**. Due to the fused rings, the ligand is a more sterically demanding than bipyridine. The synthesis of biquinoline **3** was started from quinolin-6-ol **14** because of the wide availability of the reagent compared to 6-haloquinolines (Scheme 2.3). To replace the 6-hydroxy group with a cyano group, the group was activated as a triflate by treating quinoline **14** with triflic anhydride. After workup, the crude triflate **15** was subjected to Pd-catalyzed cyanation using $Zn(CN)_2$ as the cyanide source. Chromatographic purification afforded pure quinoline-6-carbonitrile **16** in a yield of 89% over the two reaction steps. Next, quinoline **16** was converted to the quinoline *N*-oxide derivative **17** with *m*CPBA to increase its reactivity and to facilitate the C2-homocoupling. A yield of 84% was obtained when *m*CPBA in dichloromethane was used for the oxidation of quinoline **16**, which is much higher than the yield reported for H_2O_2 in acetic acid (24% yield).[186] The C2-homocoupling of quinoline *N*-oxide **17** was carried out via a deoxygenative homocoupling reaction mediated by LiO*t*Bu, as described in the literature for similar quinoline *N*-oxides.[187-188] Interestingly, instead of the expected biquinoline *N*-oxide, the homocoupling of *N*-oxide **17** directly and almost exclusively afforded deoxygenated 2,2'-biquinoline-6,6'-dicarbonitrile **3** as the coupling product. Only traces of the biquinoline *N*-oxide were observed in the crude product by LC-MS analysis.

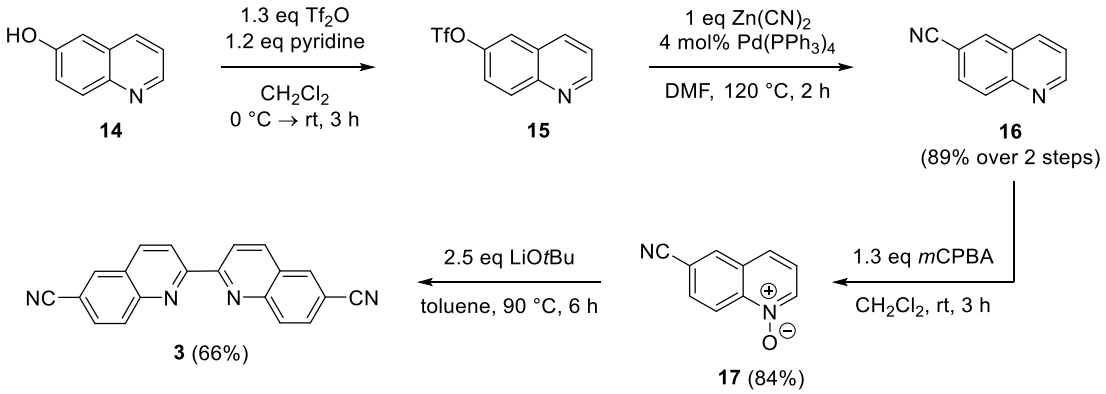

Scheme 2.3. Synthesis of 2,2'-biquinoline-6,6'-dicarbonitrile **3**.

* Thermal displacement ellipsoids indicate the magnitudes and directions of the thermal vibration of atoms in crystal structures. The size of the ellipsoids represents the space in which there is a 50% probability of finding the electron density of the atom.

With the synthesis of 2,2'-(pyridine-2,6-diyl)bis(1*H*-benzimidazole-5-carbontrile) **4**, we aimed to add a tridentate building block in our collection. Building block **4** was prepared by the condensation of 3,4-diaminobenzonitrile **18** and pyridine-2,6-dicarbaldehyde **19** in the presence of *p*-benzoquinone as oxidant and was isolated by precipitation in a yield of 53% (Scheme 2.4).

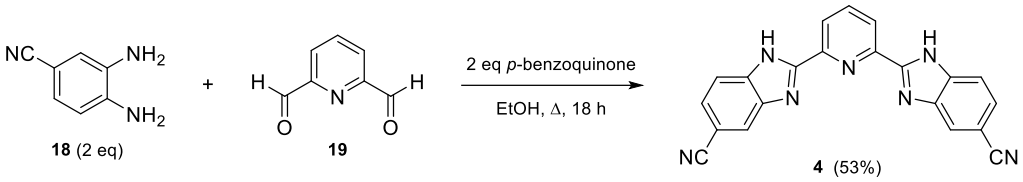

Scheme 2.4. Condensation reaction toward tridentate 2,2'-(pyridine-2,6-diyl)bis(1*H*-benzimidazole-5-carbontrile) **4**.

Tridentate coordination sites can also be generated *in situ* during the synthesis of the CTF. For example, 2-cyanopyridyl moieties in the cyclotrimerization reaction results in the formation of terpyridyl coordination sites within the obtained framework. With 6-cyanoquinoline *N*-oxide **17** in hand, selective cyanation of the *N*-oxide at the C2 position would yield quinoline-2,6-dicarbonitrile **5** containing such a 2-cyanopyridyl moiety.[186] In this regard, *N*-oxide **17** was reacted with potassium cyanide and acetyl chloride as activating agent to afford quinoline **5** in a moderate yield of 58% (Scheme 2.5a).[189] For the same reason, the synthesis of 1*H*-benzimidazole-2,5-dicarbonitrile **6** was pursued. To this end, 3,4-diaminobenzonitrile **18** was treated with methyl 2,2,2-trichloroacetimidate in acetic acid to give 2-(trichloromethyl)-1*H*-benzimidazole **20** in 75% yield (Scheme 2.5b).[190] Intermediate **20** was then reacted with an aqueous ammonia solution to give benzimidazole **6** in 89% yield.

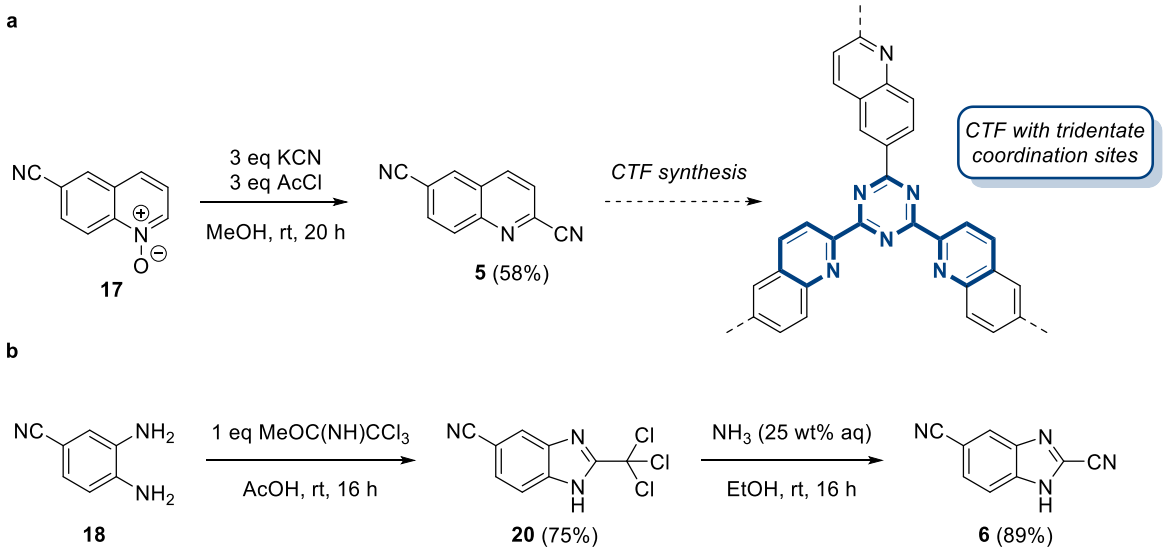

Scheme 2.5. Syntheses of building blocks which react to tridentate coordination sites during CTF synthesis (a) quinoline-2,6-dicarbonitrile **5** and (b) 1*H*-benzimidazole-2,5-dicarbonitrile **6**.

3 Conclusion

Six cyano-functionalized N-heterocyclic ligands have been synthesized. For this, straightforward synthetic methods have been elaborated considering the practical use in multigram syntheses. The cyano functionalities on the ligands make them valuable building blocks for CTFs containing metal-binding sites. The new building blocks may help in the rational design of enhanced support materials in heterogeneous catalysis. By expanding the set of experimentally available building blocks, CTFs with distinct properties can be designed, leading to their use in more advanced applications.

While the ionothermal CTF synthesis predominated in early scientific research, contemporary synthesis is increasingly based on the condensation of amidines and aldehydes rather than the cyclotrimerization of nitriles. Nevertheless, the synthetic methods for the building blocks described here are still relevant for CTF development as the nitriles can be readily converted to amidines, *e.g.*, by reaction with lithium bis(trimethylsilyl)amide (LiHMDS).[110]

4 Experimental details

4.1 General methods

Solvents and reagents were purchased from abcr, Acros, Fluorochem, Sigma-Aldrich and TCI, and were used without further purification unless otherwise stated. Anhydrous DMF was prepared by drying over activated molecular sieves (4 Å) for at least 48 h. Anhydrous CH_2Cl_2 and toluene were obtained using the MBRAUN SPS-800 solvent purification system. Zinc dust was activated prior to use by stirring in a 1 M aqueous HCl solution, filtering and washing with distilled water, ethanol, and diethyl ether, followed by drying under vacuum. Thin layer chromatography (TLC) was performed using glass-backed 0.25 mm Merck silica gel 60 F_{254} TLC plates, and spots were visualized by UV light (254 nm). Column chromatography was performed using silica gel (particle size 35–70 µm, pore diameter 6 nm). ^{1}H NMR and ^{13}C NMR spectra were recorded at 400 and 101 MHz, respectively, using a Bruker Avance III HD 400 spectrometer equipped with a ^{1}H/BB z-gradient probe (BBO, 5 mm). The spectra were recorded at 25 °C and were processed using TopSpin 3.6.2. Chemical shifts (δ) are reported in parts per million (ppm) downfield of TMS and referenced to the residual solvent peak ($CDCl_3$ δ_H = 7.26 and δ_C = 77.16; DMSO-d_6 δ_H = 2.50 and δ_C = 39.52). Coupling constants (*J*) are reported in hertz (Hz). Peaks were assigned with the aid of 2D spectra (COSY, HSQC, H2BC, HMBC). HPLC-MS analyses were performed on an Agilent 1200 Series HPLC system equipped with a Supelco Ascentis Express C18 column (3 cm × 4.6 mm, 2.7 µm fused-core particles, 90 Å) and connected to a UV-DAD detector and an Agilent 1100 Series LC/MSD-type SL mass spectrometer with electrospray ionization (ESI, capillary voltage 4 kV, fragmentor voltage

70 V) and with a mass-selective single-quadrupole detector. Infrared spectra (FT-IR) were recorded from samples in neat form with an ATR (attenuated total reflectance) accessory on a Shimadzu IRAFFINITY-1S FT-IR spectrophotometer. Melting points were determined using a Kofler heating bench system of Wagner & Munz (type WME, accuracy ± 1 °C, range 50–260 °C). For CHNS/O elemental analysis, dry samples of 2.0–2.2 mg were prepared and analyzed on a Thermo Scientific Flash 2000 analyzer.

4.2 Synthesis and characterization

2,2'-Bipyridine-5,5'-dicarbonitrile (1)

2,2'-Bipyridine-5,5'-dicarbonitrile **1** was synthesized via a modified procedure of Duan *et al.*[181] A flame-dried 250 mL flask was charged with $NiCl_2 \cdot 6H_2O$ (325 mg, 1.4 mmol, 5 mol%) and placed under an argon atmosphere. Anhydrous DMF (40 mL) was added, and the resulting green solution was heated to 40 °C. The heating plate was provided with a temperature controller (IKA® ETS-D4 fuzzy) to prevent a temperature overshoot and to maintain the temperature below 50 °C. A close monitoring of the reaction temperature was important since the temperature was found to be the key factor in avoiding the decyanation side reaction. 2-Bromo-5-cyanopyridine **8** (5.00 g, 27.3 mmol), anhydrous LiCl (1.16 g, 27.3 mmol, 1 eq) and activated zinc dust (2.14 g, 32.8 mmol, 1.2 eq) were consecutively added to the flask under a stream of argon. After raising the temperature to 50 °C, a grain of iodine and two drops of acetic acid were added to the mixture, which was then stirred for about 30 minutes to complete the conversion. Subsequently, the mixture was cooled to 0 °C and the reaction was quenched by the addition of 1 M aqueous HCl (40 mL). After 30 minutes stirring, the mixture was basified with aqueous ammonia (25 wt%) and the product was extracted with chloroform (4 x 100 mL). The combined organic fractions were dried over $MgSO_4$ and filtered. The solution was concentrated with a rotatory evaporator to ca. 20 mL and was then cooled in an ice bath to induce precipitation. The precipitate was collected by filtration, washed with cold ethanol and diethyl ether and dried under vacuum to obtain 2,2'-bipyridine-5,5'-dicarbonitrile **1** as a beige solid (2.56 g, 91%).

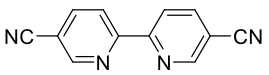

Yield: 91%. Beige solid, mp > 260 °C. **^{1}H NMR** (400 MHz, $CDCl_3$): δ 8.14 (2H, dd, *J* = 8.3, 2.0 Hz, $H^{4,4'}$), 8.64 (2H, dd, *J* = 8.3, 0.8 Hz, $H^{3,3'}$), 8.97 (2H, dd, *J* = 2.0, 0.8 Hz, $H^{6,6'}$). **^{13}C NMR** (101 MHz, $CDCl_3$): δ 110.7 ($C^{5,5'}$), 116.5 (2 x C≡N), 121.7 ($C^{3,3'}$), 140.5 ($C^{4,4'}$), 152.1 ($C^{6,6'}$), 157.0 ($C^{2,2'}$). **IR** (ATR, cm^{-1}): ν_{max} = 2239 (C≡N), 1591, 1535, 1460, 1369, 1236, 1028, 947, 845, 733, 650, 550, 488. **MS** (ESI): *m*/z (%) 207 ($[M + H]^+$, 100). Anal. Calcd for $C_{12}H_6N_4$: C, 69.90; H, 2.93; N, 27.17. Found: C, 70.04; H, 3.04; N, 27.90. The data are in accordance with those reported in the literature.[191]

2,2'-Bipyridine-5-carbonitrile (7)

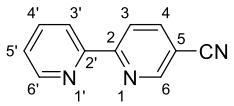

Pure 2,2'-bipyridine-5-carbonitrile was obtained from a mixture of bipyridines **1** and **7** after automated reversed-phase column chromatography (C18) using a mixture of water and acetonitrile as eluent. White powder. **^{1}H NMR** (400 MHz, $CDCl_3$): δ 7.40 (1H, ddd, *J* = 7.5, 4.8, 1.0 Hz, $H^{5'}$), 7.87 (1H, ~td, *J* = 7.8, 1.7 Hz, $H^{4'}$), 8.07 (1H, dd, *J* = 8.3, 2.0 Hz, H^4), 8.47 (1H, br d, *J* = 8.0 Hz, $H^{3'}$), 8.58 (1H, d, *J* = 8.3 Hz, H^3), 8.71–8.73 (1H, m, $H^{6'}$), 8.93 (1H, br d, *J* = 2.0 Hz, H^6). **^{13}C NMR** (101 MHz, $CDCl_3$): δ 109.4 (C^5), 117.0 (C≡N), 120.7 (C^3), 122.0 ($C^{3'}$), 125.0 ($C^{5'}$), 137.2 ($C^{4'}$), 140.1 (C^4), 149.5 ($C^{6'}$), 151.9 (C^6), 154.1 ($C^{2'}$), 159.1 (C^2). The data are in accordance with those reported in the literature.[192]

5,5'-Dibromo-2,2'-bipyridine (12)

The synthetic procedure of 5,5'-dibromo-2,2'-bipyridine **12** was based on the method reported by D'Souza *et al.*[185] A solution of 2,2'-bipyridine **9** (5.00 g, 3.2 mmol) in methanol (30 mL) was treated with a HBr solution (48 wt% in H_2O, 7.40 mL, 6.6 mmol, 2.05 eq) at 0 °C in an ice bath. After addition, the ice bath was removed, and the mixture was stirred for an additional 20 minutes at room temperature. Subsequently, the solvent was removed under reduced pressure and the residue was thoroughly dried under vacuum to obtain 2,2'-bipyridine hydrobromide salt as a pale yellow solid (10.18 g, quant.).

A 10 mL pressure resistant tube of Pyrex glass was charged with finely grounded 2,2'-bipyridine hydrobromide **10** (2.75 g, 8.7 mmol) and cooled to 0 °C. Subsequently, bromine (1.33 mL, 25.9 mmol, 3 eq) was slowly added using a disposable plastic syringe with a long needle, making sure that the tip of the needle was digging into **10**. After screwing the cap tightly onto the pressure resistant tube, the temperature was raised to 170 °C and held for 72 h. After, the tube was cooled to 0 °C before opening it. (Caution: wear protective clothing and be aware that HBr gas can escape when loosening the cap). The hard lump of crude product was crumbled with a spatula and transferred into a 500 mL flask containing Na_2SO_3 (3.0 g), NaOH (1 M, 50 mL), and $CHCl_3$ (150 mL). The mixture was stirred at room temperature until complete dissolution. The organic phase was separated, and the aqueous phase was extracted twice with $CHCl_3$ (2 x 20 mL). The combined organic fractions were dried over $MgSO_4$, filtered and evaporated. The crude product was purified by crystallization by first dissolution in DMF, followed by the addition of ethanol as the nonsolvent until tiny precipitates started to form. The solution was left overnight at room temperature and 5,5'-dibromo-2,2'-bipyridine **12** was obtained as white crystals (1.25 g, 46%).

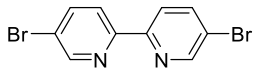

Yield 46%, based on the used amount of 2,2'-bipyridine. White crystals, mp 229 °C. **^{1}H NMR** (400 MHz, $CDCl_3$): δ 7.94 (2H, dd, *J* = 8.5, 2.2 Hz, $H^{4,4'}$), 8.29

(2H, d, *J* = 8.5 Hz, $H^{3,3'}$), 8.71 (2H, d, *J* = 2.2 Hz, $H^{6,6'}$). **^{13}C NMR** (101 MHz, $CDCl_3$): δ 121.6 ($C^{5,5'}$), 122.4 ($C^{3,3'}$), 139.8 ($C^{4,4'}$), 150.4 ($C^{6,6'}$), 153.8 ($C^{2,2'}$). **IR** (ATR, cm^{-1}): ν_{max} = 1562, 1454, 1356, 1086, 1007, 826, 725, 700, 637, 457. **MS** (ESI): *m/z* (%) 315 ($[M + H]^+$, 100). The data are in accordance with those reported in the literature.[34]

5,5'-Bis(4-cyanophenyl)-2,2'-bipyridine (2)

5,5'-Dibromo-2,2'-bipyridine **12** (2.00 g, 6.4 mmol), 4-cyanoboronic acid **13** (2.34 g, 15.9 mmol, 2.5 eq), $Pd(PPh_3)_4$ (294 mg, 0.3 mmol, 4 mol%) and K_2CO_3 (4.40 g, 31.8 mmol, 5 eq) were loaded into a two-neck flask (250 mL) equipped with a condenser and two rubber septa and placed under argon atmosphere. Degassed dioxane (100 mL) and degassed water (20 mL) were added, after which the yellow solution was heated to 90 °C for 24 h. After cooling to room temperature, the precipitate was collected by filtration and thoroughly washed with water, THF and $CHCl_3$ to afford 5,5'-bis(4-cyanophenyl)-2,2'-bipyridine **2** as an off-white solid (2.10 g, 92%).

Crystals for analytical purposes were prepared by suspending bipyridine **2** (100 mg) in DMF (28 mL, 0.01 M) and heating the suspension to 120 °C until a clear solution was obtained (ca. 15 min). The solution was then allowed to cool very slowly to room temperature during which crystals were formed. The crystals were collected by filtration, rinsed with methanol and dried under vacuum to afford bipyridine **2** as yellowish crystals (87 mg).

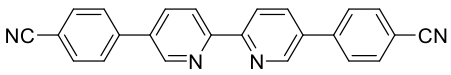

Yield 92%. Off-white solid, mp > 260 °C. **^{1}H NMR** (400 MHz, $CDCl_3$): δ 7.76–7.83 (8H, m, 8 x CH_{phenyl}), 8.07 (2H, dd, *J* = 8.3, 2.3 Hz, $H^{4,4'}$), 8.59 (2H, d, *J* = 8.3 Hz, $H^{3,3'}$), 8.95 (2H, d, *J* = 2.3 Hz, $H^{6,6'}$). **^{13}C NMR** (101 MHz, $CDCl_3$): δ 112.2 (2 x $\underline{C}_{quat}C{\equiv}N$), 118.7 (2 x C≡N), 121.5 ($C^{3,3'}$), 127.9 (2 x CH_{phenyl}), 133.1 (2 x CH_{phenyl}), 135.0 ($C^{5,5'}$), 142.2 (2 x $\underline{C}_{quat}Py$), 135.6 ($C^{4,4'}$), 147.9 ($C^{6,6'}$), 155.6 ($C^{2,2'}$). **IR** (ATR, cm^{-1}): ν_{max} = 2230 (C≡N), 1607, 1587, 1537, 1456, 1366, 1314, 1277, 1225, 1180, 1130, 1115, 1065, 1030, 999, 931, 862, 847, 827, 746, 638, 563, 525, 471, 409. **MS** (ESI): *m/z* (%) 359 ($[M + H]^+$, 100). Anal. Calcd for $C_{24}H_{14}N_4$: C, 80.43; H, 3.94; N, 15.63. Found: C, 79.32; H, 3.88; N, 15.96.

Quinoline-6-carbonitrile (16)

An oven-dried 250 mL two-neck flask equipped with a dropping funnel was charged with quinolin-6-ol **14** (4.00 g, 27.6 mmol) in dry CH_2Cl_2 (110 mL) and pyridine (2.67 mL, 33.1 mmol, 1.2 eq) and placed under argon atmosphere. The brown suspension was cooled to 0 °C in an ice bath before a solution of triflic anhydride (10.0 g, 35.4 mmol, 1.3 eq) in dry CH_2Cl_2 (30 mL) was added dropwise. The resulting black solution was allowed to warm to room temperature and

stirred for 2 h. At the end of the reaction (monitored by TLC), the reaction mixture was quenched with 1.0 M aqueous HCl (20 mL) and washed with saturated $NaHCO_3$ and brine. The water phase was extracted with CH_2Cl_2 (2 x 30 mL). The combined organic fractions were dried over anhydrous $MgSO_4$, and the solvent was removed under reduced pressure. Crude quinolin-6-yl trifluoromethanesulfonate **15** was obtained as a brown viscous liquid (7.64 g, quant.), and was used without additional purification in the next step.

To a 250 mL flask containing crude triflate **15** was added $Zn(CN)_2$ (3.24 g, 27.6 mmol, 1 eq) and $Pd(PPh_3)_4$ (1.27 g, 1.1 mmol, 4 mol%). The flask was fitted with a reflux condenser and rubber septum and placed under argon atmosphere by vacuum-argon cycles (3x). Degassed DMF (90 mL) was added, and the solution was heated at 120 °C for 2 h. Afterward, the solvent was partially removed by vacuum distillation until 20 mL of solution remained. Saturated aqueous $NaHCO_3$ (20 mL) was added and stirred for 10 min. The product was then extracted from the mixture with EtOAc (3 x 100 mL), dried over $MgSO_4$ and the solvent was evaporated under reduced pressure. The crude product was purified by column chromatography (SiO_2, PE/EtOAc 55/45) and afforded quinoline-6-carbonitrile **16** as a white solid (3.79 g, 89% over two steps).

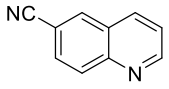

Yield 89% over two steps. White solid, mp 143 °C, R_f = 0.40 (PE/EtOAc, 55/45). **^{1}H NMR** (400 MHz, $CDCl_3$): δ 7.54 (1H, dd, *J* = 8.3, 4.2 Hz, H^3), 7.86 (1H, dd, *J* = 8.7, 1.8 Hz, H^7), 8.20 (1H, d, *J* = 8.9 Hz, H^8), 8.21–8.24 (2H, m, $H^{4,5}$), 9.06 (1H, dd, *J* = 4.3, 1.7 Hz, H^2). **^{13}C NMR** (101 MHz, $CDCl_3$): δ 110.5 (C^6), 118.5 (C≡N), 122.7 (C^3), 127.6 (C^{4a}), 130.2 (C^7), 131.2 (C^8), 134.1 (C^5), 136.4 (C^4), 149.2 (C^{8a}), 153.3 (C^2). **IR** (ATR, cm^{-1}): ν_{max} = 2224 (C≡N), 1620, 1591, 1570, 1495, 1452, 1429, 1358, 1317, 1153, 1115, 912, 833, 797, 554, 476. **MS** (ESI): *m/z* (%) 155 ([M + H]$^+$, 100). The data are in accordance with those reported in the literature.[193]

6-Cyanoquinoline *N*-oxide (17)

A 100 mL flask was charged with a solution of quinoline-6-carbonitrile **16** (1.50 g, 9.7 mmol) in 50 mL CH_2Cl_2 and cooled to 0 °C in an ice bath. 3-Chloroperbenzoic acid (70 wt%, 3.12 g, 12.7 mmol, 1.3 eq) was added portionwise over 15 min. The reaction mixture was allowed to warm to room temperature and was stirred for 3 h until complete conversion. Next, 1 M NaOH (40 mL) was added to the flask and the organic phase was separated and washed again with 1 M NaOH (15 mL). The combined aqueous fractions were extracted with *i*PrOH/$CHCl_3$ (1/4, 3 x 10 mL). The combined organic fractions were dried over $MgSO_4$, filtered and the solvent was evaporated under reduced pressure to afford 6-cyanoquinoline *N*-oxide **17** as a pale yellow solid (1.40 g, 84%).

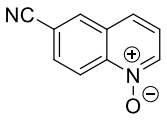

Yield 84%. Pale yellow solid, mp 209 °C. **^{1}H NMR** (400 MHz, $CDCl_3$): δ 7.44 (1H, dd, *J* = 8.5, 6.2 Hz, H^3), 7.77 (1H, d, *J* = 8.5 Hz, H^7), 7.90 (1H, d, *J* = 9.1 Hz, H^4), 8.28 (1H, s, H^5), 8.61 (1H, d, *J* = 6.2 Hz, H^2), 8.87 (1H, d, *J* = 9.1 Hz, H^8). **^{13}C NMR** (101 MHz, $CDCl_3$): δ 113.3 (C^6), 117.6 (C≡N), 121.9 (C^8), 123.2 (C^3), 125.3 (C^7), 130.2 (C^{4a}), 131.1 (C^4), 134.2 (C^5), 137.8 (C^2), 142.9 (C^{8a}). **IR** (ATR, cm^{-1}): ν_{max} = 2228 (C≡N), 1691, 1680, 1571, 1366, 1306, 1271, 1246, 1198, 1184, 849, 831, 787, 731, 523, 517, 492. **MS** (ESI): *m/z* (%) 171 ($[M + H]^+$, 100).

2,2'-Biquinoline-6,6'-dicarbonitrile (3)

A flame-dried 250 mL flask was charged with 6-cyanoquinoline *N*-oxide **17** (2.00 g, 11.8 mmol) and anhydrous toluene (60 mL), placed under nitrogen atmosphere and heated to 90 °C. Lithium *tert*-butoxide (1.0 M in THF, 29.4 mL, 2.5 eq) was slowly added dropwise to the solution. After stirring for 6 h, toluene was evaporated, and the residue was stirred in $CHCl_3$ (80 mL) and water (40 mL). The precipitated brown solid was collected by filtration and washed with $CHCl_3$. The yellow-brown sticky residue was resuspended in $CHCl_3$ (20 mL), collected again by filtration and dried under vacuum yielding 2,2'-biquinoline-6,6'-dicarbonitrile **3** as a yellow-brown solid (1.18 g, 66%).

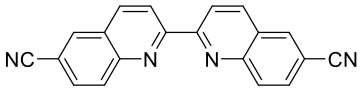

Yield 66%. Yellow-brown solid, mp > 260 °C. **^{1}H NMR** (400 MHz, DMSO-d_6): δ 6.85 (2H, d, *J* = 9.2 Hz, $H^{3,3'}$), 7.74 (2H, d, *J* = 9.2 Hz, $H^{4,4'}$), 7.83 (2H, d, *J* = 8.9, 1.8 Hz, $H^{7,7'}$), 8.18 (2H, d, *J* = 8.9 Hz, $H^{8,8'}$), 8.28 (2H, d, *J* = 1.8 Hz, $H^{5,5'}$). **^{13}C NMR** (101 MHz, DMSO-d_6): δ 102.1 ($C^{2,2'}$), 116.0 ($C^{6,6'}$), 119.4 ($C^{8,8'}$), 119.5 (2 x C≡N), 119.6 ($C^{4a,4a'}$), 130.0 ($C^{4,4'}$), 130.7 ($C^{7,7'}$), 133.4 ($C^{5,5'}$), 141.4 ($C^{8a,8a'}$), 161.7 ($C^{2,2'}$). **IR** (ATR, cm^{-1}): ν_{max} = 2230 (C≡N), 1628, 1551, 1425, 1142, 1086, 901, 820, 597, 513, 419. **MS** (ESI): *m/z* (%) 307 ($[M + H]^+$, 100). Anal. Calcd for $C_{20}H_{10}N_4$: C, 78.42; H, 3.29; N, 18.29. Found: C, 79.39; H, 3.26; N, 18.99.

2,2'-(Pyridine-2,6-diyl)bis(1*H*-benzimidazole-5-carbonitrile) (4)

3,4-Diaminobenzonitrile **18** (1.87 g, 14.1 mmol, 2 eq) and pyridine-2,6-dicarbaldehyde **19** (0.95 g, 7.0 mmol, 1 eq) were dissolved together in ethanol (100 mL). After stirring the solution for 20 minutes at room temperature, *p*-benzoquinone (1.52 g, 14.1 mmol, 2 eq) was added and the flask was equipped with a reflux condenser to heat the solution at reflux temperature for 18 h. Once complete conversion of the reagents was reached (determined by ^{1}H NMR), the mixture was cooled to room temperature. The formed precipitate was collected by filtration and thoroughly washed sequentially with cold ethanol and with diethyl ether. The filtrate was partially concentrated and stored overnight at room temperature. An additional precipitate was formed, which was also collected. After drying the combined precipitates under vacuum, the title compound **4** was obtained as a purple-gray solid (1.35 g, 53%).

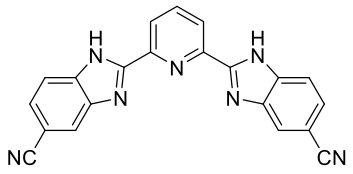

Yield 53%. Purple-gray solid, mp > 260 °C. **^{1}H NMR** (400 MHz, DMSO-d_6): δ 7.70 (2H, d, J = 8.4 Hz, $H^{6',6''}$), 7.93 (2H, d, J = 8.4 Hz, $H^{7',7''}$), 8.25 (1H, t, J = 7.8 Hz, H^{4}), 8.32 (2H, s, $H^{4',4''}$), 8.46 (2H, d, J = 7.8 Hz, $H^{3,5}$), 13.48 (2H, br s, 2 x NH). **^{13}C NMR** (101 MHz, DMSO-d_6): δ 104.8 ($C^{5',5''}$), 116.4 ($C^{7',7''}$), 119.8 (2 x C≡N), 121.7 ($C^{4',4''}$), 122.8 ($C^{3,5}$), 126.4 ($C^{6',6''}$), 139.6 (C^{4}), 147.0 ($C^{2,6}$), 153.1 ($C^{2',2''}$). **IR** (ATR, cm^{-1}): ν_{max} = 3161 (NH), 2222 (C≡N), 1620, 1599, 1445, 1416, 1312, 1236, 995, 947, 809, 735, 692. **MS** (ESI): *m*/*z* (%) 384 ([M + Na]$^+$, 100). Anal. Calcd for $C_{21}H_{11}N_7$: C, 69.80; H, 3.07; N, 27.13. Found: C, 69.06; H, 3.21; N, 27.41.

Remark: peak broadening due to rapid benzimidazole tautomerism did not allow to distinguish all expected ^{13}C signals ($C^{3a'}$, $C^{3a''}$ and $C^{7a'}$ $C^{7a''}$) from the noise signals in the acquired ^{13}C NMR spectrum.[194-195]

Quinoline-2,6-dicarbonitrile (5)

6-Cyanoquinoline *N*-oxide **17** (1.00 g, 5.9 mmol) was added to a suspension of potassium cyanide (1.15 g, 17.6 mmol, 3 eq) in 20 mL MeOH. The flask was placed under a flow of nitrogen gas, flushing liberated HCN through two consecutive gas washing bottles containing 1 M KOH solution and 1 M $Na_2S_2O_3$ solution. Acetyl chloride (1.25 mL, 17.6 mmol, 3 eq) was added dropwise over five minutes, after which the suspension was stirred at room temperature for 20 h. Over the course of the reaction a color change from yellow to pale pink was observed. Upon addition of water (30 mL) a pale pink precipitate was formed. The precipitate was collected by filtration, washed with water and Et_2O. Finally, pure quinoline-2,6-dicarbonitrile **5** was obtained after recrystallization from MeOH as pale pink crystals (606 mg, 58%).

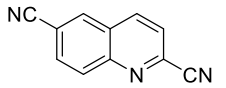

Yield 58%. Pale pink crystals, mp 225 °C. **^{1}H NMR** (400 MHz, $CDCl_3$): δ 7.84 (1H, d, J = 8.5 Hz, H^{3}), 7.99 (1H, dd, J = 8.8, 1.7 Hz, H^{7}), 8.30 (1H, d, J = 8.8 Hz, H^{8}), 8.32 (1H, d, J = 1.7 Hz, H^{5}), 8.41 (1H, d, J = 8.5 Hz, H^{4}). **^{13}C NMR** (101 MHz, $CDCl_3$): δ 148.8 (C^{8a}), 138.1 (C^{4}), 136.5 (C^{2}), 133.9 (C^{5}), 131.7 (C^{7}), 131.7 (C^{8}), 127.8 (C^{4a}), 124.9 (C^{3}), 117.6 (C^{10}≡N), 116.7 (C^{9}≡N), 113.3 (C^{6}). **IR** (ATR, cm^{-1}): ν_{max} = 2232 (C≡N), 1585, 1483, 1396, 1329, 1306, 1215, 917, 843, 833, 472. **MS** (ESI): *m*/*z* (%) 180 ([M + H]$^+$, 100). Anal. Calcd for $C_{11}H_5N_3$: C, 73.74; H, 2.81; N, 23.45. Found: C, 74.10; H, 2.86; N, 24.21.

2-(Trichloromethyl)-1*H*-benzimidazole-5-carbonitrile (20)

Methyl 2,2,2-trichloroacetimidate (620 µL, 5.0 mmol) was added dropwise to 3,4-diaminobenzonitrile **18** (666 mg, 5.0 mmol, 1 eq) in acetic acid (10 mL). After stirring for 16 h at

room temperature, water (20 mL) was added, and the suspension was stirred for five more minutes. The precipitate was collected by filtration, washed with water and dried under vacuum to afford 2-(trichloromethyl)-1*H*-benzimidazole-5-carbonitrile **20** as a white-gray solid (1.04 g, 75%).

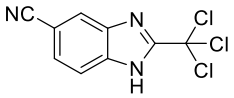

Yield 75%. White-gray solid. **^{1}H NMR** (400 MHz, DMSO-d_6): δ 7.74 (1H, d, J_{AB} = 8.4 Hz), 7.82 (1H, d, J_{AB} = 8.4 Hz), 8.29 (1H, s). **^{13}C NMR** (101 MHz, DMSO-d_6): δ 88.1, 105.8, 119.4, 127.3, 153.5.

Remark: peak broadening due to rapid benzimidazole tautomerism did not allow to distinguish all expected ^{13}C signals from the noise signals in the acquired ^{13}C NMR spectrum.[194-195]

1*H*-Benzimidazole-2,5-dicarbonitrile (6)

To a solution of 2-(trichloromethyl)-1*H*-benzimidazole-5-carbonitrile **20** (1.04 g, 4.0 mmol) in ethanol (70 mL) was aqueous ammonia solution (25 wt%, 150 mL) added. The mixture was stirred at room temperature for 16 h, after which the solvent was evaporated under reduced pressure (Caution: use a rotavapor in a fume hood). The solid residue was dispersed in 50 mL water, sonicated for five minutes, filtered and washed with water. The residue was dried under vacuum to afford 1*H*-benzimidazole-2,5-dicarbonitrile **6** as a white-gray solid (0.599 g, 89%).

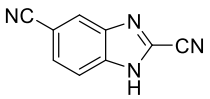

Yield 89%. White-gray solid, mp > 260 °C. **^{1}H NMR** (400 MHz, DMSO-d_6): δ 7.79 (1H, d, J_{AB} = 8.5 Hz, H^6), 7.90 (1H, d, J_{AB} = 8.5 Hz, H^7), 8.40 (1H, s, H^4). **^{13}C NMR** (101 MHz, DMSO-d_6): δ 106.8 (C^5), 111.9 ($C{\equiv}N_{imid}$), 117.1 (C^7), 119.1 ($C{\equiv}N_{benz}$), 123.4 (C^4), 127.5 (C^2), 127.7 (C^6), 138.5 (C^{7a}), 139.3 (C^{3a}). **IR** (ATR, cm^{-1}): ν_{max} = 3115 (NH), 2241 (C≡N), 1620, 1431, 1410, 1317, 1271, 1221, 1001, 823. **MS** (ESI): *m*/*z* (%) 186 ([M + NH_4]$^+$, 100), 169 ([M + H]$^+$, 26). Anal. Calcd for $C_9H_4N_4$: C, 64.28; H, 2.40; N, 33.32. Found: C, 63.91; H, 2.51; N, 34.11.

4.3 Single-crystal X-ray diffraction data for compound 2

The X-ray diffraction analysis was performed by Prof. Kristof Van Hecke (XStruct, Department of Chemistry, Faculty of Sciences, Ghent University). **CCDC 2095049** contains the supplementary crystallographic data for compound **2**. These data can be obtained free of charge from the Cambridge Crystallographic Data Centre via www.ccdc.cam.ac.uk/structures.

For the structure of compound **2**, single-crystal X-ray intensity data were collected at 100 K on a Rigaku Oxford Diffraction Supernova Dual Source (Cu at zero) diffractometer equipped with an Atlas CCD detector using ω scans and Cu Kα (λ = 1.54184 Å) radiation. The images were interpreted

and integrated with the program CrysAlis^{Pro} (Rigaku Oxford Diffraction). Using Olex2,[196] the structure was solved by direct methods using the ShelXT[197] structure solution program and refined by full-matrix least-squares on F^2 using the ShelXL[198] program package. Non-hydrogen atoms were anisotropically refined and the hydrogen atoms in the riding mode and isotropic temperature factors fixed at 1.2 times U(eq) of the parent atoms.

Crystal data for compound **2**

$C_{24}H_{14}N_4$, M = 358.39 g/mol, monoclinic, space group $P2_1/n$ (No. 14), a = 8.60090(10) Å, b = 10.41570(10) Å, c = 9.58110(10) Å, β = 97.3100(10)°, V = 851.341(16) Å^3, Z = 2, T = 100(2) K, μ(Cu Kα) = 0.672 mm^{-1}, ρ_{calc} = 1.398 g cm^{-3}, 8280 reflections measured (12.61° ≤ 2Θ ≤ 147.536°), 1700 unique (R_{int} = 0.0228, R_{sigma} = 0.0166) which were used in all calculations. The final R_1 was 0.0353 ($I > 2\sigma(I)$) and wR_2 was 0.0935 (all data).

Chapter 3

Rh@bpyCTF-catalyzed transfer hydrogenation of N-heteroarenes

Abstract | Covalent triazine frameworks (CTFs) based on polydentate ligands are highly promising supports for the coordination of well-defined active metal complexes, hereby combining the well-known reactivity of homogeneous catalysts with the robustness and recyclability of heterogeneous catalysts. Herein, we describe the immobilization of a half-sandwich Rh(III) complex on a bipyridine-based CTF and its application for the transfer hydrogenation of N-heteroarenes in water using sodium formate as a benign hydrogen source. The heterogenized catalyst exhibited excellent activity toward a wide range of quinoxalines and various other N-heteroarenes. Moreover, the catalyst maintained high activity during recycling and could be implemented in a continuous flow synthesis.

Based on | J. Everaert, K. Leus, H. Rijckaert, M. Debruyne, K. Van Hecke, R. Morent, N. De Geyter, V. Van Speybroeck, P. Van Der Voort, C. V. Stevens. Recyclable rhodium catalyst anchored onto bipyridine-covalent triazine framework for transfer hydrogenation of N-heteroarenes in water. *Green Chem.* **2023**, *25*, 3267–3277.

Contributions | Conceptualization, methodology, catalyst synthesis, catalytic experiments: JE – XPS analysis: KL, RM, NDG – STEM-EDX measurements: HR – Sorption measurements: JE, MD – Crystallography: KVH – Supervision: VVS, PVDV, CS.

1 Introduction

1,2,3,4-Tetrahydroquinoxalines and analogous partially saturated N-heterocycles are prominent structural motifs in bioactive natural products,[199] pharmaceuticals[200-205] and agrochemicals,[206] as illustrated in Figure 3.1 with representative examples such as (−)-galipinine, GSK340 and the recently FDA-approved lumateperone.[207] Furthermore, 1,2,3,4-tetrahydroquinoxaline derivatives have found utilization in organic dyes,[208-210] NIR fluorescent probes for bioimaging,[211] as well as model compounds for tetrahydrofolic acid.[212]

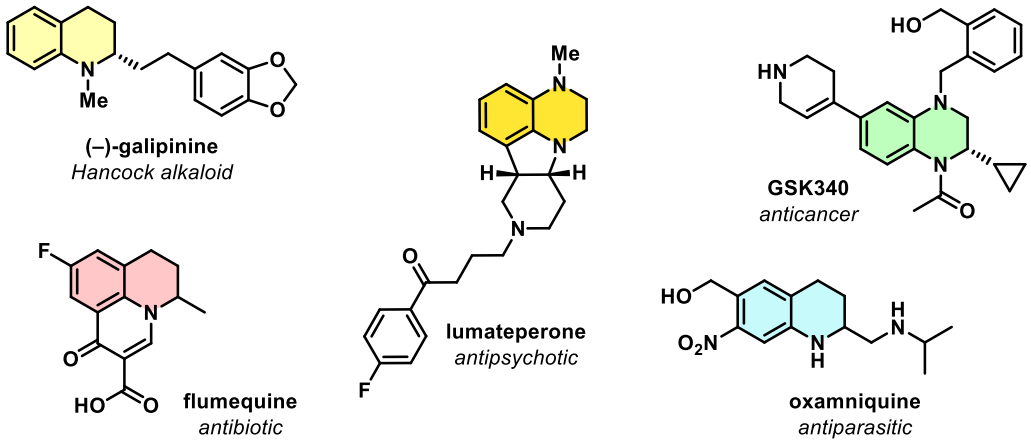

Figure 3.1. Partially saturated N-heterocycles of assorted biological interest.

In the process of drug design, these N-heterocycles serve as important building blocks for potential drug candidates with increased three-dimensionality, thereby 'escaping from flatland' and exploring a larger chemical space.[213-214] Consequently, the synthesis of partially saturated N-heterocycles has attracted widespread attention. The most straightforward route to these scaffolds is the regioselective hydrogenation of the parent azaarene. Although catalytic hydrogenation with molecular hydrogen gas is a very atom-efficient strategy, high pressures and temperatures are generally required to break the aromaticity in the substrates.[215-217] Hence, specialized reaction equipment and safety procedures must be in place for handling and storing the highly flammable hydrogen gas. As an alternative, catalytic transfer hydrogenation with H_2-surrogates, such as isopropanol or formic acid, offers a mild yet powerful method due to its operational simplicity and the widespread availability of suitable reducing agents.[218-219] The catalysts of choice to assist in the hydrogen transfer are typically half-sandwich complexes of the noble metals Ru, Rh and Ir due to their superior catalytic activities.[218] In particular, their performance in aqueous media using formate as hydrogen donor has been extensively studied over the past two decades.[220-223] In addition to the environmentally benign aspects of water as a solvent, it has been reported that transfer hydrogenation proceeds much faster in water than in organic solvents.[224-227] However, due to their homogeneous nature, their separation from the

product and recycling are difficult to achieve. These obstacles direct the use of heterogeneous catalytic systems for more sustainable processes, especially when it comes to catalysts based on precious and toxic transition metals.

The immobilization of the well-defined metal complexes on a solid porous support is an attractive strategy to overcome the abovementioned obstacles while maintaining the high activity and selectivity of the homogeneous catalyst. Moreover, heterogenization facilitates the application of the catalyst in continuous flow chemistry, which is currently gaining momentum in the fine chemical and pharmaceutical industry. In this context, covalent triazine frameworks (CTFs) have recently emerged as promising solid supports for the immobilization of active metal species.[80,228-230] The nanoporous polymeric materials are composed of organic building blocks that are covalently linked through triazine units, which provide the framework with superior thermal and chemical stability.[79,81] The modular design of CTFs allows the porosity, pore size, specific surface area and the surface functionality to be tailored to the chosen application. In addition, the versatility of these frameworks is beyond limits thanks to an ever-expanding and versatile set of available building blocks.

CTFs based on 2,2'-bipyridine building blocks possess strong bipyridine-binding sites.[141,144,148,153,174-175] Therefore, we considered the heterogenization of a well-defined metal complex on a bipyridine-based CTF (bpyCTF), allowing the preservation of its coordination environment and catalytic activity. Recently, the homogeneous [Cp*Rh(bpy)Cl]Cl complex (Cp* = η^5-C_5Me_5) has been identified as an effective catalyst for the transfer hydrogenation of various N-heteroarenes.[231] Herein, we describe the synthesis of a bpyCTF-supported Cp*Rh catalyst and its application for the transfer hydrogenation of N-heteroarenes in water using sodium formate as the hydrogen donor. The broad applicability of the heterogenized catalyst was demonstrated by the efficient hydrogenation of a wide range of quinoxalines and other N-heteroarenes. The high stability of the catalyst allowed its easy separation and reuse, and the catalyst could be implemented in a packed-bed reactor to explore its performance in the continuous flow transfer hydrogenation.

2 Results and discussion

2.1 Catalyst preparation and characterization

The bipyridine-based CTF (bpyCTF) was prepared from 2,2'-bipyridine-5,5'-dicarbonitrile **2**, which was accessed via a Ni-catalyzed reductive homocoupling of 2-bromo-5-cyanopyridine **1** (Scheme 3.1).[181,232] The homocoupling proceeded efficiently at a mild temperature and without the need for an external ligand, since the coupling product itself could serve as a ligand. The monomers were then polymerized using the classical ionothermal CTF-synthesis method.[174] To this end,

bipyridine **2** and $ZnCl_2$, which acted both as a solvent and as a Lewis acid catalyst to promote trimerization, were heated together in a sealed ampoule at 400 °C for 48 h. Treatment of the resulting CTF with water and aqueous HCl solution (1 M) to remove the remaining $ZnCl_2$ and extensive washing with organic solvents afforded bpyCTF as a glassy black powder. Figure 3.2. depicts a typical workflow of the CTF synthesis used.

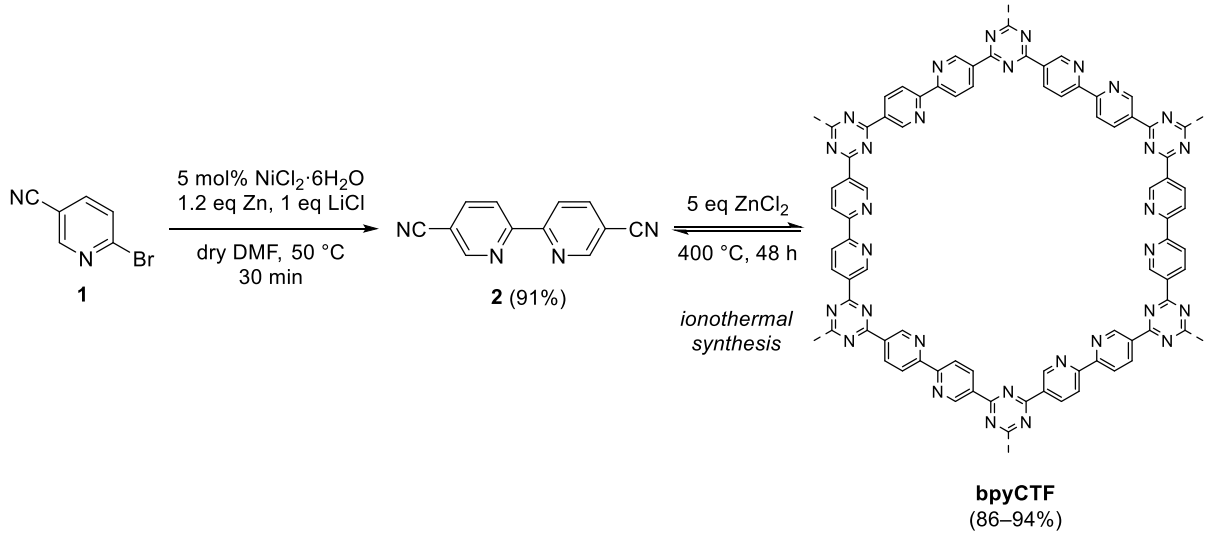

Scheme 3.1. Synthesis of bipyridine **2** and its trimerization toward bpyCTF.

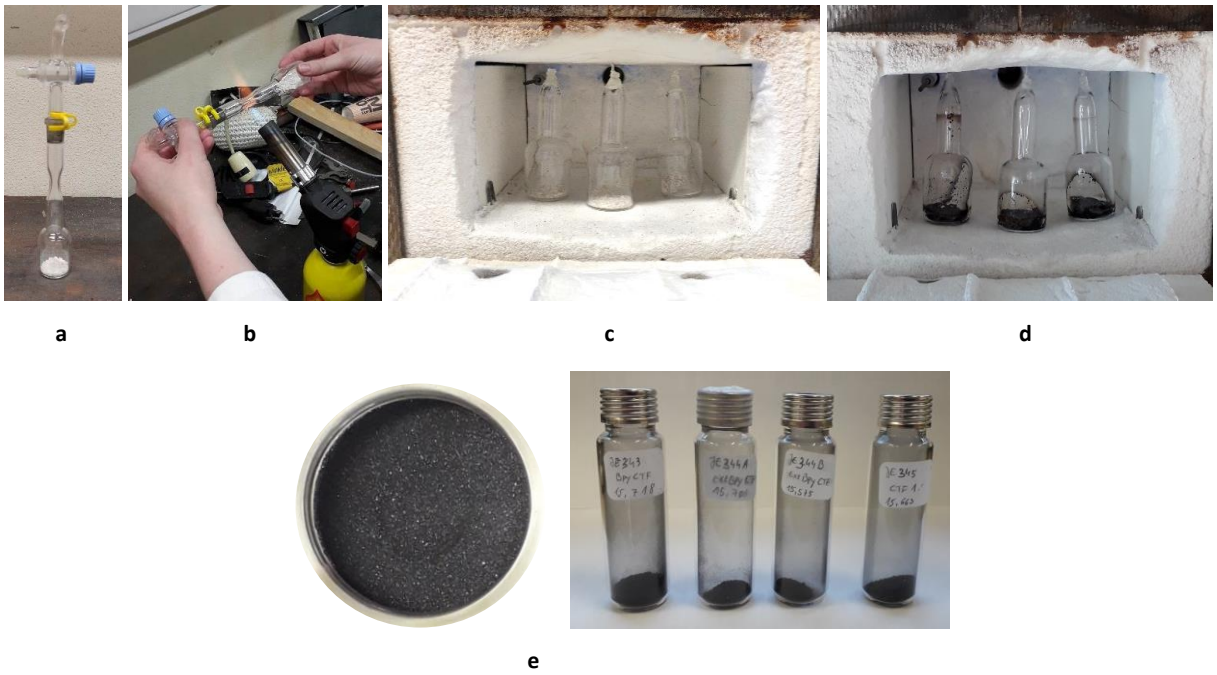

Figure 3.2. Typical workflow in the synthesis of CTFs. (a) The quartz ampoule filled with building block and $ZnCl_2$ is placed under vacuum. (b) The ampoule under vacuum is sealed by a flame. (c) The flame-sealed ampoules containing the reagents as a white powder mixture are placed in the oven and heated. (d) The flame-sealed ampoules after the ionothermal heating process containing CTF as black powder. (e) The resulting CTF powder after being washed with a range of solvents and after drying under vacuum.

The completion of the trimerization was confirmed by comparing the Fourier transform infrared (FT-IR) spectra of bpyCTF and bipyridine **2** (Figure 3.3a). The typical C≡N stretching band at 2239 cm^{-1} disappears in the spectrum of bpyCTF, whereas the characteristic stretching bands for triazine at 1513 and 1348 cm^{-1} are present.[75,174] However, the measured spectrum shows only broad absorption bands, indicating that the formed CTF deviates from the idealized framework structure. In addition, elemental analysis of bpyCTF reveals an increased C/N atomic ratio of 5.1 compared to the theoretical ratio of 3.0, demonstrating the occurrence of partial carbonization of the framework during the synthesis reaction, as is known for CTFs synthesized under the harsh ionothermal conditions (Table 3.1).[81,233] The powder X-ray diffraction (PXRD) pattern of bpyCTF features a broad diffraction peak centered at 2θ = 26°, corresponding to the (001) plane and indicating π–π stacking of the individual CTF layers (Figure 3.3b).[174] From the 2θ angle, an idealized interlayer distance of 3.5 Å is derived using Bragg's law[†]. However, the broadness of the diffraction peak indicates a limited long-range order of the material, which is the result of the harsh ionothermal conditions.

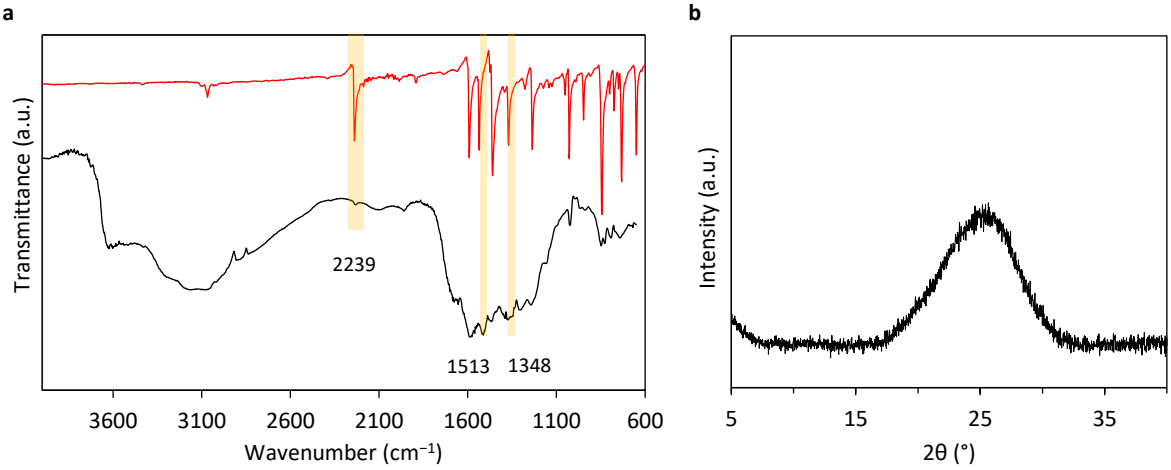

Figure 3.3. (a) FT-IR spectral comparison between 2,2'-bipyridine-5,5'-dicarbonitrile **2** (top) and bpyCTF (bottom). (b) Powder X-ray diffraction pattern of bpyCTF.

Table 3.1. Elemental analysis (C/H/N) of bpyCTF.

	Calculated	Found
C (wt%)	69.9	60.3
H (wt%)	2.9	3.1
N (wt%)	27.2	15.5
Residue (wt%)	–	21.1
C/N atomic ratio	3.0	5.1

[†] $Bragg's\ law\colon\ n\lambda = 2d\sin\theta$
$with\ n\colon an\ integer;\ \lambda\colon wavelength;\ \theta\colon glancing\ angle;\ d\colon plane\ spacing$

The numerous bipyridine motifs in bpyCTF provide excellent anchoring sites for metal complexes. Therefore, Rh@bpyCTF was readily prepared in a post-synthetic metalation approach using $[Cp^*RhCl_2]_2$ as the catalyst precursor (Scheme 3.2). The metal complex was used at a Rh/bpy ratio of 5 mol% or 0.24 mmol g^{-1} (2.5 wt%). To our delight, almost all of the added catalyst precursor was grafted to bpyCTF, as indicated by an actual Rh loading of 4.6 mol% or 0.22 mmol g^{-1} (2.3 wt%), as measured by inductively coupled plasma-optical emission spectrometry (ICP-OES). The close approximation of the actual Rh content to the targeted content demonstrates that the rhodium loading can be easily modulated by the added amount of catalyst precursor. The presence of Rh was further confirmed by combined scanning transmission electron microscopy (STEM) and energy-dispersive X-ray (EDX) spectroscopy, showing a homogeneous distribution of the Rh atoms within the framework (Figure 3.4).

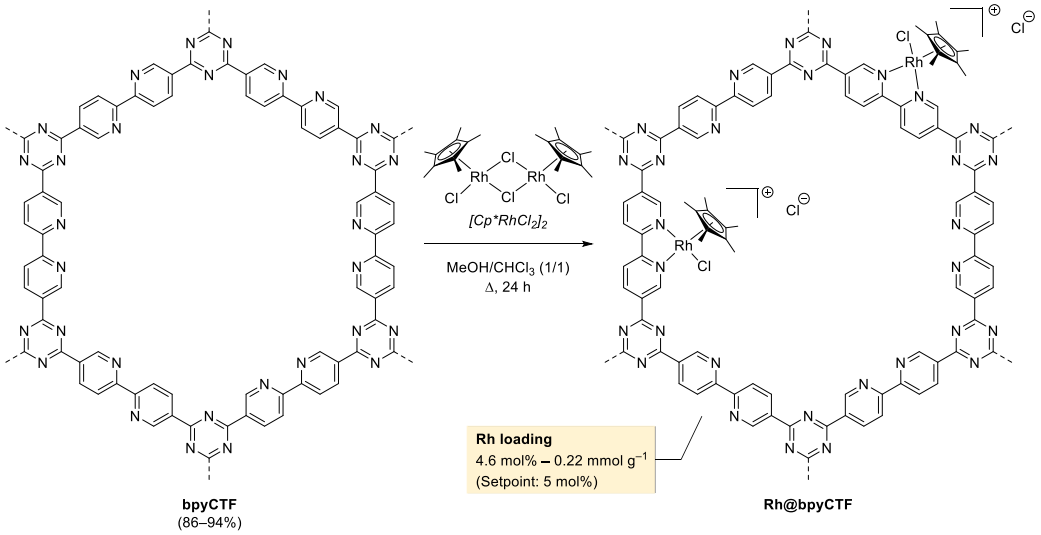

Scheme 3.2. Preparation of Rh@bpyCTF by post-synthetic metalation of bpyCTF with $[Cp^*RhCl_2]_2$.

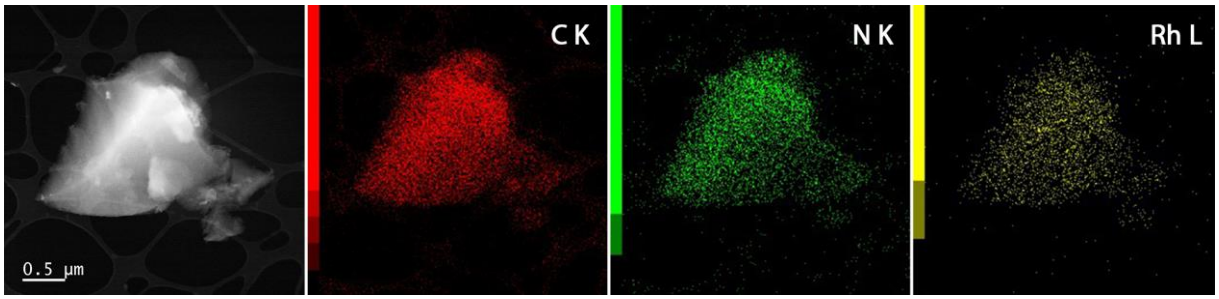

Figure 3.4. HAADF-STEM image of Rh@bpyCTF with corresponding EDX elemental mapping of carbon, nitrogen, and rhodium.

The permanent porosity of bpyCTF and Rh@bpyCTF was assessed by N_2 sorption measurements at 77 K (Figure 3.5). Both CTFs exhibit isotherms characterized by a steep increase at low relative pressures ($P/P_0 < 0.03$), after which they quickly reach a plateau. According to the IUPAC classification, the isotherms clearly represent a Type I isotherm, which is typically given by purely

microporous materials.[20] The calculated Brunauer–Emmett–Teller (BET) specific surface area for bpyCTF is 671 $m^2 g^{-1}$, which is comparable to values reported in the literature.[86,141] Furthermore, bpyCTF has a total pore volume of 0.27 $cm^3 g^{-1}$ and a narrow pore size distribution centered at 1.67 nm, highlighting its microporosity (Figure S3.).[234] Upon metalation with the Rh complex, the BET specific surface area decreased to 408 $m^2 g^{-1}$ and the total pore volume to 0.22 $cm^3 g^{-1}$, suggesting the partial pore occupation by the anchored metal complex. Nevertheless, Rh@bpyCTF still exhibits abundant porosity, which ensures the accessibility of the catalytic sites.

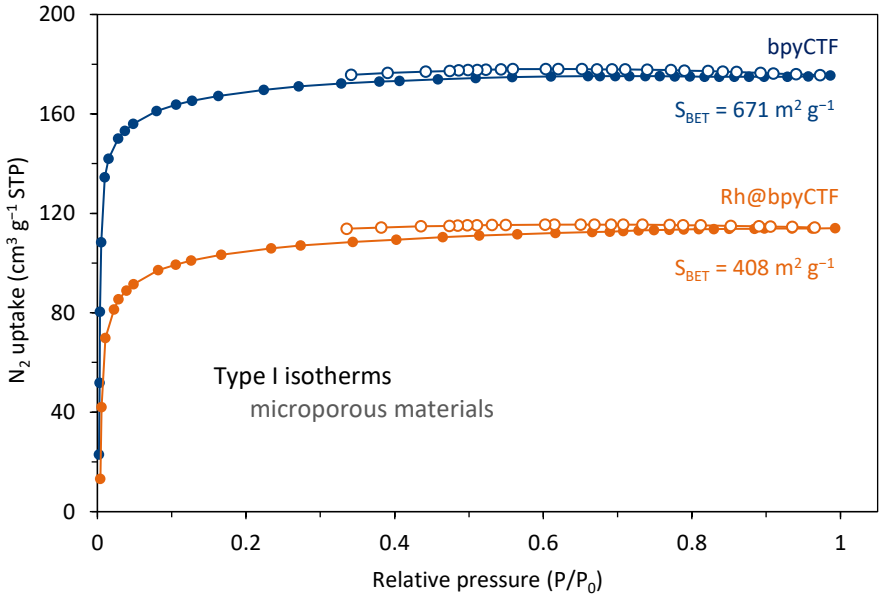

Figure 3.5. Nitrogen adsorption (●) and desorption (○) isotherms of bpyCTF and Rh@bpyCTF at 77 K.

A deeper understanding of the chemical bonding states of the elements present in the CTFs was provided by X-ray photoelectron spectroscopy (XPS). The high-resolution C 1s spectrum of Rh@bpyCTF, depicted in Figure 3.6a, remains similar to that of pristine bpyCTF (Figure S3.2) and shows two main peaks located at 284.9 and 285.7 eV, corresponding to aromatic (C=C) and bipyridine/triazine (C=N) carbon atoms, respectively.[235] The weak contributions at 288.0 and 288.9 eV indicated the minor presence of the surface oxygen species C=O and O–C=O, respectively. The binding states of nitrogen in bpyCTF were analyzed in the high-resolution N 1s XPS spectrum (Figure 3.6c). Contributions from four types of nitrogen species can be distinguished in the curve fitting. A dominant peak appears at 398.6 eV, associated with pyridinic nitrogen from the bipyridine and triazine moieties.[233,236-237] The signals at 400.0 and 401.2 eV are assigned to pyrrolic and graphitic nitrogen species, respectively. The presence of these nitrogen species confirms the occurrence of decomposition reactions during the ionothermal synthesis. In addition, nitrogen atoms coordinated to residual Zn, which would also contribute to the pyrrolic nitrogen peak, should be considered. However, since no Zn was detected in the XPS survey spectrum, its presence is insignificant (Figure S3.3). A broad, almost negligible peak at 404.6 eV can be assigned to

pyridinic *N*-oxide species presumably formed by contact with air after the synthesis. The N 1s spectrum of Rh@bpyCTF exhibits an enhanced relative intensity at 400.0 eV, confirming the coordination of bipyridine-derived pyridinic nitrogen with Rh (Figure 3.6d). As the Rh metal center withdraws valence electron density from the pyridinic nitrogen species, the core electrons of nitrogen bind more strongly to the nucleus, causing a shift of the pyridinic nitrogen peak toward higher binding energies. A similar shift was observed by Soorholtz *et al*. for a pyridine CTF coordinated to Pt.[128] In the Rh 3d XPS spectrum of Rh@bpyCTF (Figure 3.6b), the peaks observed at binding energies 309.5 and 314.2 eV are characteristic for the Rh $3d_{5/2}$ and $3d_{3/2}$ core levels, respectively, and correspond to a +3 oxidation state.[238] The $3d_{5/2}$ peak observed for Rh@bpyCTF is shifted to a significantly higher binding energy compared to the Rh $3d_{5/2}$ peak at 308.3 eV reported for the catalyst precursor used, $[Cp^*RhCl_2]_2$.[239] This shift clearly demonstrates a change in the coordination environment of the Rh cation and confirms the effective coordination by bpyCTF.

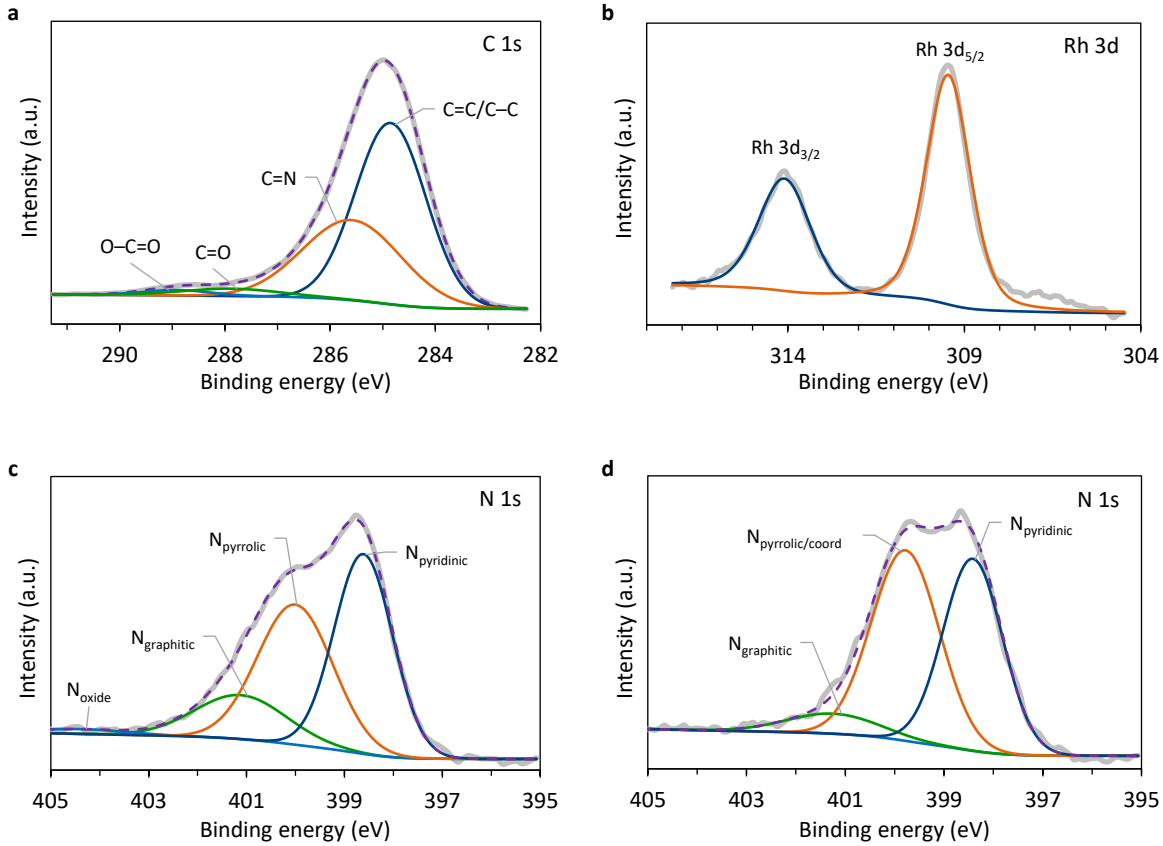

Figure 3.6. (a) High-resolution C 1s XPS spectrum and (b) Rh 3d XPS spectrum of Rh@bpyCTF. High-resolution N 1s XPS spectra of (c) bpyCTF and (d) Rh@bpyCTF.

2.2 Application of Rh@bpyCTF as transfer hydrogenation catalyst

2.2.1 Optimization of the reaction conditions

After the successful preparation of Rh@bpyCTF, we investigated the catalytic performance of the heterogeneous catalyst for the transfer hydrogenation of N-heteroarenes using an aqueous buffer solution of formic acid and sodium formate as the hydrogen source. We initially focused on the reduction of quinoxaline derivatives and therefore used 2-methylquinoxaline **3a** as a model substrate to screen for the optimal reaction conditions. It should be noted that all reactions were performed without protective atmosphere and degassing, rendering the reduction reaction more practical in use.

Previous studies on the catalytic transfer hydrogenation of ketones, imines and N-heteroarenes in water have shown that the pH value of the medium has a critical effect on the reaction rate, with acidic conditions being more favorable.[225,227,231,240-241] We therefore investigated the activity of Rh@bpyCTF at various pH values ranging from 2.0 to 6.0 by altering the ratio of formic acid to sodium formate. As expected, high catalytic activities were observed only within a certain acidic pH window, with the highest conversion achieved at pH 4.5 (Figure 3.7). This pH optimum is the same as that reported for the homogeneous [Cp*Rh(bpy)Cl]Cl complex, demonstrating that the immobilization on the bpyCTF did not affect its pH dependency in the reaction.[231]

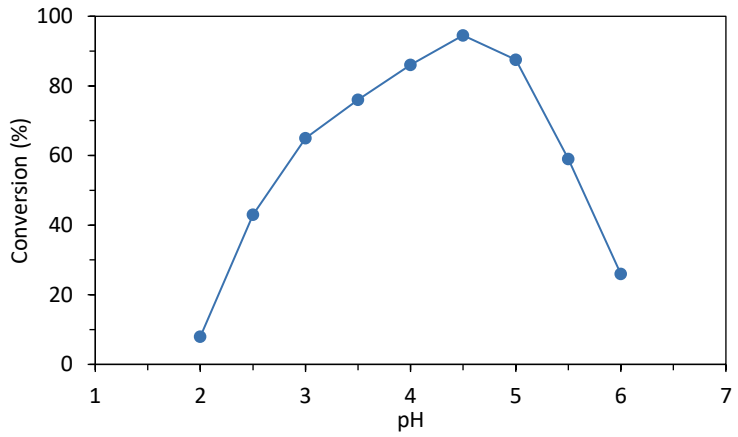

Figure 3.7. Conversion as function of the medium's initial pH value. Reaction conditions: 2-methylquinoxaline **3a** (0.5 mmol), Rh@bpyCTF (0.25 mol% Rh), aqueous HCOOH/HCOONa buffer solution (2 M, 5 mL), 80 °C. Conversions were determined by ^{1}H NMR analysis after 20 min reaction.

Similar pH-dependent activity was previously observed by Ogo and co-workers for analogous Ru(II) and Ir(III) complexes.[240,242-243] Based on their studies with carbonyl substrates, the pH-dependent behavior of the transfer reaction was rationalized by (1) the pH-dependent formation of the catalytically active species and (2) the protonation of the substrate. The latter renders the substrate more susceptible to nucleophilic attack by a hydride. Xiao and co-workers, who reported the Ir-catalyzed transfer hydrogenation of quinolines, suggested that the optimum pH is related

to the pK_a of the substrate under study, in their case quinoline (pK_a 5.4).[241,244] However, quinoxaline (pK_a 0.56),[245] being much less basic than quinoline, is far less protonated at the optimum pH of 4.5. This suggests that substrate protonation is not the dominant factor in the dependency of pH.

On the other hand, based on the studies of Ogo and colleagues,[49,53-54] the pH-dependent formation of the catalytically active species can be explained as follows: in aqueous medium, the chlorido ligand is easily displaced by a water molecule (Scheme 3.3, complex **I**), which is also a labile ligand, and thus provides an easy access to a vacant site. The p*K*a value of formic acid at the concentration studied is 3.6.[240] Thus, above pH 3.6, formic acid predominantly appears as $HCOO^-$, which binds to the Rh center to afford the formato–Rh complex **II**. The hydrido–Rh complex **III** is then generated through a β-hydrogen elimination accompanied with the evolution of CO_2.[246] This hydrido complex then serves as the active reducing species by transfer of the hydride to the substrate. At lower pH values, the hydrido ligand can be protonated to form H_2, thereby interrupting the catalytic cycle. The low activity above pH 5.5 can be rationalized by considering the deprotonation of the aqua ligand to a hydroxo ligand, which is significantly less labile and thus ligand exchange with $HCOO^-$ becomes inhibited.[240,243]

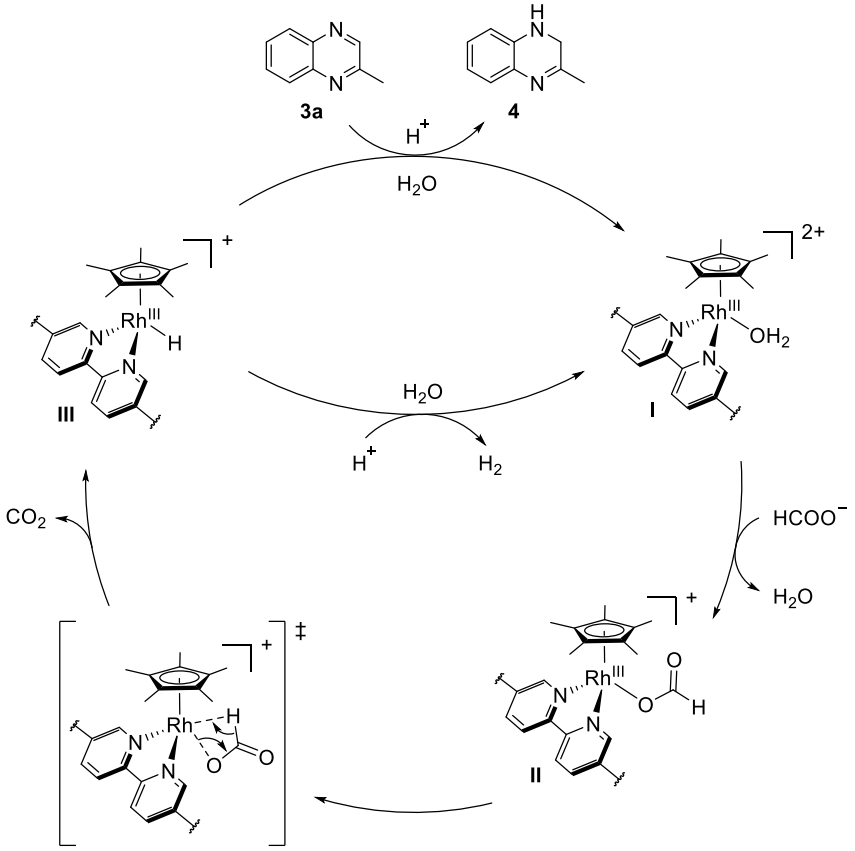

Scheme 3.3. Proposed mechanism for the transfer hydrogenation of N-heterocycles catalyzed by Rh@bpyCTF.

In addition to transfer hydrogenation, concomitant N-formylation of the hydrogenated product occurred below pH 4 and became more pronounced as the pH decreased. This side reaction has often been observed when formic acid is used as a hydrogen donor and requires an additional hydrolysis step to convert the *N*-formyl side product into the desired product.[222]

The effect of an excess of formate used in the reaction was then investigated (Figure 3.8a). As expected, the conversion rate increased rapidly with increasing concentrations of hydrogen donor. This acceleration leveled off when 40 equivalents of formate (4 M solution) was used, and almost complete conversion after 2 h was already obtained with 20 equivalents (2 M solution). Therefore, 20 equivalents of formate was considered as the optimum amount. Temperature also had a pronounced effect on the Rh@bpyCTF catalyzed transfer hydrogenation, with higher temperatures being more beneficial (Figure 3.8b). While a high conversion was achieved at 80 °C, the reaction rate decreased drastically when the reaction was carried out at room temperature, with only 4% conversion in 2 h. Even at an elevated temperature of 40 °C, the reaction proceeded slowly, reaching only 10% conversion.

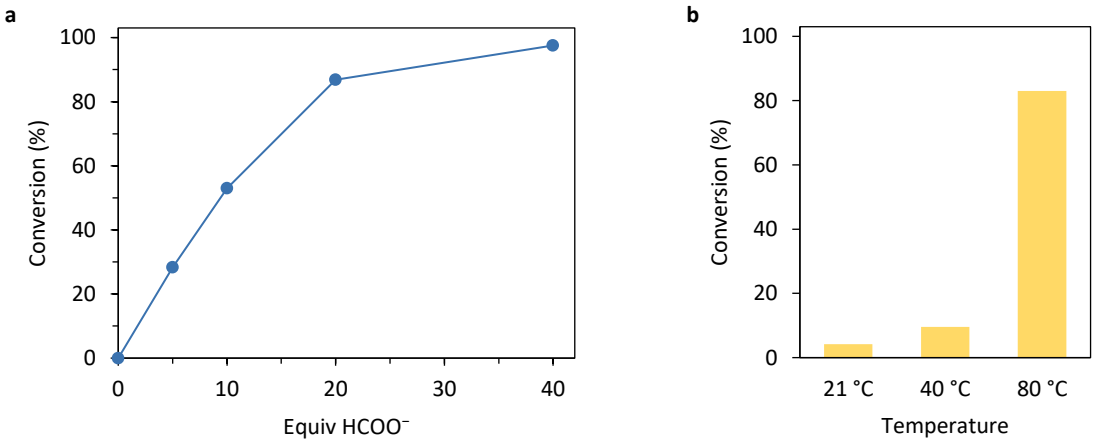

Figure 3.8. (a) Conversion as function of added equivalents formate. Reaction conditions: 2-methylquinoxaline **3a** (0.5 mmol), Rb@bpyCTF (0.25 mol% Rh), HCOOH/HCOONa buffer solution (resp. 0, 0.5, 1, 2, 4 M; pH 4.5, 5 mL), 80 °C. Conversions were determined by ^{1}H NMR analysis after 2 h reaction. (b) Temperature effect on the reaction rate of the transfer hydrogenation of 2-methylquinoxaline **3a** (0.5 mmol) catalyzed by Rh@bpyCTF in a HCOOH/HCOONa buffer solution (2 M, pH 4.5, 5 mL). Conversions were determined by ^{1}H NMR analysis after 2 h reaction.

The catalyst loadings were then reduced to assess the effectiveness of the catalyst. As a control experiment, it was verified that the transfer hydrogenation of 2-methylquinoxaline **3a** did not take place in absence of the Rh catalyst (Table 3.2, entry 1). Similarly, pristine bpyCTF itself did not show any activity. In contrast, the reaction with Rh@bpyCTF was completed in 2 h with a catalyst loading of 0.25 mol% Rh (entry 2). Reducing the loading to 0.1 mol% Rh gave a conversion of 36% after the same reaction time, but increased to 90% after 24 h (entries 4 and 5). Further reduction of the loading to 0.02 mol% Rh resulted in a conversion of only 28% after 24 h (entry 6). The catalyst precursor, $[Cp^*RhCl_2]_2$, showed no activity, while the homogeneous [Cp*Rh(bpy)Cl]Cl catalyst gave almost complete conversion in 1 h (entries 7 and 8).

Table 3.2. Rhodium-catalyzed transfer hydrogenation of 2-methylquinoxaline **3a**.[a]

Entry	Catalyst	Rh (mol%)	Time (h)	Conversion (%)[b]
1	None	–	24	0
2	bpyCTF	–	24	0
3	Rh@bpyCTF	0.25	2	> 99
4[c]	Rh@bpyCTF	0.1	2	36
5[c]	Rh@bpyCTF	0.1	24	90
6[d]	Rh@bpyCTF	0.02	24	28
7	$[Cp^*RhCl_2]_2$	0.25	24	0
8	[Cp*Rh(bpy)Cl]Cl	0.25	1	98

[a] Reaction conditions: 2-methylquinoxaline **3a** (0.5 mmol), Rh complex or Rh@bpyCTF (0.25 mol% Rh, 5.6 mg Rh@bpyCTF), aqueous HCOOH/HCOONa buffer (2 M, pH 4.5, 5 mL), 80 °C.
[b] Determined by ^{1}H NMR analysis.
[c] 1.25 mmol **3a** in 12.5 mL buffer solution.
[d] 6.25 mmol **3a** in 62.5 mL buffer solution.

The kinetic profiles of the transfer hydrogenation reaction under the homogeneous and heterogeneous catalysis are compared in Figure 3.9. In both cases, the hydrogen transfer is fast from the beginning. The rate of the heterogeneous reaction was slightly lower than that of the homogeneous counterpart, due to diffusion limitation inherent to a porous matrix such as bpyCTF.

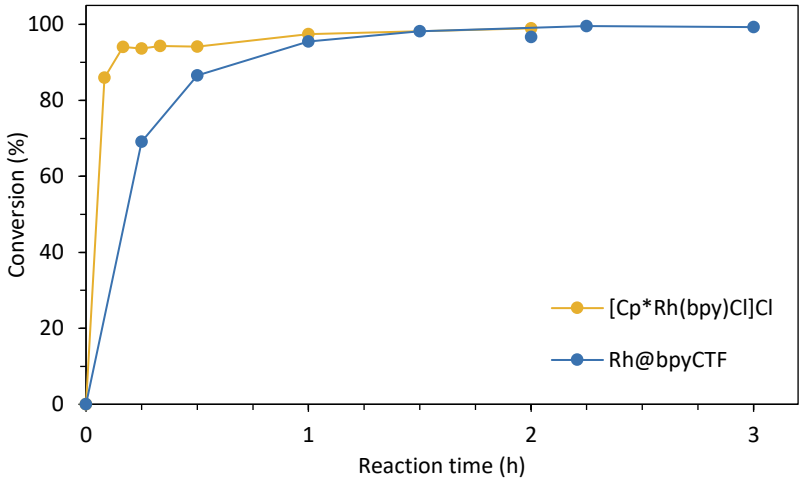

Figure 3.9. Reaction profiles for the transfer hydrogenation catalyzed by heterogeneous Rh@bpyCTF compared to homogeneous [Cp*Rh(bpy)Cl]Cl. Reaction conditions: **3a** (0.5 mmol), Rh catalyst (0.25 mol% Rh), aqueous HCOOH/HCOONa buffer solution (2 M, pH 4.5, 5 mL) at 80 °C.

2.2.2 Hot-filtration test

The heterogeneity of the Rh@bpyCTF catalyst was evaluated by a hot-filtration test. To this end, Rh@bpyCTF was removed from the reaction mixture by filtration partway through the transfer hydrogenation reaction. The filtrate was then allowed to react further for an additional 18 h. After removal of the catalyst, no further conversion of the substrate was observed, demonstrating that the catalysis is truly performed by the heterogeneous Rh@bpyCTF, and that leaching of the active

metal species is negligible (Figure 3.10). However, since potentially leached Cp*Rh species may not be active for the transfer hydrogenation without comprising a 2,2'-bipyridine ligand (see Table 3.2, entry 7), an additional filtration test was performed in which free bipyridine ligand was added to the reaction mixture from the start. Again, no increase in substrate conversion was observed, demonstrating that bpyCTF firmly coordinates the Rh complex.

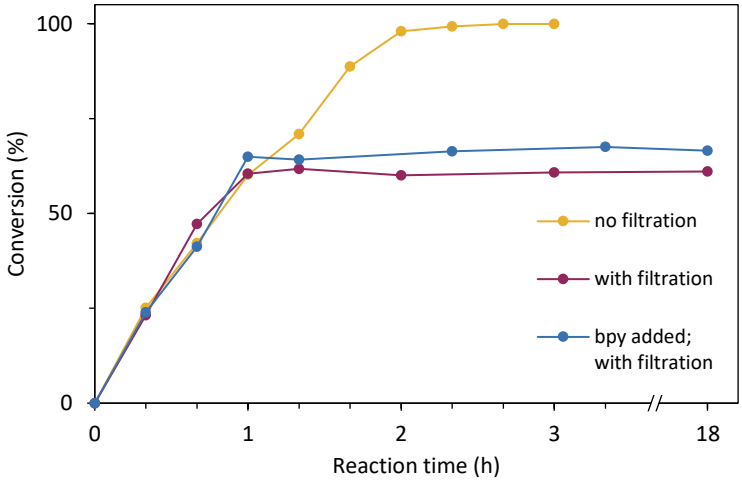

Figure 3.10. Hot-filtration test for Rh@bpyCTF. Yellow: unfiltered reaction with 2-methylquinoxaline **3a** (0.5 mmol), Rh@bpyCTF (5.6 mg, 0.25 mol% Rh), aqueous HCOOH/HCOONa solution (2 M, pH 4.5, 5 mL), 80 °C. red: the catalyst was removed by filtration after 1 h. Blue: 2,2'-bipyridine (1.25 mol%) was added from the start of the reaction. The catalyst was removed by filtration after 1 h.

2.2.3 Substrate scope

Considering the good performance of Rh@bpyCTF under the optimized conditions, the general applicability of the catalyst has been studied through the transfer hydrogenation of various quinoxalines and, by extension, of other N-heteroaromatic scaffolds. Therefore, a series of quinoxaline substrates were synthesized, comprising 2- and 2,3-substituted quinoxalines bearing small and bulky substituents and quinoxalines with electron-donating and -withdrawing groups on the C6-position. The quinoxaline substrates were prepared following known procedures. For instance, 2-*tert*-butylquinoxaline **3b** was accessed through the decarboxylative alkylation of quinoxaline **5** in a classical Minisci reaction with pivalic acid **6** (Scheme 3.4).[247] Carrying out the reaction in neat water gave additional formation of 8% 2,6-di-*tert*-butylquinoxaline, which could not be separated from the desired product by column chromatography using PE/EtOAc. In contrast, performing the reaction in a biphasic system of water and dichloromethane selectively furnished monoalkylated quinoxaline **3b**, because extraction of the more lipophilic alkylated product by the organic phase inhibited further alkylation. This way, pure 2-*tert*-butylquinoxaline **3b** was isolated in a yield of 73% after column chromatography

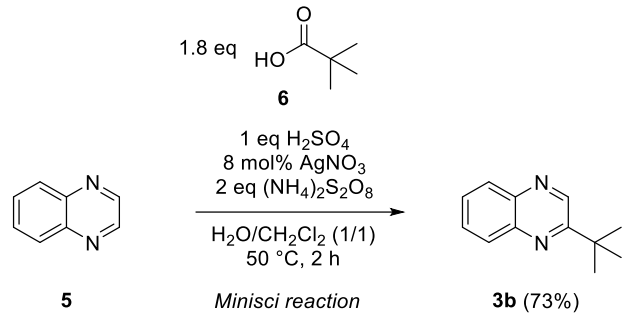

Scheme 3.4. Synthesis of 2-*tert*-butylquinoxaline **3b**.

The cyclization–oxidation of 2-bromoacetophenone **7** with benzene-1,2-diamine **8a** in the presence of pyridine gave 2-phenylquinoxaline **3c** (Scheme 3.5).[248]

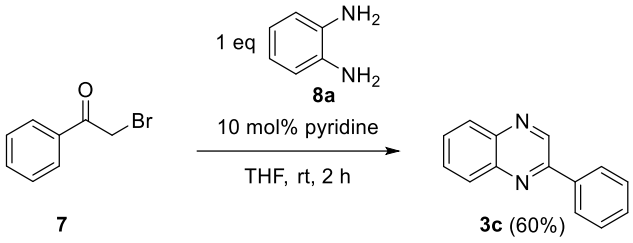

Scheme 3.5. Synthesis of 2-phenylquinoxaline **3c**.

A set of 2,3-disubstituted quinoxalines was prepared by condensation between *o*-phenylenediamines **8** and 1,2-diketones **10** (Scheme 3.6). Quinoxalines **3d,e,i–k** were of high purity after work-up by extraction and did not require any purification step for further use. In contrast, pure quinoxalines **3f** and **3h** were obtained after normal-phase column chromatography, whereas pure quinoxaline **3g** crystallized from the reaction mixture upon formation. All eight quinoxalines were isolated in good to excellent yields ranging from 72 to 99%.

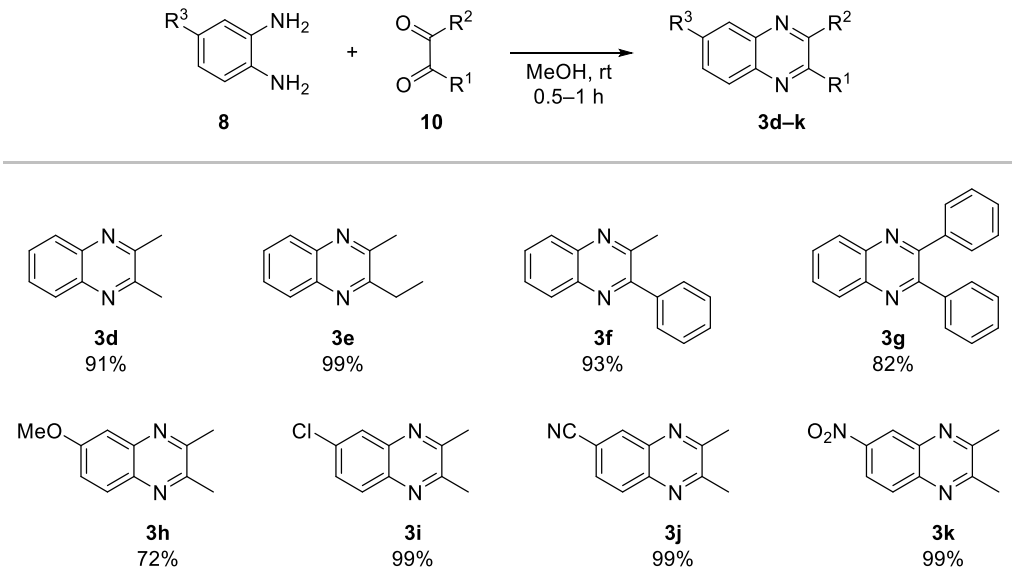

Scheme 3.6. Synthesis of 2,3-disubstituted quinoxalines **3d–k** via condensation reaction.

Next, the synthesized quinoxaline substrates were employed in the transfer hydrogenation catalyzed by Rh@bpyCTF. The reactions were carried out using an aqueous HCOOH/HCOONa buffer solution at the optimal pH 4.5 and at 80 °C. From the initial attempts, it became clear that some of the quinoxaline substrates required prolonged reaction times. To ensure the buffering capability of the reaction solution, the 2 M buffer solution was switched to a 4 M HCOOH/HCOONa buffer solution. Moreover, in the process of studying the substrate scope we found that not all the substrates dissolved well in the aqueous medium, which may lead to low conversions. Therefore, substrates were introduced into the reaction mixture as a concentrated solution in EtOAc. This addition resulted in a biphasic liquid, for which a high stirring rate was used to ensure adequate mixing. Using acetonitirle as a water miscible organic solvent resulted in a rapid decrease in catalytic activity after the first reaction cycle and was therefore abandoned.

Rh@bpyCTF exhibited high reactivity toward all the examined quinoxalines, with full conversions within 10 h or less, using a catalyst loading as low as 0.25 mol% Rh (Table 3.3). The corresponding 1,2,3,4-tetrahydroquinoxalines **11a–j** were isolated in good to excellent yields (75–96%). The 2-substituted quinoxalines **3b** and **3c**, bearing a sterically demanding *tert*-butyl and phenyl group, respectively, were easily hydrogenated to the corresponding tetrahydroquinoxalines, albeit with prolonged reaction times. The reactions with 2,3-dialkyl-substituted quinoxalines **3d,e,h–j** afforded the corresponding tetrahydroquinoxalines as mixtures of *cis*- and *trans*-isomers, with the *cis*-isomer predominating. The diastereoselectivity for tetrahydroquinoxalines **11d,e,h–j** could be determined from the chemical shifts (δ) and coupling constants (*J*) of the C2 and C3 methine protons in ^{1}H NMR spectroscopy ($\delta_{H,trans} < \delta_{H,cis}$ and $J_{H2\text{-}H3,cis} < J_{H2\text{-}H3,trans}$).[249] In contrast, only one diastereomer was observed when quinoxalines **3f** and **3g**, which both having a phenyl group on the pyrazine ring, were employed in the reaction. The relative configuration of

tetrahydroquinoxaline **11f** were readily deduced from the ^{1}H NMR spectrum ($CDCl_3$), which showed a small vicinal coupling constant of 3.2 Hz between the C2 and C3 methine protons, consistent with substituents adopting the *cis*-configuration.[250] In the case of tetrahydroquinoxaline **11g**, the ^{1}H NMR ($CDCl_3$) signal of the methine protons appeared as a singlet at 4.74 ppm, consistent with the chemical shift reported for the *cis*-isomer.[250] In addition, single-crystal X-ray diffraction analysis of **11g** unequivocally established the *cis*-configuration of the phenyl substituents (Figure 3.11).

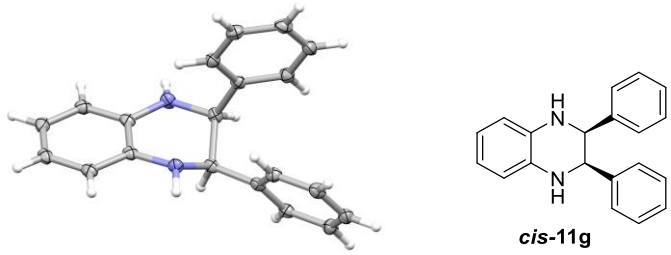

Figure 3.11. Molecular structure of *meso*-2,3-diphenyl-1,2,3,4-tetrahydroquinoxaline **11g**, showing the *cis*-configuration of the phenyl substituents. Thermal displacement ellipsoids are drawn at the 50% probability level.

Furthermore, the Rh@bpyCTF-catalyzed reaction was compatible with the electron-donating methoxy group (entry 8), and with the electron-withdrawing cyano and halogen substituents (entries 9 and 10). Quinoxalines **3h–j** were readily transformed and the corresponding tetrahydroquinoxalines **11h–j** were isolated in excellent yields. Fortunately, no dehalogenation was observed in the case of the chlorine substituted quinoxaline **3i**. Accelerated hydrogen transfer was noticed for quinoxaline **3j** because the electron-withdrawing cyano group renders the substrate more susceptible to nucleophilic attack. For 6-nitro-2,3-dimethylquinoxaline **3k**, the aromaticity of the quinoxaline scaffold was retained under these conditions, while the nitro group was chemoselectively reduced to an amino group. Further addition of fresh catalyst to the reaction mixture did not result in any reduction of the aromatic ring moiety, and thus 2,3-dimethylquinoxalin-6-amine **3k** was obtained as the final product, this in a yield of 77%.

Table 3.3. Transfer hydrogenation of quinoxalines in water catalyzed by Rh@bpyCTF.[a]

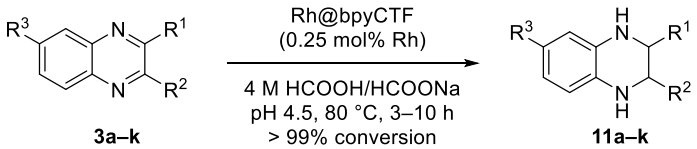

Entry	Substrate	Product	Time (h)	Yield[b] (%)
1	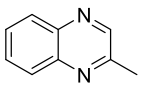 3a	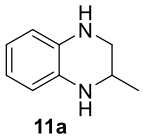 11a	3	94

Table 3.3. *Continued*

Entry	Substrate	Product	Time (h)	Yield[b] (%)
2	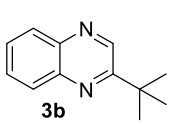 **3b**	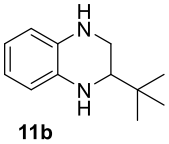 **11b**	9	80
3	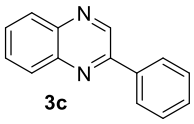 **3c**	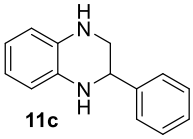 **11c**	10	85
4	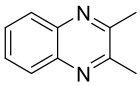 **3d**	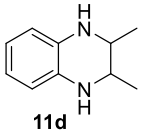 **11d**	5	76 (75/25)[c]
5	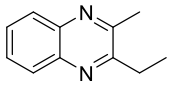 **3e**	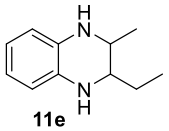 **11e**	5	82 (83/17)[c]
6	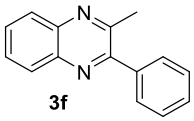 **3f**	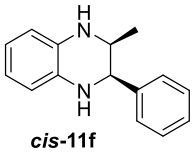 ***cis*-11f**	8	75 (100/0)[c]
7	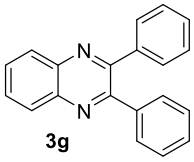 **3g**	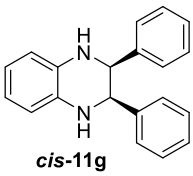 ***cis*-11g**	10	77 (100/0)[c]
8	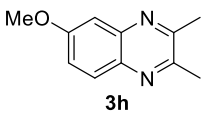 **3h**	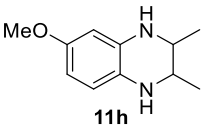 **11h**	8	95 (74/26)[c]
9	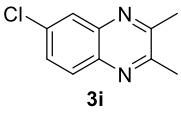 **3i**	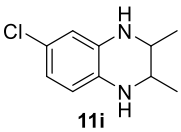 **11i**	7	92 (81/19)[c]
10	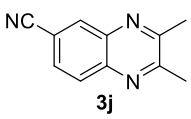 **3j**	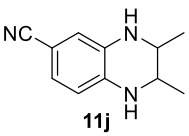 **11j**	2	96 (83/17)[c]
11	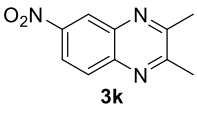 **3k**	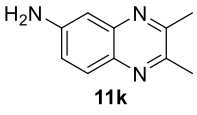 **11k**	8	77

[a] Reaction conditions: substrate **3** (0.7 mmol), Rh@bpyCTF (0.25 mol% Rh), HCOOH/HCOONa (4 M, pH 4.5, 7 mL), 80 °C.

[b] Isolated yields.

[c] *Cis*/*trans* ratio determined by ^{1}H NMR analysis ($CDCl_3$) of the crude reaction mixture.

Following the successful transformation of these quinoxaline derivatives, the potential of Rh@bpyCTF as a versatile catalyst was further demonstrated by extending the scope to various other N-heteroaromatic scaffolds (Table 3.4). Under the same reaction conditions, all investigated N-heteroarenes were reduced with full conversion, and the corresponding products could be isolated in very good to excellent yields (80–99%). 2-Methylquinoline **12a** was reduced in a clean and regioselective reaction, yielding 2-methyl-1,2,3,4-tetrahydroquinoline **13a** in very high purity and near quantitative yield (99%). 1,5-Naphthyridine **12b** was selectively hydrogenated in only one pyridine ring. The reaction with phenanthrolines **12c** and **12d**, both strong N-bidentate ligands, did not affect the activity of Rh@bpyCTF (entries 3 and 4). The reduction of 2,9-dimethyl-1,10-phenanthroline **12c** gave the partially hydrogenated 1,2,3,4-tetrahydrophenanthroline **13c** as the sole product, in line with the findings in previous reports.[251] In sharp contrast, the reduction of unsubstituted 1,10-phenanthroline achieved complete conversion in 3 h, but resulted in a mixture of tetrahydrophenanthroline and octahydrophenanthroline **13d** (THphen/OHphen = 73/27). Extending the reaction time to 24 h, resulted in complete conversion to the latter compound.

Table 3.4. Transfer hydrogenation of various N-heteroaromatic scaffolds in water catalyzed by Rh@bpyCTF.[a]

Entry	Substrate	Product	Time (h)	Yield[b] (%)
1	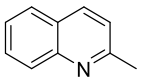 **12a**	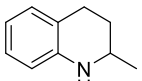 **13a**	4	99
2	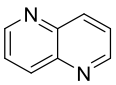 **12b**	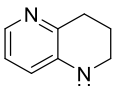 **13b**	8	85
3	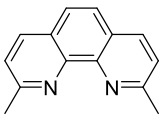 **12c**	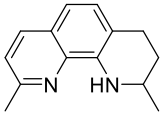 **13c**	6	87
4	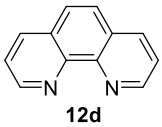 **12d**	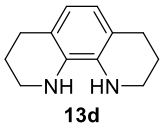 **13d**	24	82
5	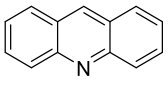 **12e**	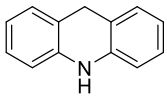 **13e**	1	91
6	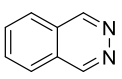 **12f**	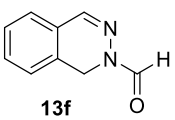 **13f**	24	80

[a] Reaction conditions: **12** (0.7 mmol), Rh@bpyCTF (0.25 mol% Rh), aqueous HCOOH/HCOONa (4 M, pH 4.5, 7 mL), 80 °C.
[b] Isolated yields.

In addition, acridine **12e** was readily reduced to the 9,10-dihydro product **13e** and obtained in a high yield of 91%. In the reduction of phthalazine **12f** only one of the imine bonds was hydrogenated, while the other imine bond remained untouched. Moreover, the hydrogenated product underwent rapid N-formylation at the amino nitrogen, and complete conversion to phthalazine-2(1*H*)-carbaldehyde **13f** was obtained. The *N*-formyl group of phthalazine-2(1*H*)-carbaldehyde **13f** could be cleaved by NaOH-mediated hydrolysis in an ethanol/water mixture under reflux conditions (Scheme 3.7). However, the targeted 1,2-dihydrophthalazine **14** could not be isolated in a pure state. ^{1}H NMR analysis revealed that the crude product also contained phthalazine **12f** to a minor extent (**14**/**12f** = 96/4). A second ^{1}H NMR analysis of the same sample four days later showed an increase in the amount of phthalazine (**14**/**12f** = 79/21), indicating that 1,2-dihydrophthalazine **14** is sensitive to air and was readily oxidized upon exposure during the hydrolysis reaction. This result is consistent with reports in the literature.[252-253] Nevertheless, a straightforward procedure for the cleavage of the *N*-formyl group is provided that can be extrapolated to other N-heterocycles.

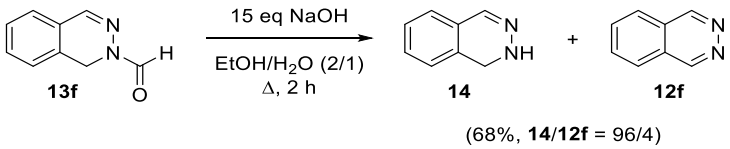

Scheme 3.7. NaOH-mediated cleavage of the *N*-formyl group.

2.2.4 Catalyst recycling experiments

To be relevant for practical applications, the catalyst must maintain its high activity over several reaction runs. Therefore, the long-term stability was studied over six runs. After each run the catalyst was recovered by filtration and dried at 100 °C before being reused in the next reaction. In general, the catalyst maintained its high activity throughout the recycling experiment, demonstrating its high stability (Figure 3.12). However, in the 5th run, the conversion toward **3a** slightly decreased to 89%, yet complete conversion was achieved with prolonged reaction times. In the 6th run, the conversion remained steady and did not decrease further. Furthermore, the crude product obtained in the first run did not contain any detectable amount of leached rhodium (< 0.003 wt%) as evidenced by ICP-OES analysis. Moreover, the Rh loading on Rh@bpyCTF after six reaction runs was still 1.9 wt% compared to the initial loading of 2.3 wt%. The decrease in Rh loading could be explained by small losses of Rh loading during catalyst recovery or by residues in the pores, making the CTF heavier. Lastly, XPS analysis of Rh@bpyCTF after recycling showed no change in the binding state of the Rh metal center (Figure S3.4).

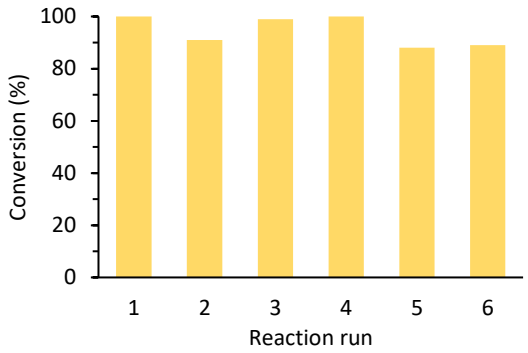

Figure 3.12. Recycling experiment with Rh@bpyCTF. Conversions to 2-methyl-1,2,3,4-tetrahydroquinoxaline **11a** were determined by ^{1}H NMR analysis after 3 h reaction. The lower conversion in reaction run 2 is most likely due to batch variability. Reaction conditions: **3a** (2.5 mmol), Rh@bpyCTF (28.1 mg, 0.25 mol% Rh), aqueous HCOOH/HCOONa solution (4 M, pH 4.5, 25 mL), 80 °C, 3 h.

2.2.5 Catalyst comparison

To demonstrate the merits of our catalytic system, we compared the Rh@bpyCTF-catalyzed transfer hydrogenation to other reported heterogeneous catalytic systems that use formic acid or formate as the hydrogen source (Table 3.5). Although a one-on-one comparison is not straightforward because of the different reaction conditions, the comparison of the catalysts showed that Rh@bpyCTF is a very efficient catalyst, achieving high reaction rates with a lower catalyst loading, and can operate effectively in water as a green solvent (entries 1 and 2 vs. 7).[254] Besides, no protective atmosphere was required, which contributes to the operational simplicity of the reaction (entry 5 vs. 7). Furthermore, by controlling the pH, we were able to selectively reduce the substrate to the non-formylated product, whereas the catalytic systems of entries 1 and 6 yielded mixtures that required an additional hydrolysis step. Rh@bpy-PMO of Matsui *et al.* showed similar high activity as Rh@bpyCTF, but lost significant activity after four reaction runs (entry 3).[255]

Table 3.5. Comparison of Rh@bpyCTF to reported heterogeneous catalysts for the transfer hydrogenation of 2-methylquinoline with formic acid or formate.

Entry	Catalyst	Conditions	TON[a]	TOF (h^{-1})[b]	Ref.
1	Au@NH_2-SBA-15 (1 mol% Au)	HCOOH (30 eq), Et_3N (5.25 eq), anhyd DMF, 130 °C	100	32	[256]
2	Au/TiO_2-R (1 mol% Au)	HCOOH (20 eq), Et_3N/DMF (1/8), 130 °C	99	235	[257]
3	Rh@bpy-PMO (0.2 mol% Rh)	HCOOH/HCOONa (8.7 eq), H_2O, 80 °C	500[c]	120	[255]
4	Ir/Si (1 mol% Ir)	HCOOH (2 eq), H_2O, 80 °C	100	7	[258]
5	Co@OMNC-700 (10.6 mol% Co)	HCOOH (8.5 eq), H_2O, N_2 atm, 140 °C	9[d]	2	[259]
6	Co@C-N_{800} (0.9 mol% Co)	HCOOH (15 eq), H_2O, 130 °C	100[d,e]	17	[260]
7	Rh@bpyCTF (0.25 mol% Rh)	HCOOH/HCOONa (40 eq), H_2O, 80 °C	400	100	This work

[a] Turnover number.
[b] Global turnover frequency over the course of the reaction.
[c] 2,3-Dimethylquinoxaline as substrate.
[d] Quinoline as substrate.
[e] Also N-formylated product, 87% selectivity.

2.3 Continuous flow transfer hydrogenation

Given the good performance of Rh@bpyCTF under batch conditions, we wanted to take full advantage of the heterogenization of the Rh catalyst and translated the batch transfer hydrogenation reaction into a continuous flow process using microreactor technology. Immobilization of the CTF-supported Rh complex in a packed-bed column results in a high local concentration of the Rh catalyst, which could lead to higher reaction rates. Moreover, separation of the catalyst from the product is inherent as the catalyst is retained in the column. Although catalytic transformations under flow conditions are receiving increasing attention, the use of COFs as catalysts in liquid flow reactions is still in its infancy, as reflected by the limited number of reported studies.[261-262]

To explore the feasibility of using Rh@bpyCTF in a continuous flow process, proof-of-concept experiments were conducted on the transfer hydrogenation of 2-methylquinoxaline. A packed-bed reactor was prepared by filling a PTFE tube with a mixture of Rh@bpyCTF and glass beads (Figure S3.6). Inert glass beads were added to overcome high back pressures due to the accommodation of fine particles. The packed-bed column was heated to 80 °C by means of a GC oven and reagents were passed through the column by using reciprocating pumps. A liquid–liquid separator (Zaiput) was integrated at the end of the setup to separate the organic product stream from the aqueous formate stream. The conversions toward the product **11a** obtained by varying the conditions are summarized in Table 3.6. Nearly complete conversion of **3a** was achieved in short contact times by using a large excess of formate (entry 1). However, the high conversion

could not be maintained for long periods of time, most probably due to displacement of the CTF particles and channel formation within the packed bed. Due to this channeling, part of the reagent stream does not get into contact with the CTF catalyst and hence is not converted. A more robust reactor configuration therefore needs to be designed. A simple modification to the current reactor would be to divide the CTF material into smaller consecutive segments separated by an inert material (Figure S3.7). This modification could result in less loose packing of the bed and therefore better containment of the CTF particles within the segments. However, an arguably more fundamental approach would be to shape the CTF catalyst into uniform pellets, or even better, to coat a monolith or 3D-printed structured reactor with the CTF catalyst, as these reactor configurations could minimize pressure drops in the reactor and could prevent mobility of the packing particles.[263]

Table 3.6. Preliminary results of the continuous flow transfer hydrogenation with a Rh@bpyCTF-catalyst bed.

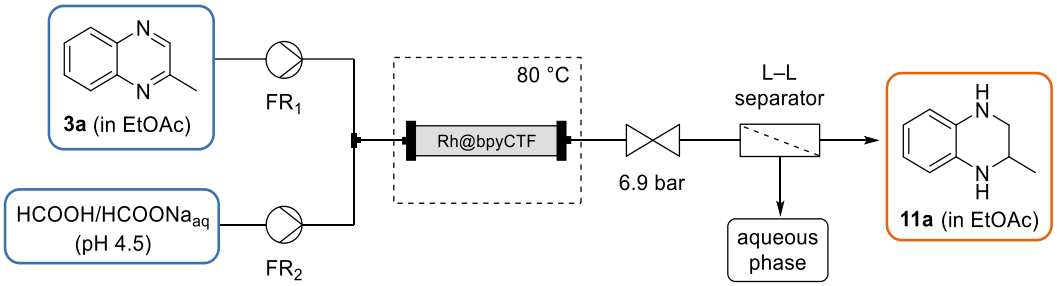

Entry[a]	[3a] (M)	[HCOO$^-$] (M)	FR$_1$ (mL min^{-1})	FR$_2$ (mL min^{-1})	HCOO$^-$ (eq)	CT[b] (s)	TOS[c] (min)	Conversion[d] 11a (%)
1	0.5	2	0.1	0.9	36	20	20	97
							25	94
2	0.25	0.5	0.2	0.8	8	20	15	58
							20	58
							25	41
3	0.25	1	0.2	0.8	16	20	15	74
							20	68
							25	62
4	0.5	2	0.1	0.4	16	40	15	99
							20	84
							25	59

[a] Experiments were performed in the given order using the same packed-bed column.
[b] Approximated mean contact time of the reactants with the catalyst bed.
[c] Time-on-stream
[d] Determined by ^{1}H NMR analysis.

3 Conclusion

A bipyridine-based CTF has been successfully applied as support for the immobilization of a Cp*Rh(III) complex. The heterogeneous Rh@bpyCTF catalyst exhibited high activity for the transfer hydrogenation of N-heteroarenes in water, using easy-to-handle sodium formate as the hydrogen donor. The reactivity was highly pH dependent, with the highest conversion rate at pH 4.5. A very wide range of quinoxalines and other N-heteroarenes underwent transfer hydrogenation to afford the products in good to excellent yields, highlighting the versatility of the catalyst. Moreover, the catalyst could be easily recovered by filtration and the recovered catalyst remained highly active for at least six reaction runs, proving the sustainable nature of this catalytic system. Additionally, the applicability of the catalyst under continuous flow conditions was explored in preliminary experiments, but the reactor design needs further optimization. All together, bpyCTF performed well as a support material for the heterogenization of molecular active metal centers, thereby bridging the gap between homogeneous and heterogeneous catalysis.

4 Experimental details

4.1 General methods

Solvents and reagents were purchased from commercial suppliers and used without further purification, unless otherwise stated. DMF was dried over activated molecular sieves (4 Å) for at least 48 h. Zinc dust was activated before use by stirring in a 1 M aqueous HCl solution, filtering and washing with distilled water, ethanol, and diethyl ether, followed by drying under vacuum. Thin layer chromatography (TLC) was performed using glass-backed 0.25 mm Merck silica gel 60 F_{254} TLC plates, and spots were visualized by UV light (254 nm). Column chromatography was performed using silica gel (particle size 35–70 µm, pore diameter 6 nm). ^{1}H NMR and ^{13}C NMR spectra were recorded at 400 and 101 MHz, respectively, using a Bruker Avance III HD 400 spectrometer equipped with a ^{1}H/BB z-gradient probe (BBO, 5 mm). The spectra were recorded at 25 °C and were processed using TopSpin 3.6.2. Chemical shifts (δ) are reported in parts per million (ppm) downfield of tetramethylsilane (internal reference) and coupling constants (*J*) are reported in hertz (Hz). Peaks were assigned with the aid of 2D spectra (COSY, HSQC, H2BC and HMBC). Infrared spectra (FT-IR) of discrete compounds were recorded from samples in neat form on a Shimadzu IRAFFINITY-1S FT-IR spectrophotometer with an ATR (attenuated total reflectance) accessory. Only selected absorbances (ν_{max}, cm^{-1}) are reported. HPLC-MS analyses were performed on an Agilent 1200 Series HPLC system equipped with a Supelco Ascentis Express C18 column (3 cm × 4.6 mm, 2.7 µm fused-core particles, 90 Å) and connected to a UV-DAD detector and an Agilent 1100 Series LC/MSD-type SL mass spectrometer with electrospray ionization (ESI,

capillary voltage 4 kV, fragmentor voltage 70 V) and with a mass-selective single-quadrupole detector.

4.2 Characterization of CTFs

4.2.1 Diffuse reflectance infrared Fourier transform spectroscopy

Infrared (DRIFT) spectra of CTFs were recorded with a Thermo Nicolet 6700 FT-IR spectrophotometer equipped with a nitrogen-cooled MCT detector and a KBr beam splitter. Samples were measured within KBr powder.

4.2.2 Nitrogen sorption analysis

Nitrogen sorption measurements were carried out on a BELSORP-mini II apparatus at 77 K. Prior to measurements, samples were degassed at 120 °C under vacuum for 16 h. Specific surface areas were calculated using the Brunauer–Emmett–Teller (BET) method. For the BET calculations, pressure ranges were chosen in accordance with the criteria described by Rouquerol *et al*.[264] The pore size distribution was determined using the quenched solid density-functional theory (QSDFT) model for N_2 adsorbed on carbons with cylindrical pores, implemented in Quantachrome's ASiQwin software (v4.0). Total pore volumes were determined at $P/P_0 = 0.99$.

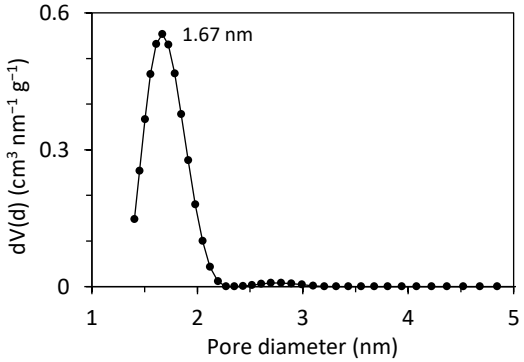

Figure S3.1. Pore size distribution of bpyCTF (QSDFT).

4.2.3 Elemental analysis

Combustion elemental analysis was performed on a Thermo Scientific Flash 2000 CHNS/O analyzer equipped with a TCD detector.

4.2.4 Powder X-ray diffraction

Powder X-ray diffraction (PXRD) patterns were collected using a Bruker D8 Advance diffractometer with a Cu Kα radiation source (λ = 1.5418 Å) at 40 kV and 45 mA and a scanning speed of 1° min^{-1}.

4.2.5 X-ray photoelectron spectroscopy

The surface chemical composition of the CTF samples was examined by XPS using the PHI 5000 VersaProbe II spectrometer equipped with a monochromatic Al Kα X-ray source (hv = 1486.6 eV). To do so, the samples were excited with an X-ray beam (size 200 µm) over an area of 500 x 500 μm^2 at a power of 50 W. Wide range survey scans and high-resolution spectra were recorded with a pass energy of 187.85 eV and 23.5 eV and a step size of 0.8 eV and 0.1 eV, respectively. All spectra were acquired at a take-off angle of 45° relative to the sample surface in the XPS chamber, where the pressure was constantly maintained below 10^{-6} Pa. The survey scans were used to determine and quantify the surface elemental composition and were analyzed using the MultiPak (v9.6) software by utilizing a Shirley background and applying the relative sensitivity factors supplied by the instrument's manufacturer. The detailed high-resolution spectra were also analyzed using the same software package via their curve fitting into different peaks to identify the corresponding chemical bonds. The energy scale of all acquired spectra was calibrated with respect to the hydrocarbon component of the C 1s spectrum (285.0 eV). The reported quantitative results are the mean values obtained from six independent analysis points measured on each sample.

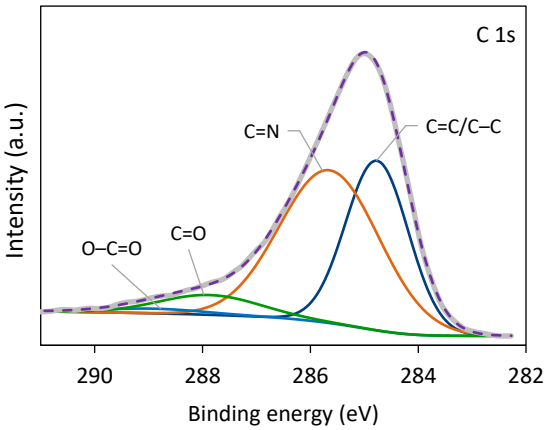

Figure S3.2. High-resolution C 1s XPS spectrum of bpyCTF.

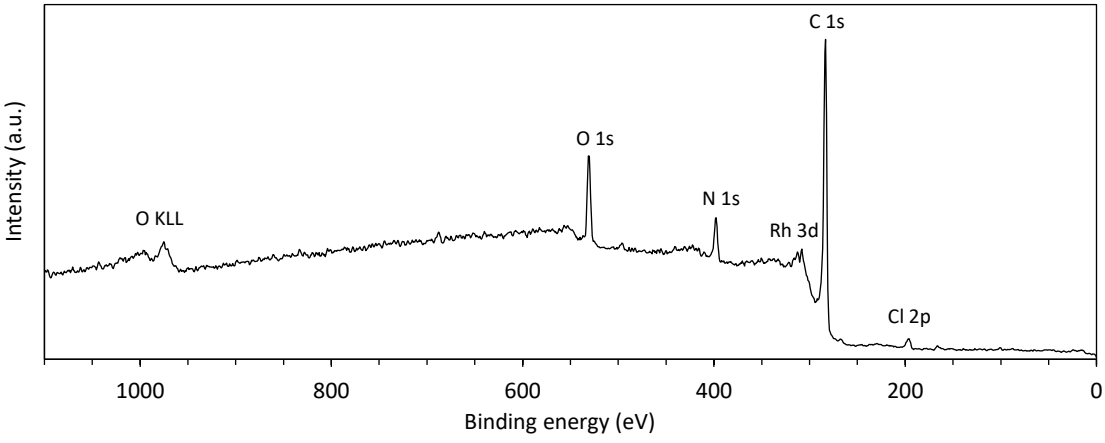

Figure S3.3. XPS survey spectrum of Rh@bpyCTF.

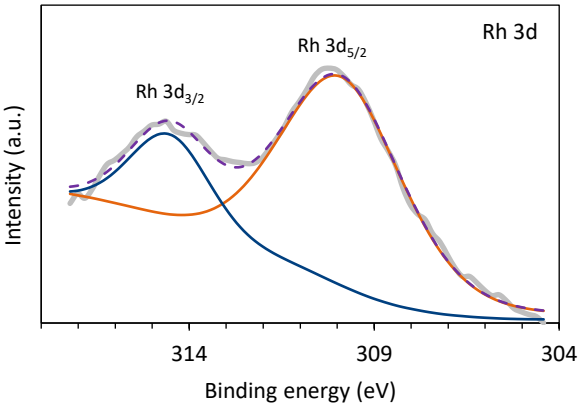

Figure S3.4. High-resolution Rh 3d XPS spectrum of Rh@bpyCTF after six reaction cycles.

4.2.6 Scanning transmission electron microscopy

Scanning transmission electron microscopy (STEM) images were taken with a high-angle annular dark-field (HAADF) detector on a JEOL JEM-2200FS TEM with a field emission gun at 200 kV. Samples were prepared by suspending the powder in ethanol and dipping a 300-mesh holey carbon copper grid into the suspensions. The elemental composition of the sample was determined via energy-dispersive X-ray (EDX) spectroscopy in HAADF-STEM mode.

4.2.7 Inductively coupled plasma-optical emission spectrometry

The immobilized amount of rhodium metal on the bpyCTF was quantified by ICP-OES analysis. The analyses, performed by Prof. Tack's research group (Ecochem, Department of Green Chemistry and Technology, Faculty of Bioscience Engineering, Ghent University), were carried out on a Thermo Scientific iCAP 7400 Duo ICP-OES instrument. Prior to analysis, the samples were subjected to microwave-assisted (Mars 6 – CEM) digestion in a closed vessel using nitric acid (67%). Thermo Scientific™ Qtegra™ Intelligent Scientific Data Solution™ (ISDS) software was used to process the results.

4.3 Catalyst synthesis

4.3.1 Synthesis of 2,2'-bipyridine-5,5'-dicarbonitrile (2)

2,2'-Bipyridine-5,5'-dicarbonitrile **2** was synthesized via a Ni-catalyzed reductive homocoupling of 2-bromo-5-cyanopyridine **1**, as described in **Chapter 2**.

4.3.2 Synthesis of bpyCTF

bpyCTF was synthesized under ionothermal conditions using $ZnCl_2$, which was dried overnight at 120 °C under vacuum prior to use. Typically, a quartz ampoule was charged with 2,2'-bipyridine-5,5'-dicarbonitrile **2** (320 mg, 1.55 mmol, 1 eq) and $ZnCl_2$ (1.06 g, 7.76 mmol, 5 eq). The ampoule

was placed under vacuum, flame-sealed and heated to 400 °C in a Nabertherm furnace oven with a heating rate of 1 °C min^{-1}. After 48 h at 400 °C, the temperature was brought to room temperature and the obtained crude solid was ground with pestle and mortar. The black powder was subsequently stirred overnight in a HCl solution (1 M) under reflux conditions to remove $ZnCl_2$ and unreacted monomer. Afterward, the solid was filtered and successively washed with water until neutral pH was reached (3 x 200 mL), THF (3 x 200 mL), ethanol (3 x 100 mL) and acetone (3 x 200 mL). The obtained black powder was dried overnight under vacuum at 120 °C prior further use.

4.3.3 Preparation of Rh@bpyCTF

$[Cp^*RhCl_2]_2$ complex (22.5 mg, 0.04 mmol) was dissolved in a mixture of anhydrous MeOH/$CHCl_3$ (1/1, 30 mL) under argon atmosphere. bpyCTF (300 mg, Rh/bpy molar ratio 0.05) was added, and the black suspension was heated to reflux temperature for 24 h. After cooling to room temperature, the solid was filtered and successively washed with MeOH (3 x 100 mL), CH_2Cl_2 (3 x 100 mL) and Et_2O (3 x 100 mL). The obtained solid was dried overnight under vacuum at 120 °C. ICP-OES analysis was performed to quantify the actual loading of Rh metal in the bpyCTF.

4.4 Transfer hydrogenation reactions

4.4.1 General procedure in the reaction conditions optimization

The stirring speed was fixed (800 rpm) in all transfer hydrogenation reactions to improve the repeatability and to allow a comparison between reactions. Aqueous formate solutions were prepared by dissolving HCOOH and HCOONa in HPLC-grade water. The quantities needed were calculated using Equation 1. The pH of the solution was verified at 21 °C using a pH meter.

$$\mathrm{pH} = \mathrm{p}K_\mathrm{a} + \log\left(\frac{[\mathrm{HCOONa}]}{[\mathrm{HCOOH}]}\right) \quad (1)$$

$$\mathrm{p}K_a\ (\mathrm{HCOOH}) = 3.6$$

In a 12 mL test tube, an aqueous HCOOH/HCOONa buffer (2 M, pH 4.5, 5 mL) was preheated to 80 °C, after which 2-methylquinoxaline **3a** (0.5 mmol) and Rh@bpyCTF (5.6 mg, 0.25 mol% Rh) were sequentially added. The test tube was provided with a cap which was not screwed tight to ensure CO_2 could still be released from the system. The reaction mixture was vigorously stirred (fixed at 800 rpm) to ensure sufficient mixing. Aliquots (300 µL) were taken basified (pH > 10) with NaOH and extracted with Et_2O (3 x 500 µL). The combined organic phases were evaporated to dryness and the residue was analyzed by ^{1}H NMR spectroscopy ($CDCl_3$).

4.4.2 Catalyst recycling experiments

Catalyst recycling experiments were performed in a 100 mL test tube with a HCOOH/HCOONa buffer solution (4 M, pH 4.5, 25 mL) and with 2-methylquinoxaline **3a** (322 µL, 2.5 mmol) in 1 mL EtOAc, and Rh@bpyCTF (28 mg, 0.25 mol% Rh). An aliquot was taken after 3 h reaction to determine the conversion by ^{1}H NMR spectroscopy ($CDCl_3$). After each run, the catalyst was recovered by filtration, whereupon it was successively washed with water, acetone and diethyl ether, and subsequently dried under vacuum at 100 °C for 5 h. The dried catalyst was then applied in the next reaction run.

4.4.3 Synthesis of [Cp*Rh(bpy)Cl]Cl

$[Cp^*Rh(\mu\text{-}Cl)Cl]_2$ dimer (30 mg, 48 µmol) and 2,2'-bipyridine (15 mg, 96 µmol) were dissolved in $CHCl_3$ (1 mL) and stirred at room temperature. Within a few minutes, an orange suspension started to form. After 1 h, the orange precipitate was collected by filtration, rinsed with cold $CHCl_3$, and dried *in vacuo* yielding [Cp*Rh(bpy)Cl]Cl as pale orange solid (38 mg, 84%). The formation of a complex with bipyridine was confirmed by ^{1}H NMR analysis (Figure S3.5). A downfield shift of the NMR signals was observed upon binding of the ligand with Rh.

(2,2'-bipyridine-κ*N,N'*)chlorido(η^5-pentamethyl cyclopentadienyl)rhodium(III) chloride

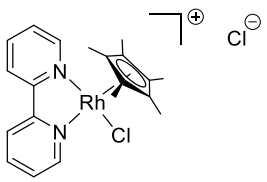

Pale orange solid. Yield 84%. **^{1}H NMR** (400 MHz, $CDCl_3$): δ 1.73 (15H, s, $C_5(C\underline{H}_3)_5$), 7.82 (2H, ddd, *J* = 7.8, 5.7, 1.1 Hz, $H^{5,5'}$), 8.26 (2H, td, *J* = 7.8, 1.3 Hz, $H^{4,4'}$), 8.85 (2H, dd, *J* = 5.7, 1.3 Hz, $H^{6,6'}$), 9.08 (2H, d, *J* = 7.8 Hz, $H^{3,3'}$). **^{13}C NMR** (101 MHz, $CDCl_3$): δ 9.2 ($C_5(\underline{C}H_3)_5$), 97.1 (d, $J_{Rh,C}$ = 8.1 Hz, $\underline{C}_5(CH_3)_5$), 125.7 ($C^{3,3'}$), 128.4 ($C^{5,5'}$), 140.8 ($C^{4,4'}$), 151.1 ($C^{6,6'}$), 154.7 ($C^{2,2'}$). **IR** (ATR, cm^{-1}): ν_{max} = 3541, 3283, 1603, 1443, 1302, 1024, 766. **MS** (ESI): m/z (%) 429/431 ($[C_{20}H_{23}N_2ClRh]^+$, 100), 197 ($[C_{20}H_{23}N_2ClRh - Cl]^{2+}$, 53).

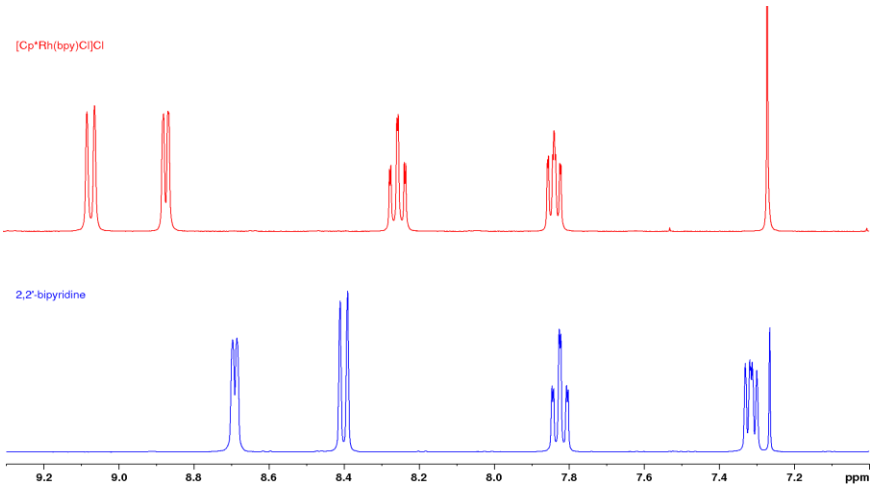

Figure S3.5. ^{1}H NMR spectra ($CDCl_3$) of free 2,2'-bipyridine (bottom) and 2,2'-bipyridine coordinated in [Cp*Rh(bpy)Cl]Cl (top). A downfield shift of the NMR signals was observed upon binding of the ligand with Rh.

4.4.4 Continuous flow transfer hydrogenation

The continuous flow setup was constructed as follows (Figure S3.6): A solution of 2-methylquinoxaline in EtOAc and an aqueous HCOOH/HCOONa buffer solution were introduced into the system by means of two ReaXus 6010R high-performance reciprocating pumps. The liquid streams were brought into contact by using a Y-connector, creating a segmented flow regime before entering the reactor column. The packed-bed reactor column was assembled by filling a PTFE (polytetrafluoroethylene) tubing (I.D. 2.4 mm, O.D. 3.2 mm) with 215 mg Rh@bpyCTF (containing 2.3 wt% Rh) mixed with 750 mg glass beads (Ø 750 µm). The packed bed had a length of 15 cm and was held in place by a cotton plug of about 2 cm at each end. The column was mounted vertically in a GC oven at 80 °C and the liquid flow was directed upward through the column. A 6.9 bar back pressure regulator (BPR) was connected to the end of the reactor column, after which the reaction mixture was flown through an ice–water bath. At the end of the setup, the liquid stream was passed through a Zaiput Flow Technologies SEP-10 liquid–liquid separator with PTFE membrane to separate the organic phase from the aqueous phase. Samples were collected and the solvent was evaporated by a stream of nitrogen gas. The conversion of 2-methylquinoxaline **3a** to 2-methyl-1,2,3,4-tetrahydroquinoxaline **11a** was determined by integration of the methyl signal of **3a** (2.79 ppm) and **11a** (1.19 ppm) in the ^{1}H NMR spectra ($CDCl_3$) of the crude reaction product.

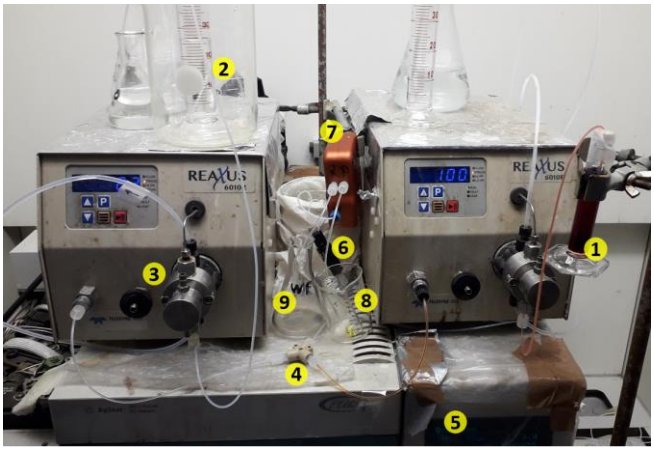

1| organic feed
2| aqueous feed
3| HPLC pump (2x)
4| Y-connector
5| GC oven
6| back pressure regulator
7| liquid–liquid separator
8| organic product stream
9| aqueous stream

Figure S3.6. Picture of the packed-bed reactor column (left) and the continuous flow setup (right).

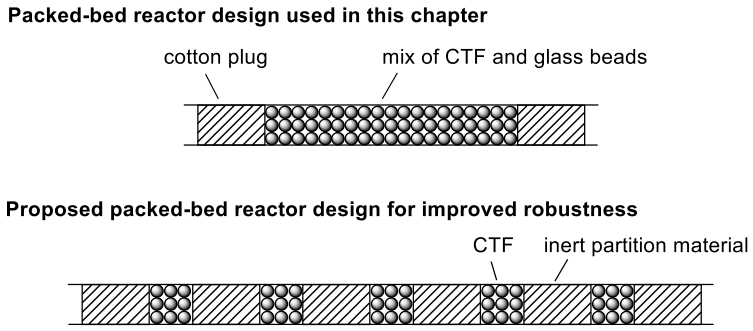

Figure S3.7. A simple modification to the reactor configuration is proposed, which could provide a first solution to prevent displacement of the CTF particles and channel formation.

4.4.5 Synthesis and characterization of transfer hydrogenation substrates

The atom numbering used in the NMR peak assignment follows the IUPAC Nomenclature of Organic Chemistry.

4.4.5.1 Synthesis of 2-(*tert*-butyl)quinoxaline (3b)

2-(*tert*-Butyl)quinoxaline **3b** was synthesized through C–H alkylation of quinoxaline via the classical Minisci-type reaction.[247] A mixture of quinoxaline **5** (300 mg, 2.30 mmol, 1 eq), pivalic acid **6** (423 mg, 4.14 mmol, 1.8 eq), H_2SO_4 (123 µl, 2.30 mmol, 1 eq), silver nitrate (31 mg, 0.18 mmol, 8 mol%) and ammonium persulfate (1.05 g, 4.60 mmol, 2 eq) in CH_2Cl_2/H_2O (1/1, 30 mL) was refluxed at 50 °C. After 2 h, the reaction mixture was basified to pH 9–10 by the addition of NaOH (1 M) and the organic phase was separated. The aqueous phase was extracted with CH_2Cl_2 (2 x 10 mL), and the combined organic phases were dried over $MgSO_4$, filtered and concentrated *in vacuo*. The crude product was purified by column chromatography on silica gel and petroleum ether/ethyl acetate 9/1 as eluent to yield 2-(*tert*-butyl)quinoxaline **3b** as a colorless oil (312 mg, 73%).

2-(tert-Butyl)quinoxaline (3b)

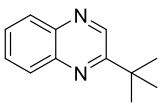

Yield 73%. Colorless oil, R_f = 0.32 (PE/EtOAc 9/1). **^{1}H NMR** (400 MHz, $CDCl_3$): δ 1.52 (9H, s, 3 x CH_3), 7.67–7.76 (2H, m, $H^{6,7}$), 8.03–8.09 (2H, m, $H^{5,8}$), 8.99 (1H, s, H^3). **^{13}C NMR** (101 MHz, $CDCl_3$): δ 29.7 (3 x CH_3), 37.2 ($\underline{C}_{quat}(CH_3)_3$), 128.9 ($C^6$), 128.9 ($C^8$), 129.3 ($C^5$), 129.6 ($C^7$), 140.8 ($C^{4a}$), 141.6 ($C^{8a}$), 143.4 ($C^3$), 163.7($C^2$). **IR** (ATR, cm^{-1}): ν_{max} = 2965, 1557, 1493, 1479, 1462, 1364, 1163, 1096, 1016, 968, 773, 424. **MS** (ESI): m/z (%) 187 ($[M + H]^+$, 100). The data are in accordance with those reported in the literature.[265]

4.4.5.2 Synthesis of 2-phenylquinoxaline (3c)

To as solution of benzene-1,2-diamine **8a** (300 mg, 2.77 mmol, 1 eq) in THF (10 mL), 2-bromoacetophenone **7** (552 mg, 2.77 mmol, 1 eq) and pyridine (22 µL, 0.28 mmol, 10 mol%) were added and the mixture was stirred in open air at room temperature for 2 h. Subsequently, water (10 mL) was added, and the reaction mixture was extracted with EtOAc (3 x 15 mL). The combined organic phases were dried over $MgSO_4$, filtered and concentrated under reduced pressure. Purification of the crude product by flash column chromatography on silica gel and petroleum ether/ethyl acetate 19/1 as eluent afforded 2-phenylquinoxaline **3c** as a yellow solid (345 mg, 60%).

2-Phenylquinoxaline (3c)

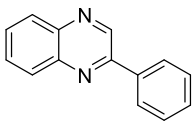

Yield 60%. Yellow solid, R_f = 0.18 (PE/EtOAc 19/1). **^{1}H NMR** (400 MHz, $CDCl_3$): δ 7.50–7.61 (3H, m, $CH_{phenyl,para}$, 2 x $CH_{phenyl,meta}$), 7.72–7.83 (2H, m, $H^{6,7}$), 8.11–8.18 (2H, m, $H^{5,8}$), 8.18–8.22 (2H, m, 2 x $CH_{phenyl,ortho}$), 9.34 (1H, s, H^3). **^{13}C NMR** (101 MHz, $CDCl_3$): δ 127.6 (2 x $CH_{phenyl,ortho}$), 129.2 (C^5, 2 x $CH_{phenyl,meta}$), 129.5 (C^6), 129.7 (C^8), 130.2 ($CH_{phenyl,para}$), 130.3 (C^7), 136.8 ($C_{quat,phenyl}$), 141.6 (C^{4a}), 142.3 (C^{8a}), 143.4 (C^3), 151.9 (C^2). **IR** (ATR, cm^{-1}): ν_{max} = 1545, 1487, 1312, 1028, 955, 764, 748, 685, 669, 550, 407. **MS** (ESI): m/z (%) 207 ($[M + H]^+$, 100). The data are in accordance with those reported in the literature.[266]

4.4.5.3 Synthesis of 2,3-disubstituted quinoxalines 3d–3k

As a representative example, the synthesis of 2,3-dimethylquinoxaline **3d** is described. To a stirred solution of benzene-1,2-diamine **8a** (324 mg, 3 mmol, 1 eq) in methanol (20 mL) was added butane-2,3-dione **10** (263 µL, 3 mmol, 1 eq). The reaction mixture was stirred at room temperature for 1 h, after which the solvent was removed *in vacuo*. Diethyl ether (25 mL) was added to the residue and the mixture was washed with water (3 x 10 mL). The organic phase was dried over $MgSO_4$, filtered and the solvent was evaporated under reduced pressure to obtain 2,3-dimethylquinoxaline **3d** as white crystals (433 mg, 91%). No further purification was necessary for all the derivatives, unless otherwise stated.

2,3-Dimethylquinoxaline (3d)

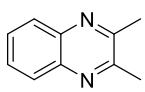

Yield 91%. White crystals. **^{1}H NMR** (400 MHz, $CDCl_3$): δ 2.73 (6H, s, 2 x CH_3), 7.63–7.68 (2H, m, $H^{6,7}$), 7.94–8.00 (2H, m, $H^{5,8}$). **^{13}C NMR** (101 MHz, $CDCl_3$): δ 23.3 (2 x CH_3), 128.5 ($C^{5,8}$), 129.0 ($C^{6,7}$), 141.2 ($C^{4a,8a}$), 153.6 ($C^{2,3}$). **IR** (ATR, cm^{-1}): ν_{max} = 1489, 1435, 1395, 1363, 1317, 1209, 1165, 988, 976, 904, 758, 669, 611. **MS** (ESI): m/z (%) 159 ($[M + H]^+$, 100). The data are in accordance with those reported in the literature.[267]

2-Ethyl-3-methylquinoxaline (3e)

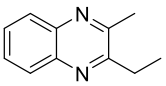

Yield 99%. Off-white solid. **^{1}H NMR** (400 MHz, $CDCl_3$): δ 1.42 (3H, t, *J* = 7.5 Hz, $CH_2C\underline{H}_3$), 2.77 (3H, s, $C^3C\underline{H}_3$), 3.04 (2H, q, *J* = 7.5 Hz, $C\underline{H}_2CH_3$), 7.63–7.69 (2H, m, $H^{6,7}$), 7.95–8.05 (2H, m, $H^{5,8}$). **^{13}C NMR** (101 MHz, $CDCl_3$): δ 12.0 ($CH_2\underline{C}H_3$), 22.7 ($C^3\underline{C}H_3$), 29.0 ($\underline{C}H_2CH_3$), 128.3 (C^8), 128.6 (C^5), 128.7(C^6), 128.8 (C^7), 141.0 and 141.2 ($C^{4a,8a}$), 153.1 (C^3), 157.6 (C^2). **IR** (ATR, cm^{-1}): ν_{max} = 1487, 1369, 1381, 1304, 1204, 1152, 1126, 903, 754, 660, 608, 422. **MS** (ESI): m/z (%) 173 ($[M + H]^+$, 100). The data are in accordance with those reported in the literature.[268]

2-Methyl-3-phenylquinoxaline (3f)

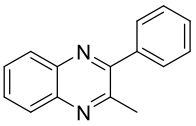

Yield 93%. White solid. **^{1}H NMR** (400 MHz, $CDCl_3$): δ 2.78 (3H, s, CH_3), 7.46–7.56 (3H, m, $CH_{phenyl,para}$, 2 x $CH_{phenyl,meta}$), 7.64–7.68 (2H, m, 2 x $CH_{phenyl,ortho}$), 7.69–7.77 (2H, m, $H^{6,7}$), 8.09–8.14 (1H, m, H^5), 8.03–8.09 (1H, m, H^8). **^{13}C NMR** (101 MHz, $CDCl_3$): δ 24.4 (CH_3), 128.3 (C^5), 128.6 (2 x $CH_{phenyl,meta}$), 128.9 (2 x $CH_{phenyl,ortho}$), 129.0 ($CH_{phenyl,para}$), 129.2 (C^7), 129.3 (C^8), 129.7 (C^6), 139.1 ($C_{quat,phenyl}$), 141.0 (C^{8a}), 141.3 (C^{4a}), 152.5 (C^2), 154.9 (C^3). **IR** (ATR, cm^{-1}): ν_{max} = 1486, 1443, 1395, 1341, 1005, 993, 756, 698, 608, 577, 478, 436. **MS** (ESI): m/z (%) 221 ($[M + H]^+$, 100). The data are in accordance with those reported in the literature.[250]

2,3-Diphenylquinoxaline (3g)

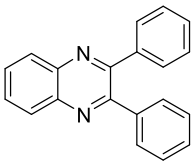

Yield 82%. White solid. **^{1}H NMR** (400 MHz, $CDCl_3$): δ 7.31–7.40 (6H, m, 4 x $CH_{phenyl,meta}$, 2 x $CH_{phenyl,para}$), 7.50–7.55 (4H, m, 4 x $CH_{phenyl,ortho}$), 7.75–7.81 (2H, m, $H^{5,8}$), 8.16–8.21 (2H, m, $H^{6,7}$). **^{13}C NMR** (101 MHz, $CDCl_3$): δ 128.4 (4 x $CH_{phenyl,meta}$), 128.9 (2 x $CH_{phenyl,para}$), 129.4 ($C^{6,7}$), 130.0 (4 x $CH_{phenyl,ortho}$), 130.1 ($C^{5,8}$), 139.3 (2 x $C_{quat,phenyl}$), 141.4 ($C^{4a,8a}$), 153.6 ($C^{2,3}$). **IR** (ATR, cm^{-1}): ν_{max} = 1477, 1443, 1396, 1346, 1059, 978, 930, 761, 696, 669, 598, 538. **MS** (ESI): m/z (%) 283 ($[M + H]^+$, 100). The data are in accordance with those reported in the literature.[250]

6-Methoxy-2,3-dimethylquinoxaline (3h)

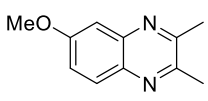

Yield 72%, after automated column chromatography (SiO_2). White solid, R_f = 0.21 (PE/EtOAc 3/2). **^{1}H NMR** (400 MHz, $CDCl_3$): δ 2.69 (3H, s, CH_3), 2.71 (3H, s, CH_3), 3.94 (3H, s, CH_3O), 7.28–7.33 (2H, m, $H^{5,7}$), 7.86 (1H, d, *J* = 8.8 Hz, H^8).

^{13}C NMR (101 MHz, $CDCl_3$): δ 22.8 (CH_3), 23.1 (CH_3), 55.7 (CH_3O), 106.2 (C^5), 121.7 (C^7), 129.3 (C^8), 137.0 (C^{8a}), 142.5 (C^{4a}), 150.6 and 153.4 ($C^{2,3}$), 160.0 (C^6). **IR** (ATR, cm^{-1}): ν_{max} = 1616, 1493, 1443, 1375, 1215, 1153, 1110, 1016, 947, 824, 598, 436. **MS** (ESI): m/z (%) 189 ($[M + H]^+$, 100). The data are in accordance with those reported in the literature.[269]

6-Chloro-2,3-dimethylquinoxaline (3i)

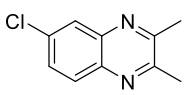

Yield 99%. Beige-brown solid. **^{1}H NMR** (400 MHz, $CDCl_3$): δ 2.72 (3H, s, CH_3), 2.73 (3H, s, CH_3), 7.60 (1H, dd, *J* = 8.9, 2.3 Hz, H^7), 7.90 (1H, d, *J* = 8.9 Hz, H^8), 7.97 (1H, d, *J* = 2.3 Hz, H^5). **^{13}C NMR** (101 MHz, $CDCl_3$): δ 23.15 (CH_3), 23.21 (CH_3), 127.4 (C^5), 129.6 (C^8), 129.8 (C^7), 134.4 (C^6), 139.6 (C^{8a}), 141.4 (C^{4a}), 153.8 and 154.6 ($C^{2,3}$). **IR** (ATR, cm^{-1}): ν_{max} = 1601, 1479, 1439, 1395, 1368, 1323, 1159, 1063, 924, 887, 831, 781, 723, 577, 428. **MS** (ESI): m/z (%) 193/195 ($[M + H]^+$, 100). The data are in accordance with those reported in the literature.[267]

2,3-Dimethylquinoxaline-6-carbonitrile (3j)

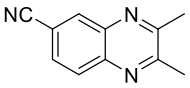

Yield 99%. Salmon pink solid. **^{1}H NMR** (400 MHz, $CDCl_3$): δ 2.77 (3H, s, CH_3), 2.78 (3H, s, CH_3), 7.81 (1H, dd, *J* = 8.6, 1.7 Hz, H^7), 8.60 (1H, d, *J* = 8.6 Hz, H^8), 8.35 (1H, d, *J* = 1.7 Hz, H^5). **^{13}C NMR** (101 MHz, $CDCl_3$): δ 23.3 (CH_3), 23.5 (CH_3), 112.2 (C^6), 118.3 (C≡N), 129.8 (C^7), 130.0 (C^8), 134.4 (C^5), 140.3 (C^{4a}), 142.7 (C^{8a}), 155.9 and 156.7 ($C^{2,3}$). **IR** (ATR, cm^{-1}): ν_{max} = 2224, 1603, 1574, 1439, 1396, 1368, 1323, 1167, 908, 835, 611, 577, 419. **MS** (ESI): m/z (%) 184 ($[M + H]^+$, 100). The data are in accordance with those reported in the literature.[269]

2,3-Dimethyl-6-nitroquinoxaline (3k)

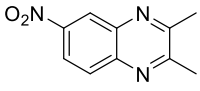

Quantitative yield. Light brown solid. **^{1}H NMR** (400 MHz, $CDCl_3$): δ 2.80 (6H, s, 2 x CH_3), 8.11 (1H, d, *J* = 9.1 Hz, H^8), 8.44 (1H, dd, *J* = 9.1, 2.4 Hz, H^7), 8.90 (1H, d, *J* = 2.4 Hz, H^5). **^{13}C NMR** (101 MHz, $CDCl_3$): δ 23.3 (CH_3), 23.5 (CH_3), 122.3 (C^7), 124.8 (C^5), 129.9 (C^8), 139.9 (C^{4a}), 143.7 (C^{8a}), 147.1 (C^6), 156.3 and 157.2 ($C^{2,3}$). **IR** (ATR, cm^{-1}): ν_{max} = 1616, 1578, 1524, 1398, 1341, 1196, 1165, 895, 845, 822, 743, 712, 420. **MS** (ESI): *m/z* (%) 204 ($[M + H]^+$, 100). The data are in accordance with those reported in the literature.[267]

4.4.6 Synthesis and characterization of transfer hydrogenation products

The atom numbering used in the NMR peak assignment follows the IUPAC Nomenclature of Organic Chemistry.

General procedure for the transfer hydrogenation toward N-heteroarenes **11** and **13**:

In a 12 mL test tube, an aqueous HCOOH/HCOONa buffer (4 M, pH 4.5, 7 mL) was preheated to 80 °C, after which N-heteroarene substrate (0.7 mmol) dissolved in EtOAc (0.7 mL), and Rh@bpyCTF (7.9 mg, 0.25 mol% Rh) were sequentially added. The test tube was provided with a cap which was not screwed tight to ensure CO_2 could still be released. The reaction mixture was vigorously stirred (fixed at 800 rpm) to ensure sufficient mixing. At complete conversion of the substrate (monitored by LC-MS), the catalyst was filtered and rinsed with water and Et_2O. After basifying the filtrate (pH > 10) with NaOH (1 M), the organic phase was separated, and the aqueous phase was extracted twice with Et_2O (2 x 15 mL). The combined organic phases were dried over $MgSO_4$, filtered and evaporated *in vacuo*. The product was purified by normal-phase column chromatography on silica gel and petroleum ether/ethyl acetate as eluent.

2-Methyl-1,2,3,4-tetrahydroquinoxaline (11a)

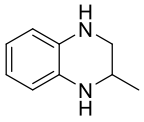

Yield 94%. Pale orange solid, R_f = 0.15 (PE/EtOAc 4/1). **^{1}H NMR** (400 MHz, $CDCl_3$): δ 1.19 (3H, d, *J* = 6.3 Hz, CH_3), 3.04 (1H, dd, *J* = 10.7, 8.2 Hz, H^{3a}), 3.32 (1H, dd, *J* = 10.7, 2.9 Hz, H^{3b}), 3.47–3.56 (1H, m, H^2), 3.60 (2H, br s, 2 x NH), 6.47–6.53 (2H, m, $H^{5,8}$), 6.55–6.62 (2H, m, $H^{6,7}$). **^{13}C NMR** (101 MHz, $CDCl_3$): δ 19.9 (CH_3), 45.7 (C^2), 48.3 (C^3), 114.4 and 114.5 ($C^{5,8}$), 118.69 and 118.71 ($C^{6,7}$), 133.2 and 133.6 ($C^{4a,8a}$). **IR** (ATR, cm^{-1}): ν_{max} = 3358, 3310, 2957, 2845, 1595, 1499, 1362, 1304, 1269, 1070, 922, 741. **MS** (ESI): m/z (%) 149 ($[M + H]^+$, 100). The data are in accordance with those reported in the literature.[270]

2-*tert*-Butyl-1,2,3,4-tetrahydroquinoxaline (11b)

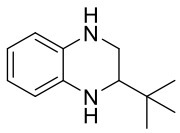

Yield 80%. Pale yellow crystals, R_f = 0.18 (PE/EtOAc 9/1). **^{1}H NMR** (400 MHz, $CDCl_3$): δ 0.99 (9H, s, 3 x CH_3), 3.10–3.18 (2H, m, $H^{2,3a}$), 3.31–3.39 (1H, m, H^{3b}), 3.64 (2H, br s, 2 x NH), 6.48–6.62 (4H, m, $H^{5,6,7,8}$). **^{13}C NMR** (101 MHz, $CDCl_3$): δ 26.0 (3 x CH_3), 32.8 ($\underline{C}_{quat}(CH_3)_3$), 42.5 ($C^3$), 59.0 ($C^2$), 114.25 and 114.32 ($C^{5,8}$), 118.2 and 118.9 ($C^{6,7}$), 133.3 and 134.6 ($C^{4a,8a}$). **IR** (ATR, cm^{-1}): ν_{max} = 3368, 2957, 1595, 1503, 1472, 1300, 1119, 1076, 1032, 905, 733. **MS** (ESI): m/z (%) 191 ($[M + H]^+$, 100). The data are in accordance with those reported in the literature.[265]

2-Phenyl-1,2,3,4-tetrahydroquinoxaline (11c)

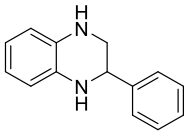

Yield 85%. Yellow solid, R_f = 0.13 (PE/EtOAc 19/1). **^{1}H NMR** (400 MHz, $CDCl_3$): δ 3.33 (1H, dd, *J* = 11.0, 8.2 Hz, H^{3a}), 3.46 (1H, dd, *J* = 11.0, 3.1 Hz, H^{3b}), 3.86 (2H, br s, 2 x NH), 4.48 (1H, dd, *J* = 8.2, 3.1 Hz, H^2), 6.55–6.61 (2H, m, $H^{5,8}$), 6.61–6.67 (2H, m, $H^{6,7}$), 7.28–7.34 (1H, m, $CH_{phenyl,para}$), 7.28–7.41 (1H, m, 2 x $CH_{phenyl,ortho}$, 2 x $CH_{phenyl,meta}$). **^{13}C NMR** (101 MHz, $CDCl_3$): δ 49.2 (C^3), 54.7 (C^2), 114.4 and 114.7 ($C^{5,8}$), 118.8 and 118.9 ($C^{6,7}$), 127.0 (2 x $CH_{phenyl,ortho}$), 127.9 ($CH_{phenyl,para}$), 128.6 (2 x $CH_{phenyl,meta}$), 132.8 and 134.1 ($C^{4a,8a}$), 141.9 ($C_{quat,phenyl}$). **IR** (ATR, cm^{-1}): ν_{max} = 3337, 2849, 1593, 1506, 1491, 1452, 1302, 1271, 1119, 743, 698. **MS** (ESI): m/z (%) 211 ($[M + H]^+$, 100). The data are in accordance with those reported in the literature.[271]

2,3-Dimethyl-1,2,3,4-tetrahydroquinoxaline (11d)

Spectral data derived from the mixture of *cis*- and *trans*-isomers (*cis*/*trans* = 55/45).

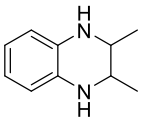

Yield 76%. White crystals, R_f = 0.20 and 0.24 (PE/EtOAc 4/1). <u>*cis*-Isomer</u>: **^{1}H NMR** (400 MHz, $CDCl_3$): δ 1.12 (6H, d, *J* = 6.4 Hz, 2 x CH_3), 3.45–3.52 (2H, m, $H^{2,3}$), 3.52 (2H, br s, 2 x NH), 6.46–6.52 (2H, m, $H^{5,8}$), 6.55–6.60 (2H, m, $H^{6,7}$). **^{13}C NMR** (101 MHz, $CDCl_3$): δ 17.2 (2 x CH_3), 49.0 ($C^{2,3}$), 114.4 ($C^{5,8}$), 118.5 ($C^{6,7}$), 133.5 ($C^{4a,8a}$). <u>*trans*-Isomer</u>: **^{1}H NMR** (400 MHz, $CDCl_3$): δ 1.17 (6H, ~d, *J* = 5.8 Hz, 2 x CH_3), 2.98–3.06 (2H, m, $H^{2,3}$), 3.52 (2H, br s, 2 x NH), 6.46–6.52 (2H, m, $H^{5,8}$), 6.55–6.60 (2H, m, $H^{6,7}$). **^{13}C NMR** (101 MHz, $CDCl_3$): δ 19.0 (2 x CH_3), 52.0 ($C^{2,3}$), 113.9 ($C^{5,8}$), 118.6 ($C^{6,7}$), 132.7 ($C^{4a,8a}$). **IR** (ATR, cm^{-1}): ν_{max} = 3335, 2968, 1597, 1503, 1439, 1373, 1285, 1152, 1082, 916, 737. **MS** (ESI): m/z (%) 163 ($[M + H]^+$, 100). The data are in accordance with those reported in the literature.[204]

***cis*-2-Ethyl-3-methyl-1,2,3,4-tetrahydroquinoxaline (*cis*-11e)**

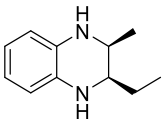

Yield 82% (*cis* + *trans*). White solid, R_f = 0.25 (PE/EtOAc 17/3). **^{1}H NMR** (400 MHz, $CDCl_3$): δ 0.98 (3H, t, *J* = 7.3 Hz, $CH_2C\underline{H}_3$), 1.12 (3H, d, *J* = 6.5 Hz, $CHC\underline{H}_3$), 1.45 (2H, quint, *J* = 7.3 Hz, $C\underline{H}_2CH_3$), 3.24 (1H, td, *J* = 7.3, 2.8 Hz, H^2), 3.52 (1H, qd, *J* = 6.5, 2.8 Hz, H^3), 3.63 (2H, br s, 2 x NH), 6.46–6.52 (2H, m, $H^{5,8}$), 6.55–6.60 (2H, m, $H^{6,7}$). **^{13}C NMR** (101 MHz, $CDCl_3$): δ 10.3 ($CH_2\underline{C}H_3$), 16.7 ($CH\underline{C}H_3$), 23.9 ($\underline{C}H_2CH_3$), 48.3 (C^3), 55.1 (C^2), 114.2 and 114.4 ($C^{5,8}$), 118.4 and 118.5 ($C^{6,7}$), 132.7 (C^{4a}), 132.8 (C^{8a}). **IR** (ATR, cm^{-1}): ν_{max} = 3374, 3345, 2961, 2932, 1595, 1503, 1460, 1437, 1371, 1281, 1169, 1119, 1040, 907, 731. **MS** (ESI): m/z (%) 177 ($[M + H]^+$, 100). The data are in accordance with those reported in the literature.[268]

trans-2-Ethyl-3-methyl-1,2,3,4-tetrahydroquinoxaline (*trans*-11e)

Spectral data derived from the mixture of *cis*- and *trans*-isomers (*cis*/*trans* = 71/28).

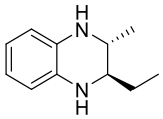

Colorless viscous oil. **^{1}H NMR** (400 MHz, $CDCl_3$): δ 0.98 (3H, t, *J* = 7.6 Hz, $CH_2C\underline{H}_3$), 1.12 (3H, d, *J* = 6.5 Hz, $CHC\underline{H}_3$), 1.45 (1H, m, $C\underline{H}_aH_bCH_3$), 1.69 (1H, dqd, *J* = 14.0, 7.6, 3.6 Hz, $CH_a\underline{H}_bCH_3$), 2.87 (1H, ddd, *J* = 7.6, 6.5, 3.6 Hz, H^2), 3.16 (1H, quint, *J* = 6.5 Hz, H^3), 3.40–3.70 (2H, br s, 2 x NH), 6.46–6.52 (2H, m, $H^{5,8}$), 6.55–6.60 (2H, m, $H^{6,7}$). **^{13}C NMR** (101 MHz, $CDCl_3$): 9.5 ($CH_2\underline{C}H_3$), 19.4 ($CH\underline{C}H_3$), 25.5 ($\underline{C}H_2CH_3$), 49.7 (C^3), 57.1 (C^2), 114.0 ($C^{5,8}$), 118.4 and 118.5 ($C^{6,7}$), 133.1 (C^{4a}), 133.3 (C^{8a}). **MS** (ESI): m/z (%) 177 ($[M + H]^+$, 100). The data are in accordance with those reported in the literature.[268]

cis-2-Methyl-3-phenyl-1,2,3,4-tetrahydroquinoxaline (*cis*-11f)

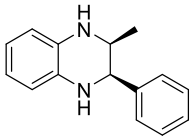

Yield 75%. Yellow viscous oil, R_f = 0.11 (PE/EtOAc 19/1). **^{1}H NMR** (400 MHz, $CDCl_3$): δ 0.94 (3H, d, *J* = 6.5 Hz, CH_3), 3.71 (1H, qd, *J* = 6.5, 3.2 Hz, H^2), 3.94 (2H, br s, 2 x NH), 4.50 (1H, d, *J* = 3.2 Hz, H^3), 6.53–6.59 (2H, m, $H^{5,8}$), 6.60–6.68 (2H, m, $H^{6,7}$), 7.24–7.34 (5H, m, 5 x CH_{phenyl}). **^{13}C NMR** (101 MHz, $CDCl_3$): δ 17.6 (CH_3), 49.5 (C^2), 58.5 (C^3), 113.9 and 114.8 ($C^{5,8}$), 118.4 and 119.3 ($C^{6,7}$), 127.3 ($CH_{phenyl,para}$), 127.6 (2 x $CH_{phenyl,ortho}$), 128.2 (2 x $CH_{phenyl,meta}$), 132.3 and 133.2 ($C^{4a,8a}$), 141.8 ($C_{quat,phenyl}$). **IR** (ATR, cm^{-1}): ν_{max} = 3362, 2968, 1595, 1503, 1452, 1368, 1277, 1146, 735, 698. **MS** (ESI): m/z (%) 225 ($[M + H]^+$, 100). The data are in accordance with those reported in the literature.[250]

cis-2,3-Diphenyl-1,2,3,4-tetrahydroquinoxaline (*cis*-11g)

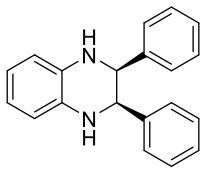

Yield 77%. White solid, R_f = 0.11 (PE/EtOAc 4/1). **^{1}H NMR** (400 MHz, $CDCl_3$): δ 4.08 (2H, br s, 2 x NH), 4.74 (2H, s, $H^{2,3}$), 6.60–6.67 (2H, m, $H^{5,8}$), 6.67–6.73 (2H, m, $H^{6,7}$), 6.85–6.91 (4H, m, 4 x $CH_{phenyl,ortho}$) 7.07–7.19 (6H, m, 4 x $CH_{phenyl,meta}$ 2 x $CH_{phenyl,para}$). **^{13}C NMR** (101 MHz, $CDCl_3$): δ 59.5 ($C^{2,3}$), 114.1 ($C^{5,8}$), 118.9 ($C^{6,7}$), 127.3 (2 x $CH_{phenyl,para}$), 127.7 (4 x $CH_{phenyl,meta}$), 127.9 (4 x $CH_{phenyl,ortho}$), 133.1 ($C^{4a,8a}$), 140.6 (2 x $C_{quat,phenyl}$). **IR** (ATR, cm^{-1}): ν_{max} = 3412, 3024, 2828, 1605, 1508, 1450, 1319, 1279, 1107, 735, 698. **MS** (ESI): m/z (%) 287 ($[M + H]^+$, 100). The data are in accordance with those reported in the literature.[250]

Crystals suitable for X-ray diffraction analysis were obtained from a saturated solution in chloroform by slow evaporation of the solvent at room temperature.

cis-6-Methoxy-2,3-dimethyl-1,2,3,4-tetrahydroquinoxaline (_cis_-11h)

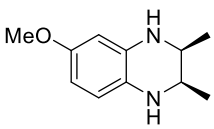

Yield 95% (*cis* + *trans*). Colorless oil, R_f = 0.23 (PE/EtOAc 3/2). **^{1}H NMR** (400 MHz, $CDCl_3$): δ 1.109 (3H, d, *J* = 6.4 Hz, CH_3), 1.110 (3H, d, *J* = 6.4 Hz, CH_3), 3.24 (2H, br s, 2 x NH), 3.38–3.51 (2H, m, $H^{2,3}$), 3.70 (3H, s, CH_3O), 6.11 (1H, d, *J* = 2.5 Hz, H^5), 6.17 (1H, dd, *J* = 8.4, 2.5 Hz, H^7), 6.45 (1H, d, *J* = 8.4 Hz, H^8). **^{13}C NMR** (101 MHz, $CDCl_3$): δ 17.1 (2 x CH_3), 49.19 and 49.24 ($C^{2,3}$), 55.6 (CH_3O), 100.9 (C^5), 103.2 (C^7), 115.6 (C^8), 126.1 (C^{8a}), 134.0 (C^{4a}), 153.5 (C^6). **IR** (ATR, cm^{-1}): ν_{max} = 3360, 2967, 2832, 1616, 1599, 1512, 1441, 1375, 1260, 1202, 1165, 1040, 829, 785. **MS** (ESI): m/z (%) 193 ($[M + H]^+$, 100). The data are in accordance with those reported in the literature.[272]

trans-6-Methoxy-2,3-dimethyl-1,2,3,4-tetrahydroquinoxaline (_trans_-11h)

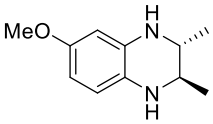

Colorless oil, R_f = 0.31 (PE/EtOAc 3/2). **^{1}H NMR** (400 MHz, $CDCl_3$): δ 1.155 (3H, d, *J* = 6.1 Hz, CH_3), 1.158 (3H, d, *J* = 6.1 Hz, CH_3), 2.89–3.08 (2H, m, $H^{2,3}$), 3.38 (2H, br s, 2 x NH), 3.70 (3H, s, CH_3O), 6.12 (1H, ~d, *J* = 2.5 Hz, H^5), 6.14–6.20 (1H, m, H^7), 6.45 (1H, d, *J* = 8.3 Hz, H^8). **^{13}C NMR** (101 MHz, $CDCl_3$): δ 18.9 (CH_3), 19.1 (CH_3), 52.2 and 52.4 ($C^{2,3}$), 55.6 (CH_3O), 100.4 (C^5), 103.1 (C^7), 115.1 (C^8), 127.2 (C^{8a}), 134.8 (C^{4a}), 153.4 (C^6). The data are in accordance with those reported in the literature.[272]

6-Chloro-2,3-dimethyl-1,2,3,4-tetrahydroquinoxaline (11i)

Spectral data derived from the mixture of *cis*- and *trans*-isomers (*cis*/*trans* = 81/19).

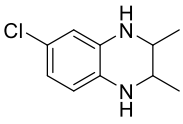

Yield 92%. White solid, R_f = 0.26 and 0.34 (PE/EtOAc 4/1). <u>*cis*-Isomer</u>: **^{1}H NMR** (400 MHz, $CDCl_3$): δ 1.11 (6H, d, *J* = 6.4 Hz, 2 x CH_3), 2.86–3.87 (2H, br s, 2 x NH), 3.42–3.51 (2H, m, $H^{2,3}$), 6.38 (1H, d, *J* = 8.2 Hz, H^8), 6.44 (1H, d, *J* = 2.3 Hz, H^5), 6.50 (1H, dd, *J* = 8.2, 2.3 Hz, H^7). **^{13}C NMR** (101 MHz, $CDCl_3$): δ 16.8 (CH_3), 17.0 (CH_3), 48.8 and 48.9 ($C^{2,3}$), 113.8 (C^5), 115.4 (C^8), 117.9 (C^7), 123.5 (C^6), 130.3 (C^{8a}), 133.8 (C^{4a}). <u>*trans*-Isomer</u>: **^{1}H NMR** (400 MHz, $CDCl_3$): δ 1.16 (3H, d, *J* = 5.9 Hz, CH_3), 1.17 (3H, d, *J* = 5.9 Hz, CH_3), 2.86–3.87 (2H, br s, 2 x NH), 2.93–3.05 (2H, m, $H^{2,3}$), 6.38 (1H, d, *J* = 8.2 Hz, H^8), 6.45 (1H, d, *J* = 2.3 Hz, H^5), 6.50 (1H, dd, *J* = 8.2, 2.3 Hz, H^7). **^{13}C NMR** (101 MHz, $CDCl_3$): δ 18.9 (CH_3), 18.9 (CH_3), 51.8 ($C^{2,3}$), 113.3 (C^5), 114.6 (C^8), 117.8 (C^7), 123.2 (C^6), 131.6 (C^{8a}), 134.5 (C^{4a}). **IR** (ATR, cm^{-1}): ν_{max} = 3358, 3283, 2970, 2928, 2860, 1595, 1503, 1439, 1375, 1287, 1242, 1180, 1088, 962, 853, 795. **MS** (ESI): m/z (%) 197/199 ($[M + H]^+$, 100). The data are in accordance with those reported in the literature.[268]

2,3-Dimethyl-1,2,3,4-tetrahydroquinoxaline-6-carbonitrile (11j)

Spectral data derived from the mixture of *cis*- and *trans*-isomers (*cis*/*trans* = 83/17).

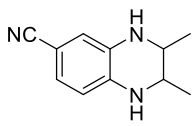

Yield 96%. Colorless viscous oil, R_f = 0.12 (PE/EtOAc 4/1). <u>*cis*-Isomer</u>: **^{1}H NMR** (400 MHz, $CDCl_3$): δ 1.12 (3H, d, *J* = 6.5 Hz, CH_3), 1.14 (3H, d, *J* = 6.5 Hz, CH_3), 3.47 (1H, dd, *J* = 6.5, 3.0 Hz, H^3), 3.56 (1H, dd, *J* = 6.5, 3.0 Hz, H^2), 3.96 (2H, br s, 2 x NH), 6.40 (1H, d, *J* = 8.1 Hz, H^8), 6.67 (1H, d, *J* = 1.8 Hz, H^5), 6.866 (1H, d, *J* = 8.1, 1.8 Hz, H^7). **^{13}C NMR** (101 MHz, $CDCl_3$): δ 17.0 (CH_3), 17.3 (CH_3), 48.3 (C^3), 49.0 (C^2), 99.29 (C^6), 112.9 (C^8), 116.3 (C^5), 120.9 (C≡N), 123.76 (C^7), 132.1 (C^{4a}), 137.1 (C^{8a}). <u>*trans*-Isomer</u>: **^{1}H NMR** (400 MHz, $CDCl_3$): δ 1.19 (6H, d, *J* = 6.3 Hz, 2 x CH_3), 2.96 (1H, quint, *J* = 6.3 Hz, H^3), 3.09 (1H, quint, *J* = 6.3 Hz, H^2), 3.96 (2H, br s, 2 x NH), 6.41 (1H, d, *J* = 8.1 Hz, H^8), 6.68 (1H, d, *J* = 1.8 Hz, H^5), 6.872 (1H, dd, *J* = 8.1, 1.8 Hz, H^7). **^{13}C NMR** (101 MHz, $CDCl_3$): δ 18.8 (CH_3), 18.9 (CH_3), 51.2 (C^3), 52.0 (C^2), 99.26 (C^6), 112.5 (C^8), 115.9 (C^5), 120.9 (C≡N), 123.82 (C^7), 132.8 (C^{4a}), 137.7 (C^{8a}). **IR** (ATR, cm^{-1}): ν_{max} = 3354, 2970, 2207, 1599, 1522, 1443, 1377, 1296, 858, 802. **MS** (ESI): m/z (%) 188 ($[M + H]^+$, 100).

2,3-Dimethylquinoxalin-6-amine (11k)

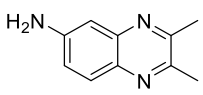

Yield 77%. Yellow solid, R_f = 0.22 (EtOAc). **^{1}H NMR** (400 MHz, $CDCl_3$): δ 2.65 (3H, s, CH_3), 2.66 (3H, s, CH_3), 4.06 (2H, br s, NH_2), 7.06–7.10 (2H, m, $H^{5,7}$), 7.76 (1H, dd, *J* = 8.3, 0.8 Hz, H^8). **^{13}C NMR** (101 MHz, $CDCl_3$): δ 22.7 (CH_3), 23.2 (CH_3), 108.2 (C^5), 120.6 (C^7), 129.3 (C^8), 136.0 (C^{8a}), 142.8 (C^{4a}), 147.0 (C^6), 149.3 and 153.4 ($C^{2,3}$). **IR** (ATR, cm^{-1}): ν_{max} = 3321, 3204, 1643, 1614, 1501, 1377, 1341, 1242, 1159, 1126, 995, 947, 827. **MS** (ESI): m/z (%) 174 ($[M + H]^+$, 100).

2-Methyl-1,2,3,4-tetrahydroquinoline (13a)

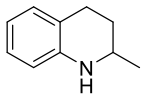

Yield 99%. Colorless oil, which turns bordeaux-brown upon standing, R_f = 0.36 (PE/EtOAc 9/1). **^{1}H NMR** (400 MHz, $CDCl_3$): δ 1.20 (3H, d, *J* = 6.3 Hz, CH_3), 1.58 (1H, dddd, 12.7, 11.4, 9.9, 5.2 Hz, H^{3a}), 1.92 (1H, dddd, 12.7, 5.6, 3.6, 2.9 Hz, H^{3b}), 2.72 (1H, ddd, 16.5, 5.2, 3.6 Hz, H^{4a}), 2.83 (1H, ddd, 16.5, 11.4, 5.6 Hz, H^{4b}), 3.40 (1H, dqd, *J* = 9.9, 6.3, 2.9 Hz, H^2), 3.68 (1H, br s, NH), 6.46 (1H, dd, *J* = 8.4, 0.9 Hz, H^8), 6.60 (1H, td, *J* = 7.4, 0.9 Hz, H^6), 6.93–6.98 (2H, m, $H^{5,7}$). **^{13}C NMR** (101 MHz, $CDCl_3$): δ 22.6 (CH_3), 26.6 (C^4), 30.2 (C^3), 47.2 (C^2), 114.0 (C^8), 117.0 (C^6), 121.1 (C^{4a}), 126.7 (C^7), 129.3 (C^5), 144.8 (C^{8a}). **IR** (ATR, cm^{-1}): ν_{max} = 3393, 2924, 1607, 1584, 1485, 1306, 1275, 1256, 1152, 743. **MS** (ESI): m/z (%) 148 ($[M + H]^+$, 100). The data are in accordance with those reported in the literature.[273]

1,2,3,4-Tetrahydro-1,5-naphthyridine (13b)

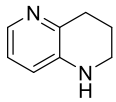

Yield 85%. White solid. **^{1}H NMR** (400 MHz, $CDCl_3$): δ 2.00-2.07 (2H, m, $NCH_2C\underline{H}_2$), 2.93 (2H, t, *J* = 6.5 Hz, $C_{quat}C\underline{H}_2$), 3.27–3.32 (2H, m, $NC\underline{H}_2$), 3.79 (1H, br s, NH), 6.72 (1H, dd, *J* = 8.0, 1.4 Hz, H^8), 6.88 (1H, dd, *J* = 8.0, 4.7 Hz, H^7), 7.86 (1H, dd, *J* = 4.7, 1.4 Hz, H^6). **^{13}C NMR** (101 MHz, $CDCl_3$): δ 21.8 (C^4), 30.4 (C^3), 41.5 (C^2), 120.2 (C^8), 121.9 (C^7), 138.0 (C^6), 140.9 (C^{8a}), 142.8 (C^{4a}). **IR** (ATR, cm^{-1}): ν_{max} = 3223, 2932, 1580, 1456, 1352, 1298, 1269, 1227, 1190, 1125, 1098, 1011, 791, 731. **MS** (ESI): m/z (%) 135 ($[M + H]^+$, 100). The data are in accordance with those reported in the literature.[274]

2,9-Dimethyl-1,2,3,4-tetrahydro-1,10-phenanthroline (13c)

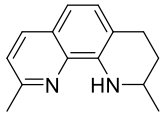

Yield 87%. Pale yellow solid, R_f = 0.52 (PE/EtOAc 17/3). **^{1}H NMR** (400 MHz, $CDCl_3$): δ 1.37 (3H, *J* = 6.1 Hz, C^2CH_3), 1.72 (1H, dddd, *J* = 12.8, 10.9, 9.5, 5.3 Hz, H^{3a}), 2.00–2.07 (1H, m, H^{3b}), 2.68 (3H, s, C^9CH_3), 2.85 (1H, ddd, *J* = 16.6, 5.3, 3.8 Hz, H^{4a}), 2.99 (1H, ddd, *J* = 16.6, 10.9, 5.7 Hz, H^{4b}), 3.58 (1H, dqd, *J* = 9.5, 6.1, 2.9 Hz, H^2), 5.85 (1H, br s, NH), 6.93 (1H, d, *J* = 8.2 Hz, H^6), 7.09 (1H, d, *J* = 8.2 Hz, H^5), 7.15 (1H, d, *J* = 8.3 Hz, H^8), 7.87 (1H, d, *J* = 8.3 Hz, H^7). **^{13}C NMR** (101 MHz, $CDCl_3$): δ 22.5 ($C^2\underline{C}H_3$), 25.1 ($C^9\underline{C}H_3$), 26.6 (C^4), 30.0 (C^3), 46.6 (C^2), 113.2 (C^6), 116.5 (C^{4a}), 121.2 (C^8), 125.3 (C^{6a}), 127.8 (C^5), 135.9 (C^7), 136.8 (C^{10a}), 140.0 (C^{10b}), 155.7 (C^9). **IR** (ATR, cm^{-1}): ν_{max} = 3362, 2968, 1595, 1503, 1452, 1368, 1277, 735, 698. **MS** (ESI): m/z (%) 213 ($[M + H]^+$, 100). The data are in accordance with those reported in the literature.[275]

1,2,3,4,7,8,9,10-Octahydro-1,10-phenanthroline (13d)

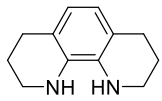

Yield 82%. Off-white crystals, R_f = 0.16 (PE/EtOAc 4/1). **^{1}H NMR** (400 MHz, $CDCl_3$): δ 1.83–1.92 (4H, m, 2 x $NCH_2C\underline{H}_2$), 2.73 (4H, t, *J* = 6.3 Hz, 2 x $C_{quat}CH_2$), 3.19 (2H, br s, 2 x NH), 3.29 (4H, m, 2 x NCH_2), 6.45 (2H, s, $H^{5,6}$). **^{13}C NMR** (101 MHz, $CDCl_3$): δ 22.5 (2 x $NCH_2\underline{C}H_2$), 26.9 (2 x $C_{quat}\underline{C}H_2$), 42.6 (2 x NCH_2), 119.1 ($C^{5,6}$), 120.5 ($C^{4a,6a}$), 132.8 ($C^{10a,10b}$). **IR** (ATR, cm^{-1}): ν_{max} = 3246, 2922, 2833, 1616, 1582, 1489, 1437, 1422, 1327, 1261, 1246, 1194, 1171, 1109, 1007, 779. **MS** (ESI): m/z (%) 189 ($[M + H]^+$, 100). The data are in accordance with those reported in the literature.[276]

9,10-Dihydroacridine (13e)

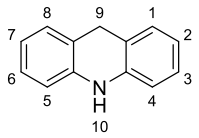

Yield 91%. White crystals, R_f = 0.36 (PE/EtOAc 9/1). **^{1}H NMR** (400 MHz, $CDCl_3$): δ 4.05 (2H, s, CH_2), 5.93 (1H, br s, NH), 6.66 (2H, dd, *J* = 7.9, 1.0 Hz, $H^{4,5}$), 6.84 (2H, td, *J* = 7.4, 1.0 Hz, $H^{2,7}$), 7.04–7.12 (4H, m, $H^{3,6,1,8}$). **^{13}C NMR** (101 MHz, $CDCl_3$): δ 31.4 (CH_2), 113.4 ($C^{4,5}$), 120.1 ($C^{8a,9a}$), 120.6 ($C^{2,7}$), 127.0 ($C^{3,6}$), 128.6 ($C^{1,8}$), 140.1 ($C^{4a,10a}$). **IR** (ATR, cm^{-1}): ν_{max} = 3372, 1599, 1582, 1454, 1294, 743, 714, 607, 532, 434. **MS** (ESI): m/z (%) 182 ($[M + H]^+$, 100). The data are in accordance with those reported in the literature.[277]

Phthalazine-2(1*H*)-carbaldehyde (13f)

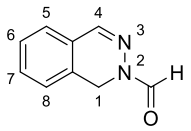

Yield 80%. Pale yellow crystals, R_f = 0.37 (PE/EtOAc 7/3). **^{1}H NMR** (400 MHz, $CDCl_3$): δ 4.94 (2H, s, CH_2), 7.17 (1H, d, *J* = 7.5 Hz, H^8), 7.25 (1H, dd, *J* = 7.5, 0.9 Hz, H^5), 7.35 (1H, t, *J* = 7.5 Hz, H^6), 7.44 (1H, td, *J* = 7.5, 0.9 Hz, H^7), 7.53 (1H, s, H^4), 8.72 (1H, s, N(C=O)H). **^{13}C NMR** (101 MHz, $CDCl_3$): δ 41.1 (CH_2), 124.3 (C^{4a}), 126.2 (C^8), 126.5 (C^5), 128.5 (C^6), 129.0 (C^{8a}), 132.0 (C^7), 143.0 (C^4), 164.7 (N(C=O)H). **IR** (ATR, cm^{-1}): ν_{max} = 2893, 1670, 1396, 1356, 1331, 1221, 1209, 1136, 1105, 912, 760, 642, 588. **MS** (ESI): m/z (%) 161 ($[M + H]^+$, 100). The data are in accordance with those reported in the literature.[278]

4.4.6.1 Deformylation of phthalazine-2(1*H*)-carbaldehyde (13f)

The formyl group of phthalazine-2(1*H*)-carbaldehyde **13f** (64 mg, 0.40 mmol, 1 eq) was hydrolyzed by treatment with 1 M NaOH (240 µL, 6.00 mmol, 15 eq) under reflux conditions diluted in an ethanol/water mixture (2/1, 6 mL). After 2 h, the mixture was extracted with Et_2O (4 x 10 mL) and the combined organic layers were dried over $MgSO_4$, filtered and concentrated under vacuum to obtain the deformylated product. ^{1}H NMR analysis showed that the product obtained not only contained the targeted 1,2-dihydrophthalazine **14**, but also phthalazine **12f** to a minor extent (**14**/**12f** = 96/4). Over time, the fraction of phthalazine increased, suggesting that 1,2-dihydrophthalazine **14** spontaneously oxidizes on exposure to air.

1,2-Dihydrophthalazine (14)

Spectral data derived from the mixture of compound **14** and phthalazine **12f** (^{1}H NMR: **14**/**12f** = 96/4; ^{13}C NMR: **14**/**12f** = 79/21).

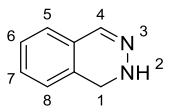

Yield 68%. White solid, R_f = 0.19 (PE/EtOAc 70/30). **^{1}H NMR** (400 MHz, $CDCl_3$): δ 4.23 (2H, s, CH_2), 5.91 (1H, br s, NH), 7.04–7.08 (1H, m, H^8), 7.10–7.15 (1H, m, H^5), 7.25–7.35 (2H, m, $H^{6,7}$), 7.49 (1H, s, H^4). **^{13}C NMR** (101 MHz, $CDCl_3$): δ 44.9 (CH_2),

124.4 (C^5), 125.2 (C^8), 126.2 (C^{4a}), 127.9 (C^6), 130.3 (C^7), 131.0 (C^{8a}), 140.3 (C^4). **IR** (ATR, cm^{-1}): ν_{max} = 3265, 1439, 1317, 1088, 1018, 912, 793, 725, 590. **MS** (ESI): m/z (%) 133 ($[M + H]^+$, 100). The data are in accordance with those reported in the literature.[253]

4.4.6.2 Single-crystal X-ray diffraction data for compound *cis*-11g

The X-ray diffraction analysis was performed by Prof. Kristof Van Hecke (XStruct, Department of Chemistry, Faculty of Sciences, Ghent University). **CCDC 2226036** contains the supplementary crystallographic data for compound ***cis*-11g**. These data can be obtained free of charge from The Cambridge Crystallographic Data Centre via www.ccdc.cam.ac.uk/structures.

For the structure of compound ***cis*-11g**, single-crystal X-ray intensity data were collected at 100 K on a Rigaku Oxford Diffraction Supernova Dual Source (Cu at zero) diffractometer equipped with an Atlas CCD detector using ω scans and Cu Kα (λ = 1.54184 Å) radiation. The images were interpreted and integrated with the program CrysAlis^{Pro} (Rigaku Oxford Diffraction). Using Olex2,[196] the structure was solved with the SHELXT[197] structure solution program using intrinsic phasing and refined with the SHELXL[198] refinement package using least-squares minimization. Non-hydrogen atoms were anisotropically refined and the hydrogen atoms in the riding mode and isotropic temperature factors fixed at 1.2 times U(eq) of the parent atoms.

Crystal data for compound ***cis*-11g**

$C_{20}H_{18}N_2$, M = 286.36 g/mol, monoclinic, space group $P2_1/n$ (No. 14), a = 12.54957(13) Å, b = 5.45668(4) Å, c = 21.5051(3) Å, β = 100.0457(10)°, V = 1450.07(3) Å^3, Z = 4, T = 100(2) K, μ(Cu Kα) = 0.595 mm^{-1}, F(000) = 608, ρ_{calc} = 1.312 g cm^{-3}, 38566 reflections measured (7.628° ≤ 2Θ ≤ 147.574°), 2917 unique (R_{int} = 0.0278, R_{sigma} = 0.0107) which were used in all calculations. The final R_1 was 0.0351 ($I > 2\sigma(I)$) and wR_2 was 0.0962 (all data).

Chapter 4

CTF-1 as metal-free catalyst for aerobic oxidations in continuous flow

Abstract | To further explore the use of CTFs in flow reactions, simple CTF-1 is used as a metal-free heterogeneous catalyst for continuous aerobic oxidation reactions. Previously, our collaborative partner COMOC has demonstrated the ability of ionothermally prepared CTFs to activate molecular oxygen as the ultimate green oxidant for organic synthesis. This activity was then exploited to establish the CTF-catalyzed oxidative aerobic coupling of amines in batch mode. In this chapter, the aerobic oxidation reaction is translated into a continuous flow process for improved oxygen gas mass transfer and safety. In addition, as the CTF is contained in a packed-bed reactor, catalyst separation steps are avoided.

A major part of the research in this chapter is covered in the Master thesis of Jolien De Ketelaere and most of the experimental work was done in collaboration with her.[279]

Contributions | CTF synthesis: JDK, JE – CTF characterization: JE, JDK – Batch and flow experiments: JDK – Gas chromatography analysis: JDK, JE – Supervision: JE, CS.

1 Introduction

Besides the great promise of CTFs as support materials, they also exhibit catalytic activity in several transformations themselves. Doping of nanocarbon materials (carbon nanotubes, graphene, fullerenes) with defective nitrogen species is known to be an effective strategy to modulate the electronic properties and enhance the reactivity of the materials.[280-281] Analogous nitrogen species arise in CTFs when they are synthesized by the ionothermal method. Such sites have shown promising catalytic activity in aerobic oxidation reactions by promoting the activation of molecular oxygen. Recently, CTFs have been described in the aerobic oxidative coupling of amines by Zheng *et al.*[282] Similarly, the group of Van Der Voort have demonstrated their activity for the selective aerobic oxidation of benzyl alcohols to benzaldehydes.[123] Although several catalysts based on transition metals, including Ru,[283] Pd,[284-285] Au,[286] and Fe,[287] have been developed for these types of oxidation reactions, metal-free catalysis with carbonaceous materials provides a desirable alternative from a green perspective.[288-289] Being metal-free means that the high cost of noble metals, leaching problems, and concerns about metal residues in the product are eliminated. It should be noted that the term "metal-free" can be tricky in the context of catalysis, as traces of metal impurities in the reagents, solvents or other additives have been found to be non-innocent and actually catalyzed the reaction under study.[290-291] Hence, an alternative term could be "no-added-metal", indicating that metals have not been deliberately added to the reaction mixture. Nevertheless, the common term "metal-free" will continue to be used in this chapter.

Molecular oxygen is recognized as the ultimate green oxidant in organic synthesis.[292] In the meantime, traditional oxidation methods use stoichiometric amounts of hazardous metal oxidants such as manganese- and chromium-based reagents. These reagents have serious toxicity issues associated with their use and generate large amounts of waste. The high demand for more sustainable oxidation processes necessitates the replacement of the toxic oxidants and the development of efficient methodologies using oxygen gas as a clean oxidant. However, gas–liquid reactions in batch synthesis may suffer from limitations in mass transfer and, therefore, often require long reaction times and high pressures. In addition, the triad of high-pressured oxygen gas, flammable organic solvents and high temperatures poses additional challenges regarding safety. In this regard, the use of continuous flow reactor technology is an attractive approach to address these process challenges and safety hazards.[293] Increased mass transfer by the enlarged gas–liquid interfacial area, easier scale-up and improved safety because of the small reaction volumes, are just a few of the advantages offered by flow chemistry.[294]

In light of this premise, we aimed to explore CTFs as a metal-free catalyst in continuous flow using aerobic oxidations as model reactions. To this end, several designs of packed-bed reactors were evaluated. Here, we describe the results from our initial experiments, which can serve as a starting point for a more comprehensive study.

2 Results and discussion

As mentioned in the introduction, the Van Der Voort group, our research partners, have recently elaborated on the aerobic oxidation of benzyl alcohols catalyzed by CTFs.[123] These reactions were carried out on a small scale (*i.e.*, 0.33 mmol) in batch mode. The conversion of alcohol proceeded in toluene as the optimal solvent using Cs_2CO_3 as the base (Scheme 4.1). CTF-1, prepared from benzene-1,4-dicarbonitrile, was found to be one of the most effective CTFs for the conversion due to its high nitrogen content and was preferred because of its cheap and readily available building block. Following their research, we first attempted to translate the alcohol oxidation reaction into a continuous flow process.

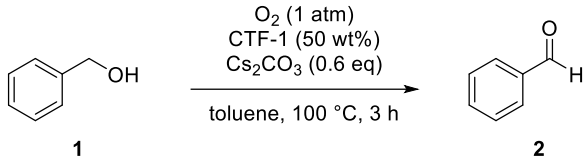

Scheme 4.1. Aerobic oxidation of benzyl alcohol **1** catalyzed by CTF-1 in batch according to Van Der Voort *et al.*[123]

Unfortunately, a few obstacles were soon encountered in the translation of the batch reaction. Cesium carbonate, the inorganic base in the reaction, presented a first obstacle. Due to the low solubility of Cs_2CO_3 in toluene, the base had to be mixed in the reactor column or integrated into the setup as a separate column preceding the reactor column. Unfortunately, pressures higher than 30 bar were encountered for both setups, exceeding the limits of some reactor components. Screening for an organic, alternative base was to no avail. Furthermore, since finding the optimal reaction conditions was a process of trial and error, the need for large amounts of CTF-1 posed another challenge. The ionothermal synthesis of CTFs is ideally performed in small batches to ensure high porosity and surface area of the resulting material. Producing a few grams of CTFs is therefore an arduous task. CTF synthesis at large scale remains a bottleneck.

Because of these obstacles, the aerobic oxidation of benzyl alcohols was abandoned as a model reaction and replaced by the aerobic oxidative coupling of benzylamine **3** to *N*-benzylidene-benzylamine **4** (Scheme 4.2).[123,282] The absence of an externally added base in this reaction simplified the flow setup. Schiff base imines are regarded as versatile intermediates for the synthesis of fine chemicals, biologically active compounds and pharmaceuticals. The C=N bond in imines is a highly reactive functionality that allows numerous transformations, including nucleophilic additions, cycloadditions and multicomponent reactions.[295] Imines are traditionally prepared by the condensation of amines with ketones or aldehydes, but the oxidative coupling of amines with oxygen gas or air has received much attention as an alternative synthetic route. A key challenge in the oxidation reaction, however, is to avoid the formation of side products such as

benzaldehyde, *N*-benzylbenzamide, benzaldoxime and benzonitrile.[296] Therefore, the development of highly selective catalysts is desirable.

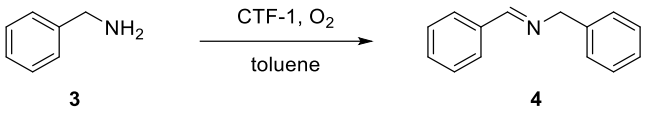

Scheme 4.2. Aerobic oxidative coupling of benzylamine **3**.

2.1 CTF synthesis and characterization

CTF-1 was synthesized from benzene-1,4-dicarbonitrile **5** in the ionothermal synthesis using five equivalents of $ZnCl_2$ (Scheme 4.3). After heating at 400 °C for 48 h, oligomers and $ZnCl_2$ were removed by extensive washing with water and organic solvents, and by treatment in 1 M HCl under reflux conditions. CTF-1 was eventually obtained as a glassy black powder.

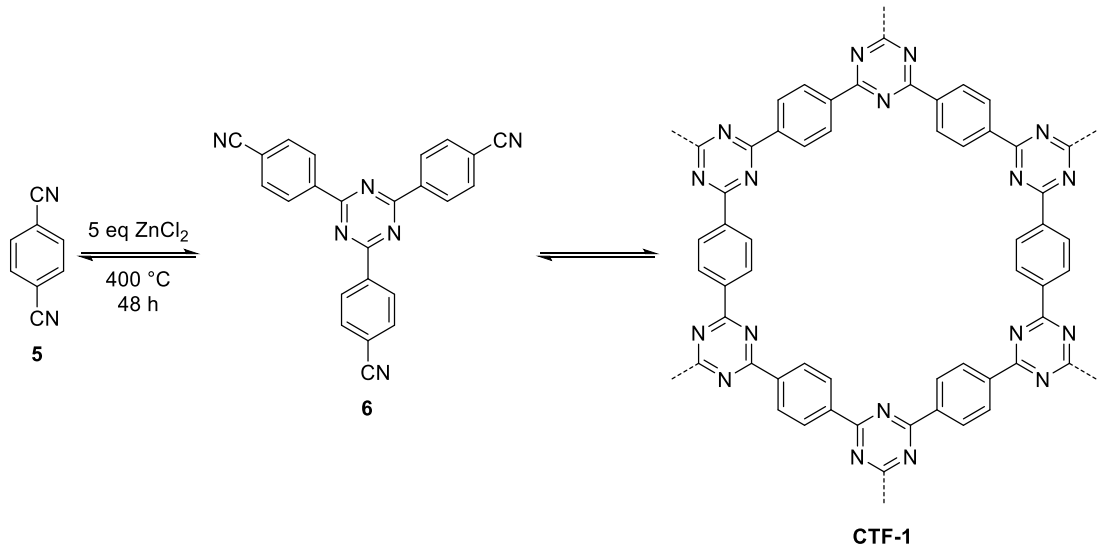

Scheme 4.3. Synthesis of CTF-1.

The complete formation of triazine linkages was confirmed by Fourier transform infrared (FT-IR) spectroscopy. As shown in Figure 4.1a, the absorption bands for the triazine units are present at 1523 and 1350 cm^{-1}, while the characteristic absorption band for the nitrile group at 2231 cm^{-1} disappears completely from the spectrum.[85] Based on the absence of sharp diffraction signals in the powder X-ray diffraction (PXRD) pattern (Figure 4.1b), CTF-1 was found to be amorphous, which was also the case for the CTF-1 reported by Van Der Voort *et al*.[123] This contrasts with the first report on CTF-1 by Thomas *et al.* who observed an intense (100) diffraction peak at about 2θ = 7° in the PRXD pattern, indicating the formation of a crystalline CTF.[75] The spectrum of our CTF-1 only shows a broad (001) diffraction band centered at about 23°, indicating a graphitic-like layering of the two-dimensional sheets by π–π stacking interactions.[75] The nominal distance between the

layers is calculated as approximately 3.8 Å and is slightly larger than the value of 3.4 Å reported in the literature.[75,85] The elemental analysis of CTF-1 revealed a C/N atomic ratio that strongly deviates from the theoretical ratio (Table 4.1) and is due to partial carbonization of the framework under the harsh ionothermal conditions.

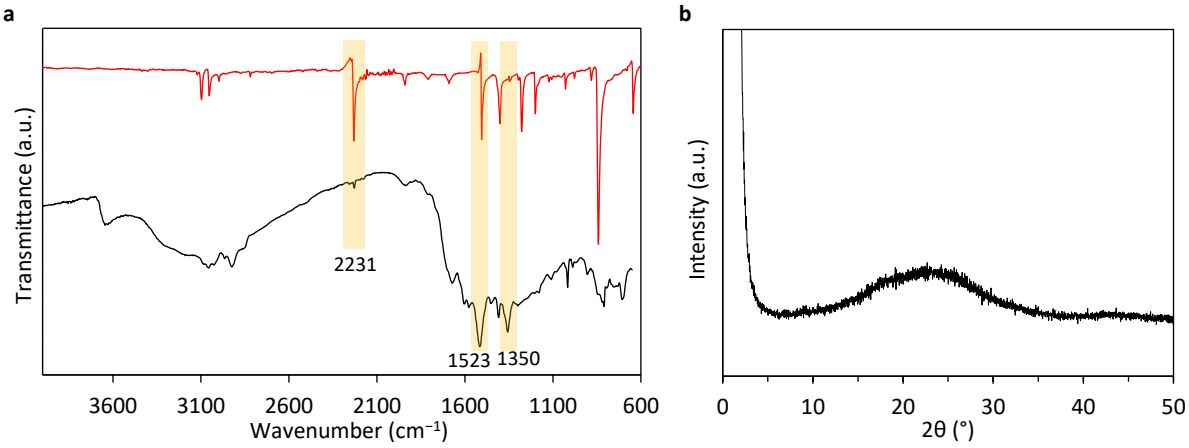

Figure 4.1. (a) FT-IR spectral comparison between benzene-1,4-dicarbonitrile **5** (top) and CTF-1 (bottom). (b) Powder X-ray diffraction pattern of CTF-1.

Table 4.1. Elemental composition of CTF-1 obtained from CHN analysis.

	Calculated	Found
C (wt%)	75.0	68.6
H (wt%)	3.2	2.6
N (wt%)	21.9	10.3
Residue (wt%)	–	18.5
C/N atomic ratio	4.0	7.8

Sorption measurements with N_2 at 77 K were performed to assess the permanent porosity of CTF-1 (Figure 4.2a). The material has a high BET surface area of 1566 $m^2\,g^{-1}$ and a total pore volume of 0.77 $cm^3\,g^{-1}$, which are very similar to the 1495 $m^2\,g^{-1}$ and 0.86 $cm^3\,g^{-1}$ of the CTF-1 reported by Van Der Voort *et al.*[123] The steep increase at relative pressures $P/P_0 < 0.05$ and following plateau point to the purely microporous nature of the material (type I isotherm). In addition, the quenched solid density-functional theory (QSDFT) method, developed for carbons (slit/cylindrical pores, adsorption branch) was applied to calculate the pore size distribution. As shown in Figure 4.2b, CTF-1 shows a narrow distribution of the pore sizes. To gain insights into the local chemical environment of the material, X-ray photoelectron spectroscopy (XPS) analysis was conducted (Figure 4.2c). From the analysis, three different nitrogen species can be distinguished in the curve fitting of the N 1s XPS spectrum. The first signal observed at 398.6 eV can be assigned to pyridinic nitrogen atoms (C–N=C) within the triazine units. The peaks at 400.2 and 401.3 eV arise from pyrrolic and graphitic nitrogen, respectively, which originate from decomposition reactions during

the trimerization at high temperatures.[297] The ratio of the nitrogen species is determined as about 1.4/1.1/1 pyridinic/pyrrolic/graphitic nitrogen, indicating a high content of graphitic nitrogen.

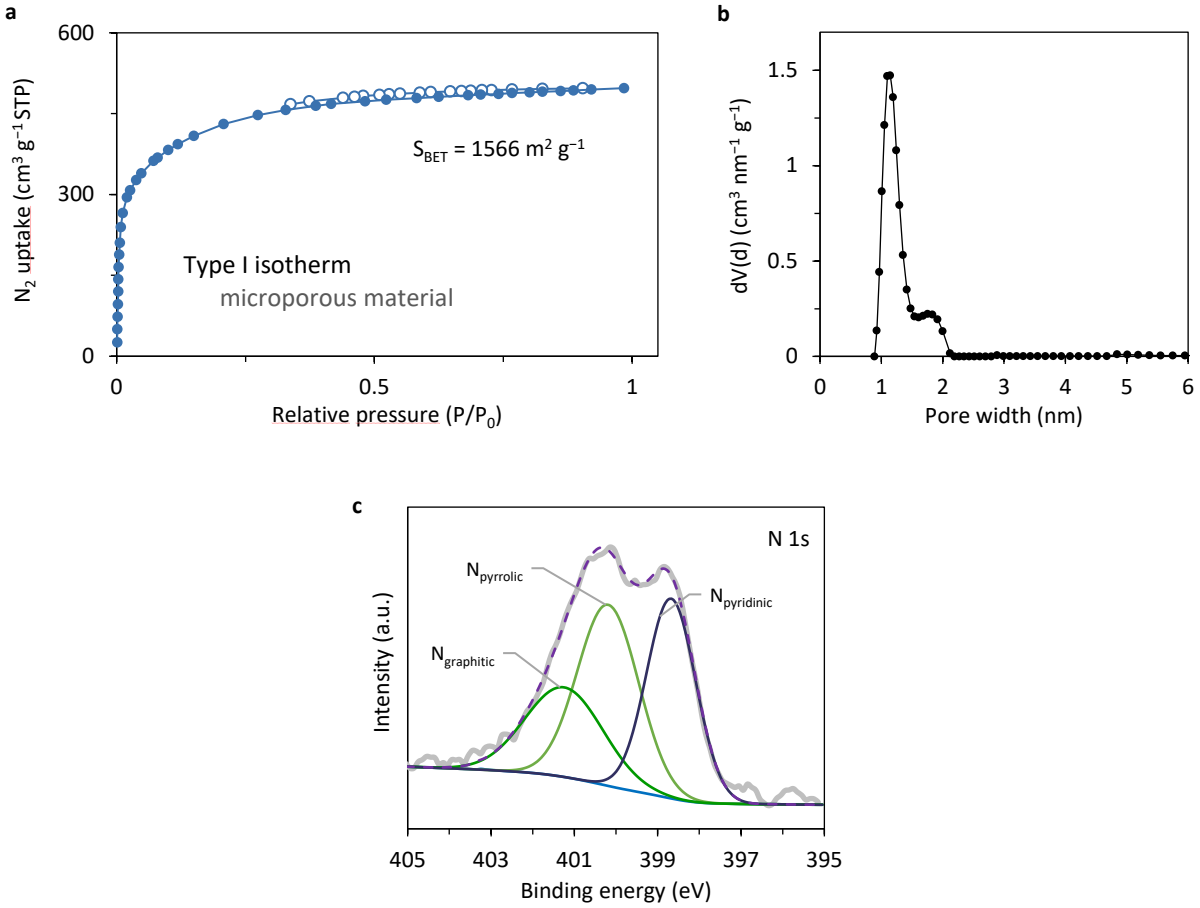

Figure 4.2. (a) Nitrogen adsorption (●) and desorption (○) isotherms of CTF-1 at 77 K. (b) Pore size distribution (QSDFT) and (c) high-resolution N 1s XPS spectrum of CTF-1.

2.2 Oxidative coupling of benzylamine

Before implementing CTF-1 in a flow reactor, our study was initiated by preliminary experiments in batch mode. Herein, CTF-1 was used in the oxidative coupling of benzylamine **3** with O_2 as the terminal oxidant and benzylamine as a model substrate. The influence of temperature on the catalytic activity was examined, and the results are listed in Table 4.2. At 60 °C in toluene, a poor conversion of only 16% was achieved after 4 h of reaction, but with *N*-benzylidenebenzylamine **4** as the only product formed. In comparison, Van Der Voort *et al.* reported a conversion of 99% after 12 h reaction in toluene at 60 °C using their CTF-1 in the same amount, though at a higher concentration (1 M).[123] By extending the reaction time to 18 h, our CTF-1 achieved only 42% conversion, indicating a lower activity than the CTF-1 prepared by Van Der Voort *et al.* As expected, raising the temperature led to a sharp increase in the conversion, reaching 84% at 100 °C. Meanwhile, the higher temperature did not deteriorate the high selectivity of the reaction and imine **4** remained the sole product. In addition to toluene, the reaction in acetonitrile, the

preferred solvent in the photocatalytic oxidative coupling,[298] also gave a high conversion. A blank control experiment confirmed that the oxidation did not proceed in the absence of CTF. As $ZnCl_2$ is used in the ionothermal synthesis, minute amounts of Zn are usually left in the CTF material. For CTF-1, a content of 0.1 wt% of Zn was determined by ICP-OES. However, previous studies have confirmed the inactivity of zinc residues in the reaction.[123,282] Nevertheless, a thorough ICP-MS analysis of the CTF should be considered to really rule out the possible contribution of small amounts of any metal impurity in the reaction.

Table 4.2. Condition screening for the aerobic oxidative coupling of benzylamine **3** catalyzed by CTF-1 in a batch reaction.[a]

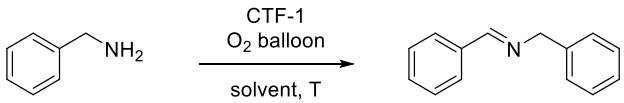

3 **4**

Entry	Solvent	T (°C)	Conv. in 4 h (%)[b]
1	toluene	60	16
2	toluene	80	62
3	toluene	100	84
4	CH_3CN	80	73
Blank[c]	toluene	100	4

[a] Reaction condition: amine **3** (0.33 mmol), CTF-1 (17 mg, 50 wt%), solvent (1 mL), O_2 (1 atm).
[b] Determined by GC-MS analysis using *n*-dodecane as an internal standard.
[c] No catalyst was added.

The reaction operates independently of light, and although the actual active sites and the reaction mechanism have not been fully elucidated yet, it is generally believed that graphitic nitrogen plays a prominent role in the activation of molecular oxygen.[299-302] A reaction mechanism has been proposed by our collaboration partner, Van Der Voort and co-workers, and is depicted in Scheme 4.4.[119,171] Herein, CTF-1 assists in the activation of molecular oxygen by reducing O_2 to the superoxide radical anion ($O_2^{\bullet-}$). Meanwhile, benzylamine **3** is oxidized by the generated positively charged hole to form the radical cation **7** which in turn reacts with $O_2^{\bullet-}$ to form imine **8** and hydrogen peroxide. Imine intermediate **8** may then readily react, following two different pathways: In pathway a, the nucleophilic attack of benzylamine **3** on the generated imine **8**, followed by the elimination of ammonia results in imine **4** as the final product. In pathway b, the decomposition of hydrogen peroxide produces water which can hydrolyze imine **8** and yield aldehyde **2**.[299,303] The aldehyde, in turn, can undergo condensation with amine **3** to give the final coupling product **4**. Since benzaldehyde **2** was never detected in our experiments, neither in ^1H NMR analysis nor in GC-MS, we believe that pathway b is not the operative pathway here. In addition, since we never observed hydrogen peroxide in ^1H NMR analysis, we assume that

hydrogen peroxide, a strong oxidant, can also react with benzylamine **3** to produce another equivalent of imine **8** and water.

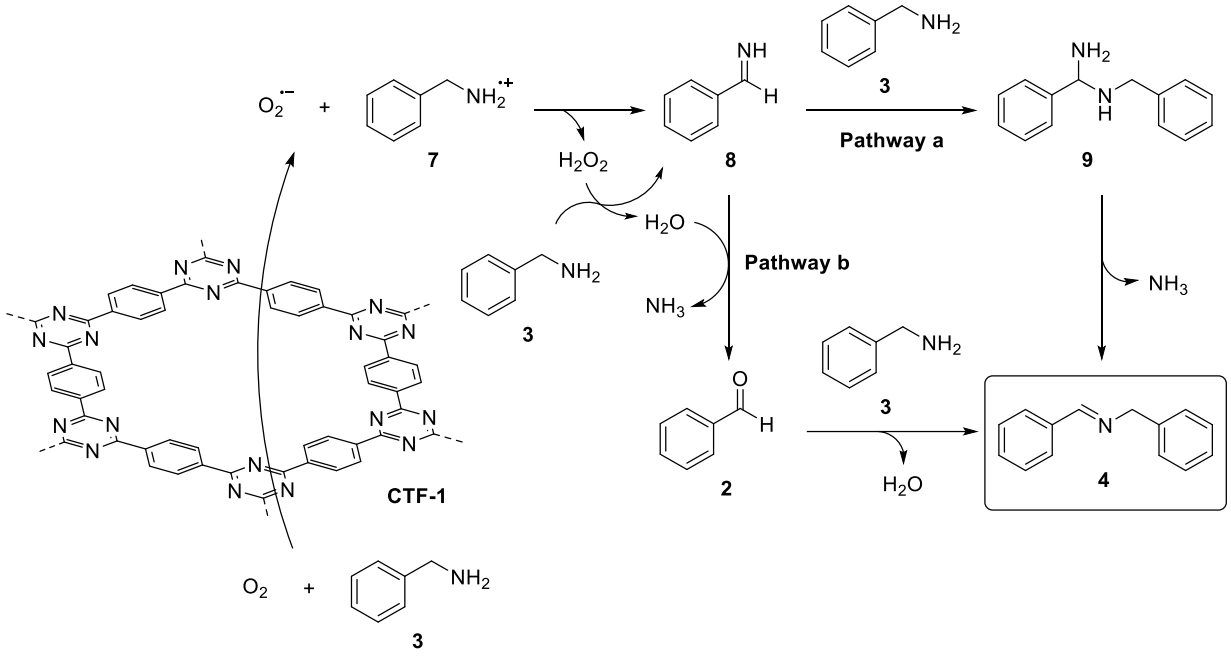

Scheme 4.4. Proposed mechanism for the oxidative coupling of benzylamine **3** catalyzed by CTF-1 by Van Der Voort *et al*.[123]

2.3 Implementation in continuous flow

CTF-1 was then integrated into a continuous flow setup as a packed bed by using an Omnifit® column (Scheme 4.5). The catalytic performance was evaluated in toluene and at a constant oxygen flow rate of 3 mL_N min^{-1}. The influence of the liquid flow rate and of the temperature were investigated and the results are shown in Figure 4.3. A flow rate of 5 mmol h^{-1} (0.25 mL min^{-1}) and a temperature of 80 °C resulted in a stable conversion of about 15%. Increasing the residence time by reducing the liquid flow rate to 3 mmol h^{-1} (0.15 mL min^{-1}) did not affect the conversion. On the other hand, increasing the temperature had a significant positive effect on the activity of the reaction, reaching a conversion of 80% at 100 °C. At 80 and 90 °C, the formation of imine **4** remained stable during the 70 min on-stream experiment. At 100 °C, however, a gradual downward trend in the conversion was observed, indicating a slight loss of catalytic activity. It should be noted that all reactions were carried out in the order of increasing temperature using the same catalyst bed.

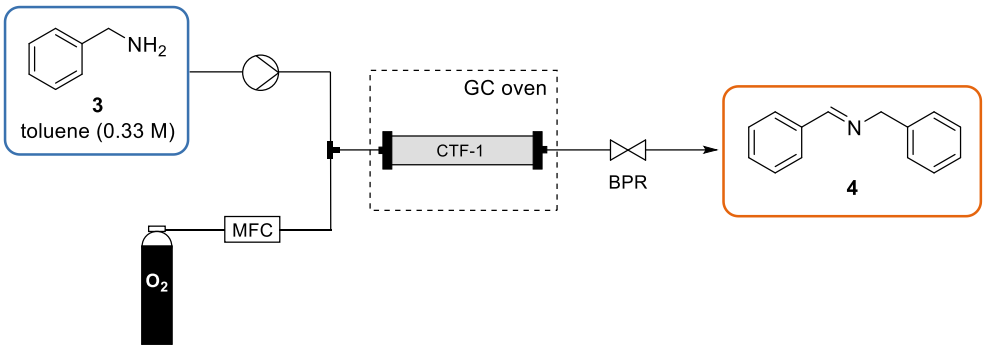

Scheme 4.5. Continuous flow oxidative coupling of benzylamine **3** using a CTF-1 catalyst bed.

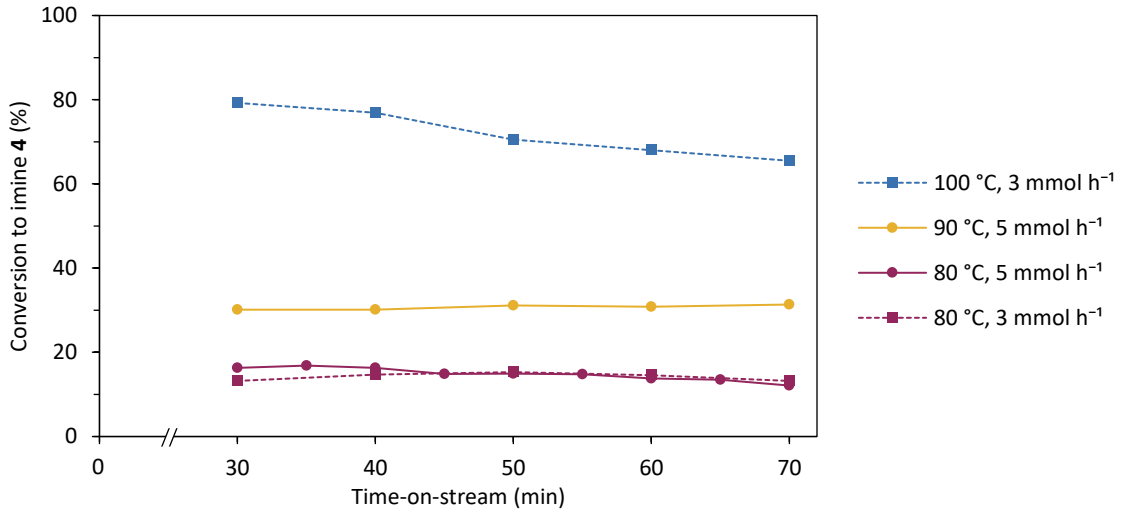

Figure 4.3. Influence of temperature and flow rate on the conversion of benzylamine **3** to *N*-benzylidenebenzylamine **4**. Sampling started after 30 min on stream when steady state was reached.

3 Conclusion

Although this research project was initially plagued by practical difficulties, we have demonstrated the use of CTFs as metal-free catalysts in continuous flow. To this end, CTF-1 was applied in the oxidative coupling of benzylamine **3** using oxygen gas as a green oxidant. The high selectivity of CTF-1 resulted in the formation of *N*-benzylidenebenzylamine **4** as the sole product. CTF-1 demonstrated a stable conversion for 70 minutes, but longer time periods should also be evaluated. At high steady-state conversions, a gradual decrease in conversion may indicate some degree of deactivation of the metal-free catalyst. As a note, since $ZnCl_2$ was used in the ionothermal synthesis of the metal-free CTF catalyst, it would be more appropriate to replace the Zn catalyst with, *e.g.*, polyphosphoric acid to obtain a genuinely metal-free process.[96] Furthermore, a thorough ICP-MS analysis of the CTF should be considered to really rule out the possible contribution of small amounts of any metal impurity to the reaction.

This proof-of-concept study may provide a starting point for a more in-depth investigation. We anticipate that this study could promote the employment of CTFs in continuous flow chemistry.

4 Experimental details

4.1 General methods

Solvents and reagents were purchased from commercial suppliers and used without further purification, unless otherwise stated. ^{1}H NMR and ^{13}C NMR spectra were recorded at 400 and 101 MHz, respectively, using a Bruker Avance III HD 400 spectrometer equipped with a ^{1}H/BB z-gradient probe (BBO, 5 mm). The spectra were recorded at 25 °C and were processed using TopSpin 3.6.2. Chemical shifts (δ) are reported in parts per million (ppm) downfield of tetramethylsilane (internal reference) and coupling constants (*J*) are reported in hertz (Hz). Peaks were assigned with the aid of 2D spectra (COSY, HSQC, H2BC and HMBC). Infrared spectra (FT-IR) of the small compounds were recorded from samples in neat form on a Shimadzu IRAFFINITY-1S FT-IR spectrophotometer with an ATR (attenuated total reflectance) accessory. GC-MS analysis was performed on an Agilent 8890 GC System equipped with an Agilent J&W HP-5ms (30 m x 0.25 mm x 0.25 µm) column and an Agilent 5977B mass spectrometer with quadrupole mass analyzer and extractor EI source (electron ionization, 70 eV).

The infrared (DRIFT) spectrum of the CTF was recorded in the region 650–4000 cm^{-1} with a Thermo Nicolet 6700 FT-IR spectrophotometer equipped with a nitrogen-cooled MCT detector and a KBr beam splitter. Powder X-ray diffraction (PXRD) patterns were collected on a Thermo Scientific ARL X'TRA diffractometer with a Cu Kα radiation source (λ = 1.5418 Å) at 40 kV and 40 mA and a scanning speed of 1° min^{-1}. Combustion elemental analysis was performed on a Thermo Scientific Flash 2000 CHNS/O analyzer equipped with a TCD detector. Nitrogen sorption measurements were carried out on a BELSORP-mini II at 77 K. Prior to measurements, samples were degassed at 120 °C under vacuum for 16 h. Specific surface areas were calculated using the Brunauer–Emmett–Teller (BET) method. For the BET calculations, pressure ranges were chosen in accordance with the criteria described by Rouquerol *et al*.[264] The pore size distribution was determined using the quenched solid density-functional theory (QSDFT) model for N_2 adsorbed on carbon with slit/cylindrical pores, implemented in Quantachrome's ASiQwin software (v4.0). Total pore volumes were determined at P/P_0 = 0.99. X-ray photoelectron spectroscopy (XPS) was performed using the PHI 5000 VersaProbe II spectrometer equipped with a monochromatic Al Kα X-ray source (hν = 1486.6 eV). The samples were excited with an X-ray beam (size 200 µm) over an area of 500 x 500 $µm^2$ at a power of 50 W. Wide range survey scans and high-resolution spectra were recorded with a pass energy of 187.85 eV and 23.5 eV and a step size of 0.8 eV and 0.1 eV, respectively. All spectra were acquired at a take-off angle of 45° relative to the sample surface in the XPS chamber,

where the pressure was constantly maintained below 10^{-6} Pa. The survey scans were used to determine and quantify the surface elemental composition and were analyzed using the MultiPak (v9.6) software. The energy scale of all acquired spectra was calibrated with respect to the hydrocarbon component of the C 1s spectrum (285.0 eV). The reported quantitative results are the mean values obtained from six independent analysis points measured on each sample.

4.2 Synthesis of CTF-1

The preparation of CTF-1 was carried out following the ionothermal synthesis approach described by Antonietti *et al.*[81] To this end, benzene-1,4-dicarbonitrile **5** (300 mg, 2.34 mmol, 1 eq) and anhydrous $ZnCl_2$ (1.56 g, 11.71 mmol, 5 eq) were transferred in a quartz ampoule. The ampoule was flame-sealed under vacuum and heated to 400 °C for 48 h with a heating rate of 1 °C min^{-1}. After cooling, the obtained black solid was ground and washed thoroughly with water to remove most of the $ZnCl_2$. The powder was then further stirred in 1 M HCl for 18 h under reflux conditions to remove remaining $ZnCl_2$. After this, the powder was filtered and washed successively with water (3 x 200 mL), THF (3 x 200 mL), ethanol (3 x 100 mL) and acetone (3 x 200 mL). The resultant black powder was subsequently dried overnight under vacuum at 120 °C.

4.3 Aerobic oxidative coupling of benzylamine

An Omnifit® column (L 100 mm x I.D. 10 mm) with one adjustable endpiece and one fixed endpiece was used to immobilize the catalyst (Figure S4.1). The packed bed, containing CTF-1 (200 mg) and resin diluent (550 mg Amberlite™ XAD-16, particle size of 0.2–0.4 mm) had a bulk volume of about 2 mL. The column was installed in a GC oven, thermostated at the desired temperature. By using a WADose-Lite HP HPLC pump, a solution of benzylamine **3** in toluene (0.33 M) was flown upward through the column concurrently with a stream of pure oxygen gas. A mass flow controller (EL-FLOW®-F-201CM Bronkhorst High-Tech) kept the oxygen flow at a constant rate of 3 mL_N. All parts were connected by polytetrafluoroethylene (PTFE) tubing (I.D. 2.4 mm, O.D. 3.2 mm) and a 2.8 bar back pressure regulator (BPR) was connected to the end of the reactor. The eluent was collected after reaching steady state and analyzed by GC-MS.

Figure S4.1. Omnifit® column.

4.4 Calibration curves

Conversions were quantified using the calibration curves in Figure S4.2. To establish the calibration curve for *N*-benzylidenebenzylamine **4**, the compound was synthesized according to the following procedure: benzylamine **3** (0.536 g, 5 mmol, 1 eq) and benzaldehyde **2** (0.53 g, 5 mmol, 1 eq) were combined in 50 mL of THF and $MgSO_4$ (1.2 g, 10 mmol, 2 eq) was added. After stirring for 2 h under reflux conditions, the reaction mixture was filtered, and the solvent was evaporated to obtain *N*-benzylidenebenzylamine **4** as a pale orange oil in 97% yield. The spectral data are in accordance with those reported in the literature.[304]

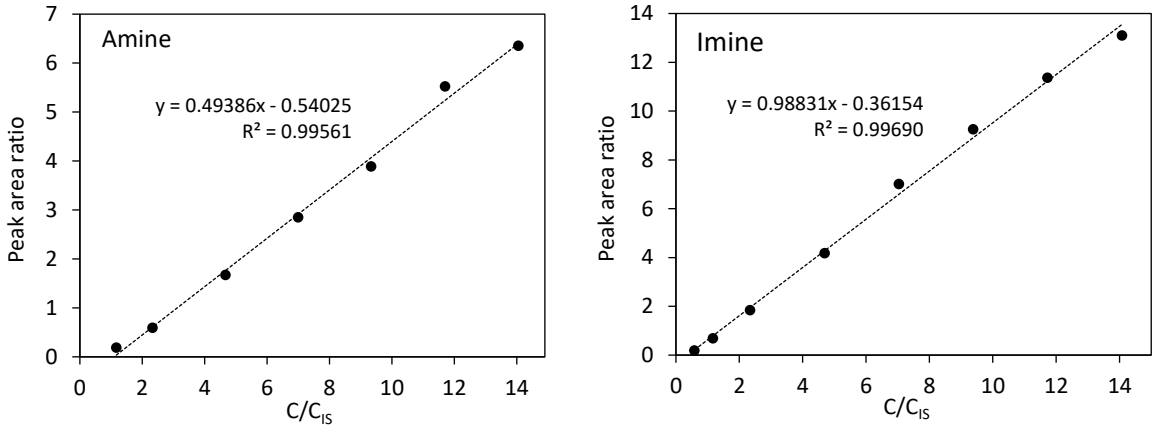

Figure S4.2. GC-MS standard curve of benzylamine **3** and *N*-benzylidenebenzylamine **4** with *n*-dodecane as internal standard (IS).

Chapter 5

Conclusions & outlook

The development of functional materials is instrumental in advancing technological solutions to address pressing societal problems, such as combating climate change, preventing environmental pollution and creating clean energy pathways. Almost three decades ago, the toolbox for nanoporous material design was extended with the concept of reticular chemistry, where judiciously chosen rigid building blocks are assembled in a predesigned manner into a porous ordered framework held together by strong directional bonds. This concept led to the advent of covalent organic frameworks (COFs), which are composed exclusively of organic building blocks. Due to their high porosity, modular design and versatility, COFs have attracted widespread attention in materials sciences. By varying the building blocks, a huge versatility of COFs can be envisaged. This flexibility in design paves the way to engineer these materials on an atomic scale, and has sparked their development for a wide variety of applications, including gas storage, separation, (photo)catalysis, energy storage, sensing, etc.

As a subclass of COFs, covalent triazine frameworks (CTFs) are endowed with high chemical and thermal stability by the triazine nodes connecting the building blocks. This high stability allows them to be used under various conditions. In this PhD thesis, we focused on their application in catalysis and explored their potential as a promising platform for the development of heterogeneous catalysts. Since the modular nature of CTFs allows for the incorporation of a wide variety of molecular building blocks, the construction of CTFs starts with a judicious selection of these precursors. Therefore, access to a wide range of building blocks is crucial. As inferred from the literature review in **Chapter 1**, the incorporation of (poly)pyridyl moieties has so far been limited to simple pyridines and bipyridines. The reason for this lack in diversity can be found in the challenging synthesis of these building blocks which are often plagued by low solubility, low reactivity and low selectivity of the compounds. Therefore, in **Chapter 2**, synthetic procedures were developed toward six nitrogen-containing ligands, which may provide an answer to this lack of available nitrogen-containing building blocks. The synthesized compounds, harboring two cyano groups, can serve as valuable building blocks in the preparation of CTFs, enriching the materials with numerous chelating sites to firmly anchor active metal complexes. The use of a different building block in the CTF synthesis will give rise to a CTF containing coordination sites with a different coordination environment, and thus perhaps a different reactivity. In the first instance, a 2,2'-bipyridine-based CTF was selected as support for the preparation of a heterogeneous catalyst for use in batch and flow reactions. Indeed, as described in **Chapter 3**, the anchoring of a homogeneous Cp*Rh(III) complex on a bipyridine-based CTF, resulted in a highly active and reusable catalyst for the transfer hydrogenation of various N-heteroarenes with formate as the hydrogen source. Although the CTF prepared by the ionothermal synthesis method was far from crystalline, the lack of structural order in the material did not impose restrictions on obtaining an effective heterogeneous catalyst, though it did complicate a thorough characterization. The heterogeneous nature of the catalyst enabled easy recovery and reuse of

the expensive Rh complex. However, the activity of the heterogeneous catalyst proved to be slightly lower than that of the homogeneous counterpart, presumably because of the lower catalyst dispersion in the reaction medium and because of mass transfer limitations within the porous framework. These factors are inherently associated with anchoring of individual molecules to porous supports and especially need to be addressed in reactions where the catalysis itself is very fast. Since straightforward separation and recycling represent the main goals of catalyst immobilization, persistent reusability of the catalysts can justify the lower activity. In this regard, the bpyCTF-supported Rh catalyst was found to maintain its high activity for at least six reaction cycles, which is very encouraging. Just as in most studies in the literature, the durability of the catalyst was evaluated over only a handful of recycles. It must be admitted that these brief recycling experiments do not provide grounds for making claims about the long-term stability of the catalyst and its industrial viability.

Due to time constraints, CTFs prepared from the other nitrogen-containing ligands from **Chapter 2** could not be evaluated as metal support, but should definitely be included in future research as it would be interesting to note a remarkable difference in reactivity.

Heterogeneous catalysis has for a long time been at the center of the production of simple bulk products such as ammonia, sulfuric acid, hydrocarbons and propylene oxide. As the target molecules in the pharmaceutical, agrochemical, and fine chemical industries are structurally more sophisticated, the aspect of selectivity—in all its types (chemo-, regio- and stereo-)—becomes more important than reaction speed. Low activity can be compensated by increasing the amount of catalyst in the reaction or by raising the temperature. In this regard, the immobilization of molecular metal complexes is thé approach that promises the highest level of selectivity, governed by the ligands, while enabling catalyst recycling. At the same time, it renders the metal complex more suitable for use in flow chemistry. This application aspect was touched upon in **Chapter 3** and **Chapter 4**, wherein respectively the transfer hydrogenation and amine oxidation were demonstrated in flow. However, there is still scope for further optimization. Great improvements in the reactor design could be made using a structured packing instead of CTF as a powder. Shaping the CTF into uniform granules or by coating on a monolith could minimize pressure drops and improve mass transfer. While the number of publications on CTFs and COFs is already enormous, few of them report on their use in continuous flow reactions. As the fine chemical industry is increasingly using flow technology in its production, future research should target advancements of CTFs in flow chemistry, which could stimulate the transfer of CTFs from academia to industry.

This PhD thesis has focused on CTFs because the triazine linkage gives these materials a high degree of chemical robustness that is not found in other subclasses of COFs although required for catalytic reactions. Prominent imine COFs, hydrazone COFs and β-ketoenamine COFs have shown chemical erosion because of reaction with strong nucleophiles such as benzylamine, while in

Chapter 4, CTF-1 showed excellent stability in the metal-free oxidative aerobic coupling reaction of benzylamine in batch and flow.[305-306] Due to this robustness, CTFs definitely outperform many other organic frameworks in reactions that proceed under extreme temperature or pH.

However, the low reactivity of the triazine ring is accompanied by the challenge of obtaining crystalline CTFs. During this doctoral research, the conventional ionothermal synthesis method was mainly used to prepare CTFs. Although this method yielded CTFs as amorphous black solids with structural defects, it was chosen because the CTFs obtained had high surface areas (> 500 m^2), which were in line with the values reported in the literature. In the case of the thermal reactions under study in **Chapter 3** and **Chapter 4**, the present of defects and absence of structural order were less of a requirement to obtain an effective catalyst. For the ionothermal synthesis, the traditional protocol described by Thomas *et al.* was straightforward to adopt in our lab, though CTF-1 described in **Chapter 4** did not show any crystallinity, unlike CTF-1 reported by Thomas *et al.*[75] This variability illustrates the difficulty of reproducibility in COF synthesis. During this PhD research, several attempts to synthesize photoactive CTFs by using the superacid method have only yielded CTFs as non-porous solids (S_{BET} < 16 m^2). More than in the organic synthesis of single compounds, it takes time, practice and experience to become familiar with the COF synthesis protocols, and often a small change in the synthesis operations (*e.g.*, the stirring rate[307]) compared to the reported procedures can already have a substantial effect on the resulting COF. Therefore, better and more communication of the synthesis procedures should be provided, *e.g.*, by including pictures of videos from the synthesis to the publication. In addition, not only successes should be shared, but also failures should be communicated. The latter is particularly important for accelerating research, as finding the right reaction conditions is typically difficult to rationalize. As mentioned several times in this thesis, the production of CTFs on a large scale remains challenging and represents a real hurdle for the further development of these materials. In general, CTFs are currently synthesized on a small scale in sealed ampoules. However, due to batch-to-batch variations in the properties, which are not uncommon, each batch needs to be characterized. Hence, straightforward large-scale synthetic methods should be sought which ensure that the resulting CTFs have consistent properties across different batches.

In **Chapter 3** the rationale for selecting a Rh complex was to investigate the effect of anchoring to a CTF on its catalytic performance. The Cp*Rh complex is a well-known and active homogeneous catalyst for transfer hydrogenation, which was most likely to yield an active heterogeneous counterpart after immobilization to the bpyCTF. Since Rh is very rare and therefore expensive, recycling of the metal catalyst is important to reduce the economic cost. In addition, due to its high toxicity, it is crucial in the pharmaceutical industry that traces of the metal are removed from final products to prevent harm to humans. Therefore, firmly anchoring of Rh to CTFs is an attractive solution to avoid leaching of the metal in final products. However, in recent years, the use of earth-abundant, 3d-block transition metals (such as Mn, Fe, Co, Ni) has become a major

area of interest, partly driven by economic and environmental constraints, partly by curiosity about peculiar reactivity. Most salts of first-row metals are less toxic than noble metals, which is advantageous for the pharmaceutical industry.[308] Future research could focus more on the immobilization of these earth-abundant metals on CTFs as substitutes for the commonly used platinum-group metals. As first-row metals tend to be less reactive than noble metals, catalysts could exhibit better chemoselectivity. The activity and selectivity could be governed through engineering of the CTF building block.

Mild synthetic approaches, such as the amidine-based polycondensation, have unlocked the application of CTFs in photochemical transformations. Hence, extensive research should be undertaken to develop CTFs as heterogeneous photocatalyst as such, or in conjunction with photoactive metal complexes. The fully conjugated frameworks are highly suitable for harvesting visible light for chemical transformations and energy storage. By varying the building blocks, the opto-electronic properties can be tuned. For photochemical applications, high structural order in the conjugated CTF material is particularly important, as it favors the separation, mobility and lifetime of charge carriers so that reactions can actually take place. Current methods for the synthesis of crystalline CTFs should be further optimized and their synthetic scalability should be improved.

The incomplete understanding of the reaction mechanism and catalytic behavior of CTFs poses obstacles to reaction optimization and rational material design. Advanced characterization techniques that can be applied *in situ* need to be in place to elucidate such mechanisms.

As this doctoral thesis is situated at the crossroad of homogeneous and heterogeneous catalysis, it was striking during the research how separate these areas of research are. Hence, combined efforts could lead to further advances to transform CTFs, and other COFs, from an academic curiosity to a fully-fledged tool to tackle the pressing challenges of modern society.

Summary

Catalysts are indispensable in the chemical industry as they are a vital tool for improving the sustainability of chemical transformations. Scientists are therefore constantly striving to enhance catalyst performance. Covalent triazine frameworks (CTFs), a relatively new class of nanoporous solids, are gaining widespread attention as promising materials in heterogeneous catalysis. This interest stems from their extensive tunability, high surface area and extraordinary stability, which make them attractive as support materials for active metal species. The immobilization of metal complexes on solid supports is a pivotal strategy to bridge the gap between homogeneous and heterogenous catalysis, combining high activity and selectivity with the ease of catalysts recovery and reuse. This PhD research aimed the further exploration of the potential of CTFs in heterogeneous catalysis, with an emphasis on their practical utilization as catalyst and catalyst support.

In the first part of the thesis, synthetic routes toward six N-heterocyclic ligands were elaborated (Figure I). The ligands, which vary in their denticity and extent of aromaticity, were functionalized with cyano groups, allowing their use as building blocks for CTFs. These building blocks are especially appealing for CTFs in heterogeneous catalysis applications since they provide the CTFs with numerous nitrogen binding sites for stable anchoring of active metal complexes. By access to a wide variety of building blocks, CTFs with distinct properties can be prepared, which may help in a rational design of advanced support materials for heterogeneous catalysis.

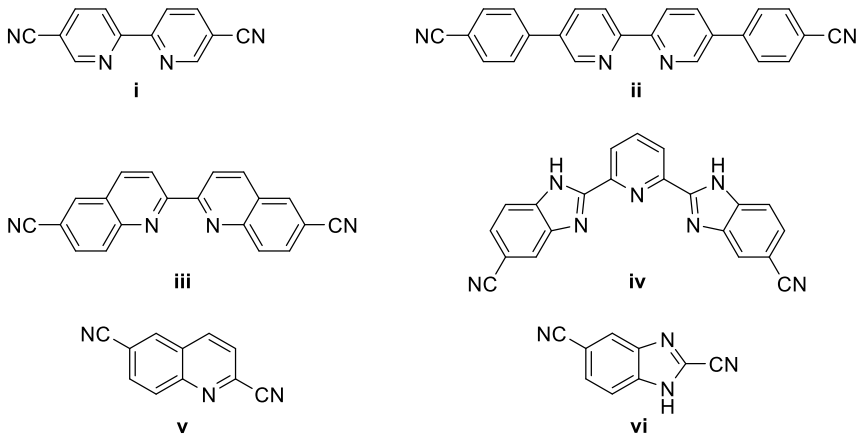

Figure I. Set of synthesized cyano-functionalized N-heterocyclic ligands

Following the synthesis of the building blocks, CTFs were synthesized and thoroughly characterized. Their performance in catalytic reactions was investigated through two case studies.

In the first case study, a bipyridine-based CTF was synthesized and functionalized with a half-sandwich Rh(III) complex. The heterogeneous Rh@bpyCTF catalyst was subsequently applied in the transfer hydrogenation of N-heteroarenes toward prominent scaffolds in drug design. Hydrogenation in water with sodium formate as the hydrogen source is an attractive alternative to the traditional hydrogenation with high-pressure hydrogen gas because of its mild reaction conditions and operational simplicity. At 80 °C, a wide range of quinoxalines was efficiently converted by the heterogeneous catalyst in short reaction times, achieving excellent yields (Scheme I). The substrate scope could be successfully extended to various other N-heteroaromatic scaffolds, demonstrating the versatility of the catalyst. The rate of the reaction in aqueous medium was shown to be highly pH dependent, with the highest reaction rate at pH 4.5. The catalyst maintained high activity over at least six reaction cycles, and its performance was briefly investigated in the continuous flow transfer hydrogenation by placing the catalyst in a packed-bed reactor. A high conversion was achieved, but decreased in a short time. Hence, the design of the packed-bed reactor and the reaction conditions still await further optimization to maintain high conversions for extended periods of time. Overall, bpyCTF appeared to be an attractive support for the heterogenization of molecular active metal centers, thereby bridging the gap between homogeneous and heterogeneous catalysis.

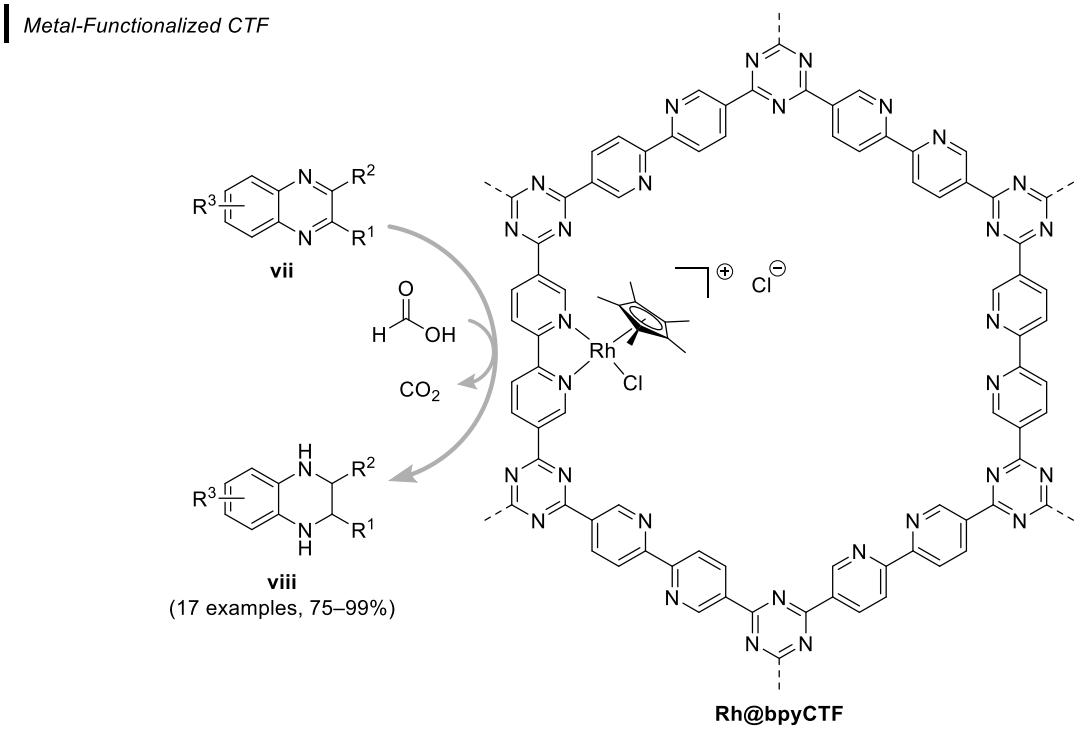

Scheme I. Transfer hydrogenation of quinoxalines **vii** catalyzed by Rh@bpyCTF.

In the second case study, a CTF itself was used as a metal-free catalyst and its application in continuous flow reactions was pursued. Previous research by our research partner, the COMOC group (Department of Chemistry, Ghent University), demonstrated the activation of molecular oxygen on ionothermally synthesized CTFs in batch. This catalytic activity was further explored in this PhD thesis in continuous flow, using the oxidative coupling of benzylamine **ix** as a model reaction (Scheme II). To this end, CTF-1 was ionothermally synthesized from benzene-1,4-dicarbonitrile and integrated into a packed-bed column. The high selectivity of the nitrogen-rich CTF resulted in the formation of *N*-benzylidenebenzylamine **x** as the sole product. The CTF demonstrated stable conversions for at least 70 minutes. At high steady-state conversions, a gradual decrease in conversion over time may indicate the deactivation of the metal-free catalyst. Since the reaction in batch took place in toluene at high temperatures under an oxygen atmosphere, translating this aerobic oxidation reaction into a continuous flow process offered increased mass transfer, easier scale-up and a safer process. This case study provided practical knowledge of applying CTF materials in a packed-bed reactor under continuous flow.

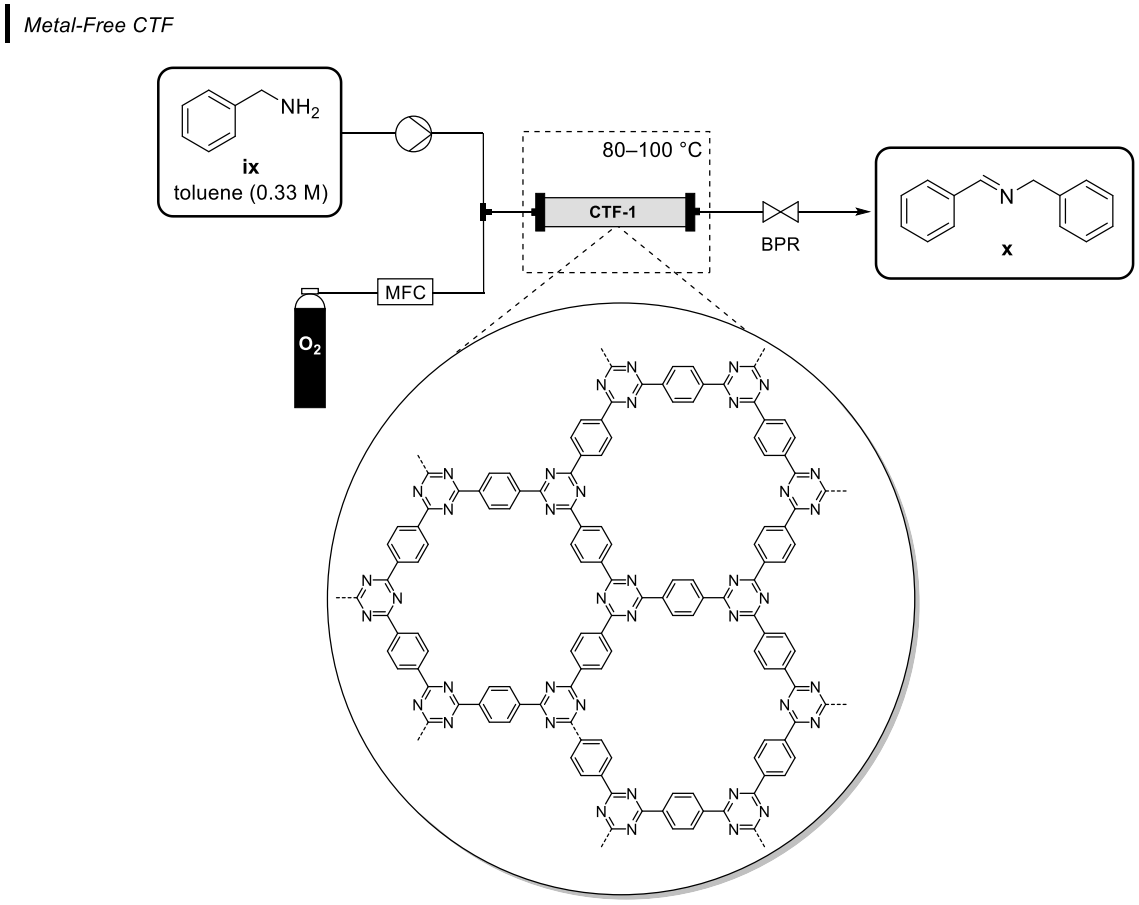

Scheme II. CTF-catalyzed aerobic oxidative coupling of benzylamine **ix** in continuous flow.

Samenvatting

Katalysatoren zijn onmisbaar in de chemische industrie vermits ze een essentieel instrument zijn om de duurzaamheid van chemische transformaties te verbeteren. Wetenschappers streven er daarom voortdurend naar de prestaties van katalysatoren te verbeteren. Covalente triazine roosters (CTF's), een relatief nieuwe klasse van nanoporeuze vaste stoffen, krijgen steeds meer aandacht als veelbelovende materialen voor heterogene katalyse. Deze belangstelling komt voort uit de mogelijkheid om ze op maat te maken, de hoge specifieke oppervlakte en de buitengewone stabiliteit, die hen aantrekkelijk maken als dragermateriaal voor actieve metalen. Het immobiliseren van metaalcomplexen op vaste dragers is een cruciale strategie om de kloof tussen homogene en heterogene katalyse te overbruggen, waarbij hoge activiteit en selectiviteit worden gecombineerd met het gemak van terugwinning en hergebruik van de katalysatoren. Dit proefschrift richtte zich op het verder verkennen van het potentieel van CTF's in heterogene katalyse, met de nadruk op hun praktisch gebruik als katalysator en katalysatordrager.

In het eerste deel van deze doctoraatsthesis werden syntheseroutes naar zes N-heterocyclische liganden uitgewerkt (Figuur I). De liganden, die variëren in hun denticiteit en grootte van aromatisch systeem, werden gefunctionaliseerd met cyaangroepen, waardoor ze als bouwstenen voor CTF's kunnen worden gebruikt. Deze bouwstenen zijn bijzonder aantrekkelijk voor CTF's in heterogene katalysetoepassingen, aangezien zij de CTF's voorzien van talrijke stikstofhoudende bindingsplaatsen voor een stabiele verankering van actieve metaalcomplexen. Door toegang te hebben tot een groot aantal verscheiden bouwstenen kunnen CTF's met verschillende eigenschappen worden bereid, wat kan bijdragen tot een ontwerpen van geavanceerde dragermaterialen voor heterogene katalyse.

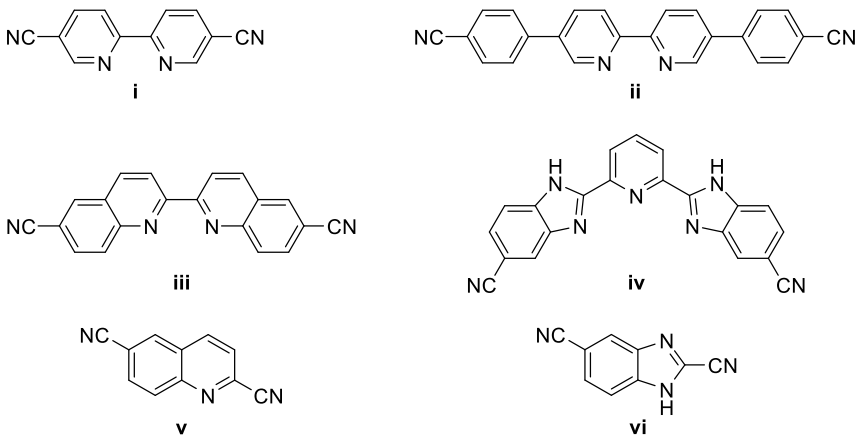

Figuur I. Overzicht van de gesynthetiseerde N-heterocyclische liganden met cyaangroepen.

Na de synthese van de bouwstenen werden CTF's gesynthetiseerd en grondig gekarakteriseerd. Hun prestaties in katalytische reacties werden onderzocht aan de hand van twee casestudies.

In de eerste casestudy werd een CTF gesynthetiseerd op basis van bipyridine bouwstenen, waaraan vervolgens een Rh(III)-complex werd verankerd. De heterogene Rh@bpyCTF werd vervolgens toegepast als katalysator voor de transfer-hydrogenering van N-heteroarenen naar prominente verbindingen bij het ontwerpen van geneesmiddelen. Hydrogenering in water met een buffer van mierenzuur en natriumformiaat als waterstofbron is een aantrekkelijk alternatief voor de traditionele hydrogenering met waterstofgas onder hoge druk vanwege de milde reactieomstandigheden en de operationele eenvoud. De heterogene katalysator kon bij 80 °C op efficiënte wijze een breed scala aan chinoxalinen omzetten in korte reactietijden en met hoge opbrengsten (Schema II). Het substraatbereik werd met succes uitgebreid naar diverse andere N-heteroaromatische verbindingen, hetgeen de veelzijdigheid van de katalysator aantoont. De snelheid van de reactie in waterig medium bleek sterk pH-afhankelijk te zijn, met de hoogste reactiesnelheid bij pH 4,5. De katalysator behield een hoge activiteit gedurende zes reactiecycli, en zijn prestaties werden kort onderzocht in de continue transfer-hydrogenering in flow door de katalysator in een gepakte kolomreactor te plaatsen. Er werd een hoge omzettingsgraad bereikt, maar deze daalde snel in korte tijd. Het ontwerp van de reactor en de reactieomstandigheden dienen daarom nog verder te worden geoptimaliseerd om gedurende langere tijd hoge omzettingen te handhaven. In het algemeen bleek bpyCTF een erg geschikte drager te zijn voor het verankeren van moleculair actieve metalen, waardoor de kloof tussen homogene en heterogene katalyse wordt gedicht.

Metaal-Gefunctionaliseerde CTF

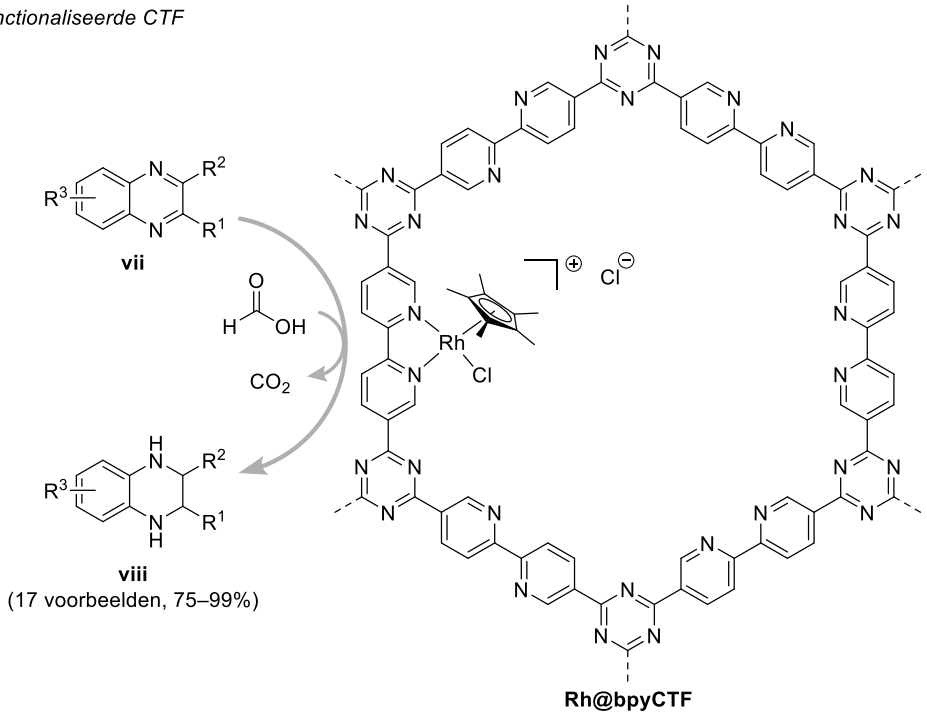

Reactieomstandigheden: Rh@bpyCTF (0,25 mol% Rh); 4 M $HCOOH/HCOONa_{aq}$; pH 4,5; 80 °C; 3–10 u.

Schema I. Transfer-hydrogenering van chinoxalinen **vii** gekatalyseerd door Rh@bpyCTF.

In de tweede casestudy werd een CTF op zich als metaalvrije katalysator gebruikt en werd de toepassing ervan in continue flowreacties nagestreefd. Eerder onderzoek door onze onderzoekspartner, de COMOC-groep (Departement Chemie, Universiteit Gent), toonde de activering van moleculaire zuurstof op ionothermaal gesynthetiseerde CTF's aan in batch. Deze katalytische activiteit werd in deze doctoraatsthesis verder onderzocht in continue flow, met de oxidatieve koppeling van benzylamine **ix** als modelreactie (Schema II). Hiervoor werd CTF-1 ionothermaal gesynthetiseerd uit benzeen-1,4-dicarbonitril en geïntegreerd in een gepakte kolom. De hoge selectiviteit van de stikstofrijke CTF resulteerde in de vorming van *N*-benzylideenbenzylamine **x** als enige product. De CTF vertoonde stabiele omzettingen gedurende ten minste 70 minuten. Bij hoge evenwichtsomzettingen werd echter een geleidelijke afname van de omzettingsgraad waargenomen doorheen de tijd, wat kan wijzen op de deactivering van de metaalvrije katalysator. Aangezien de reactie in batch plaatsvond in brandbaar tolueen bij hoge temperaturen onder een zuurstofatmosfeer, bood het omzetten van deze aërobe oxidatiereactie naar continue flow meer massaoverdracht, eenvoudigere opschaling en een veiliger proces. Deze casestudy leverde praktische kennis op over de toepassing van CTF-materialen in een gepakte reactor onder continue doorstroom.

Metaalvrije CTF

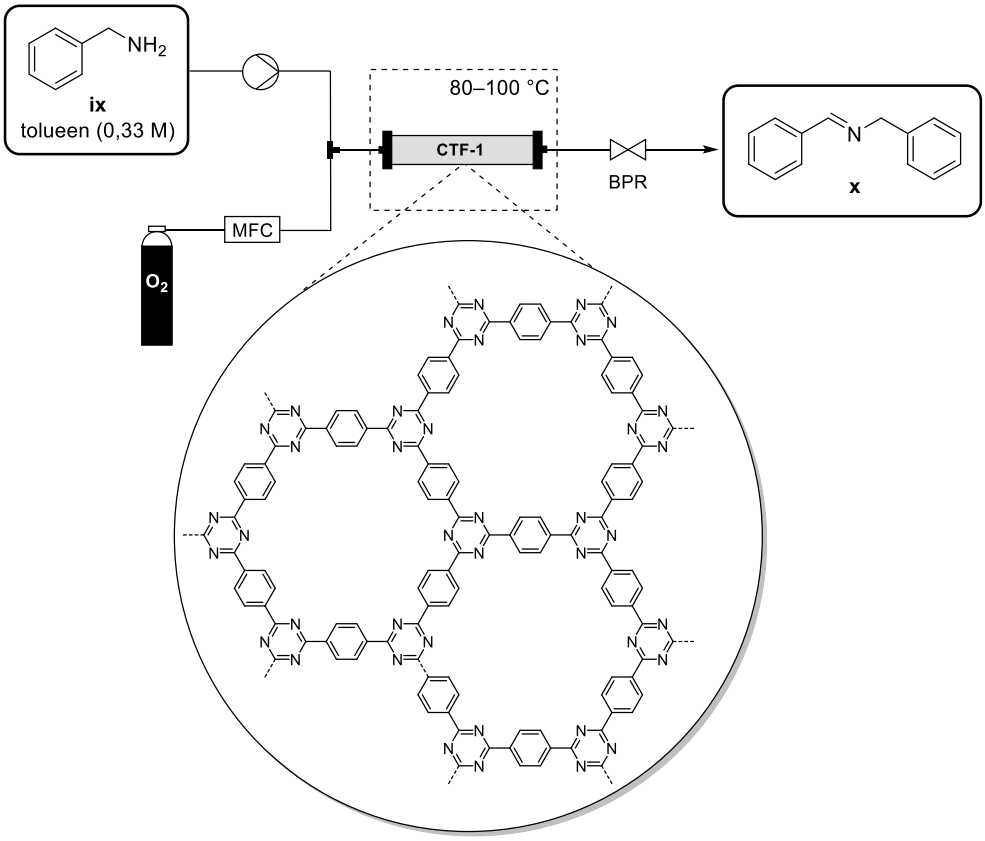

Schema II. CTF-gekatalyseerde aërobe oxidatieve koppeling van benzylamine **ix** in continue flow.

References

1. P. T. Anastas, J. C. Warner, *Green Chemistry: Theory and Practice*, Oxford University Press, Oxford, **1998**.
2. P. T. Anastas, N. Eghbali, *Chem. Soc. Rev.* **2010**, *39*, 301–312.
3. K. P. de Jong, in *Synthesis of Solid Catalysts* (Ed.: K. P. de Jong), Wiley-VCH, Weinheim, **2009**, pp. 1–11.
4. I. Fechete, Y. Wang, J. C. Védrine, *Catal. Today* **2012**, *189*, 2–27.
5. G. Ertl, *Angew. Chem. Int. Ed.* **2008**, *47*, 3524–3535.
6. I. Chorkendorff, J. W. Niemantsverdriet, *Concepts of Modern Catalysis and Kinetics*, 1st ed., Wiley-VCH, Weinheim, **2003**.
7. A. Schmid, J. S. Dordick, B. Hauer, A. Kiener, M. Wubbolts, B. Witholt, *Nature* **2001**, *409*, 258–268.
8. L. Hedstrom, Enzyme Specificity and Selectivity, in *Encyclopedia of Life Sciences*, John Wiley & Sons, Ltd, Chichester, **2010**.
9. R. J. Lundgren, M. Stradiotto, *Ligand Design in Metal Chemistry: Reactivity and Catalysis*, 1st ed., John Wiley & Sons, Ltd, Chichester, **2016**.
10. R. H. Crabtree, *The Organometallic Chemistry of the Transition Metals*, 6th ed., John Wiley & Sons, Inc, Hoboken (NJ), **2014**.
11. D. J. Cole-Hamilton, *Science* **2003**, *299*, 1702–1706.
12. L. Liu, A. Corma, *Chem. Rev.* **2018**, *118*, 4981–5079.
13. G. A. Somorjai, *Nature* **2004**, *430*, 730–730.
14. J. K. Nørskov, T. Bligaard, B. Hvolbæk, F. Abild-Pedersen, I. Chorkendorff, C. H. Christensen, *Chem. Soc. Rev.* **2008**, *37*, 2163–2171.
15. J. M. Thomas, R. Raja, D. W. Lewis, *Angew. Chem. Int. Ed.* **2005**, *44*, 6456–6482.
16. C. Copéret, A. Comas-Vives, M. P. Conley, D. P. Estes, A. Fedorov, V. Mougel, H. Nagae, F. Núñez-Zarur, P. A. Zhizhko, *Chem. Rev.* **2016**, *116*, 323–421.
17. F. M. Wisser, Y. Mohr, E. A. Quadrelli, J. Canivet, *ChemCatChem* **2020**, *12*, 1270–1275.
18. A. E. C. Collis, I. T. Horváth, *Catal. Sci. Technol.* **2011**, *1*, 912–919.
19. A. G. Slater, A. I. Cooper, *Science* **2015**, *348*, aaa8075.

20. M. Thommes, K. Kaneko, A. V. Neimark, J. P. Olivier, F. Rodriguez-Reinoso, J. Rouquerol, K. S. W. Sing, *Pure Appl. Chem.* **2015**, *87*, 1051–1069.

21. C. S. Cundy, P. A. Cox, *Chem. Rev.* **2003**, *103*, 663–702.

22. W. J. Roth, P. Nachtigall, R. E. Morris, P. S. Wheatley, V. R. Seymour, S. E. Ashbrook, P. Chlubná, L. Grajciar, M. Položij, A. Zukal, O. Shvets, J. Čejka, *Nat. Chem.* **2013**, *5*, 628–633.

23. V. Van Speybroeck, K. Hemelsoet, L. Joos, M. Waroquier, R. G. Bell, C. R. A. Catlow, *Chem. Soc. Rev.* **2015**, *44*, 7044–7111.

24. J. S. Beck, J. C. Vartuli, W. J. Roth, M. E. Leonowicz, C. T. Kresge, K. D. Schmitt, C. T. W. Chu, D. H. Olson, E. W. Sheppard, S. B. McCullen, J. B. Higgins, J. L. Schlenker, *J. Am. Chem. Soc.* **1992**, *114*, 10834–10843.

25. C. T. Kresge, M. E. Leonowicz, W. J. Roth, J. C. Vartuli, J. S. Beck, *Nature* **1992**, *359*, 710–712.

26. J. Y. Ying, C. P. Mehnert, M. S. Wong, *Angew. Chem. Int. Ed.* **1999**, *38*, 56–77.

27. C. Liu, X. Ye, Y. Wu, *Catal. Lett.* **1996**, *36*, 263–266.

28. D. E. De Vos, M. Dams, B. F. Sels, P. A. Jacobs, *Chem. Rev.* **2002**, *102*, 3615–3640.

29. N. Carlsson, H. Gustafsson, C. Thörn, L. Olsson, K. Holmberg, B. Åkerman, *Adv. Colloid Interface Sci.* **2014**, *205*, 339–360.

30. D. Zhao, Q. Huo, J. Feng, B. F. Chmelka, G. D. Stucky, *J. Am. Chem. Soc.* **1998**, *120*, 6024–6036.

31. D. Zhao, J. Feng, Q. Huo, N. Melosh, G. H. Fredrickson, B. F. Chmelka, G. D. Stucky, *Science* **1998**, *279*, 548–552.

32. S. Inagaki, S. Guan, Y. Fukushima, T. Ohsuna, O. Terasaki, *J. Am. Chem. Soc.* **1999**, *121*, 9611–9614.

33. B. J. Melde, B. T. Holland, C. F. Blanford, A. Stein, *Chem. Mater.* **1999**, *11*, 3302–3308.

34. T. Asefa, M. J. MacLachlan, N. Coombs, G. A. Ozin, *Nature* **1999**, *402*, 867–871.

35. P. Van Der Voort, D. Esquivel, E. De Canck, F. Goethals, I. Van Driessche, F. J. Romero-Salguero, *Chem. Soc. Rev.* **2013**, *42*, 3913–3955.

36. M. Waki, Y. Maegawa, K. Hara, Y. Goto, S. Shirai, Y. Yamada, N. Mizoshita, T. Tani, W.-J. Chun, S. Muratsugu, M. Tada, A. Fukuoka, S. Inagaki, *J. Am. Chem. Soc.* **2014**, *136*, 4003–4011.

37. H. Li, M. Eddaoudi, M. O'Keeffe, O. M. Yaghi, *Nature* **1999**, *402*, 276–279.

38. M. Eddaoudi, J. Kim, N. Rosi, D. Vodak, J. Wachter, M. O'Keeffe, O. M. Yaghi, *Science* **2002**, *295*, 469–472.

39. H. Deng, S. Grunder, K. E. Cordova, C. Valente, H. Furukawa, M. Hmadeh, F. Gándara, A. C. Whalley, Z. Liu, S. Asahina, H. Kazumori, M. O'Keeffe, O. Terasaki, J. F. Stoddart, O. M. Yaghi, *Science* **2012**, *336*, 1018–1023.

40. H. Furukawa, N. Ko, Y. B. Go, N. Aratani, S. B. Choi, E. Choi, A. Ö. Yazaydin, R. Q. Snurr, M. O'Keeffe, J. Kim, O. M. Yaghi, *Science* **2010**, *329*, 424–428.

41. O. K. Farha, I. Eryazici, N. C. Jeong, B. G. Hauser, C. E. Wilmer, A. A. Sarjeant, R. Q. Snurr, S. T. Nguyen, A. Ö. Yazaydın, J. T. Hupp, *J. Am. Chem. Soc.* **2012**, *134*, 15016–15021.

42. K. Leus, T. Bogaerts, J. De Decker, H. Depauw, K. Hendrickx, H. Vrielinck, V. Van Speybroeck, P. Van Der Voort, *Microporous Mesoporous Mater.* **2016**, *226*, 110–116.

43. M. Ding, X. Cai, H.-L. Jiang, *Chem. Sci.* **2019**, *10*, 10209–10230.

44. A. P. Côté, A. I. Benin, N. W. Ockwig, M. O'Keeffe, A. J. Matzger, O. M. Yaghi, *Science* **2005**, *310*, 1166–1170.

45. O. M. Yaghi, M. O'Keeffe, N. W. Ockwig, H. K. Chae, M. Eddaoudi, J. Kim, *Nature* **2003**, *423*, 705–714.

46. C. S. Diercks, O. M. Yaghi, *Science* **2017**, *355*, eaal1585.

47. H. M. El-Kaderi, J. R. Hunt, J. L. Mendoza-Cortés, A. P. Côté, R. E. Taylor, M. O'Keeffe, O. M. Yaghi, *Science* **2007**, *316*, 268–272.

48. F. J. Uribe-Romo, J. R. Hunt, H. Furukawa, C. Klöck, M. O'Keeffe, O. M. Yaghi, *J. Am. Chem. Soc.* **2009**, *131*, 4570–4571.

49. S. J. Lyle, P. J. Waller, O. M. Yaghi, *Trends Chem.* **2019**, *1*, 172–184.

50. X. Guan, F. Chen, S. Qiu, Q. Fang, *Angew. Chem. Int. Ed.* **2023**, *62*, e202213203.

51. K. S. Rawat, S. Borgmans, T. Braeckevelt, C. V. Stevens, P. Van Der Voort, V. Van Speybroeck, *ACS Appl. Nano Mater.* **2022**, *5*, 14377–14387.

52. C. J. Doonan, D. J. Tranchemontagne, T. G. Glover, J. R. Hunt, O. M. Yaghi, *Nat. Chem.* **2010**, *2*, 235–238.

53. H. Fan, A. Mundstock, A. Feldhoff, A. Knebel, J. Gu, H. Meng, J. Caro, *J. Am. Chem. Soc.* **2018**, *140*, 10094–10098.

54. A. Halder, M. Ghosh, A. Khayum M, S. Bera, M. Addicoat, H. S. Sasmal, S. Karak, S. Kurungot, R. Banerjee, *J. Am. Chem. Soc.* **2018**, *140*, 10941–10945.

55. D. Zhu, G. Xu, M. Barnes, Y. Li, C.-P. Tseng, Z. Zhang, J.-J. Zhang, Y. Zhu, S. Khalil, M. M. Rahman, R. Verduzco, P. M. Ajayan, *Adv. Funct. Mater.* **2021**, *31*, 2100505.

56. S.-Y. Ding, J. Gao, Q. Wang, Y. Zhang, W.-G. Song, C.-Y. Su, W. Wang, *J. Am. Chem. Soc.* **2011**, *133*, 19816–19822.

57. H. Hu, Q. Yan, R. Ge, Y. Gao, *Chin. J. Catal.* **2018**, *39*, 1167–1179.

58. S. Yang, W. Hu, X. Zhang, P. He, B. Pattengale, C. Liu, M. Cendejas, I. Hermans, X. Zhang, J. Zhang, J. Huang, *J. Am. Chem. Soc.* **2018**, *140*, 14614–14618.

59. H. Chen, H. S. Jena, X. Feng, K. Leus, P. Van Der Voort, *Angew. Chem. Int. Ed.* **2022**, *61*, e202204938.

60. X. Wu, X. Han, Q. Xu, Y. Liu, C. Yuan, S. Yang, Y. Liu, J. Jiang, Y. Cui, *J. Am. Chem. Soc.* **2019**, *141*, 7081–7089.

61. A. M. Kaczmarek, Y.-Y. Liu, M. K. Kaczmarek, H. Liu, F. Artizzu, L. D. Carlos, P. Van Der Voort, *Angew. Chem. Int. Ed.* **2020**, *59*, 1932–1940.

62. F. Haase, B. V. Lotsch, *Chem. Soc. Rev.* **2020**, *49*, 8469–8500.

63. L. Bourda, C. Krishnaraj, P. Van Der Voort, K. Van Hecke, *Mater. Adv.* **2021**, *2*, 2811–2845.

64. J.-S. M. Lee, A. I. Cooper, *Chem. Rev.* **2020**, *120*, 2171–2214.

65. L. Tan, B. Tan, *Chem. Soc. Rev.* **2017**, *46*, 3322–3356.

66. N. B. McKeown, S. Makhseed, P. M. Budd, *Chem. Commun.* **2002**, 2780–2781.

67. P. M. Budd, B. S. Ghanem, S. Makhseed, N. B. McKeown, K. J. Msayib, C. E. Tattershall, *Chem. Commun.* **2004**, 230–231.

68. C. Li, A. L. Ward, S. E. Doris, T. A. Pascal, D. Prendergast, B. A. Helms, *Nano Lett.* **2015**, *15*, 5724–5729.

69. J.-X. Jiang, F. Su, A. Trewin, C. D. Wood, N. L. Campbell, H. Niu, C. Dickinson, A. Y. Ganin, M. J. Rosseinsky, Y. Z. Khimyak, A. I. Cooper, *Angew. Chem. Int. Ed.* **2007**, *46*, 8574–8578.

70. Y. Tian, G. Zhu, *Chem. Rev.* **2020**, *120*, 8934–8986.

71. T. Ben, H. Ren, S. Ma, D. Cao, J. Lan, X. Jing, W. Wang, J. Xu, F. Deng, J. M. Simmons, S. Qiu, G. Zhu, *Angew. Chem. Int. Ed.* **2009**, *48*, 9457–9460.

72. M. Rose, W. Böhlmann, M. Sabo, S. Kaskel, *Chem. Commun.* **2008**, 2462–2464.

73. J. Fritsch, M. Rose, P. Wollmann, W. Böhlmann, S. Kaskel, *Materials* **2010**, *3*, 2447–2462.

74. J. Fritsch, F. Drache, G. Nickerl, W. Böhlmann, S. Kaskel, *Microporous Mesoporous Mater.* **2013**, *172*, 167–173.

75. P. Kuhn, M. Antonietti, A. Thomas, *Angew. Chem. Int. Ed.* **2008**, *47*, 3450–3453.

76. W. G. Toland, US Patent 3060179, **1962**.

77. H. A. Vogel, US Patent 3654192, **1972**.

78. G. H. Miller, US Patent 3775380, **1973**.

79. R. Palkovits, M. Antonietti, P. Kuhn, A. Thomas, F. Schüth, *Angew. Chem. Int. Ed.* **2009**, *48*, 6909–6912.

80. J. Artz, *ChemCatChem* **2018**, *10*, 1753–1771.

81. P. Kuhn, A. Forget, D. Su, A. Thomas, M. Antonietti, *J. Am. Chem. Soc.* **2008**, *130*, 13333–13337.

82. P. Kuhn, A. Thomas, M. Antonietti, *Macromolecules* **2009**, *42*, 319–326.

83. P. Katekomol, J. Roeser, M. Bojdys, J. Weber, A. Thomas, *Chem. Mater.* **2013**, *25*, 1542–1548.

84. M. J. Bojdys, J. Jeromenok, A. Thomas, M. Antonietti, *Adv. Mater.* **2010**, *22*, 2202–2205.

85. K. Schwinghammer, S. Hug, M. B. Mesch, J. Senker, B. V. Lotsch, *Energy Environ. Sci.* **2015**, *8*, 3345–3353.

86. S. Hug, L. Stegbauer, H. Oh, M. Hirscher, B. V. Lotsch, *Chem. Mater.* **2015**, *27*, 8001–8010.

87. Y. Zhao, K. X. Yao, B. Teng, T. Zhang, Y. Han, *Energy Environ. Sci.* **2013**, *6*, 3684–3692.

88. C. Krishnaraj, H. S. Jena, F. Lecoeuvre, K. Leus, P. Van Der Voort, *Molecules* **2021**, *26*, 3670.

89. E. Saputra, B. A. Prawiranegara, H. Sugesti, M. W. Nugraha, P. S. Utama, *J. Water Process Eng.* **2022**, *48*, 102874.

90. J. Liu, D. Zhou, Z. Xu, S. Zheng, *Environ. Pollut.* **2017**, *226*, 379–384.

91. N. Tahir, C. Krishnaraj, K. Leus, P. Van Der Voort, *Polymers* **2019**, *11*, 1326.

92. S.-Y. Yu, J. Mahmood, H.-J. Noh, J.-M. Seo, S.-M. Jung, S.-H. Shin, Y.-K. Im, I.-Y. Jeon, J.-B. Baek, *Angew. Chem. Int. Ed.* **2018**, *57*, 8438–8442.

93. B. Rickborn, F. R. Jensen, *J. Org. Chem.* **1962**, *27*, 4608–4610.

94. M. S. Meier, Phosphorus(V) Oxide, in *Encyclopedia of Reagents for Organic Synthesis*, **2001**.

95. S.-Y. Yu, J. C. Kim, H.-J. Noh, Y.-K. Im, J. Mahmood, I.-Y. Jeon, S. K. Kwak, J.-B. Baek, *Cell Rep. Phys. Sci.* **2021**, *2*, 100653.

96. T. Sun, Y. Liang, W. Luo, L. Zhang, X. Cao, Y. Xu, *Angew. Chem. Int. Ed.* **2022**, *61*, e202203327.

97. S. J. Ren, M. J. Bojdys, R. Dawson, A. Laybourn, Y. Z. Khimyak, D. J. Adams, A. I. Cooper, *Adv. Mater.* **2012**, *24*, 2357–2361.

98. X. Zhu, C. Tian, S. M. Mahurin, S.-H. Chai, C. Wang, S. Brown, G. M. Veith, H. Luo, H. Liu, S. Dai, *J. Am. Chem. Soc.* **2012**, *134*, 10478–10484.

99. A. Bhunia, D. Esquivel, S. Dey, R. Fernández-Terán, Y. Goto, S. Inagaki, P. Van Der Voort, C. Janiak, *J. Mater. Chem. A* **2016**, *4*, 13450–13457.

100. W. Huang, Z. J. Wang, B. C. Ma, S. Ghasimi, D. Gehrig, F. Laquai, K. Landfester, K. A. I. Zhang, *J. Mater. Chem. A* **2016**, *4*, 7555–7559.

101. W. Huang, B. C. Ma, H. Lu, R. Li, L. Wang, K. Landfester, K. A. I. Zhang, *ACS Catal.* **2017**, *7*, 5438–5442.

102. Z. Yang, H. Chen, S. Wang, W. Guo, T. Wang, X. Suo, D.-e. Jiang, X. Zhu, I. Popovs, S. Dai, *J. Am. Chem. Soc.* **2020**, *142*, 6856–6860.

103. T. Sun, Y. Liang, Y. Xu, *Angew. Chem. Int. Ed.* **2022**, *61*, e202113926.

104. K. Wang, L.-M. Yang, X. Wang, L. Guo, G. Cheng, C. Zhang, S. Jin, B. Tan, A. Cooper, *Angew. Chem. Int. Ed.* **2017**, *56*, 14149–14153.

105. R. Sun, X. Wang, X. Wang, B. Tan, *Angew. Chem. Int. Ed.* **2022**, *61*, e202117668.

106. M. Liu, Q. Huang, S. Wang, Z. Li, B. Li, S. Jin, B. Tan, *Angew. Chem. Int. Ed.* **2018**, *57*, 11968–11972.

107. M. Liu, K. Jiang, X. Ding, S. Wang, C. Zhang, J. Liu, Z. Zhan, G. Cheng, B. Li, H. Chen, S. Jin, B. Tan, *Adv. Mater.* **2019**, *31*, 1807865.

108. J. Liu, M. Liu, X. Wang, X. Wang, B. Tan, *Small* **2022**, *18*, 2200984.

109. S. Zhang, G. Cheng, L. Guo, N. Wang, B. Tan, S. Jin, *Angew. Chem. Int. Ed.* **2020**, *59*, 6007–6014.

110. M. Alves Fávaro, D. Ditz, J. Yang, S. Bergwinkl, A. C. Ghosh, M. Stammler, C. Lorentz, J. Roeser, E. A. Quadrelli, A. Thomas, R. Palkovits, J. Canivet, F. M. Wisser, *ACS Appl. Mater. Interfaces* **2022**, *14*, 14182–14192.

111. H. Lim, M. C. Cha, J. Y. Chang, *Macromol. Chem. Phys.* **2012**, *213*, 1385–1390.

112. P. Puthiaraj, S.-M. Cho, Y.-R. Lee, W.-S. Ahn, *J. Mater. Chem. A* **2015**, *3*, 6792–6797.

113. S. Dey, A. Bhunia, D. Esquivel, C. Janiak, *J. Mater. Chem. A* **2016**, *4*, 6259–6263.

114. S. Xiong, X. Fu, L. Xiang, G. Yu, J. Guan, Z. Wang, Y. Du, X. Xiong, C. Pan, *Polym. Chem.* **2014**, *5*, 3424–3431.

115. E. Troschke, S. Grätz, T. Lübken, L. Borchardt, *Angew. Chem. Int. Ed.* **2017**, *56*, 6859–6863.

116. M. Debruyne, V. Van Speybroeck, P. Van Der Voort, C. V. Stevens, *Green Chem.* **2021**, *23*, 7361–7434.

117. H. Salemi, M. Debruyne, V. Van Speybroeck, P. Van Der Voort, M. D'Hooghe, C. V. Stevens, *J. Mater. Chem. A* **2022**, *10*, 20707–20729.

118. J. Roeser, K. Kailasam, A. Thomas, *ChemSusChem* **2012**, *5*, 1793–1799.

119. O. Buyukcakir, S. H. Je, S. N. Talapaneni, D. Kim, A. Coskun, *ACS Appl. Mater. Interfaces* **2017**, *9*, 7209–7216.

120. T.-T. Liu, R. Xu, J.-D. Yi, J. Liang, X.-S. Wang, P.-C. Shi, Y.-B. Huang, R. Cao, *ChemCatChem* **2018**, *10*, 2036–2040.

121. Y.-M. Li, L. Yang, L. Sun, L. Ma, W.-Q. Deng, Z. Li, *J. Mater. Chem. A* **2019**, *7*, 26071–26076.

122. H. S. Jena, C. Krishnaraj, J. Schmidt, K. Leus, K. Van Hecke, P. Van Der Voort, *Chem. Eur. J.* **2020**, *26*, 1548–1557.

123. S. Abednatanzi, P. G. Derakhshandeh, K. Leus, H. Vrielinck, F. Callens, J. Schmidt, A. Savateev, P. Van Der Voort, *Sci. Adv.* **2020**, *6*, eaaz2310.

124. S. Abednatanzi, P. G. Derakhshandeh, S. Dalapati, S. K. P. Veerapandian, A.-C. Froissart, J. D. Epping, R. Morent, N. De Geyter, P. Van Der Voort, *ACS Appl. Mater. Interfaces* **2022**, *14*, 15287–15297.

125. Z. Qian, Z. J. Wang, K. A. I. Zhang, *Chem. Mater.* **2021**, *33*, 1909–1926.

126. Y. Zhang, H. Lv, Z. Zhang, L. Wang, X. Wu, H. Xu, *Adv. Mater.* **2021**, *33*, 2008264.

127. L. He, F. Weniger, H. Neumann, M. Beller, *Angew. Chem. Int. Ed.* **2016**, *55*, 12582–12594.

128. M. Soorholtz, L. C. Jones, D. Samuelis, C. Weidenthaler, R. J. White, M.-M. Titirici, D. A. Cullen, T. Zimmermann, M. Antonietti, J. Maier, R. Palkovits, B. F. Chmelka, F. Schüth, *ACS Catal.* **2016**, *6*, 2332–2340.

129. R. A. Periana, D. J. Taube, S. Gamble, H. Taube, T. Satoh, H. Fujii, *Science* **1998**, *280*, 560–564.

130. C. E. Chan-Thaw, A. Villa, P. Katekomol, D. Su, A. Thomas, L. Prati, *Nano Lett.* **2010**, *10*, 537–541.

131. C. E. Chan-Thaw, A. Villa, L. Prati, A. Thomas, *Chem. Eur. J.* **2011**, *17*, 1052–1057.

132. T. He, L. Liu, G. Wu, P. Chen, *J. Mater. Chem. A* **2015**, *3*, 16235–16241.

133. W.-H. Wang, Y. Himeda, J. T. Muckerman, G. F. Manbeck, E. Fujita, *Chem. Rev.* **2015**, *115*, 12936–12973.

134. A. V. Bavykina, M. G. Goesten, F. Kapteijn, M. Makkee, J. Gascon, *ChemSusChem* **2015**, *8*, 809–812.

135. A. V. Bavykina, E. Rozhko, M. G. Goesten, T. Wezendonk, B. Seoane, F. Kapteijn, M. Makkee, J. Gascon, *ChemCatChem* **2016**, *8*, 2217–2221.

136. A. V. Bavykina, A. I. Olivos-Suarez, D. Osadchii, R. Valecha, R. Franz, M. Makkee, F. Kapteijn, J. Gascon, *ACS Appl. Mater. Interfaces* **2017**, *9*, 26060–26065.

137. K. Park, G. H. Gunasekar, N. Prakash, K.-D. Jung, S. Yoon, *ChemSusChem* **2015**, *8*, 3410–3413.

138. G. H. Gunasekar, K. Park, H. Jeong, K.-D. Jung, K. Park, S. Yoon, *Catalysts* **2018**, *8*, 295.

139. G. H. Gunasekar, J. Shin, K.-D. Jung, K. Park, S. Yoon, *ACS Catal.* **2018**, *8*, 4346–4353.

140. G. H. Gunasekar, K. Park, V. Ganesan, K. Lee, N.-K. Kim, K.-D. Jung, S. Yoon, *Chem. Mater.* **2017**, *29*, 6740–6748.

141. P. Sudakar, G. H. Gunasekar, I. H. Baek, S. Yoon, *Green Chem.* **2016**, *18*, 6456–6461.

142. S. Padmanaban, G. H. Gunasekar, M. Lee, S. Yoon, *ACS Sustain. Chem. Eng.* **2019**, *7*, 8893–8899.

143. G. H. Gunasekar, K.-D. Jung, S. Yoon, *Inorg. Chem.* **2019**, *58*, 3717–3723.

144. K. Park, G. H. Gunasekar, S.-H. Kim, H. Park, S. Kim, K. Park, K.-D. Jung, S. Yoon, *Green Chem.* **2020**, *22*, 1639–1649.

145. A. Iemhoff, M. Vennewald, J. Artz, C. Mebrahtu, A. Meledin, T. E. Weirich, H. Hartmann, A. Besmehn, M. Aramini, F. Venturini, F. W. Mosselmans, G. Held, R. Arrigo, R. Palkovits, *ChemCatChem* **2022**, *14*, e202200179.

146. Q.-Q. Dang, C.-Y. Liu, X.-M. Wang, X.-M. Zhang, *ACS Appl. Mater. Interfaces* **2018**, *10*, 27972–27978.

147. Z. Wang, C. Liu, Y. Huang, Y. Hu, B. Zhang, *Chem. Commun.* **2016**, *52*, 2960–2963.

148. S. Rajendiran, P. Natarajan, S. Yoon, *RSC Adv.* **2017**, *7*, 4635–4638.

149. S. Rajendiran, K. Park, K. Lee, S. Yoon, *Inorg. Chem.* **2017**, *56*, 7270–7277.

150. Z. Guo, H. Wang, Z. Lv, Z. Wang, T. Nie, W. Zhang, *J. Organomet. Chem.* **2011**, *696*, 3668–3672.

151. J. Artz, S. Mallmann, R. Palkovits, *ChemSusChem* **2015**, *8*, 672–679.

152. J. Artz, R. Palkovits, *ChemSusChem* **2015**, *8*, 3832–3838.

153. S. Abednatanzi, P. G. Derakhshandeh, P. Tack, F. Muniz-Miranda, Y. Y. Liu, J. Everaert, M. Meledina, F. Vanden Bussche, L. Vincze, C. V. Stevens, V. Van Speybroeck, H. Vrielinck, F. Callens, K. Leus, P. Van Der Voort, *Appl. Catal. B Environ.* **2020**, *269*, 118769.

154. Y. Xiong, X. Zhang, *Chin. J. Chem .* **2011**, *29*, 1143–1148.

155. P. Liu, J. Yang, Y. Ai, S. Hao, X. Chen, F. Li, *J. Catal.* **2021**, *396*, 281–290.

156. C. Yang, S. Hao, L. Shen, P. Liu, J. Yang, F. Li, *Mater. Chem. Front.* **2022**, *6*, 3006–3015.

157. H. S. Jena, C. Krishnaraj, G. Wang, K. Leus, J. Schmidt, N. Chaoui, P. Van Der Voort, *Chem. Mater.* **2018**, *30*, 4102–4111.

158. E. C. Constable, P. J. Steel, *Coord. Chem. Rev.* **1989**, *93*, 205–223.

159. C. Kaes, A. Katz, M. W. Hosseini, *Chem. Rev.* **2000**, *100*, 3553–3590.

160. D. W. Thompson, A. Ito, T. J. Meyer, *Pure Appl. Chem.* **2013**, *85*, 1257–1305.

161. I. A. I. Mkhalid, J. H. Barnard, T. B. Marder, J. M. Murphy, J. F. Hartwig, *Chem. Rev.* **2010**, *110*, 890–931.

162. N. Elgrishi, M. B. Chambers, X. Wang, M. Fontecave, *Chem. Soc. Rev.* **2017**, *46*, 761–796.

163. L. Tong, R. P. Thummel, *Chem. Sci.* **2016**, *7*, 6591–6603.

164. Y.-J. Yuan, Z.-T. Yu, D.-Q. Chen, Z.-G. Zou, *Chem. Soc. Rev.* **2017**, *46*, 603–631.

165. F. Gao, Y. Wang, J. Zhang, D. Shi, M. Wang, R. Humphry-Baker, P. Wang, S. M. Zakeeruddin, M. Grätzel, *Chem. Commun.* **2008**, 2635–2637.

166. B. Pashaei, S. Karimi, H. Shahroosvand, P. Abbasi, M. Pilkington, A. Bartolotta, E. Fresta, J. Fernandez-Cestau, R. D. Costa, F. Bonaccorso, *Chem. Soc. Rev.* **2019**, *48*, 5033–5139.

167. S. Monro, K. L. Colón, H. Yin, J. Roque, P. Konda, S. Gujar, R. P. Thummel, L. Lilge, C. G. Cameron, S. A. McFarland, *Chem. Rev.* **2019**, *119*, 797–828.

168. G. F. Swiegers, T. J. Malefetse, *Chem. Rev.* **2000**, *100*, 3483–3538.

169. F. E. Poynton, S. A. Bright, S. Blasco, D. C. Williams, J. M. Kelly, T. Gunnlaugsson, *Chem. Soc. Rev.* **2017**, *46*, 7706–7756.

170. V. Marin, E. Holder, R. Hoogenboom, U. S. Schubert, *Chem. Soc. Rev.* **2007**, *36*, 618–635.

171. G. R. Newkome, E. He, C. N. Moorefield, *Chem. Rev.* **1999**, *99*, 1689–1746.

172. K. Manna, T. Zhang, F. X. Greene, W. Lin, *J. Am. Chem. Soc.* **2015**, *137*, 2665–2673.

173. U. S. Schubert, C. Eschbaumer, *Angew. Chem. Int. Ed.* **2002**, *41*, 2892–2926.

174. S. Hug, M. E. Tauchert, S. Li, U. E. Pachmayr, B. V. Lotsch, *J. Mater. Chem.* **2012**, *22*, 13956–13964.

175. N. Tahir, F. Muniz-Miranda, J. Everaert, P. Tack, T. Heugebaert, K. Leus, L. Vincze, C. V. Stevens, V. Van Speybroeck, P. Van der Voort, *J. Catal.* **2019**, *371*, 135–143.

176. G. Watson, P. G. Derakhshandeh, S. Abednatanzi, J. Schmidt, K. Leus, P. Van der Voort, *Molecules* **2021**, *26*.

177. Merck KGaA, Sigma-Aldrich Catalogue: [2,2'-Bipyridine]-5,5'-dicarbonitrile (accessed July 7, 2021), https://www.sigmaaldrich.com/BE/en/product/bldpharmatechltd/bl3h160bbc59?context=bbe.

178. P. N. W. Baxter, J. A. Connor, *J. Organomet. Chem.* **1988**, *355*, 193–196.

179. C. Janiak, S. Deblon, H.-P. Wu, *Synth. Commun.* **1999**, *29*, 3341–3352.

180. C. P. Whittle, *J. Heterocycl. Chem.* **1977**, *14*, 191–194.

181. L.-Y. Liao, X.-R. Kong, X.-F. Duan, *J. Org. Chem.* **2014**, *79*, 777–782.

182. M. Zembayashi, K. Tamao, J.-i. Yoshida, M. Kumada, *Tetrahedron Lett.* **1977**, *18*, 4089–4091.

183. J. E. M. Lewis, R. J. Bordoli, M. Denis, C. J. Fletcher, M. Galli, E. A. Neal, E. M. Rochette, S. M. Goldup, *Chem. Sci.* **2016**, *7*, 3154–3161.

184. F. M. Romero, R. Ziessel, *Tetrahedron Lett.* **1995**, *36*, 6471–6474.

185. D. M. D'Souza, D. A. Leigh, M. Papmeyer, S. L. Woltering, *Nat. Protoc.* **2012**, *7*, 2022–2028.

186. E. Hayashi, N. Shimada, *Yakugaku Zasshi* **1977**, *97*, 123–126.

187. H. Wang, Y. Pei, J. Bai, J. Zhang, Y. Wu, X. Cui, *RSC Adv.* **2014**, *4*, 26244–26246.

188. A. K. Jha, N. Jain, *Eur. J. Org. Chem.* **2017**, *2017*, 4765–4772.

189. J. R. Quinn, S. C. Zimmerman, *J. Org. Chem.* **2005**, *70*, 7459–7467.

190. L. Garuti, M. Roberti, A. Pession, E. Leoncini, S. Hrelia, *Biorg. Med. Chem. Lett.* **2001**, *11*, 3147-3149.

191. J. M. Veauthier, C. N. Carlson, G. E. Collis, J. L. Kiplinger, K. D. John, *Synthesis* **2005**, 2683–2686.

192. A. Lützen, M. Hapke, *Eur. J. Org. Chem.* **2002**, *2002*, 2292-2297.

193. P. Yu, B. Morandi, *Angew. Chem. Int. Ed.* **2017**, *56*, 15693–15697.

194. S. Singh, Samantha L. Cooper, J. R. Glenn, J. Beresford, L. R. Percival, J. D. A. Tyndall, S. J. Hill, L. E. Kilpatrick, A. J. Vernall, *RSC Adv.* **2018**, *8*, 16362–16369.

195. F. Su, Z. Sun, W. Su, X. Liang, *J. Mol. Struct.* **2018**, *1173*, 690–696.

196. O. V. Dolomanov, L. J. Bourhis, R. J. Gildea, J. A. K. Howard, H. Puschmann, *J. Appl. Crystallogr.* **2009**, *42*, 339–341.

197. G. Sheldrick, *Acta Crystallogr. Sect. A* **2015**, *71*, 3–8.

198. G. Sheldrick, *Acta Crystallogr. Sect. C* **2015**, *71*, 3–8.

199. S. G. Davies, A. M. Fletcher, P. M. Roberts, J. E. Thomson, *Eur. J. Org. Chem.* **2019**, *2019*, 5093–5119.

200. Y. Matsumoto, R. Tsuzuki, A. Matsuhisa, T. Yoden, Y. Yamagiwa, I. Yanagisawa, T. Shibanuma, H. Nohira, *Biorg. Med. Chem.* **2000**, *8*, 393–404.

201. C. T. Eary, Z. S. Jones, R. D. Groneberg, L. E. Burgess, D. A. Mareska, M. D. Drew, J. F. Blake, E. R. Laird, D. Balachari, M. O'Sullivan, A. Allen, V. Marsh, *Biorg. Med. Chem. Lett.* **2007**, *17*, 2608–2613.

202. E. Vitaku, D. T. Smith, J. T. Njardarson, *J. Med. Chem.* **2014**, *57*, 10257–10274.

203. R. P. Law, S. J. Atkinson, P. Bamborough, C.-w. Chung, E. H. Demont, L. J. Gordon, M. Lindon, R. K. Prinjha, A. J. B. Watson, D. J. Hirst, *J. Med. Chem.* **2018**, *61*, 4317–4334.

204. H.-X. Lei, K. Zhang, Y.-X. Qin, R.-J. Dong, D.-Z. Chen, H. Zhou, X.-H. Sheng, *J. Mol. Struct.* **2021**, *1228*, 129485.

205. D. Cao, J. Yu, H. Wang, Z. Luo, X. Liu, L. He, J. Qi, L. Fan, L. Tang, Z. Chen, J. Li, J. Cheng, S. Wang, *Science* **2022**, *375*, 403–411.

206. X. Zhang, H. Xu, H. Su, X. Yang, T. Sun, X. Lu, F. Shi, H. Duan, X. Liu, Y. Ling, *J. Agric. Food. Chem.* **2022**, *70*, 1776–1787.

207. H. A. Blair, *Drugs* **2020**, *80*, 417–423.

208. V. Satam, R. Rajule, S. Bendre, P. Bineesh, V. Kanetkar, *J. Heterocycl. Chem.* **2009**, *46*, 221–225.

209. Y. Chandrasekaran, G. K. Dutta, R. B. Kanth, S. Patil, *Dyes and Pigments* **2009**, *83*, 162–167.

210. A. Wojcik, R. Nicolaescu, P. V. Kamat, Y. Chandrasekaran, S. Patil, *J. Phys. Chem. A* **2010**, *114*, 2744–2750.

211. W. Chen, S. Xu, J. J. Day, D. Wang, M. Xian, *Angew. Chem. Int. Ed.* **2017**, *56*, 16611–16615.

212. S. J. Benkovic, P. A. Benkovic, D. R. Comfort, *J. Am. Chem. Soc.* **1969**, *91*, 5270–5279.

213. F. Lovering, J. Bikker, C. Humblet, *J. Med. Chem.* **2009**, *52*, 6752–6756.

214. M. Aldeghi, S. Malhotra, D. L. Selwood, A. W. E. Chan, *Chem. Biol. Drug Des.* **2014**, *83*, 450–461.

215. Y.-G. Zhou, *Acc. Chem. Res.* **2007**, *40*, 1357–1366.

216. D.-S. Wang, Q.-A. Chen, S.-M. Lu, Y.-G. Zhou, *Chem. Rev.* **2012**, *112*, 2557–2590.

217. R. Gunasekar, R. L. Goodyear, I. P. Silvestri, J. Xiao, *Org. Biomol. Chem.* **2022**, *20*, 1794–1827.

218. D. Wang, D. Astruc, *Chem. Rev.* **2015**, *115*, 6621–6686.

219. R. Nie, Y. Tao, Y. Nie, T. Lu, J. Wang, Y. Zhang, X. Lu, C. C. Xu, *ACS Catal.* **2021**, *11*, 1071–1095.

220. A. Robertson, T. Matsumoto, S. Ogo, *Dalton Trans.* **2011**, *40*, 10304–10310.

221. Y. Wei, X. Wu, C. Wang, J. Xiao, *Catal. Today* **2015**, *247*, 104–116.

222. D. Talwar, H. Y. Li, E. Durham, J. Xiao, *Chem. Eur. J.* **2015**, *21*, 5370–5379.

223. J. Fidalgo, M. Ruiz-Castañeda, G. García-Herbosa, A. Carbayo, F. A. Jalón, A. M. Rodríguez, B. R. Manzano, G. Espino, *Inorg. Chem.* **2018**, *57*, 14186–14198.

224. X. Wu, X. Li, W. Hems, F. King, J. Xiao, *Org. Biomol. Chem.* **2004**, *2*, 1818–1821.

225. X. Wu, X. Li, F. King, J. Xiao, *Angew. Chem. Int. Ed.* **2005**, *44*, 3407–3411.

226. X. Wu, X. Li, A. Zanotti-Gerosa, A. Pettman, J. Liu, A. J. Mills, J. Xiao, *Chem. Eur. J.* **2008**, *14*, 2209–2222.

227. Q. Lei, Y. Wei, D. Talwar, C. Wang, D. Xue, J. Xiao, *Chem. Eur. J.* **2013**, *19*, 4021–4029.

228. M. Liu, L. Guo, S. Jin, B. Tan, *J. Mater. Chem. A* **2019**, *7*, 5153–5172.

229. C. Krishnaraj, H. S. Jena, K. Leus, P. Van Der Voort, *Green Chem.* **2020**, *22*, 1038–1071.

230. A. Iemhoff, M. Vennewald, R. Palkovits, *Angew. Chem. Int. Ed.* **2023**, *62*, e202212015.

231. L. Zhang, R. Qiu, X. Xue, Y. Pan, C. Xu, H. Li, L. Xu, *Adv. Synth. Catal.* **2015**, *357*, 3529–3537.

232. J. Everaert, M. Debruyne, F. Vanden Bussche, K. Van Hecke, T. S. A. Heugebaert, P. Van Der Voort, V. Van Speybroeck, C. V. Stevens, *Synthesis* **2023**, *55*, 333–340.

233. D. Y. Osadchii, A. I. Olivos-Suarez, A. V. Bavykina, J. Gascon, *Langmuir* **2017**, *33*, 14278–14285.

234. A. V. Neimark, Y. Lin, P. I. Ravikovitch, M. Thommes, *Carbon* **2009**, *47*, 1617–1628.

235. M. Ayiania, M. Smith, A. J. R. Hensley, L. Scudiero, J.-S. McEwen, M. Garcia-Perez, *Carbon* **2020**, *162*, 528–544.

236. K. Stańczyk, R. Dziembaj, Z. Piwowarska, S. Witkowski, *Carbon* **1995**, *33*, 1383–1392.

237. K. Artyushkova, *J. Vac. Sci. Technol. A* **2020**, *38*, 031002.

238. F. M. Wisser, P. Berruyer, L. Cardenas, Y. Mohr, E. A. Quadrelli, A. Lesage, D. Farrusseng, J. Canivet, *ACS Catal.* **2018**, *8*, 1653–1661.

239. Y. Hayashi, K. Toriumi, K. Isobe, *J. Am. Chem. Soc.* **1988**, *110*, 3666–3668.

240. S. Ogo, T. Abura, Y. Watanabe, *Organometallics* **2002**, *21*, 2964–2969.

241. C. Wang, C. Li, X. Wu, A. Pettman, J. Xiao, *Angew. Chem. Int. Ed.* **2009**, *48*, 6524–6528.

242. S. Ogo, N. Makihara, Y. Kaneko, Y. Watanabe, *Organometallics* **2001**, *20*, 4903–4910.

243. T. Abura, S. Ogo, Y. Watanabe, S. Fukuzumi, *J. Am. Chem. Soc.* **2003**, *125*, 4149–4154.

244. J. Tan, W. Tang, Y. Sun, Z. Jiang, F. Chen, L. Xu, Q. Fan, J. Xiao, *Tetrahedron* **2011**, *67*, 6206–6213.

245. A. Albert, in *Physical Methods in Heterocyclic Chemistry, Vol. 3* (Ed.: A. R. Katritzky), Academic Press, New York, **1971**, pp. 1–26.

246. H.-Y. T. Chen, C. Wang, X. Wu, X. Jiang, C. R. A. Catlow, J. Xiao, *Chem. Eur. J.* **2015**, *21*, 16564–16577.

247. F. Fontana, F. Minisci, M. C. Nogueira Barbosa, E. Vismara, *Tetrahedron* **1990**, *46*, 2525–2538.

248. J. Figueras, *J. Org. Chem.* **1966**, *31*, 803–806.

249. R. A. Archer, H. S. Mosher, *J. Org. Chem.* **1967**, *32*, 1378–1381.

250. Z. Zhang, H. Du, *Angew. Chem. Int. Ed.* **2015**, *54*, 623–626.

251. L. Wang, J. Lin, C. Xia, W. Sun, *J. Org. Chem.* **2021**, *86*, 16641–16651.

252. A. Hisrch, D. G. Orphanos, *J. Heterocycl. Chem.* **1966**, *3*, 38–41.

253. C.-K. Sha, C.-P. Tsou, *J. Chin. Chem. Soc.* **1991**, *38*, 183–186.

254. D. Prat, A. Wells, J. Hayler, H. Sneddon, C. R. McElroy, S. Abou-Shehada, P. J. Dunn, *Green Chem.* **2016**, *18*, 288–296.

255. K. Matsui, Y. Maegawa, M. Waki, S. Inagaki, Y. Yamamoto, *Catal. Sci. Technol.* **2018**, *8*, 534–539.

256. B. Vilhanová, J. A. van Bokhoven, M. Ranocchiari, *Adv. Synth. Catal.* **2017**, *359*, 677–686.

257. L. Tao, Q. Zhang, S.-S. Li, X. Liu, Y.-M. Liu, Y. Cao, *Adv. Synth. Catal.* **2015**, *357*, 753–760.

258. J.-F. Zhang, R. Zhong, Q. Zhou, X. Hong, S. Huang, H.-Z. Cui, X.-F. Hou, *ChemCatChem* **2017**, *9*, 2496–2505.

259. G. Li, H. Yang, H. Zhang, Z. Qi, M. Chen, W. Hu, L. Tian, R. Nie, W. Huang, *ACS Catal.* **2018**, *8*, 8396–8405.

260. A. K. Kar, R. Srivastava, *ACS Sustain. Chem. Eng.* **2019**, *7*, 13136–13147.

261. R. S. B. Gonçalves, A. B. V. de Oliveira, H. C. Sindra, B. S. Archanjo, M. E. Mendoza, L. S. A. Carneiro, C. D. Buarque, P. M. Esteves, *ChemCatChem* **2016**, *8*, 743–750.

262. N. Wang, F. Wang, F. Pan, S. Yu, D. Pan, *ACS Appl. Mater. Interfaces* **2021**, *13*, 3209–3220.

263. G. Vilé, D. Ng, Z. Xie, I. Martinez-Botella, J. Tsanaktsidis, C. H. Hornung, *ChemCatChem* **2022**, *14*, e202101941.

264. J. Rouquerol, P. Llewellyn, F. Rouquerol, in *Stud. Surf. Sci. Catal., Vol. 160* (Eds.: P. L. Llewellyn, F. Rodriquez-Reinoso, J. Rouqerol, N. Seaton), Elsevier, Amsterdam, **2007**, pp. 49–56.

265. W. Tang, L. Xu, Q.-H. Fan, J. Wang, B. Fan, Z. Zhou, K.-h. Lam, A. S. C. Chan, *Angew. Chem. Int. Ed.* **2009**, *48*, 9135–9138.

266. M. Darabantu, L. Boully, A. Turck, N. Plé, *Tetrahedron* **2005**, *61*, 2897–2905.

267. J. Peralta-Cruz, M. Díaz-Fernández, A. Ávila-Castro, D. Ortegón-Reyna, A. Ariza-Castolo, *New J. Chem.* **2016**, *40*, 5501–5515.

268. J. Qin, F. Chen, Z. Ding, Y.-M. He, L. Xu, Q.-H. Fan, *Org. Lett.* **2011**, *13*, 6568–6571.

269. A. Go, G. Lee, J. Kim, S. Bae, B. M. Lee, B. H. Kim, *Tetrahedron* **2015**, *71*, 1215–1226.

270. G. H. Fisher, H. P. Schultz, *J. Org. Chem.* **1974**, *39*, 635–640.

271. N. Mršić, T. Jerphagnon, A. J. Minnaard, B. L. Feringa, J. G. de Vries, *Adv. Synth. Catal.* **2009**, *351*, 2549–2552.

272. S. Li, W. Meng, H. Du, *Org. Lett.* **2017**, *19*, 2604–2606.

273. W. Yoshihisa, O. Tetsuo, T. Yasushi, H. Takao, T. Yasuo, *Bull. Chem. Soc. Jpn.* **1984**, *57*, 2440–2444.

274. J. R. Cabrero-Antonino, R. Adam, K. Junge, R. Jackstell, M. Beller, *Catal. Sci. Technol.* **2017**, *7*, 1981–1985.

275. C. Bianchini, V. Dal Santo, A. Meli, S. Moneti, R. Psaro, L. Sordelli, F. Vizza, *Inorg. Chim. Acta* **2008**, *361*, 3677–3680.

276. W. M. Czaplik, J.-M. Neudörfl, A. J. von Wangelin, *Green Chem.* **2007**, *9*, 1163–1165.

277. J. Wu, C. Wang, W. Tang, A. Pettman, J. Xiao, *Chem. Eur. J.* **2012**, *18*, 9525–9529.

278. F. Chen, B. Sahoo, C. Kreyenschulte, H. Lund, M. Zeng, L. He, K. Junge, M. Beller, *Chem. Sci.* **2017**, *8*, 6239–6246.

279. J. De Ketelaere, Metaalvrije, CTF-gekatalyseerde benzylische oxidaties in flowreactoren. Master thesis, Ghent University **2021**.

280. Y. Shao, J. Sui, G. Yin, Y. Gao, *Appl. Catal. B Environ.* **2008**, *79*, 89–99.

281. M. Inagaki, M. Toyoda, Y. Soneda, T. Morishita, *Carbon* **2018**, *132*, 104–140.

282. H. Zheng, S. Shi, X. Wang, L. Zhao, G. Zhu, M. Liu, J. Gao, J. Xu, *ChemistrySelect* **2019**, *4*, 5073–5080.

283. K. Yamaguchi, N. Mizuno, *Chem. Eur. J.* **2003**, *9*, 4353–4361.

284. D. I. Enache, J. K. Edwards, P. Landon, B. Solsona-Espriu, A. F. Carley, A. A. Herzing, M. Watanabe, C. J. Kiely, D. W. Knight, G. J. Hutchings, *Science* **2006**, *311*, 362–365.

285. R. E. Rodríguez-Lugo, M. A. Chacón-Terán, S. De León, M. Vogt, A. J. Rosenthal, V. R. Landaeta, *Dalton Trans.* **2018**, *47*, 2061–2072.

286. B. Zhu, M. Lazar, B. G. Trewyn, R. J. Angelici, *J. Catal.* **2008**, *260*, 1–6.

287. K. Gopalaiah, A. Saini, *Catal. Lett.* **2016**, *146*, 1648–1654.

288. D. S. Su , J. Zhang, B. Frank, A. Thomas, X. Wang, J. Paraknowitsch, R. Schlögl, *ChemSusChem* **2010**, *3*, 169–180.

289. L. Liu, Y.-P. Zhu, M. Su, Z.-Y. Yuan, *ChemCatChem* **2015**, *7*, 2765–2787.

290. N. E. Leadbeater, *Nat. Chem.* **2010**, *2*, 1007–1009.

291. L. K. Boerner, in *C&EN, Vol. 100*, **2022**, pp. 20–26.

292. C. A. Hone, C. O. Kappe, *Top. Curr. Chem.* **2018**, *377*, 2.

293. B. Pieber, C. O. Kappe, in *Organometallic Flow Chemistry* (Ed.: T. Noël), Springer International Publishing, Cham, **2016**, pp. 97–136.

294. H. P. L. Gemoets, Y. Su, M. Shang, V. Hessel, R. Luque, T. Noël, *Chem. Soc. Rev.* **2016**, *45*, 83–117.

295. S. Kobayashi, H. Ishitani, *Chem. Rev.* **1999**, *99*, 1069–1094.

296. A. M. Meireles, V. S. da Silva, J. S. Rebouças, D. C. da Silva Martins, *ChemistrySelect* **2019**, *4*, 3275–3280.

297. W. J. Gammon, O. Kraft, A. C. Reilly, B. C. Holloway, *Carbon* **2003**, *41*, 1917–1923.

298. M. A. Bajada, A. Vijeta, A. Savateev, G. Zhang, D. Howe, E. Reisner, *ACS Appl. Mater. Interfaces* **2020**, *12*, 8176–8182.

299. F. Su, S. C. Mathew, L. Möhlmann, M. Antonietti, X. Wang, S. Blechert, *Angew. Chem. Int. Ed.* **2011**, *50*, 657–660.

300. X. Qiu, C. Len, R. Luque, Y. Li, *ChemSusChem* **2014**, *7*, 1684–1688.

301. H. Watanabe, S. Asano, S.-i. Fujita, H. Yoshida, M. Arai, *ACS Catal.* **2015**, *5*, 2886–2894.

302. O. V. Zalomaeva, O. Y. Podyacheva, A. N. Suboch, L. S. Kibis, O. A. Kholdeeva, *Appl. Catal. A Gen.* **2022**, *629*, 118424.

303. F. Su, S. C. Mathew, G. Lipner, X. Fu, M. Antonietti, S. Blechert, X. Wang, *J. Am. Chem. Soc.* **2010**, *132*, 16299–16301.

304. P. Eisenberger, A. M. Bailey, C. M. Crudden, *J. Am. Chem. Soc.* **2012**, *134*, 17384–17387.

305. A. Jiménez-Almarza, A. López-Magano, R. Mas-Ballesté, J. Alemán, *ACS Appl. Mater. Interfaces* **2022**, *14*, 16258–16268.

306. M. Debruyne, Development of porous organic polymers as heterogeneous photocatalysts. PhD thesis, Ghent University **2023**.

307. J. Liu, W. Zan, K. Li, Y. Yang, F. Bu, Y. Xu, *J. Am. Chem. Soc.* **2017**, *139*, 11666-11669.

308. V. Papa, Y. Cao, A. Spannenberg, K. Junge, M. Beller, *Nat. Catal.* **2020**, *3*, 135–142.

Curriculum vitae

Personalia

Jonas Everaert

Experience

2017–present PhD candidate in Bioscience Engineering: Chemistry and Bioprocess Technology
SynBioC Research Group, Department of Green Chemistry and Technology
Faculty of Bioscience Engineering, Ghent University

PhD thesis	Synthesis and application of covalent triazine frameworks in heterogeneous catalysis
Promotors	Prof. dr. ir. Christian Stevens Prof. dr. ir. Veronique Van Speybroeck
Funding	2018–2022 Research Foundation - Flanders (FWO) 2017–2018 Special Research Fund (BOF-GOA), Ghent University

Education

2014–2016 Master of Science in Bioscience Engineering: Chemistry and Bioprocess Technology
Faculty of Bioscience Engineering, Ghent University

Master thesis	Chemical modification of petroselinic acid-based sophorolipids
Promotors	Prof. dr. ir. Christian Stevens Prof. dr. ir. Inge Van Bogaert
Award	DOW Chemical Prize for Sustainable Chemistry 2016

2011–2014 Bachelor of Science in Bioscience Engineering: Chemistry and Food Technology
Faculty of Bioscience Engineering, Ghent University

Bachelor thesis	The use of affinity tags in protein purification
Promotor	Prof. dr. Tom Desmet

Scientific publications in international peer-reviewed journals (A1)

1. M. Debruyne, S. Borgmans, S. Radhakrishnan, E. Breynaert, H. Vrielinck, K. Leus, A. Laemont, J. De Vos, K. Singh Rawat, S. Vanlommel, H. Rijckaert, H. Salemi, **J. Everaert**, F. Vanden Bussche, D. Poelman, R. Morent, N. De Geyter, P. Van Der Voort, V. Van Speybroeck, C. V. Stevens. Engineering of phenylpyridine- and bipyridine-based covalent organic frameworks for the photocatalytic tandem aerobic oxidation/Povarov cyclization. *Submitted*

2. **J. Everaert**, K. Leus, H. Rijkaert, M. Debruyne, K. Van Hecke, V. Van Speybroeck, P. Van Der Voort, C. V. Stevens. Recyclable rhodium catalyst anchored onto bipyridine covalent triazine framework for transfer hydrogenation of N-heteroarenes in water. *Green Chem.* **2023**, *25*, 3267–3277. (IF 11.034)

3. M. Pala, **J. Everaert**, A. Ollivier, R. Raeymaekers, K. Quataert, S. L. K. W. Roelants, W. Soetaert, C. V. Stevens. Ozonolysis of symmetrical bola sophorosides yields key precursors for the development of functional sophorolipid derivatives. *ACS Sustain. Chem. Eng.* **2022**, *10*, 12234–12244. (IF 9.224)

4. **J. Everaert**, M. Debruyne, F. Vanden Bussche, K. Van Hecke, T. S. A. Heugebaert, P. Van Der Voort, V. Van Speybroeck, C. V. Stevens. Synthesis of nitrile-functionalized polydentate N-heterocycles as building blocks for covalent triazine frameworks. *Synthesis* **2023**, *55*, 333–340. (Published online in 2021). (IF 3.019)

5. A. A. Ba, **J. Everaert**, A. Poirier, P. Le Griel, W. Soetaert, S. L. K. W. Roelants, D. Hermida-Merino, C. V. Stevens, N. Baccile. Synthesis and self-assembly of aminyl and alkynyl substituted sophorolipids. *Green Chem.* **2020**, *22*, 8323–8336. (IF 10.182)

6. L. De Bruecker, **J. Everaert**, P. Van Der Voort, C. V. Stevens, M. Waroquier, V. Van Speybroeck. Structural and photophysical properties of various polypyridyl ligands: A combined experimental and computational study. *ChemPhysChem* **2020**, *21*, 2489–2505. (IF 3.102)

7. F. Vanden Bussche, A. M. Kaczmarek, S. K. P. Veerapandian, **J. Everaert**, M. Debruyne, S. Abednatanzi, P. Van Der Voort, C. V. Stevens. N-rich porous polymer with isolated Tb^{3+}-ions displays unique temperature dependent behavior through the absence of thermal quenching. *Chem. Eur. J*. **2020**, *26*, 15596–15604. (IF 5.236)

8. S. Abednatanzi, P. G. Derakhshandeh, P. Tack, F. Muniz-Miranda, Y.-Y. Liu, **J. Everaert**, M. Meledina, F. Vanden Bussche, L. Vincze, C. V. Stevens, V. Van Speybroeck, H. Vrielinck, F. Callens, K. Leus, P. Van Der Voort. Elucidating the promotional effect of a covalent triazine framework in aerobic oxidation. *Appl. Catal. B Environ.* **2020**, *269*, 118769. (IF 19.503)

9. E. I. P. Delbeke, **J. Everaert**, O. Lozach, T. Le Gall, M. Berchel, T. Montier, P.-A. Jaffrès, P. Rigole, T. Coenye, M. Brennich, N. Baccile, S. L. K. W. Roelants, W. Soetaert, I. N. A. Van Bogaert, K. M. Van Geem, C. V. Stevens. Lipid-based quaternary ammonium sophorolipid amphiphiles with antimicrobial and transfection activities. *ChemSusChem* **2019**, *12*, 3642–3653. (IF 7.962)

10. N. Baccile, E. I. P. Delbeke, M. Brennich, C. Seyrig, **J. Everaert**, S. L. K. W. Roelants, W. Soetaert, I. N. A. Van Bogaert, K. M. Van Geem, C. V. Stevens. Asymmetrical, symmetrical, divalent, and Y-shaped (bola)amphiphiles: The relationship between the molecular structure and self-assembly in amino derivatives of sophorolipid biosurfactants. *J. Phys. Chem. B* **2019**, *123*, 3841–3858. (IF 2.857)

11. N. Tahir, F. Muniz-Miranda, **J. Everaert**, P. Tack, T. S. A. Heugebaert, K. Leus, L. Vincze, C. V. Stevens, V. Van Speybroeck, P. Van Der Voort. Immobilization of Ir(I) complex on covalent triazine frameworks for C–H borylation reactions: A combined experimental and computational study. *J. Catal.* **2019**, *371*, 135–143. (IF 7.888)

12. E. I. P. Delbeke, **J. Everaert**, O. Lozach, T. Le Gall, M. Berchel, T. Montier, P.-A. Jaffrès, P. Rigole, T. Coenye, M. Brennich, N. Baccile, S. L. K. W. Roelants, W. Soetaert, I. N. A. Van Bogaert, K. M. Van Geem, C. V. Stevens. Synthesis and biological evaluation of bolaamphiphilic sophorolipids. *ACS Sustain. Chem. Eng.* **2018**, *6*, 8992–9005. (IF 6.970)

13. E. I. P. Delbeke, **J. Everaert**, E. Uitterhaegen, S. Verweire, A. Verlee, T. Talou, W. Soetaert, I. N. A. Van Bogaert, C. V. Stevens. Petroselinic acid purification and its use for the fermentation of new sophorolipids. *AMB Express* **2016**, *6*, 28. (IF 1.825)

Active participations at conferences (C3)

1. **J. Everaert**, V. Van Speybroeck, P. Van Der Voort, C. V. Stevens. Rhodium anchored onto a covalent triazine framework as heterogeneous catalyst for transfer hydrogenation of N-heterocycles in water. **Oral presentation**, *Chemical Research in Flanders Symposium – Chemistry Conference for Young Scientists (CRF-ChemCYS 2022)*, October 12–14, **2022**, Blankenberge, Belgium.

2. **J. Everaert**, J. De Ketelaere, V. Van Speybroeck, P. Van Der Voort, C. V. Stevens. Covalent triazine frameworks as heterogeneous catalysts in metal-free aerobic oxidation and rhodium-catalyzed transfer hydrogenation. **Poster presentation**, *17th Belgian Organic Synthesis Symposium (BOSS XVII)*, July 3–8, **2022**, Namur, Belgium.

3. **J. Everaert**, N. Tahir, F. Muniz-Miranda, P. Tack, T. S. A. Heugebaert, K. Leus, L. Vincze, C. V. Stevens, V. Van Speybroeck, P. Van Der Voort. Immobilization of Ir(I) complex on covalent triazine frameworks for C–H borylation reactions: A combined experimental and computational study. **Poster presentation**, *2nd Chemical Research in Flanders Symposium (CRF-2)*, October 14–16, **2019**, Blankenberge, Belgium.

4. **J. Everaert**, E. I. P. Delbeke, I. N. A. Van Bogaert, C. V. Stevens. Chemical modification of petroselinic acid-based sophorolipids for high added-value applications **Poster presentation**, *21st Merck Organic Chemistry Symposium (MOCS)*, December 7–8, **2017**, Blankenberge, Belgium.

Other research projects closely involved

2020 – 2021 | Efficient synthesis of ω-glycoside biosurfactants
IOF-StarTT, Ghent University

2018 – 2020 | AppliSurf: development, characterization and application of a portfolio of new biosurfactants
VIS project, VLAIO

Tutoring of master thesis students and internship students

2020 – 2021 **Jolien De Ketelaere**
Metaalvrije, CTF-gekatalyseerde benzylische oxidaties in flowreactoren
Awarded with the INEOS Award for best thesis on sustainable chemistry

2020 – 2021 **Casper Van Poucke**
Towards a scalable modification procedure for boosting the antifouling activity of chitosan

2019 – 2020 **Cato Vanleysen**
Covalent triazine frameworks as a hive for rhodium complexes: A reusable catalyst for transfer hydrogenation
Awarded with the DOW Chemistry Award and the INEOS Award for best thesis on sustainable chemistry.

2018 – 2019 **Astrid Ollivier**
De ontwikkeling van veilige, groene en schaalbare methoden voor de chemische derivatisatie van bola sophorosiden

2018 **Abdoul Aziz Ba**
Modification chimique de glycolipides et de sophorolipides et études de leurs propriétés physico-chimiques